National Library
of Canada

Canadian Theses Service

Ottawa, Canada
K1A 0N4

Bibliothèque nationale
du Canada

Services des thèses canadiennes

CANADIAN THESES

NOTICE

The quality of this microfiche is heavily dependent upon the quality of the original thesis submitted for microfilming. Every effort has been made to ensure the highest quality of reproduction possible.

If pages are missing, contact the university which granted the degree.

Some pages may have indistinct print especially if the original pages were typed with a poor typewriter ribbon or if the university sent us an inferior photocopy.

Previously copyrighted materials (journal articles, published tests, etc.) are not filmed.

Reproduction in full or in part of this film is governed by the Canadian Copyright Act, R.S.C. 1970, c. C-30.

THIS DISSERTATION
HAS BEEN MICROFILMED
EXACTLY AS RECEIVED

THÈSES CANADIENNES

AVIS

La qualité de cette microfiche dépend grandement de la qualité de la thèse soumise au microfilmage. Nous avons tout fait pour assurer une qualité supérieure de reproduction.

S'il manque des pages, veuillez communiquer avec l'université qui a conféré le grade.

La qualité d'impression de certaines pages peut laisser à désirer, surtout si les pages originales ont été dactylographiées à l'aide d'un ruban usé ou si l'université nous a fait parvenir une photocopie de qualité inférieure.

Les documents qui font déjà l'objet d'un droit d'auteur (articles de revue, examens publiés, etc.) ne sont pas microfilmés.

La reproduction, même partielle, de ce microfilm est soumise à la Loi canadienne sur le droit d'auteur, SRC 1970, c. C-30.

LA THÈSE A ÉTÉ
MICROFILMÉE TELLE QUE
NOUS L'AVONS REÇUE

NL-339 (r. 86/06)

Canada

THE UNIVERSITY OF ALBERTA

# MEGAVOLTAGE PHOTON
# DOSE MODIFICATION RESULTING FROM
# TISSUE COMPENSATOR RETRACTION

by

©

DONALD MURRAY ROBINSON

A THESIS
SUBMITTED TO THE FACULTY OF GRADUATE STUDIES AND RESEARCH
IN PARTIAL FULFILMENT OF THE REQUIREMENTS OF THE DEGREE
OF MASTER OF SCIENCE

DEPARTMENT OF PHYSICS

EDMONTON, ALBERTA
FALL, 1986

Permission has been granted to the National Library of Canada to microfilm this thesis and to lend or sell copies of the film.

The author (copyright owner) has reserved other publication rights, and neither the thesis nor extensive extracts from it may be printed or otherwise reproduced without his/her written permission.

L'autorisation a été accordée à la Bibliothèque nationale du Canada de microfilmer cette thèse et de prêter ou de vendre des exemplaires du film.

L'auteur (titulaire du droit d'auteur) se réserve les autres droits de publication; ni la thèse ni de longs extraits de celle-ci ne doivent être imprimés ou autrement reproduits sans son autorisation écrite.

ISBN 0-315-32291-8

# THE UNIVERSITY OF ALBERTA

## RELEASE FORM

NAME OF AUTHOR: DONALD MURRAY ROBINSON

TITLE OF THESIS: "MEGAVOLTAGE PHOTON DOSE MODIFICATION RESULTING FROM TISSUE COMPENSATOR RETRACTION"

DEGREE FOR WHICH THESIS WAS PRESENTED: MASTER OF SCIENCE

YEAR THIS DEGREE GRANTED: 1986

Permission is hereby granted to THE UNIVERSITY OF ALBERTA LIBRARY to reproduce single copies of this thesis and to lend or sell such copies for private, scholarly or scientific research purposes only.

The author reserves other publication rights, and neither the thesis nor extensive extracts from it may be printed or otherwise reproduced without the authors's written permission.

Don Robinson

PERMANENT ADDRESS:

10419 68 AVE
EDMONTON, ALBERTA
CANADA, T6H 2A8

DATED: August 1, 1986

THE UNIVERSITY OF ALBERTA

FACULTY OF GRADUATE STUDIES AND RESEARCH

The undersigned certify that they have read, and recommend to the Faculty of Graduate Studies and Research, for acceptance, a thesis entitled

Megavoltage Photon
Dose Modification Resulting From
Tissue Compensator Retraction

submitted by Donald Murray Robinson in partial fulfillment of the requirements for the degree of Master of Science.

..............................

Supervisor

..............................

Douglas M Sheppard
..............................

..............................

..............................

Date

This work is dedicated to
my parents who equipped me
to begin this journey.

# Abstract

Tissue compensators are a widely used radiotherapy technique intended to accommodate large changes in patient contours. In order to preserve the build-up characteristics of high energy beams, resulting in so called "skin sparing" these compensators are commonly retracted away from the patient surface to a distance which will re-establish the open field build-up curve. To accommodate the change in geometry the lateral dimensions of the compensator are reduced while the thickness along any ray path remains fixed.

Removing the compensator from the surface results in a progressive change in the dose received at points within the phantom, and the nature and magnitude of the change is not readily predicted by simple analytical techniques.

Experimental results for $^{60}$Co, 6MV, and 15MV photon beams are investigated, for field sizes from 5X5cm$^2$ to 20X20cm$^2$, for depths in phantom up to 13cm, and for compensator materials of polystyrene and lead. These are compared with predictions based upon scatter and attenuation.

It is concluded that in many cases the magnitude of the resultant dose alteration is sufficient to warrant a

more accurate treatment than is presently undertaken.

# ACKNOWLEDGEMENTS

Many thanks go to the entire staff of the Medical Physics Department at the Cross Cancer Institute for their assistance during the course of this work. In particular, I would like to thank my supervisor, Dr. J.W. Scrimger, for his guidance and encouragement through our many stimulating and challenging discussions. Special thanks also goes to Dr. J.J. Battista and S.R. Usiskin who were always willing to talk through a problem or an idea.

I would also like to thank Colin Field, Rick Crilly, snd Wayne Logos for their assistance with many of the technical aspects of this work; Finn Mortensen and Frank Dolynchuk for the experimental apparatus and phantoms which they produced for me; and Sig Laban and Don Burdeniuk for their assistance with many aspects of the operation of the accelerators.

I wish to express my gratitude to Brenda Taylor for the generous donation of her time in the typing of portions of this thesis.

Finally I would like to thank Ken and Sue Light and Dylan and Bev Coe for their friendship and encouragement which made the completion of this work possible.

This work was sponsored by the Alberta Heritage

Foundation for Medical Research, The Provincial Cancer Hospitals Board (Alberta), and the Physics Department of the University of Alberta.

# TABLE OF CONTENTS

Chapter Page

I INTRODUCTION .............................. 1

II INTERACTION OF RADIATION WITH MATTER .... 6

2.1 Photon Interactions ................ 6

2.2.1 Photon Attenuation .......... 6

2.1.2 Coherent Scattering .......... 14

2.1.3 Photoelectric Effect ........ 17

2.1.4 Compton Scattering .......... 20

2.1.5 Pair and Triplet Production . 26

2.1.6 Other Interactions .......... 33

2.1.7 Relative Cross Sections ..... 37

2.2 Electron Interactions ............... 39

2.2.1 Interactions with Atomic Electrons .................... 39

2.2.1.1 Moller scattering ..... 42

2.2.1.2 Bhabha Scattering ..... 44

2.2.2 Interactions with the Nucleus ...................... 46

2.2.3 Stopping power .............. 48

2.2.4 Bremsstrahlung .............. 52

2.2.5 Positron Annihilation ....... 53

2.2.6 Electronic Range ............ 56

III THE PRODUCTION OF RADIATION FOR MEDICAL USE. 58

3.1 Cobalt 60 Radiation ................ 58

3.2 Medical Linear Accelerators ......... 62

3.2.1 Major Components ............ 62

3.2.2 Principles of Operation ..... 64

3.2.2.1 Microwave Power Supplies ............. 64

3.2.2.2 The Waveguide ........ 68

3.2.2.3 The Accelerator Structure ............ 68

3.2.2.4 The Bending Magnet ... 73

3.2.2.5 The treatment Head ... 75

IV DOSIMETRY .............................. 79

4.1 Energy Transfer ..................... 79

4.1.1 Basic Concepts .............. 79

4.1.2 Kerma ....................... 79

4.1.3 Electronic Equilibrium ...... 81

4.2 Cavity Theory ...................... 84

4.3 Methods of Photon Dosimetry ........ 92

4.3.1 Ionizational Methods ........ 92

4.3.1.1 Standard Air Chamber . 92

4.3.1.2 Practical Ion Chambers ............. 95

4.3.1.3 Solid State Detectors. 96

4.3.1.4 Thermoluminescent Detectors (TLD) ...... 97

4.3.2 Actinometry ................. 98

4.3.2.1 The Fricke Dosimeter . 98

4.3.2.2 Film Dosimetry ....... 100
4.3.3 Calorimetry ................ 101
4.4 Dosimetric Functions ............... 103
4.5.1 Tissue-Air Ratio ............ 104
4.5.2 Scatter-Air Ratio ........... 106
4.5.3 Tissue-Phantom Ratio ........ 108
4.5.4 Percentage Depth Dose ....... 110
V RETRACTED TISSUE COMPENSATORS .......... 112
5.1 Introduction ...................... 112
5.2 Experimental Parameters ............ 127
5.2.1 Experimental Setup .......... 127
5.2.2 Radiation Sources ........... 131
5.2.2.1 Cobalt 60 ............ 131
5.2.2.2 6MV .................. 131
5.2.2.3 15MV ................. 132
5.2.3 Dosimetry Devices ........... 133
5.3 Experimental Results ............... 134
5.3.1 Alteration of Surface Dose .. 135
5.3.1.1 Analysis .............. 155
5.3.2 Alteration of Dose at Depth . 167
5.3.2.1 Analysis ............. 193
5.4 Scatter and Attenuation ............. 229
5.4.1 Quantitative Analysis of the Experimental Data ........... 229
5.4.2 End Point Calculations ...... 232
5.4.3 ATP Predictions ............. 241

5.4.4 Pedagogic Model Predictions . 244

5.5 Monte Carlo Modeling ............... 247

5.5.1 EGS Results ................ 251

VI CONCLUSIONS ........................ 256

REFERENCES ............................ 258

# LIST OF TABLES

Table Page

1. Photon interactions with matter. .............. 36

2. Cross sections for polystyrene and lead at $^{60}$Co, 6MV, and 15MV. ...................... 166

3. Comparison between experiment and end point calculations, ATP, and the Pedagogic model at $^{60}$Co. ...................... 235

4. Comparison between experiment and end point calculations, ATP, and the Pedagogic model at 6MV. ...................... 236

5. Comparison between experiment and end point calculations, ATP, and the Pedagogic model at 15MV. ...................... 237

## LIST OF FIGURES

Figure Page

1. Restoration of partial skin sparing by compensator retraction. .......................... 4
2. Attenuation of a narrow parallel beam by a thin absorber. ................................ 7
3. Attenuation by means of scattering and absorption. ........................................ 9
4. Attenuation modified by scatter from a broad beam ........................................... 9
5. Scattering of photons through an angle into the solid angle d . ........................ 13
6. Coherent(or Rayleigh) scattering. .............. 16
7. The photoelectric effect. ...................... 18
8. Photoelectric cross sections for water and lead. ............................................ 19
9. Compton scattering. ............................ 21
10. The angular distribution of compton scattered photons. ............................... 24
11. The angular distribution of compton recoil electrons. ..................................... 25
12. The effect of binding energy on the Klein - Nishina cross section for 300keV photons in lead. .......................................... 27
13. Energy levels of a free electron. .............. 29
14. Feynman diagram of a particle and an antiparticle. ....................................... 32
15. Feynman diagram of pair production. ............ 34
16. Relative importance of photon interactions. ...................................... 34
17. Photon interaction cross sections for water. ............................................ 40

## LIST OF FIGURES (CON'T)

Figure Page

18. Photon interaction cross sections for lead. .......... 41
19. Feynman diagrams of Moller scattering. .......... 43
20. Feynman diagrams of Bhabha scattering. .......... 45
21. The reduction in the collision stopping power due to the polarization or density effect. .......... 51
22. The relative importance of radiation losses compared to collision losses in different materials. .......... 54
23. Feynman diagrams of positron annihilation. .......... 55
24. The decay scheme of $^{60}$Co. .......... 59
25. Three methods of $^{60}$Co source exposure. .......... 61
26. Major components of a linear accelerator. .......... 63
27. A cross sectional view of a magnetron. .......... 65
28. The basic principles of a klystron. .......... 66
29. The basic principles of a travelling wave accelerator. .......... 70
30. The basic principles of a standing wave accelerator. .......... 72
31. A 270° achromatic beam bending magnet. .......... 74
32. The principle components of a treatment head. .......... 77
33. A non-divergent photon beam incident normal to a flat slab of absorber material. .......... 82

## LIST OF FIGURES (CON'T)

Figure Page

34. Variation of absorbed dose and kerma with depth in an absorber. .......... 85

35. A small cavity in a medium. .......... 88

36. Schematic representation of a standard air chamber. .......... 93

37. Basic geometry for dosimetric functions. .......... 105

38. Tissue Air Ratio (TAR) geometry. .......... 107

39. Percentage Depth Dose (PDD) geometry. .......... 109

40. Tissue Phantom Ratio (TPR) geometry. .......... 111

41. An x-ray beam incident normal to the surface of a homogeneous phantom. .......... 113

42. A plot of dose as a function of depth for the geomerty of figure #41. .......... 114

43. Isodose curves in a homogeneous phantom with a flat surface. .......... 116

44 Isodose curves in a homogeneous phantom with a curved surface. .......... 117

45. The effect of bolus on isodose curves. .......... 119

46. Restoration of partial skin sparing by compensator retraction. .......... 121

47. Diagramatic representation of experimental setup. .......... 128

48. A plot of relative dose R(%) at the surface as a function of retraction distance r for a Pb compensator of 1.75mm thickness. (E(γ)=$^{60}$Co) .......... 137

49. A plot of relative dose R(%) at the surface as a function of retraction distance r for a Polystyrene compensator of 2cm thickness. (E(γ)= $^{60}$Co) .......... 138

## LIST OF FIGURES (CON'T)

Figure Page

50. A plot of relative dose R(%) at the surface as a function of retraction distance r for a Pb compensator of 6.25mm thickness. ($E(\gamma)={}^{60}Co$) .......................... 139

51. A plot of relative dose R(%) at the surface as a function of retraction distance r for a Polystyrene compensator of 7cm thickness. ($E(\gamma)={}^{60}Co$) .................. 140

52. A plot of the ratio of [dose Pb/dose Poly] at the surface as a function of retraction distance for a Pb compensator of 1.75mm thickness and a polystyrene compensator of 2cm thickness. ($E(\gamma)={}^{60}Co$) ...................... 141

53. A plot of the ratio of [dose Pb/dose Poly] at the surface as a function of retraction distance for a Pb compensator of 6.25mm thickness and a polystyrene compensator of 7cm thickness. ($E(\gamma)={}^{60}Co$) ...................... 142

54. A plot of relative dose R(%) at the surface as a function of retraction distance r for a Pb compensator of 1.75mm thickness. ($E(\gamma)$=6MV) .......................... 143

55. A plot of relative dose R(%) at the surface as a function of retraction distance r for a Polystyrene compensator of 2cm thickness. ($E(\gamma)$=6MV) .................. 144

56. A plot of relative dose R(%) at the surface as a function of retraction distance r for a Pb compensator of 6.26mm thickness. ($E(\gamma)$=6MV) .......................... 145

57. A plot of relative dose R(%) at the surface as a function of retraction distance r for a Polystyrene compensator of 7cm thickness. ($E(\gamma)$= 6MV) .................. 146

LIST OF FIGURES (CON'T)

Figure Page

58. A plot of the ratio of [dose Pb/dose Poly] at the surface as a function of retraction distance for a Pb compensator of 1.75mm thickness and a polystyrene compensator of 2cm thickness. (E(γ)=6MV) .................... 147

59. A plot of the ratio of [dose Pb/dose Poly] at the surface as a function of retraction distance for a Pb compensator of 6.25mm thickness and a polystyrene compensator of 7cm thickness. (E(γ)=6MV) .................... 148

60. A plot of relative dose R(%) at the surface as a function of retraction distance r for a Pb compensator of 1.75mm thickness. (E(γ)=15MV) ........................ 149

61. A plot of relative dose R(%) at the surface as a function of retraction distance r for a Polystyrene compensator of 2cm thickness. (E(γ)=15MV) ................ 150

62. A plot of relative dose R(%) at the surface as a function of retraction distance r for a Pb compensator of 6.25mm thickness. (E(γ)=15MV) ........................ 151

63. A plot of relative dose R(%) at the surface as a function of retraction distance r for a Polystyrene compensator of 7cm thickness. (E(γ)=15MV) ................ 152

64. A plot of the ratio of [dose Pb/dose Poly] at the surface as a function of retraction distance for a Pb compensator of 1.75mm thickness and a polystyrene compensator of 2cm thickness. (E(γ)=15MV) .................... 153

65. A plot of the ratio of [dose Pb/dose Poly] at the surface as a function of retraction distance for a Pb compensator of 6.25mm thickness and a polystyrene compensator of 7cm thickness. (E(γ)=15MV) .................... 154

66. Surface dose due to scattered electrons and photons. .................................. 157

## LIST OF FIGURES (CON'T)

Figure Page

67. A plot of relative dose R(%) at 4cm depth as a function of retraction distance r for a Pb compensator of 1.75mm thickness. ($E(\gamma)={}^{60}Co$) .................................... 169

68. A plot of relative dose R(%) at 4cm depth as a function of retraction distance r for a polysturene compensator of 2cm thickness ($E(\gamma)={}^{60}Co$) .................................... 170

69. A plot of relative dose R(%) at 4cm depth as a function of retraction distance r for a Pb compensator of 6.25mm thickness. ($E(\gamma)={}^{60}Co$) .................................... 171

70. A plot of relative dose R(%) at 4cm depth as a function of retraction distance r for a polystyrene compensator of 7cm thickness ($E(\gamma)={}^{60}Co$) .................................... 172

71. A plot of relative dose R(%) at 12cm depth as a function of retraction distance r for a Pb compensator of 1.75mm thickness. ($E(\gamma)={}^{60}Co$) .................................... 173

72. A plot of relative dose R(%) at 12cm depth as a function of retraction distance r for a polystyrene compensator of 2cm thickness ($E(\gamma)={}^{60}Co$) .................................... 174

73. A plot of relative dose R(%) at 12cm depth as a function of retraction distance r for a Pb compensator of 6.25mm thickness. ($E(\gamma)={}^{60}Co$) .................................... 175

74. A plot of relative dose R(%) at 12cm depth as a function of retraction distance r for a polystyrene compensator of 7cm thickness ($E(\gamma)={}^{60}Co$) .................................... 176

75. A plot of relative dose R(%) at 4cm depth as a function of retraction distance r for a Pb compensator of 1.75mm thickness. ($E(\gamma)$=6MV) .................................... 177

## LIST OF FIGURES (CON'T)

Figure Page

76. A plot of relative dose R(%) at 4cm depth as a function of retraction distance r for a polystyrene compensator of 2cm thickness ($E(\gamma)$=6MV) .................................... 178

77. A plot of relative dose R(%) at 4cm depth as a function of retraction distance r for a Pb compensator of 6.25mm thickness. ($E(\gamma)$=6MV) .................................... 179

78. A plot of relative dose R(%) at 4cm depth as a function of retraction distance r for a polystyrene compensator of 7cm thickness ($E(\gamma)$=6MV) .................................... 180

79. A plot of relative dose R(%) at 13cm depth as a function of retraction distance r for a Pb compensator of 1.75mm thickness. ($E(\gamma)$=6MV) .................................... 181

80. A plot of relative dose R(%) at 13cm depth as a function of retraction distance r for a polystyrene compensator of 2cm thickness ($E(\gamma)$=6MV) .................................... 182

81. A plot of relative dose R(%) at 13cm depth as a function of retraction distance r for a Pb compensator of 6.25mm thickness. ($E(\gamma)$=6MV) .................................... 183

82. A plot of relative dose R(%) at 13cm depth as a function of retraction distance r for a polystyrene compensator of 7cm thickness ($E(\gamma)$=6MV) .................................... 184

83. A plot of relative dose R(%) at 6cm depth as a function of retraction distance r for a Pb compensator of 1.75mm thickness. ($E(\gamma)$=15MV) .................................. 185

84. A plot of relative dose R(%) at 6cm depth as a function of retraction distance r for a polystyrene compensator of 2cm thickness ($E(\gamma)$=15MV) .................................. 186

## LIST OF FIGURES (CON'T)

Figure Page

85. A plot of relative dose R(%) at 6cm depth as a function of retraction distance r for a Pb compensator of 6.25mm thickness. ($E(\gamma)$=15MV) .................................... 187

86. A plot of relative dose R(%) at 6cm depth as a function of retraction distance r for a polystyrene compensator of 7cm thickness ($E(\gamma)$=15MV) .................................... 188

87. A plot of relative dose R(%) at 12cm depth as a function of retraction distance r for a Pb compensator of 1.75mm thickness. ($E(\gamma)$=15MV) .................................... 189

88. A plot of relative dose R(%) at 12cm depth as a function of retraction distance r for a polystyrene compensator of 2cm thickness ($E(\gamma)$=15MV) .................................... 190

89. A plot of relative dose R(%) at 12cm depth as a function of retraction distance r for a Pb compensator of 6.25mm thickness. ($E(\gamma)$=15MV) .................................... 191

90. A plot of relative dose R(%) at 12cm depth as a function of retraction distance r for a polystyrene compensator of 7cm thickness ($E(\gamma)$=15MV) .................................... 192

91. The dose at a depth d in a phantom due to a single scattering point in a retracted compensator. .................................... 196

92. Diagramatic representation of the Pedagogic model. .................................... 203

93. A plot of the Klein-Nishina cross section as a function of photon scattering angle for incident photon energies of $^{60}$Co, 6MV, and 15MV. .................................... 209

94. A plot of the energy of a compton scattered photon as a function of scattering angle for incident photon energies of $^{60}$Co, 6MV, and 15MV. .................................... 210

## LIST OF FIGURES (CON'T)

Figure Page

95. A plot of the linear attenuation coefficient of polystyrene as a function of photon scattering angle for incident photon energies of $^{60}$Co, 6MV, and 15MV. .......... 211

96. A plot of the linear attenuation coefficient of lead as a function of photon scattering angle for incident photon energies of $^{60}$Co, 6MV, and 15MV. .......... 212

97. A plot of the average energy absorbed in polystyrene as a function of photon scattering angle for incident photon energies of $^{60}$Co, 6MV, and 15MV. ................ 213

98. A plot of the product of the mass attenuation coefficient and the average energy absorbed in polystyrene as a function of photon scattering angle for incident photon energies of $^{60}$Co, 6MV, 15MV. ..... 214

99. Geometry of the "end point" calculations. ...... 233

100. Graphical extrapolation of the zero field linear attenuation coefficient for polystyrene at 6MV. ............................ 239

101. Graphical extrapolation of the zero field linear attenuation coefficient for polystyrene at 15MV. ........................... 240

102. The treatment of retracted compensators by ATP. ............................................ 242

103. Comparison between experimental results and the Pedagogic model for a 10X10cm field at 4cm depth for a Pb compensator of 6.25mm thickness. ($E(\gamma)$=$^{60}$Co) .................. 248

104. Comparison between experimental results and the Pedagogic model for a 10X10cm field at 4cm depth for a Pb compensator of 6.25mm thickness. ($E(\gamma)$=6MV) .................. 249

## LIST OF FIGURES (CON'T)

Figure Page

105. Comparison between experimental results and the Pedagogic model for a 10X10cm field at 4cm depth for a Pb compensator of 6.25mm thickness. ($E(\gamma)$=15MV) ................ 250

106. Comparison between experimental results and EGS for a 10X10cm field at 10cm depth for a polystyrene compensator of 2cm thickness. ($E(\gamma)={}^{60}$Co) ........................ 252

107. Comparison between experimental results and EGS for a 10X10cm field at 4cm depth for a polystyrene compensator of 7cm thickness. ($E(\gamma)$=6MV) ........................ 253

108. Comparison between experimental results and EGS for a 10X10cm field at 6cm depth for a polystyrene compensator of 7cm thickness. ($E(\gamma)$=15MV) ........................ 254

# I INTRODUCTION

The discovery of x-rays dates back to 1895 when Wilhelm Roentgen, while investigating the properties of electrons, discovered that rays generated by a cathode ray tube produced fluorescence in a platinum-barium-cyanide screen located at some distance from the tube. Roentgen was able to show that these rays, which he called x-rays, had great penetrating power through matter. The first apparatus which reliably produced these x-rays was constructed by Coolidge a few years later.

Within a few years of their discovery, x-rays were being employed in medical treatment. Among those first to be treated with x-rays were patients with tumors located on the surface of the skin. Other conditions treated with radiation in the early 1900's were tuberculosis, chronic ear infections, peptic ulcers, and such skin diseases as ring worm, scabies, and eczema. All of these diseases were untreatable by any other method at that time.

Today radiotherapy stands as one of the three major modalities employed in cancer treatment. Varying degrees of damage are exhibited by all cells upon exposure to radiation. Thus in radiotherapy treatment it is always preferable to arrange the radiation beams in such a manner that a high dose is delivered at the tumor site, while at the same time as low a dose as possible is delivered elsewhere, so as to inflict maximum damage to the tumor while inflicting as little damage as is possible to the surrounding healthy tissue. Clinical experience has shown that as little a difference as ±10% lies between a dose that will do significant damage to a tumor without damaging the surrounding tissue and one that will(1). The ICRU concludes that "the available evidence for certain types of tumors points to the need for an accuracy of 5% in the delivery of an absorbed dose to a target volume if the eradication of the primary tumor is sought".(2)

It is therfore necessary to be able to determine as accurately as possible the dose that will be delivered to different regions of the body resulting from irradiation. In doing so it is often desirable to have the isodose curves(contours of constant dose) within a patient unaltered by the patient's surface coutour. In the case of highly irregular surface areas, most notably the head and neck regions, the problem of compensating for patient contour can be most acute.

One method of solving this problem is to fill in the "missing tissue" with a unit density material, called bolus. This procedure has the advantage of presenting the incident beam with a flat surface. This solution, however, has the disadvantage of the loss of skin sparing. Skin sparing, which is a particular advantage of high energy photon treatment, is lost due to the occurance of the build-up region within the bolus material rather than below the patient's skin. However, if the bolus, or tissue compensating material, is retracted away from the patient's surface, as is shown in Fig.#1, then partial skin sparing will be restored. The degree to which skin sparing is restored is dependent upon a number of factors, one of which is the distance of retraction. Such retracted tissue compensators can be constructed of a unit density material, such as wax, or a material of higher density, such as lead(with correspondingly reduced thickness).

Retraction of the compensator material not only alters the surface or skin dose, as mentioned above, but it also alters the dose at a given depth. The alteration of dose at depth is primarily due to a reduction in first order scattering and alteration of the primary ray path.

The investigation of both the alteration in surface dose and dose at depth resulting from this retraction process is the objective of this work. The alteration in

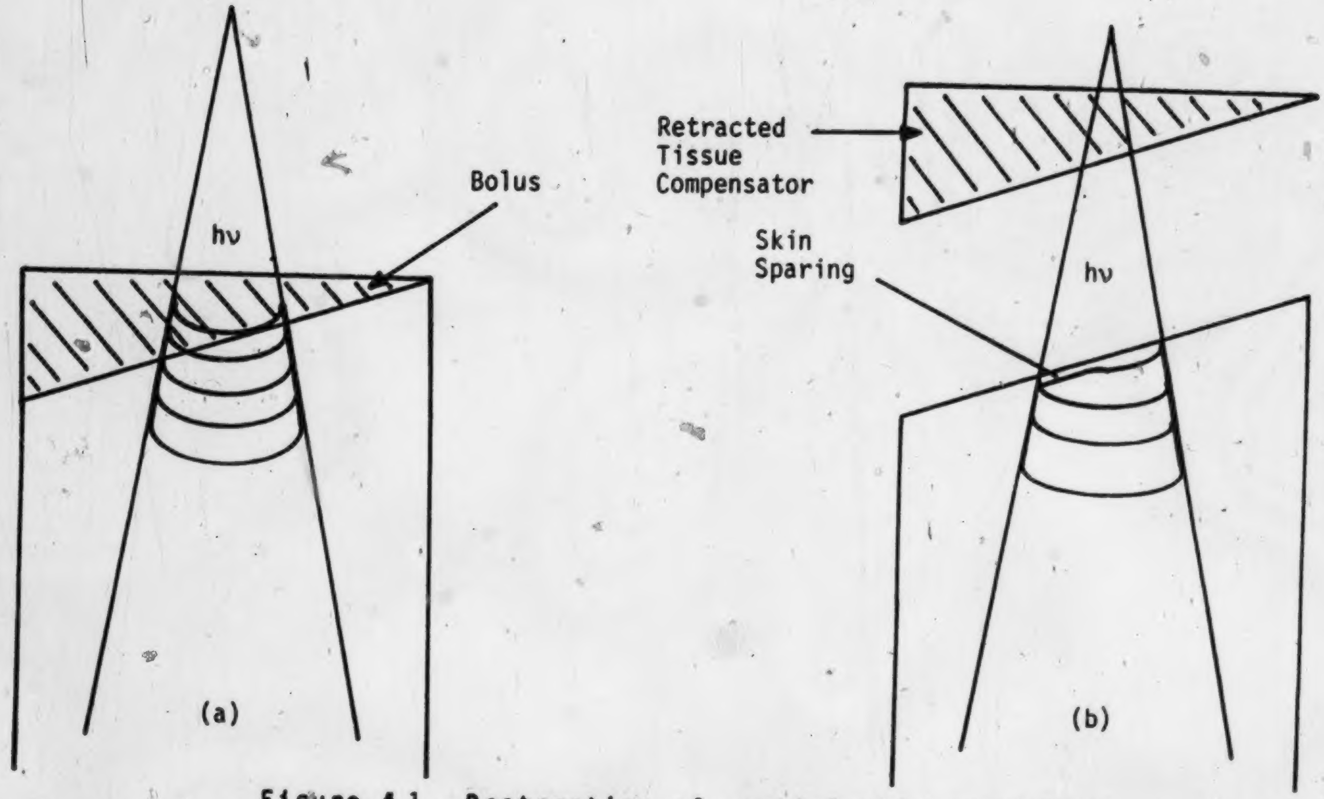
hν
Bolus
(a)
Retracted
Tissue
Compensator
Skin
Sparing
hν
(b)

Figure # 1. Restoration of partial skin sparing by compensator retraction. a)Relatively high dose to phantom surface with compensator unretracted. b)Relatively low dose to phantom surface with compensator retracted.

dose was investigated as a function of retraction distance, field size, measurement depth, compensator thickness, compensator material, and energy of the x-ray beam.

This study has been organized into both theoretical and experimental sections. The theoretical section, which covers the basic concepts of the interaction of radiation with matter, the production of radiation for radiotherapy treatment, and dosimetry, consists of chapters II through IV while the experimental section is contained in chapter V. Conclusions are presented in chapter VI.

# II Interactions of Radiation with Matter

## 2.1 Photon Interactions

### 2.1.1 Photon Attenuation

If a parallel beam of X-rays is incident upon a thickness of material the fluence of the emergent beam is found to be less than that of the incident beam. The narrow parallel incident beam of fluence $\Phi_o$ of Fig.#2 which transits the slab of material of infinitesimal thickness dx will be diminished in fluence by an amount d according to the relation

$$d\Phi \propto -\Phi dx$$

or

$$d\Phi = -\mu\Phi dx \qquad [2.1]$$

The constant of proportionality, $\mu$, is called the linear attenuation coefficient, and it represents the fraction of energy removed from the beam per unit path length. Rearranging [2.1] one obtains

$$\frac{d\Phi}{\Phi} = -\mu dx \qquad [2.2]$$

and upon integration [2.2] becomes

$$\Phi = \Phi_o e^{-\mu x} \qquad [2.3]$$

where $\Phi_o$ is the initial beam fluence and $\Phi$ the resultant

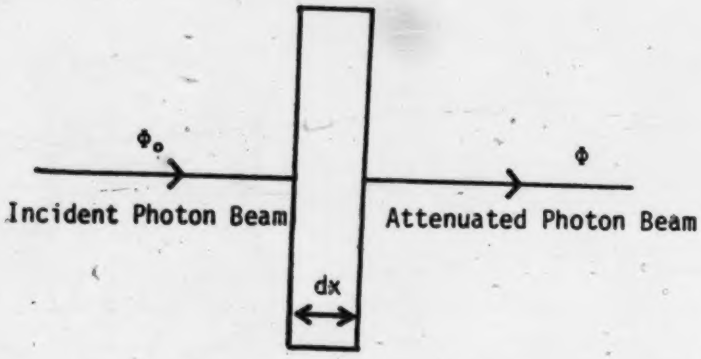
$\Phi_o$
$\Phi$
Incident Photon Beam
Attenuated Photon Beam
dx

Figure #2. Attenuation of a narrow parallel beam by a thin absorber.

beam fluence upon transiting a thickness x of material. The thickness t of absorber required to attenuate the beam by a factor of e is called the mean-free-path of the incident photons. Such a thickness, or path length, represents the mean distance traversed by a photon in the absorber medium between successive interactions and is equal to the inverse of the linear attenuation coefficient $\mu^{-1}$.

The decrease in fluence of the beam is the result of the removal of photons from the beam due to the interaction of a fraction of the photons of the beam with the matter through which the beam is passing. These interaction processes are statistical in nature and hence so to is the removal of photons from the beam. Thus the linear attenuation coefficient, $\mu$, is(for narrow beams) also the probability of photon interaction per unit path length. These interactions which remove photons from the beam can be classified into two general categories: interactions which remove a photon by absorption and interactions which remove a photon by scattering it out of the incident beam. These two types of interactions are illustrated in Fig.#3.

The above does not strictly apply to the situation in which the beam is non-narrow, or broad. The reason for this, as illustrated in Fig.#4, is that some of the

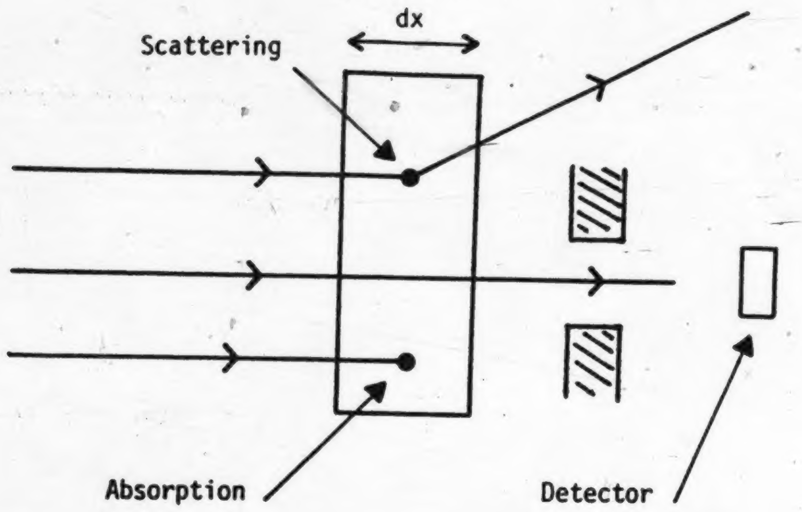
dx
Scattering
Absorption
Detector

Figure #3. Attenuation of a primary beam by scattering and absorption.

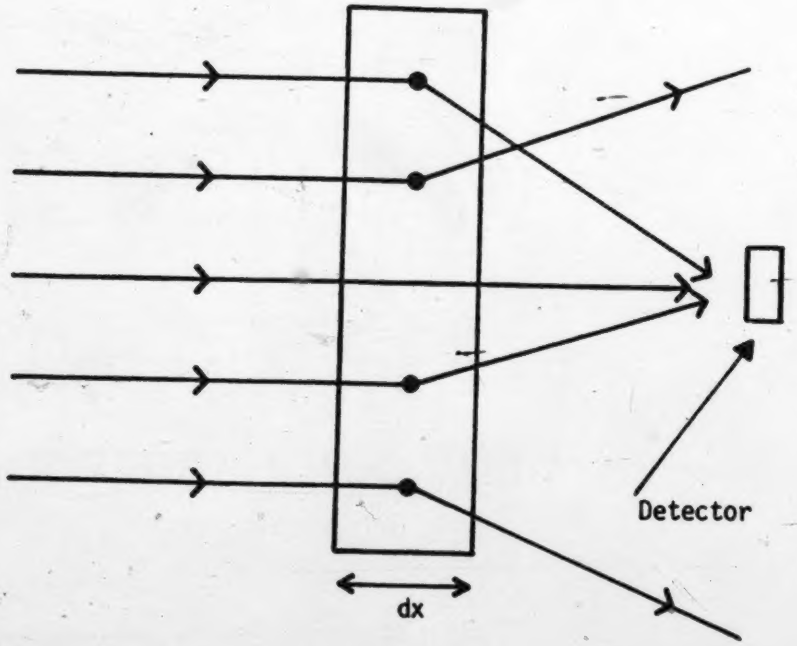
Detector
dx

Figure #4. Attenuation of a broad beam.

scattered photons generated from a relatively large area may be scattered in such a manner as to be incident upon the detector. Thus the attenuation of the incident beam as measured by the detector in the broad beam geometry of Fig.#4 will be less than that measured by the detector in the narrow beam geometry of Fig.#3. Attenuation for broad beam geometry will no longer be strictly exponential, but may be described by

$$\Phi = \Phi_o e^{-\mu x} B(x,A,d,h\nu) \qquad [2.4]$$

where B is a modification factor, often refered to as a "build-up" factor, which is a function of absorber thickness x, beam area A, distance of detector from the absorber d, and incident beam energy hν.

An X-ray photon may interact with the orbital electrons, the Coulomb field of the nucleus, or the nucleus itself of an atom. Thus the probability of interaction will be proportional to the number of interaction sites and hence will be proportional to the density of the absorber. It is often convenient to express attenuation independent of absorber density and this may be achieved by dividing the linear attenuation coefficient $\mu$ by the density $\rho$ of the absorber material. The attenuation coefficient $\mu/\rho$ thus generated is called the mass attenuation coefficient. If the units of $\mu$ are expressed in $cm^{-1}$ then the units of $\mu/\rho$ are $cm^2/g$ and

$\mu/\rho$ thus specifies the fraction by which an incident beam is reduced by a layer of absorber of thickness 1g/cm$^2$. Similarly one may also define atomic and electronic attenuation coefficients respectively as

$$
\begin{aligned}
{}_a\mu &= \left(\frac{\mu}{\rho}\right)\left(\frac{A}{N_o}\right) \\
{}_e\mu &= \left(\frac{\mu}{\rho}\right)\left(\frac{\overline{A}}{N_o\overline{Z}}\right)
\end{aligned}
\qquad [2.5]
$$

where A is the atomic weight of the absorber, $N_o$ is Avogadro's number, and Z is the effective atomic number of the absorber material. If the absorber is an element then $\overline{Z}$=Z, the atomic number of that element, whereas if the the absorber is a compound then $\overline{Z}$ is a weighted average over the atomic numbers of the elements of which the compound is composed. Attenuation coefficients for a large number of atomic numbers over a large range of photon energies have been tabulated and published by Hubble(3) and the National Bureau of Standards(4).

An X-ray beam may be characterized in terms of its fluence, $\Phi$, which is the number, dN, of photons incident normal to area dA

$$\Phi = \frac{dN}{dA} \qquad [2.6]$$

With the concept of fluence, $\Phi$, one may define another quantity termed the scattering cross-section $\sigma$.

Consider an X-ray beam of fluence $\Phi$ incident upon a target as depicted in Fig.#5. Of the N photons incident upon area A of the target, dN photons are scattered through an angle into the solid angle $d\Omega$ and are detected by the detector. If there are n independent interaction or scattering sites in the irradiated area A then the number, dN, of photons scattered into the solid angle $d\Omega$ is given by

$$-dN = An\frac{d\sigma}{d\Omega}(\theta)\,d\Omega\,dx\,\rho_e \qquad [2.7]$$

where $\sigma(\theta)$ (which has units of area) is the constant of proportionality specifying the probability of a photon being scattered through an angle $\theta$ into the solid angle $d\Omega$. One may also write $\sigma(\theta)$ as

$$\frac{d\sigma}{d\Omega}(\theta)\,d\Omega = d\sigma(\theta) \qquad [2.8]$$

and thus $\frac{d\sigma}{d\Omega}(\theta)$ is called the differential cross section of the scattering event. Photons may be scattered into any angle and hence the probability of a photon being scattered by the target may be obtained by integrating the differential scattering cross section, $\sigma(\theta)$ , over all solid angles

$$\sigma_{TOT} = \oint\frac{d\sigma}{d\Omega}(\theta)\,d\Omega = \oint\sigma(\theta)\,d\Omega \qquad [2.9]$$

to obtain the total scattering cross section $\sigma_{TOT}$.

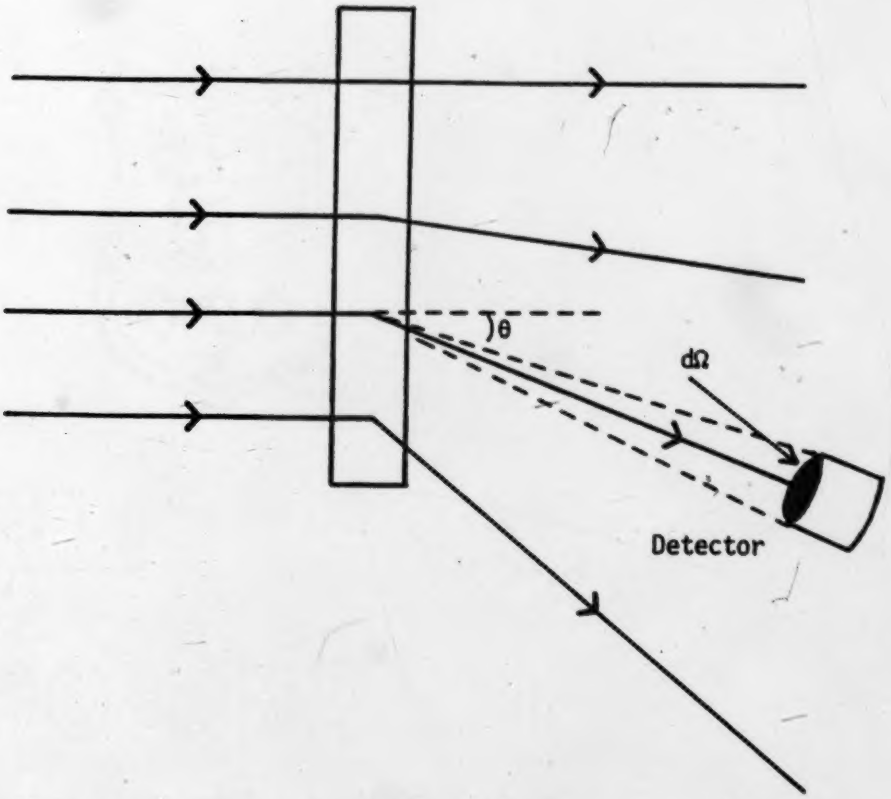
θ
dΩ
Detector

Figure #5. Scattering of dN photons through an angle of θ into the the solid angle dΩ.

Thus the total number of photons $dN_{TOT}$ scattered out of the beam(assuming narrow beam geometry) is

$$dN_{TOT} = \oint dN = \Phi n \oint \sigma(\theta) d\Omega = \Phi n \sigma_{TOT} \qquad [2.10]$$

Now the number $N_{TOT}$ of photons incident on the target is A and hence the fractional decrease(or attenuation) of the beam due to the target is

$$\frac{dN_{TOT}}{N_{TOT}} = \frac{dN_{TOT}}{\Phi A} = \frac{n}{A} \sigma_{TOT} \qquad [2.11]$$

Thus if the scattering sites are taken to be the atoms in the target then

$$ {}_a\sigma_{TOT} = \mu_a = \frac{\mu}{\rho} \frac{A}{N_o}$$

or [2.12]

$$ {}_e\sigma_{TOT} = \mu_e = - \frac{A}{N_o Z}$$

if the scattering sites are taken to be the electrons. A large number of cross sections are of the order of $10^{-24}$ $cm^2$ and thus cross sections are often given in terms of barns(b), where

$$1 \text{ barn} = 1b = 10^{-24} \text{ cm}^2 \qquad [2.13]$$

### 2.1.2 Coherent Scattering

There are a number of different mechanisms by which photons may interact with the matter through which they pass. Each of the interactions serves to attenuate the primary beam and in the process transfer a varying amount of energy to matter. One such interaction which transfers no energy to the attenuating medium is that of Coherent scattering.

The process of coherent(or Rayleigh) scattering is depicted in Fig.#6. Here an X-ray photon is incident upon an atom but does not result in the excitation or ionization of the atom. The photon is scattered by the bound electrons of the atom and the scattered photon exits without a loss of energy. The differential cross section for coherent scattering is given by

$$\frac{d\sigma}{d\Omega}_{COH} = \frac{r_o^2}{2}\,(1+\cos^2\theta)[F(q,Z)]^2 \qquad - \quad [2.14]$$

where $r_o = 2.81794\mathrm{X}10^{-15}$ m(the classical electron radius) and F(q,Z) is the atomic form factor. The square of this atomic form factor gives the probability that the Z electrons of the interacting atom will recieve a recoil momentum q without the absorbtion of energy. This interaction occures mainly for low energy photons interacting with high Z atoms and the resulting scattered photons are strongly forward - peaked. Thus coherent scattering serves to diverge the incident X-ray beam.

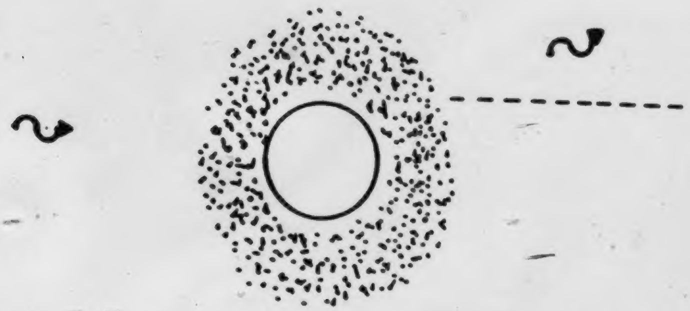

Figure #6. Coherent(or Rayleigh) scattering in which an incident photon is scattered without a change in energy.

### 2.1.3 The Photoelectric Effect

Another important interaction is the photoelectric effect. When an X-ray photon undergoes a photoelectric interaction with an atom, as shown in Fig.#7, the photon is completely absorbed by the atom and its energy is imparted to one of the atoms bound electrons. This electron is thus ejected from the atom with an energy

$$E = h\nu - E_B \qquad [2.15]$$

where hν is the energy of the incident photon and $E_B$ is the binding energy of the electron in the atom. The excited atom thus created returns to ground state via emission of fluorescent radiation and Auger electrons. Thus a photoelectric interaction can only occur if the energy of the incident photon(hν) is greater than the binding energy of the electron to be ejected. The photoelectric cross section, τ, is a decreasing function of incident photon energy with discontinuities existing at the binding energies of different electron shells as shown in Fig.#8. The photoelectric cross sectin is also an increasing function of binding energy with approximately 80% of photoelectric interactions involving the K-shell electrons. The atomic photoelectric cross section varies approximately as

$$_a\tau \propto \frac{Z^4}{(h\nu)^3} \qquad [2.16]$$

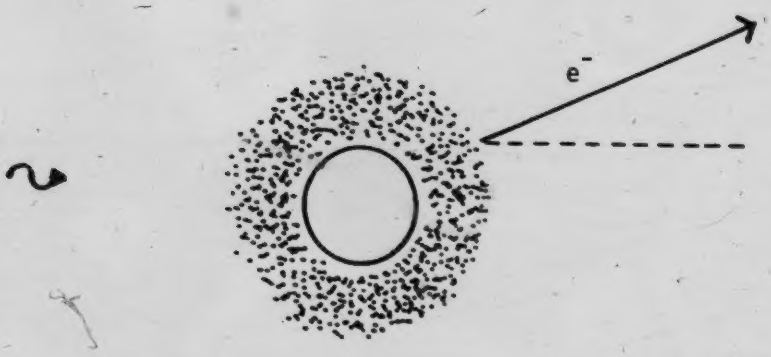

Figure #7. The photoelectric effect. An incident photon is absorbed by an atom resulting in the ejection of a bound electron.

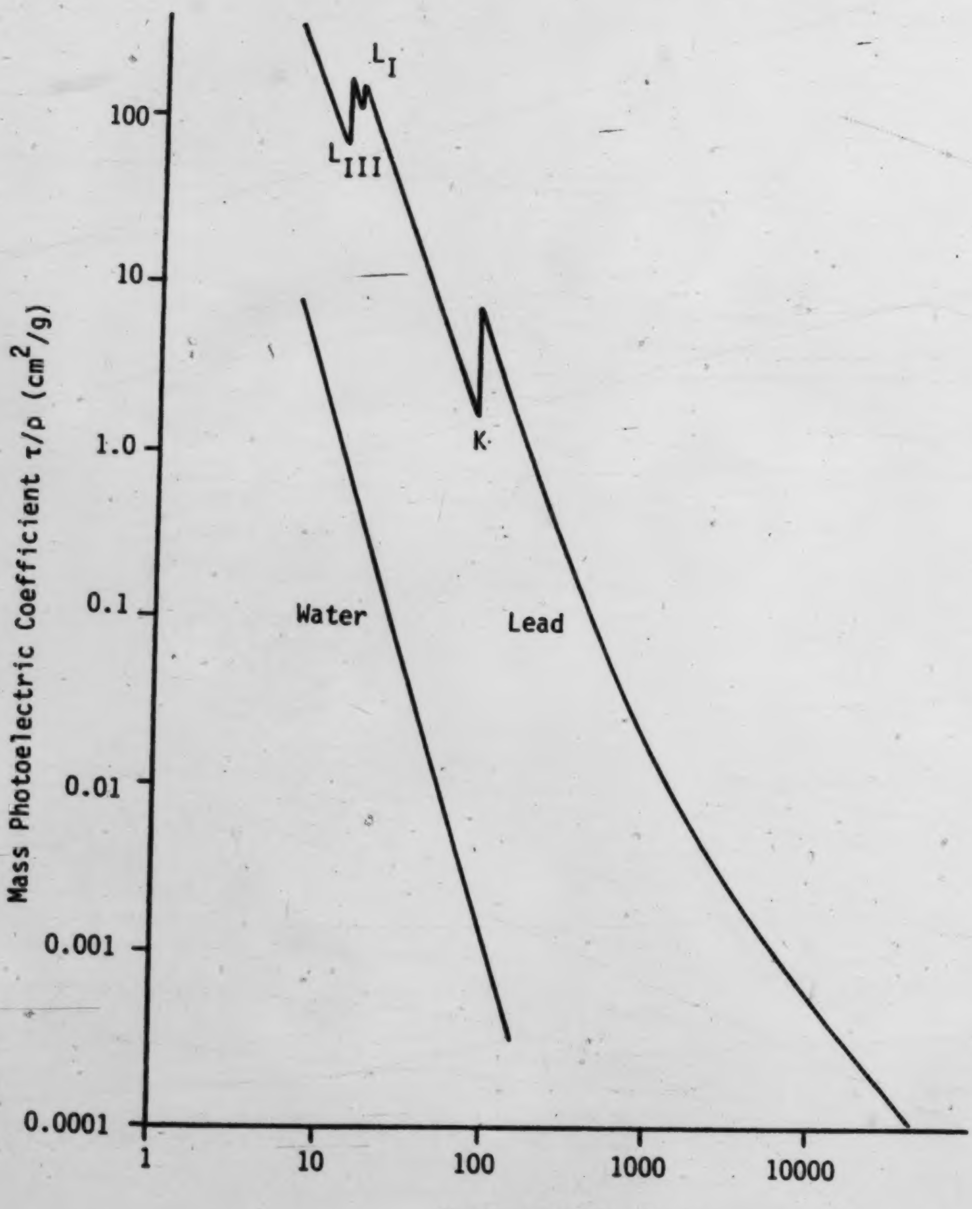

Figure #8. Photoelectric cross sections for water and lead showing the discontinuities at the binding energies of different electron shells for low energies, and

$$ {}_a\tau \propto \frac{Z^5}{h\nu} \qquad [2.17] $$

for high energies.

### 2.1.4 Compton Scattering

Compton scattering is an inelastic interaction between an incident photon and what is considered to be a loosely bound(ie: virtually free) electron at rest in which the incident photon imparts some of its energy to the electron, resulting in a scattered photon of reduced energy, and an electron set in motion with some finite energy, as shown in Fig.#9. This is the most important interaction for the photon energies of interest in this work. In a first approximation the binding energy is taken to be negligible in comparison to the energy, $h\nu$, of the incident photon and the interaction is treated as being elastic. Thus the incident photon of energy $h\nu$ is scattered at an angle $\theta$ with energy $h\nu'$ and a recoil electron is ejected at an angle $\phi$ with energy E. Applying conservation of energy and momentum to this situation yields the following relations between angle and energy for the scattered photon and recoil electron.

$$ h\nu' = h\nu \frac{1}{1+\alpha(1-\cos\theta)} \qquad [2.18] $$

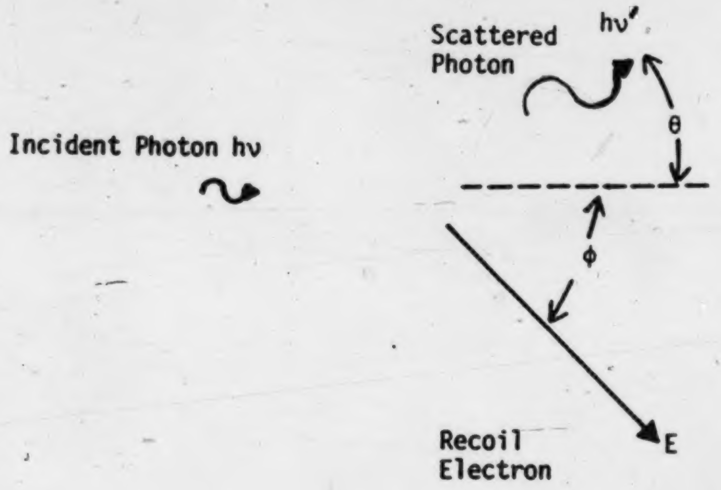
Scattered Photon
$h\nu'$
$\theta$
Incident Photon $h\nu$
$\phi$
Recoil Electron
E

Figure #9. Compton Scattering.

$$E = h\nu \frac{\alpha(1-\cos\theta)}{1+\alpha(1-\cos\theta)} \qquad [2.19]$$

where

$$\alpha = \frac{h\nu}{m_o c^2}$$

$m_o$ = rest mass of electron

and

$$\cot\phi = (1+\alpha)\tan(\frac{\theta}{2}) \qquad [2.20]$$

Maximum energy transfer occures when $\theta = 180^\circ$ and $\theta = 0^\circ$. This condition yields

$$E_{max} = h\nu \frac{2\alpha}{1+2\alpha} \qquad [2.21]$$

$$h\nu'_{min} = h\nu \frac{1}{1+2\alpha} \qquad [2.22]$$

The compton electron may be scattered at any angle from 0° to 180° and the differential cross section $\frac{d_e\sigma}{d\Omega}(\theta)$ giving the probability of a photon being scattered at an angle $\theta$ into the solid angle $d\Omega$ per electron is given by the Klein-Nishina cross section formula

$$\frac{d_e\sigma}{d\Omega}(\theta) = \frac{e^4}{2m_o^2c^4}\left[\frac{1}{1+\alpha(1-\cos\theta)}\right]^2\left[1+\cos^2\theta+\frac{\alpha^2(1-\cos\theta)^2}{1+\alpha(1-\cos\theta)}\right] \qquad [2.23]$$

Now the energy of the scattered photon is given by [2.18] and hence the differential Compton photon energy scattering cross section is then

$$\frac{d_e\sigma}{d\Omega}(\theta)_s = \frac{e^4}{2m_o^2c^4}\left(\frac{1}{1+\alpha(1-\cos\theta)}\right)^3\left(1+\cos^2\theta+\frac{\alpha^2(1-\cos\theta)^2}{1+\alpha(1-\cos\theta)}\right) \quad [2.24]$$

and the differential cross section specifying the energy imparted to the recoil electron, $\frac{d_e\sigma}{d\Omega}(\theta)_a$ , is given by

$$\frac{d_e\sigma}{d\Omega}(\theta)_a = \frac{d_e\sigma}{d\Omega}(\theta) = \frac{d_e\sigma}{d\Omega}(\theta)_s \quad [2.25]$$

The angular distribution of scattered photons and recoil electrons are illustrated in Fig.#10 and Fig.#11 respectively.

For low incident photon energies the binding of the electron must be taken into account. The momentum, q, imparted to the electron in Fig.#9 is

$$q^2 = \frac{(h\nu)^2}{c^2} + \frac{(h\nu')^2}{c^2} - \frac{2h\nu h\nu'}{c^2}\cos\theta \quad [2.26]$$

and since binding effects will be important when small amounts of momentum are imparted to the electron, the approximation $h\nu-h\nu'\cong 0$ can be made, and [2.26] becomes

$$q^2 \cong \frac{2(h\nu)^2}{c^2}(1-\cos\theta)$$

or

$$q^2 \cong \frac{4(h\nu)^2}{c^2}\left(\frac{1}{2}(1-\cos\theta)\right) \quad [2.27]$$

and

$$q \cong \frac{2h\nu}{c}\sin(\theta/2) \quad [2.28]$$

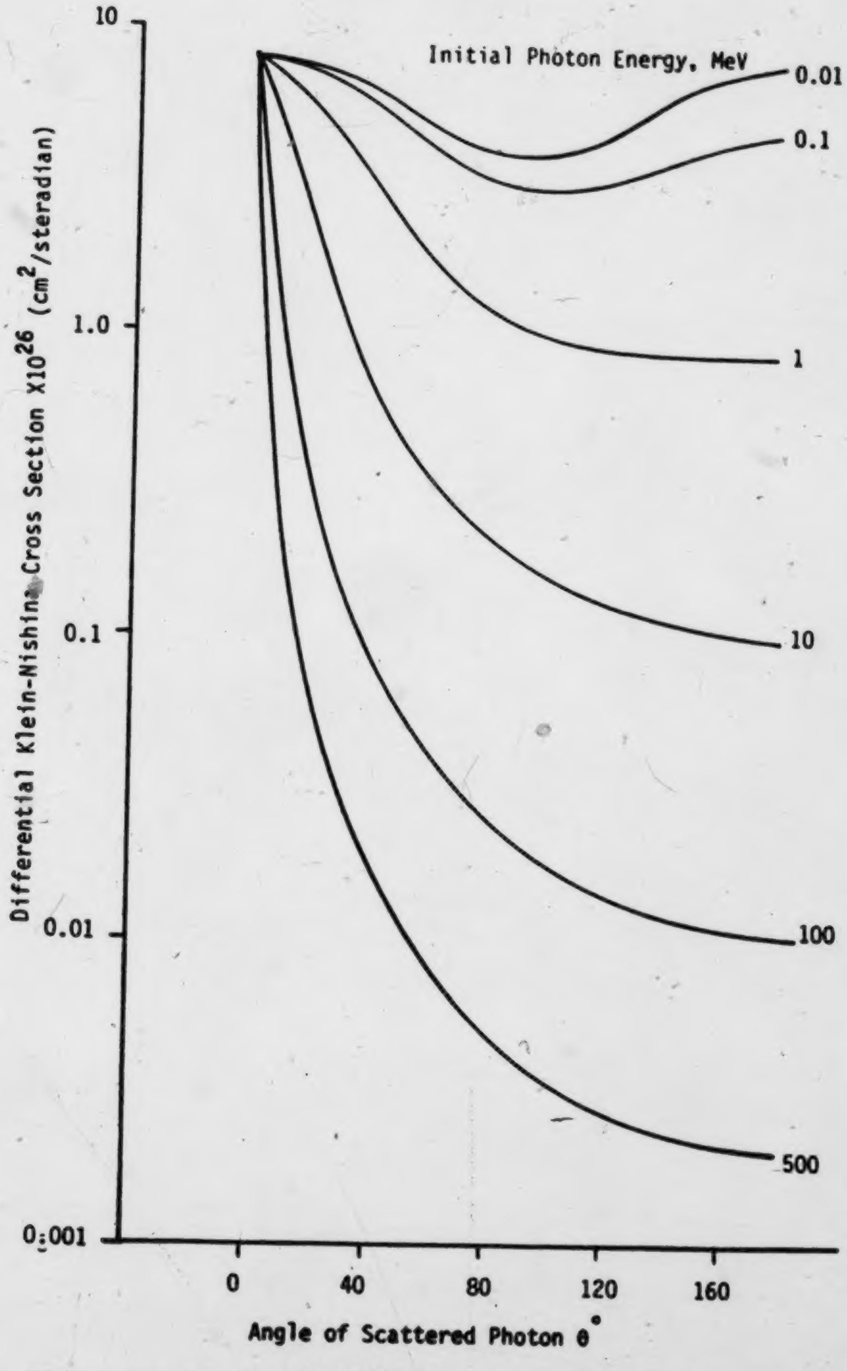

Figure #10. Angular distribution of compton scattered photons.

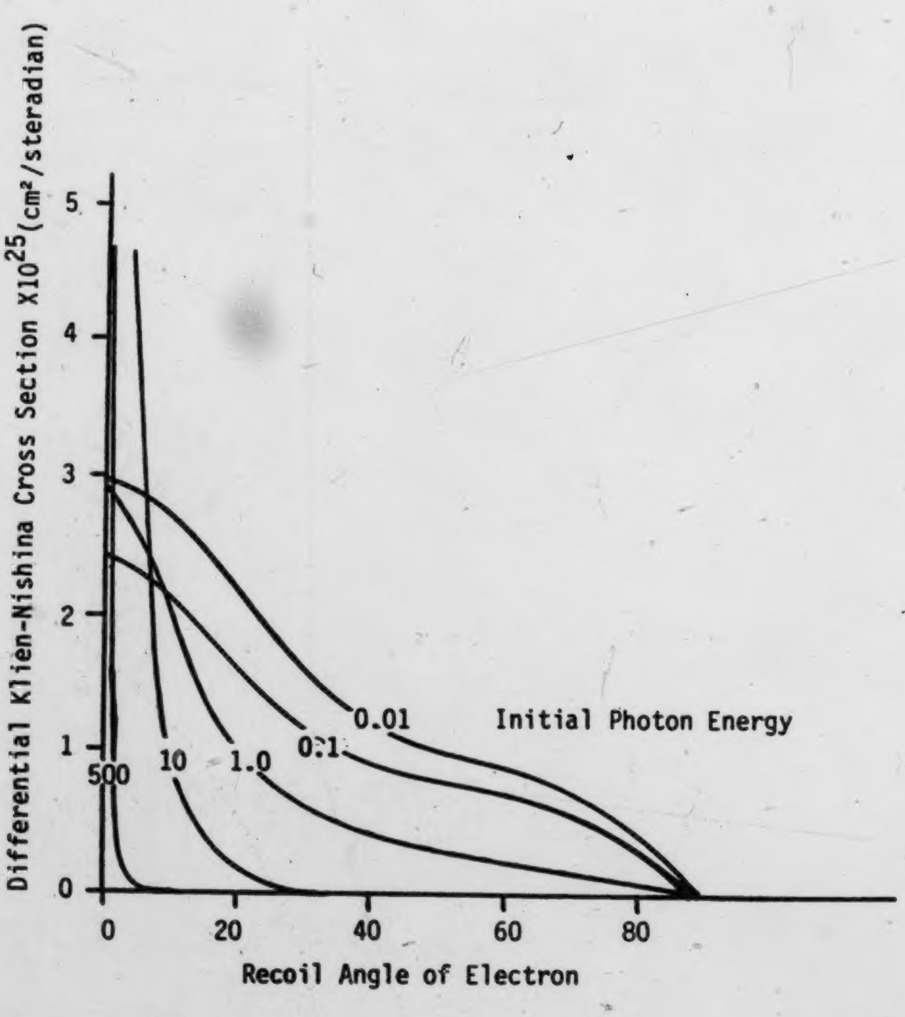

Figure #11. The angular distribution of ompton recoil electrons.

Using this approximation, Heisenberg and Bewilogua have generated a multiplicative correction factor, called the "incoherent scattering function" $S(h\nu, \theta, Z)$, for the Klein-Nishina differential cross section formula which takes into account the binding of the atomic electrons. This correction factor, $S(h\nu, \theta, Z)$, gives the probability "that any energy absorbtion whatsoever results when a photon of frequency is scattered by an angle and transfers a momentum $p \cong h\nu 2\sin(\theta/2)/c$ to the electrons of an atom with atomic number Z"(5). Thus the modified Klein-Nishina cross section, called the incoherent scattering cross section, is given by

$$\frac{d_e\sigma}{d\Omega}(\theta)_{inc} = S(h\nu, \theta, Z)\,\frac{d_e\sigma}{d\Omega}(\theta) \qquad [2,29]$$

The main effect of this binding correction is to decrease the differential cross section at low incident photon energies as shown in Fig.#12. Calculated Compton energy and angular distributions along with the Klein-Nishina cross sections for incident photons of energy 10KeV to 500MeV have been published in graphical form by Nelms as an NBS circular.(6)

### 2.1.5 Pair and Triplet Production

At energies of greater than $2m_oc^2$ an incident photon may interact with a nucleus and be converted into

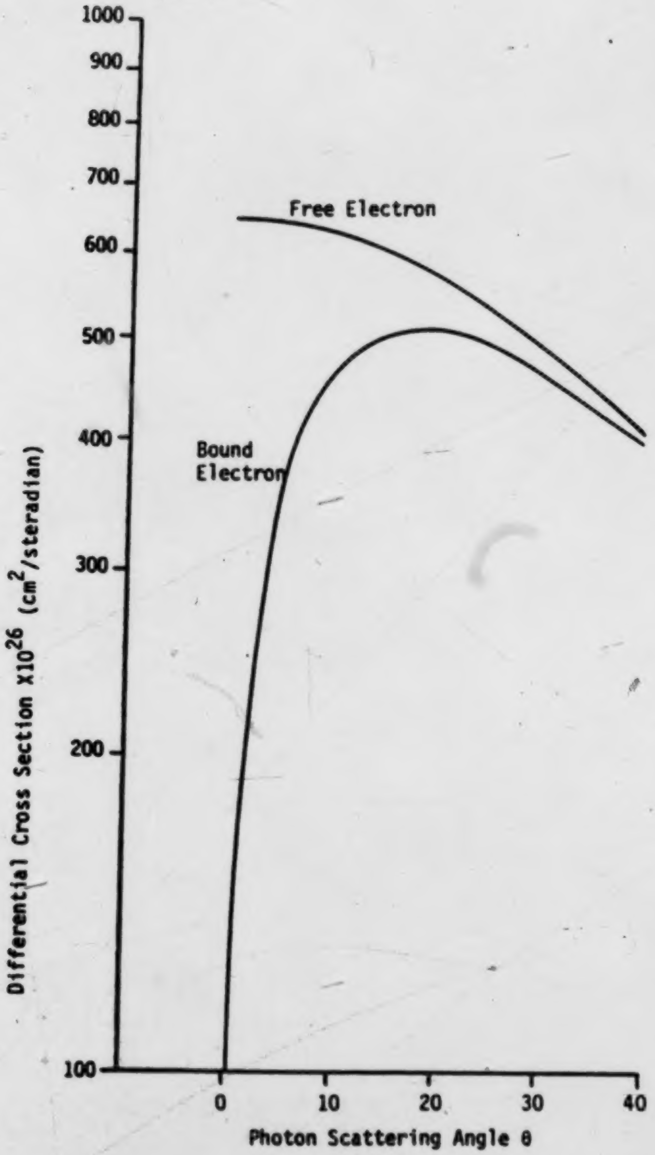

Figure #12. The effect of binding energy on the Klein - Nishina cross section for 300keV photons in lead.

an electron-positron pair. Such an interaction is referred to as pair production. The interaction of a photon with an electron to produce an electron-positron pair is refered to as triplet production and has a threshold incident photon energy of $4m_oc^2$.

This process may be understood by considering the relativistic energy of a massive particle

$$E^2 = p^2c^2 + m_o^2c^4 \qquad [2.30]$$

The energy of this particle is then

$$E = \pm \sqrt{p^2c^2 + m_o^2c^4} \qquad [2.31]$$

Classically the negative root is discarded as being physically meaningless, but this is not the case in relativistic quantum mechanics as it has been shown that negative energy states are required to form a complete set of eigenfunctions for a given observable. Thus the energy states of a particle may be represented as shown in Fig.#13 so that a particle may have any energy from $m_oc^2$ to $+\infty$ and from $-m_oc^2$ to $-\infty$. The assumption of Dirac for this situation is that all of the negative energy levels are filled at all points in space and hence, in the case of electrons, a vacuum consists of a sea of electrons occupying all of the negative energy levels. Such a picture suggests the possibility of raising an

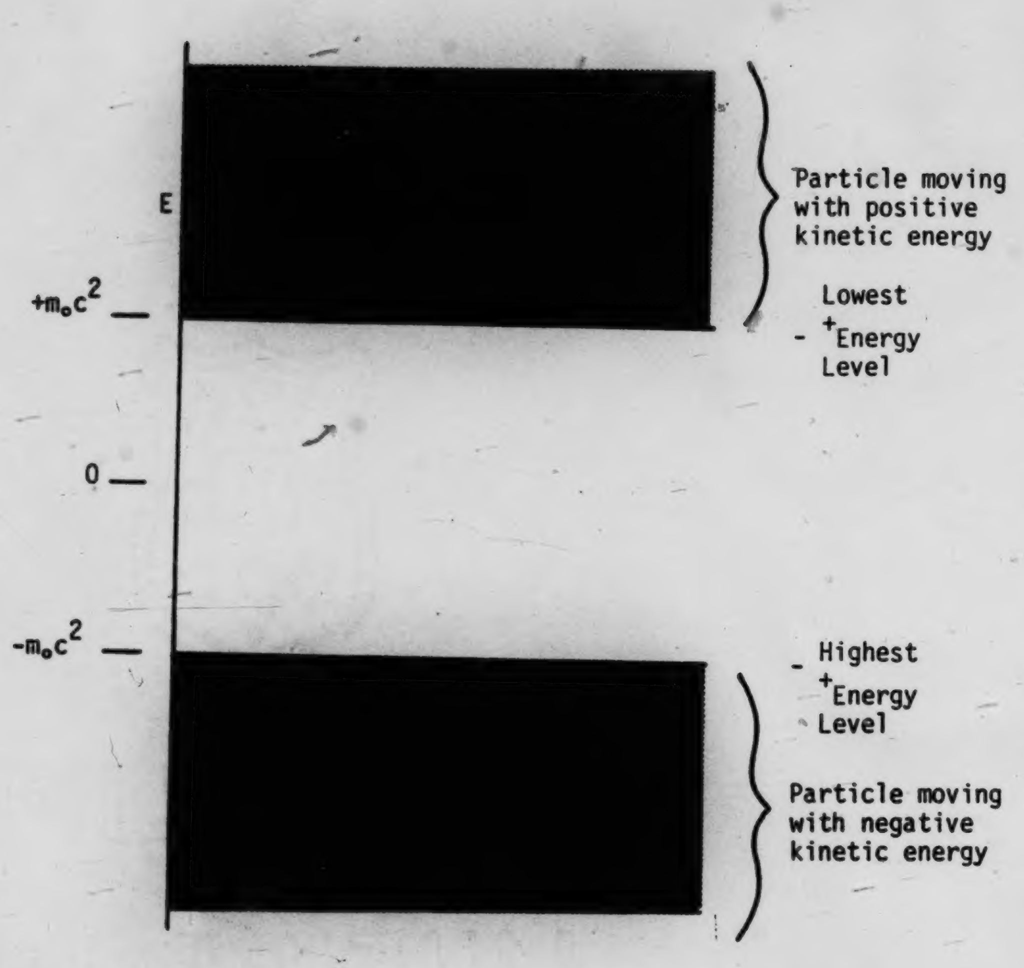
E
$+m_oc^2$
0
$-m_oc^2$
Particle moving with positive kinetic energy
Lowest $\pm$ Energy Level
Highest $\pm$ Energy Level
Particle moving with negative kinetic energy

Figure #13. Energy levels of a free electron.

electron from a negative energy level to a positive energy level by the absorbtion of a photon of energy $h\nu \geqslant 2m_o c^2$. Energy conservation requires the presence of a third particle, such as a nucleus or an electron(of positive energy), in this excitation process. The vacancy or hole created in the negative energy levels by this excitation process is identified as an antiparticle and thus, in the case of electrons, the excitation process creates both an electron and a positron.

A solution of the time-dependent Schrodinger equation for a free particle in one dimension may be written as

$$\Psi_k(x,t) = Ae^{i(kx-\omega t)} \qquad [2.32]$$

where

$$E = \hbar\omega$$

and

$$p = \hbar k$$

or

$$\Psi_k(x,t) = Ae^{(i/\hbar)(px-Et)} \qquad [2.33]$$

For positive E this represents a particle moving in the x direction according to

$$px - E^+t = \text{constant} \qquad [2.34]$$

or, choosing the constant=0,

$$x = \left(\frac{E^+}{p}\right)t \qquad [2.35]$$

For the hole or antiparticle with $E^- < 0$ one has

$$\Psi_k(x,t) = Ae^{(i/\hbar)(px-E^-t)} \qquad [2.36]$$

and [2.35] becomes

$$x = \left(\frac{E^-}{p}\right)t = -\frac{|E^-|}{p}t = \frac{|E^-|}{p}(-t) \qquad [2.37]$$

and thus the positron thus created may be considered as either a particle of negative energy moving forward in time or a particle of positive energy moving backward in time. Consideration of the motion of such an antiparticle in a magnetic field requires that the antiparticle moving backward in time have an opposite charge to that of its complimentary particle moving forward in time. This situation may be represented graphically in a Feynman diagram as shown in Fig.#14. Here the positive energy particle(electron) moves forward in time in the positive x direction while the antiparticle with positive energy(positron) also moves in the positive x direction but backwards in time. The arrow of each particle points in the direction of the particles momentum.

Pair production may be represented in a Feynman

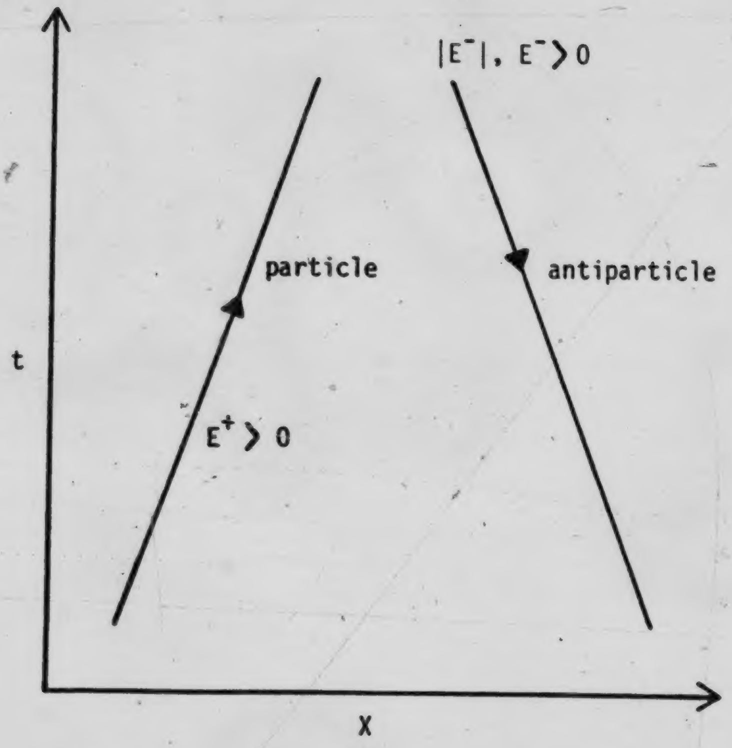
|E⁻|, E⁻ > 0
particle
antiparticle
t
E⁺ > 0
X

Figure #14. Feynman diagram of a particle and an antiparticle. The particle with positive energy is moving forwards in time and the antiparticle with positive energy is moving backwards in time.

diagram, as shown in Fig.#15, and be given one of two equivalent interpretations. In the first interpretation a photon is converted, in the presence of another particle(not shown), into an electron-positron pair. The electron moves forward in time with positive energy while the positron also moves forward in time but with negative energy. In the second interpretation a positron with positive energy is moving backward in time in the positive x direction. This positron is scattered into an electron moving forward in time by an incident photon.

The atomic cross section, ${}_a\pi$ , for pair production is found to be roughly proportional to $Z^2$.

$$ {}_a\pi \cong Z^2 \qquad [2.38] $$

Values of pair and triplet production cross sections have been tabulated by Hubble in NSRDS-NBS 29.(7)

### 2.1.6 Other Interactions

Photons may undergo interactions with matter other than the four(coherent scattering, photoelectric effect, compton scattering, and pair and triplet production) interactions discussed above, but their importance in the energy range employed in this work is negligible. The possible photon interactions with matter may be classified according to the particle with which the

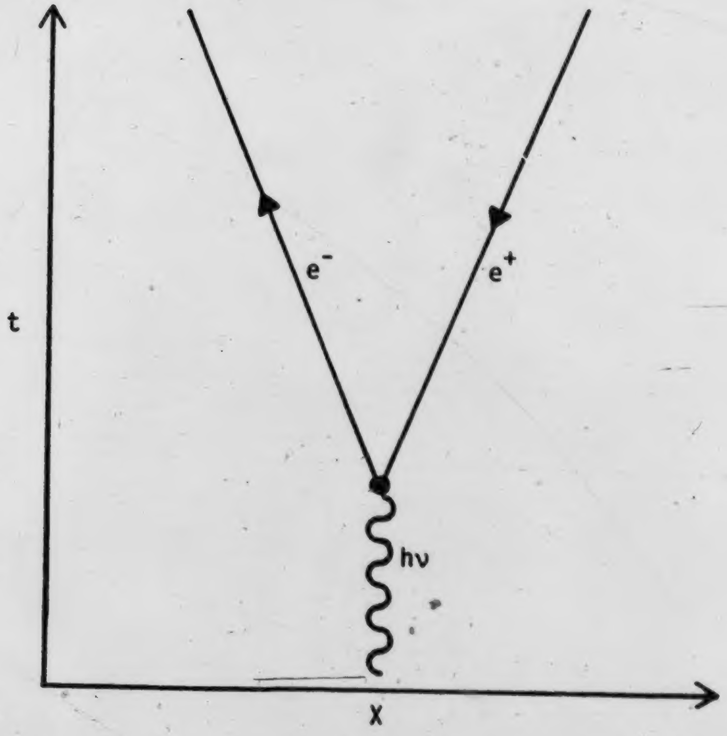

Figure #15. Feynman diagram of pair production.

photon interacts and the type of interaction which takes place. These interactions are presented in table #1 according to this classification. This table is adapted from Hubble(8). Of the interactions listed, only the photonuclear reactions ($\gamma$,n) and ($\gamma$,p) for which $\sigma_{\gamma n} \propto Z$ needs mention. This interaction consists of the absorbtion of an incident photon by a nucleus and the subsequent emission of a neutron or proton by the nucleus. This interaction is characterized by a broad peak(or "giant resonance") in its cross section centered about 24MeV for low Z nuclei and decreasing to about 12MeV for high Z nuclei. For lead, which was used in this work, the threshhold energy for ($\gamma$,n) and ($\gamma$,p) are 7.4MeV and 8.0MeV respectively and the cross section peak occurs at 13.6MeV with peak width at half maximum of 3.8MeV. The value of $\sigma_{\gamma n}$ at this peak is 0.5b and as such constitutes only about 2.7% of the total attenuation cross section of lead at this energy value. This photon energy occurs as only one component of the 15MV spectrum of photon energies ranging from 0 to 15MeV with mean energy of about 5MeV and hence the contribution to the total cross section due to this photonuclear interaction may be safely ignored. The total attenuation cross section is the sum of all cross sections contributing at this energy. The contributions to photon attenuation resulting from the other

| Interaction with | Type of Interaction | | |
|---|---|---|---|
| | Absorption | Elastic (coherent) | Inelastic (incoherent) |
| Atomic electrons | Photoelectric effect<br>* | Rayleigh scattering | Compton Scattering<br>* |
| Nucleons | Photonuclear reactions | Elastic nuclear scattering | Nuclear resonance scattering |
| Electric field of charged particles | Pair and Triplet production<br>* | Delbruck scattering | |
| Mesons | Photomeson production | | |

* of special interest in this work

Table #1. Photon interactions with matter.

interactions in table #1 are either zero or negligible for the energies considered herein(0-15MeV).

### 2.1.7 Relative Cross Sections

At any given incident photon energy a number or all of the above mentioned interaction processes may be taking place according to their relative probabilities. In the energy range of interest in this work(0-15MeV) all processes except coherent scattering, photoelectric effect, Compton scattering, and pair and triplet production may be safely ignored. The total photon cross section at any given energy is the sum of the cross sections of each individual interaction taking place at that energy. Thus for the energy ranges employed in this work the total photon cross section, $\mu$ , may be expressed as-

$$\mu = \sigma_{COH} + \tau + \sigma_{inc} + \pi \qquad [2.39]$$

The relative significance of the three interactions(photoelectric, compton, and pair) which transfer energy from the X-ray beam to the attenuating medium are illustrated in Fig.#16. From Fig.#16 the Compton interaction is seen to be dominant over a wide spectrum of energy for media of low atomic number. The total photon cross section along with the individual

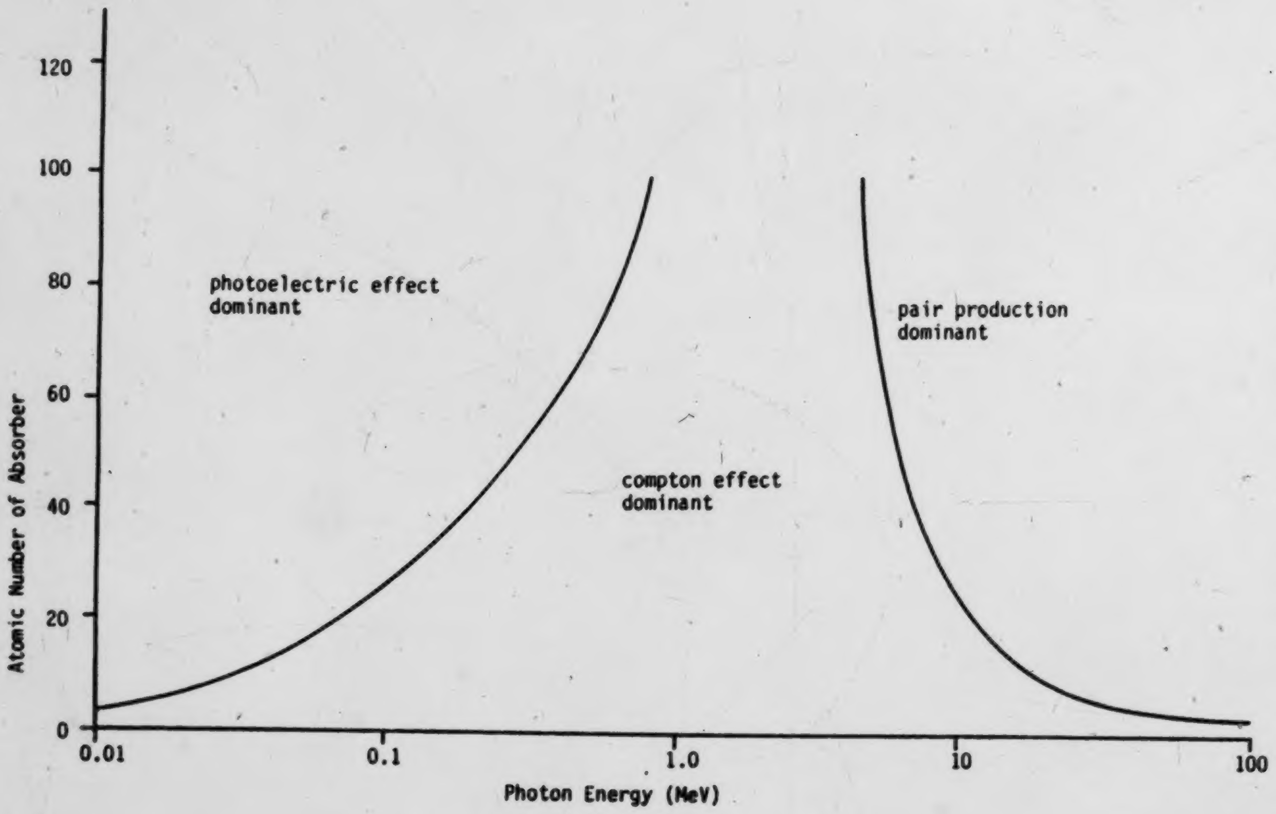

Figure #16. Relative importance of photon interactions.

interaction cross sections of which it is composed are shown in Fig.#17 and #18 for water and lead respectively.

## 2.2 Electron Interactions

Electrons and positrons generated by the photoelectric effect, Compton scattering, and pair production transfer their energy to the medium in which they are produced by way of subsequent interactions with the electrons and nuclei of the medium and thus undergo scattering. The main energy loss mechanism for electrons is that of electron-electron(or electron-positron) Coulomb interactions but electron scattering from such interactions is small. Conversely, interactions with the nucleus result in little energy loss but produce significant scattering.

### 2.2.1 Interactions with Atomic Electrons

Electrons and positrons undergo both elastic and inelastic collisions with the electrons of the medium in which they interact. The incident electrons and positrons impart a portion of their energy to the electrons of the medium in each collision interaction. Depending on whether the energy imparted by the incident electron or positron is greater than or less than the binding energy of the recipient electron either

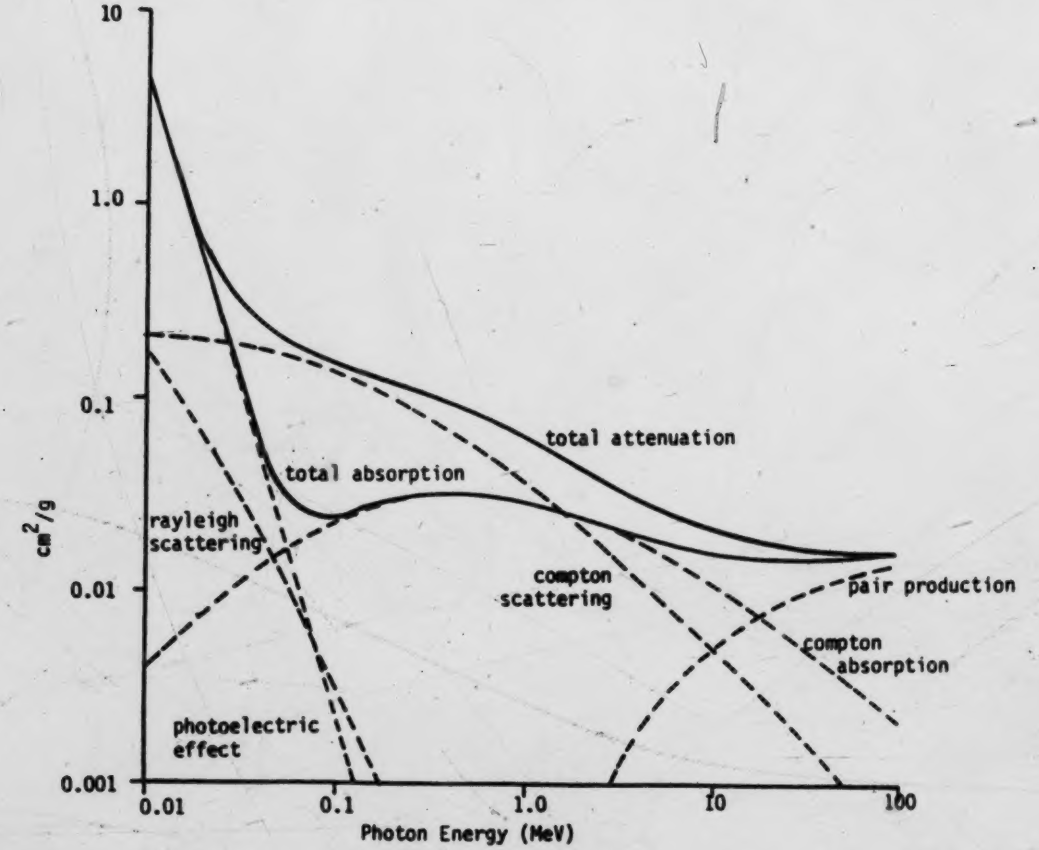

Figure #17. Photon interaction cross sections for water.

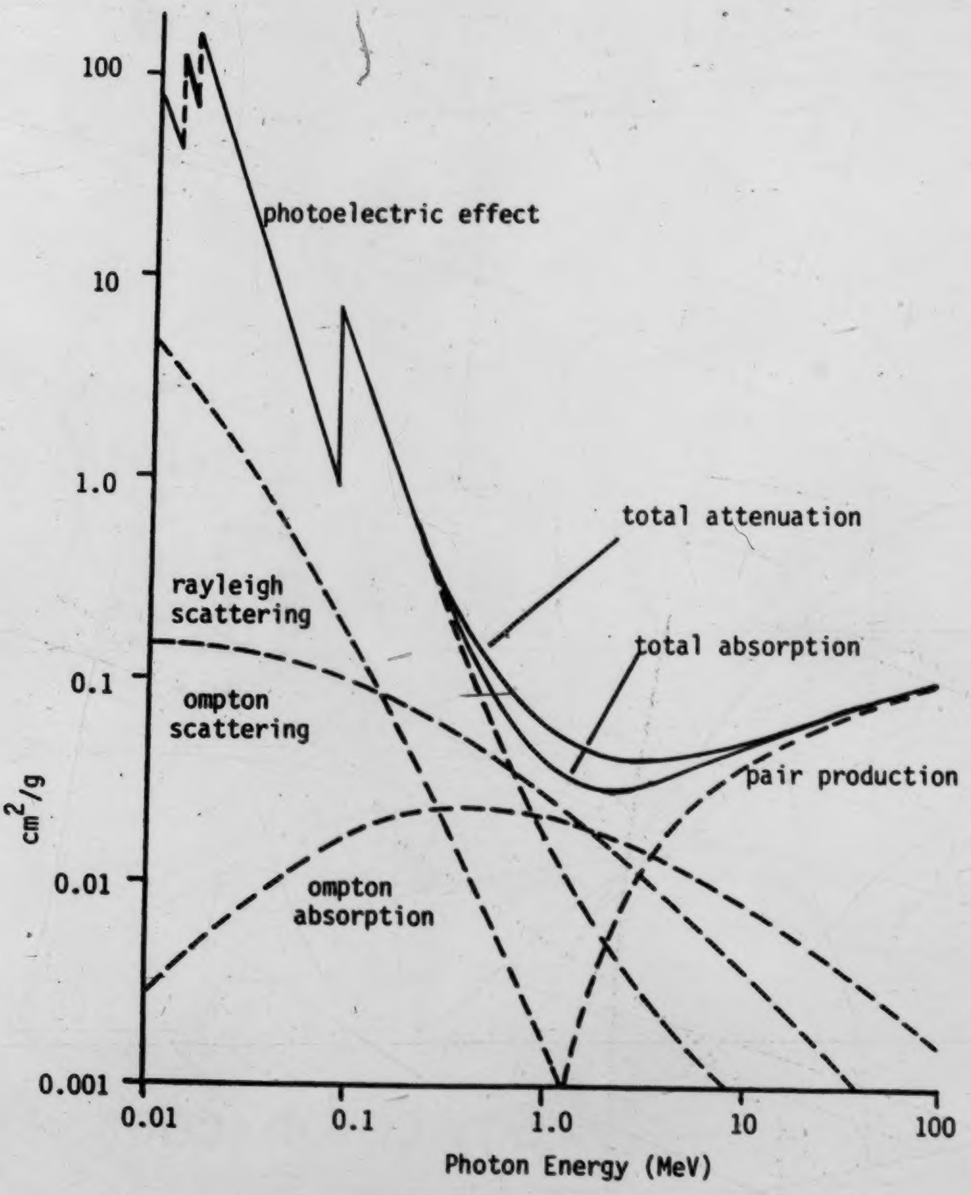

Figure #18. Photon interaction cross sections for lead.

ionization or excitation will occur. If the binding energy is negligible compared to the energy imparted then the collision is considered an elastic collision. If the binding energy is a significant portion of the energy imparted then the collision is considered to be inelastic. The electrons ejected from the atom in the these collisions are called δ-rays and may have energies up to half that of the incident electron and up to the entire amount of the incident positron's energy. These δ-rays impart their energy to the medium in the same manner as does the incident electron or positron. While the elastic collision has the potential for far greater energy loss by the incident electron or positron, the inelastic collision has a far greater probability of occurence and it is by inelastic collisions that incident electrons and positrons lose the majority of their energy and deposite dose.

### 2.2.1.1 Moller Scattering

The scattering of an electron by an electron is called Moller scattering and occurs by two processes as depicted in the Feynman diagrams of Fig.#19(a) and (b). Both processes involve the exchange of a spacelike virtual photon ,which transmits only momentum in the center of mass reference frame, between two indistinguishable electrons and hence the maximum energy

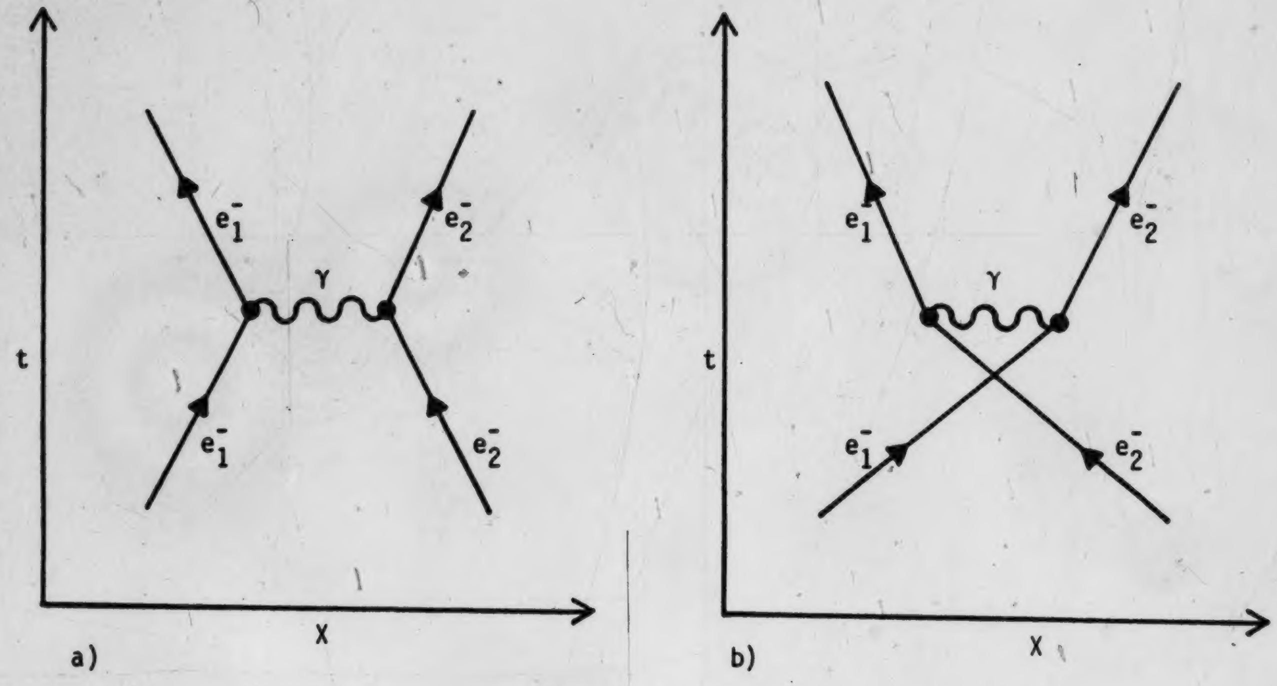
t
$e_1^-$
$e_2^-$
$\gamma$
$e_1^-$
$e_2^-$
X
a)
t
$e_1^-$
$e_2^-$
$\gamma$
$e_1^-$
$e_2^-$
X
b)

Figure #19. Feynman diagrams of Moller scattering involving the exchange of a virtual spacelike photon.

that the incident electron can impart to the other electron is half its incident energy. Since the two interacting particles are identical the determination of which particular process occured is impossible and hence the amplitudes of the wave functions describing each process must be added in order to determine the total cross section for Moller scattering.

### 2.2.1.2 Bhabha Scattering

The scattering of a positron by an electron is called Bhabha scattering and also occurs by two processes as depicted in the Feynman diagrams of Fig.#20(a) and (b). Here the two interacting particles are distinguishable by their charges but the outcomes of the two processes are indistinguishable and hence again the sum of the amplitudes of their individual wave functions is required to determine the correct Bhabha scattering cross section. While the outcome of the two processes are indistinguishable the processes are quite different. The contribution to the total cross section from the process in Fig.#20(a), which is called the photon exchange term, results from the exchange of a spacelike virtual photon which, as in the case of Moller scattering, transmits momentum only in the center of mass reference frame while the contribution from the process in Fig.#20(b), which is called the annihilation

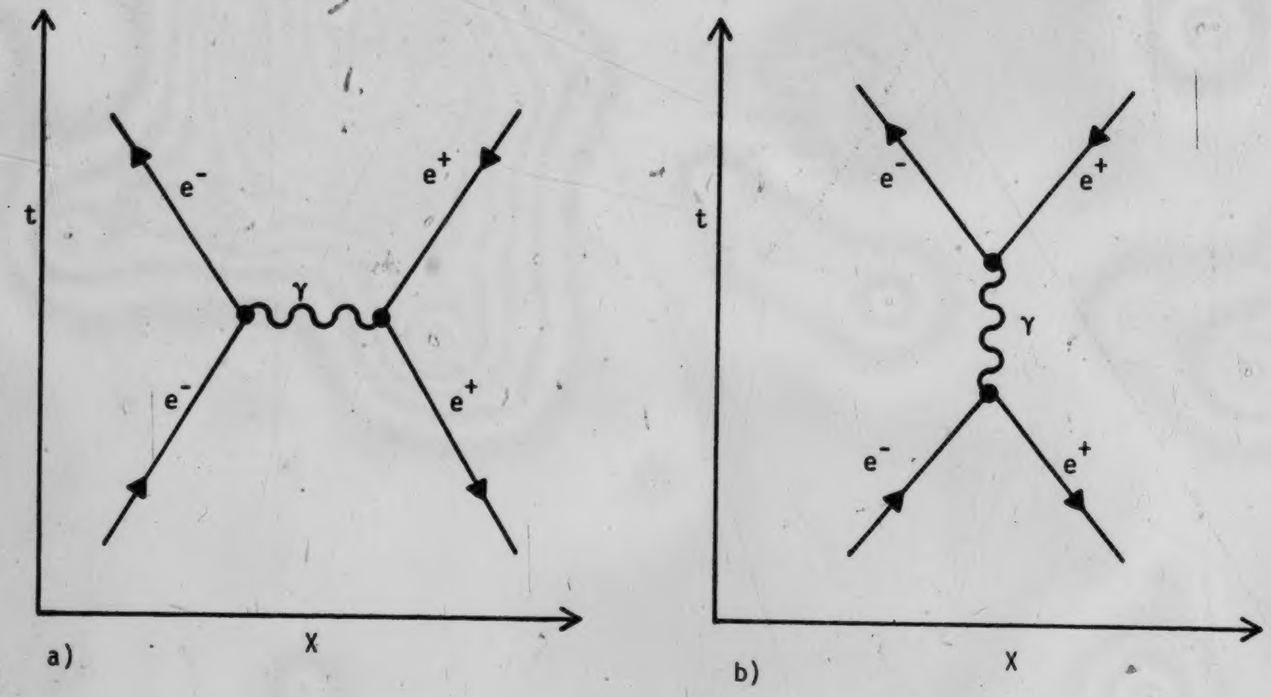
t
$e^-$
$e^+$
$\gamma$
$e^-$
$e^+$
X
a)
t
$e^-$
$e^+$
$\gamma$
$e^-$
$e^+$
X
b)

Figure #20. Feynman diagrams of Bhabha scattering involving a)the exchange of a virtual spacelike photon, b)the exchange of a virtual timelike photon.

term, results from the exchange of a timelike virtual photon which transmits only energy.

### 2.2.2 Interactions with the Nucleus

Incident electrons and positrons also undergo both elastic and inelastic collisions with the nuclei of the medium. The energy lost by incident electrons and positrons in an elastic collision with a nucleus is much smaller than that lost in collisions with electrons due to the large difference in the mass of the electron/positron and that of a nucleus. Thus in spite of the fact that the elastic scattering by a nucleus is more probable than scattering by electrons(nuclear scattering being proportional to $Z^2$ while electronic scattering is proportional to Z) the contribution to energy loss by elastic nuclear scattering can be ignored. Inelastic scattering can, on the other hand, result in significant energy losses. The collision is inelastic due to the creation of a Bremsstrahlung photon in the collision process.

The classical scattering of an electron of velocity v by a nucleus of atomic number Z is given by the Rutherford formula

$$\frac{d\sigma}{d\Omega}(\theta) = \left(\frac{1}{4\pi\varepsilon_o}\right)^2 \left(\frac{Ze^2}{2m_o v^2}\right)^2 \frac{(1-\beta)^2}{\sin^4(\theta/2)} \qquad [2.40]$$

where m is the rest mass of the electron, v is the velocity of the electron, θ is the angle of scatter, and β is v/c where c is the speed of light. This analysis does not take into account the screening of the nuclear charge by the atomic electrons nor electron spin. A more accurate cross section, in the form of an infinite series, which takes into account electron spin but not electronic screening was derived by Mott(9) and is accurate for low Z elements. Other cross sections have been derived which take screening into account according to different considerations. The scattering cross sections due to electron-electron interactions differ from those of electron-nucleus interactions only in their dependence on Z. Electron-nucleus scattering is proportional to $Z^2$ while electron-electron scattering is proportional to Z.

The above cross sections concern single scattering events only, but the probability of an electron undergoing multiple deflections becomes large in comparison to that of single scattering when the interaction medium becomes "thick". In the case of multiple scattering the distribution of angular deflections produces a Gaussian distribution(if energy losses are neglected). Neither the multiple scattering Gaussian distribution cross section nor the single scattering cross sections address the transition region called plural scattering. Plural scattering has been treated by a number of people, such as Goudsmit and Saunderson(10),Moliere(11), and Snyder and Scott(12). Of these treatments the Moliere theory has been used in the EGS4 Monte Carlo modeling system used in this work. The Moliere theory gives the angular distribution as a series of terms, of which the first term is a Gaussian term, and is valid only for small angle deflections. The Moliere theory has been modified by Bethe(11) to cover a larger range of scattering angles.

### 2.2.3 Stopping Power

The predominance of inelastic electron-electron interactions as the collisional energy loss(to the medium) mechanism for electrons and positrons gives rise to the approximation of continuous slowing down of the incident electron or positron by means of an infinite number of infinitesimal energy losses along its track. In reality the incident electron or positron undergoes a large number of small but finite energy losses along with a few large energy losses($\delta$-rays) along its track. In this regard an expression for the mean electron-electron collisional energy loss per unit path length, dE/dx, or linear "Stopping Power" $S_{COL}$, has been derived. Often written in terms of the mass stopping power,$(S/\rho)_{COL}$, this relativistic quantum mechanical expression, originally due to Bethe, is

$$\frac{1}{\rho}\frac{dE}{dx}_{COL} = \frac{S^-}{\rho} = \frac{2\pi e^4 N_o}{m_o v^2}\frac{Z}{A}\left(\ln\frac{E^2(E+2m_oc^2)}{2m_oc^2I^2} + (1-\beta^2)\right. \qquad [2.41]$$

$$\left. + \frac{1}{2} + \frac{\frac{1}{8}E^2 - (2Em_oc^2 + m_o^2c^4)\ln 2}{(E + m_oc^2)^2} - \delta\right)$$

For positrons the mass stopping power is given by

$$\frac{S^+}{\rho} = \frac{2\pi e^4 N_o}{m_o v^2}\frac{Z}{A}\left(\ln\frac{E^2(E + 2m_oc^2)}{2m_oc^2I^2} + 2\ln\left(\frac{E}{m_oc^2}\right)\right. \qquad [2.42]$$

$$- \beta\left(2 - \frac{\frac{5}{4}\frac{E}{m_oc^2}}{\frac{E}{m_oc^2} + 2} + \frac{\left(\frac{E}{m_oc^2} + 1\right)\left(\frac{E}{m_oc^2} + 3\right) - \frac{1}{3}\frac{E^2}{m_o^2c^4}}{\left(\frac{E}{m_oc^2} + 2\right)^2}\right.$$

$$\left.\left. - \frac{\frac{1}{4}\left(\frac{E}{m_oc^2} + 1\right)\left(\frac{E}{m_oc^2} + 3\right)\frac{E^3}{m_o^3c^6} - \frac{1}{12}\frac{E^3}{m_o{}^3c^6}}{\left(\frac{E}{m_oc^2} + 2\right)^3}\right)\right)$$

where $v$ = velocity of the electron or positron
$\beta$ = $v/c$
$m_o$ = rest mass of the electron or positron
$E$ = relativistic energy of the electron or positron
$I$ = the mean excitation energy of the medium
$N_o$ = Avogadro's number
$\delta$ = the density correction factor

These expressions for mass stopping power may also be arrived at by means their respective cross sections. For electrons, [2.41] may be derived by integrating the Moller cross section with respect to energy from a lower limit determined by the mean excitation energy, I, to an upper limit of E/2. For positrons, [2.42] may be derived by integrating the Bhabha cross section over a similar energy range except that the upper energy limit becomes E since a positron may deposit up to all of its energy in a collision. Values of the mean excitation energy and stopping power for the elements and a number of compounds have been tabulated by Berger and Seltzer(13).

The energy dependence of the collisional stopping power is shown in Fig.#21. The stopping power is seen to decrease with increasing energy for low energies, then go through a minimum, and then increase with increasing energy for high energies. The rise in $S_{COL}$ at high energies is due to the domination of the relativistic terms at these energies. This relativistic rise is dampened by the density correction factor as shown. This density effect results from the relativistic contraction of the electric field of the electron along its line of motion. This compressed electric field serves to more highly polarize atoms and molecules near to the electron's track and these polarized atoms and molecules in turn screen more distant atoms and molecules from the full field of the electron. This results in lower energy losses to the the more distant atoms and molecules and hence lower $S_{COL}$. This effect is more pronounced for condensed media and hence the name "density effect".

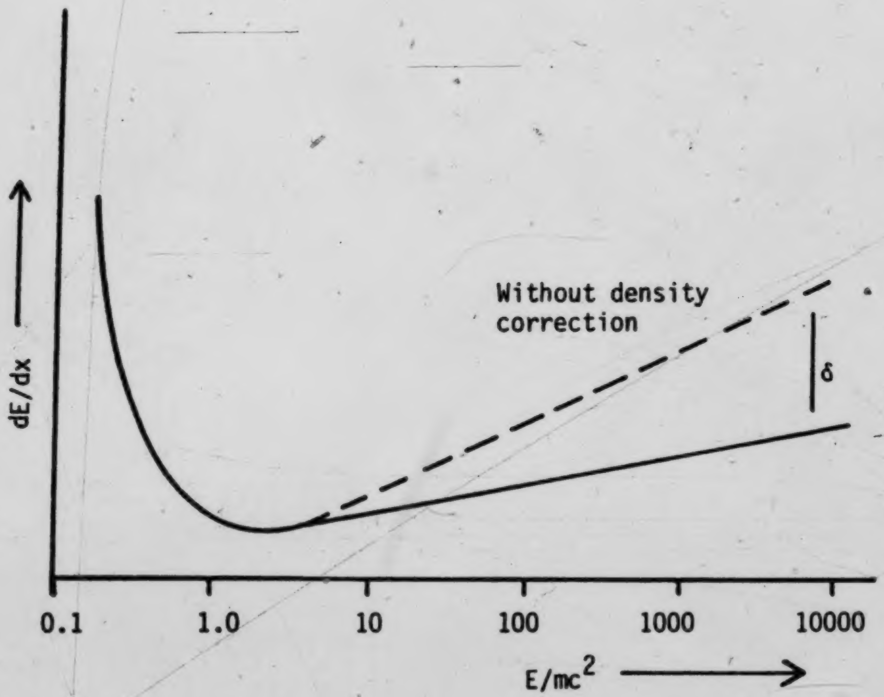

Figure #21. The reduction in the collision stopping power due to the polarization or density effect.

### 2.2.4 Bremsstrahlung

The photon generated when an electron or positron undergoes an inelastic collision with a nucleus is called Bremsstrahlung. The differential cross section for electrons and positrons for this process is given approximately by

$$\frac{d\sigma}{d\Omega}_{rad} \cong \frac{1}{137}\,\frac{e^2}{m_o c^2}\,BZ^2\,\frac{E + m_o c^2}{E}\,\frac{1}{h\nu} \qquad [2.43]$$

where $m_o$ = rest mass of electron or positron
$h\nu$ = energy of Bremsstrahlung photon generated
$E$ = electron or positron relativistic energy
$B$ = a slowly varying function of $Z$ and $E$

One may define a radiative stopping power for this process as

$$\frac{dE}{dx}_{rad} = S_{rad} = \int_0^E \frac{d\sigma}{d\Omega}\,h\nu\,d(h\nu) \qquad [2.44]$$

and one obtains, approximately,

$$S_{rad} \propto Z^2 E \qquad [2.45]$$

The approximate ratio of $S_{rad}$ and $S_{COL}$ are given by

$$\frac{\left(\frac{S}{\rho}\right)_{rad}}{\left(\frac{S}{\rho}\right)_{COL}} \cong \frac{EZ}{1600 m_o c^2} \qquad [2.46]$$

and this ratio for a number of materials is shown in Fig.#22. The total stopping power for a medium may be obtained by adding the collisional and radiative stopping powers

$$\frac{1}{\rho}\frac{dE}{dx}_{TOT} = \frac{1}{\rho}\frac{dE}{dx}_{COL} + \frac{1}{\rho}\frac{dE}{dx}_{rad} \qquad [2.47]$$

$$\frac{S}{\rho}_{TOT} = \frac{S}{\rho}_{COL} + \frac{S}{\rho}_{rad}$$

### 2.2.5 Positron Annihilation

The positron loses its energy by ionization and excitation and bremsstrahlung as does an electron. Since it is an antiparticle, however, the positron will eventually be captured by an electron in the medium and will undergo annihilation with that electron. This process is more probable for low energy positrons than for high energy positrons. This process is depicted in the Feynman diagrams of Fig.#23.

In Fig.#23(a) an electron moving forward in time is scattered by two photons into a positron moving backward in time. This is the case for a free positron annihilation with a free electron. Two photons are required as the end product in order to conserve momentum and their combined energy must be $\geqslant 2m_oc^2$ . If both the free electron and the free positron can be

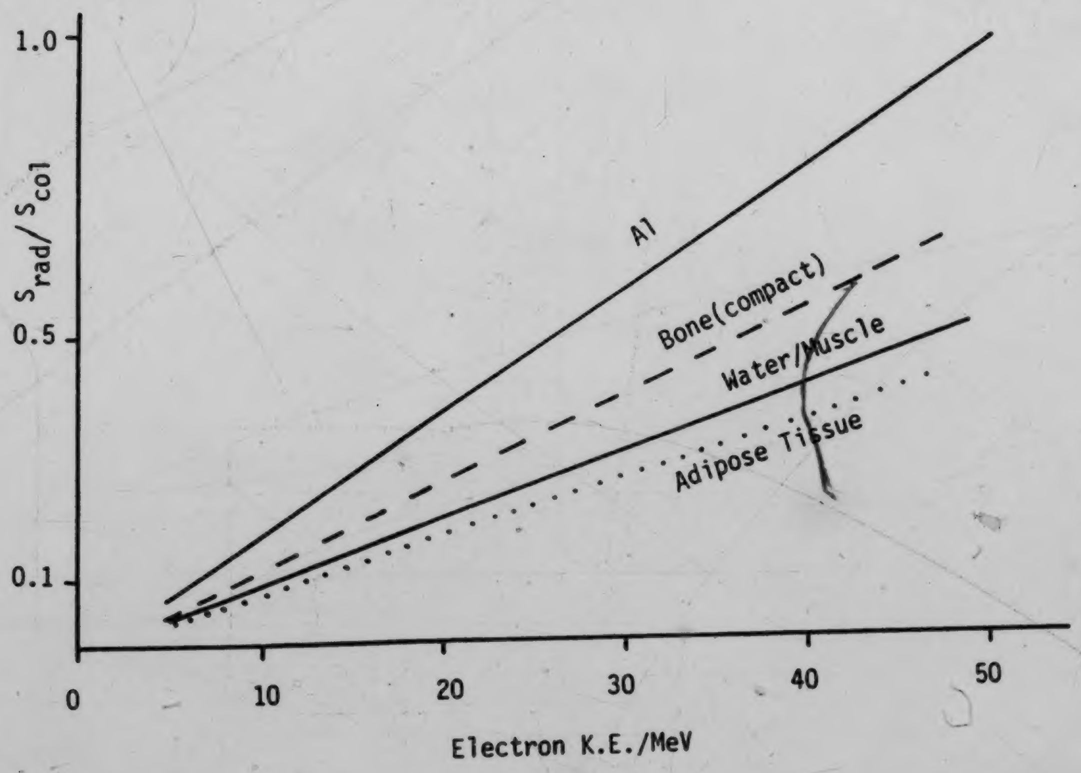

Figure #22. The relative importance of radiation losses compared to collision losses in different materials.

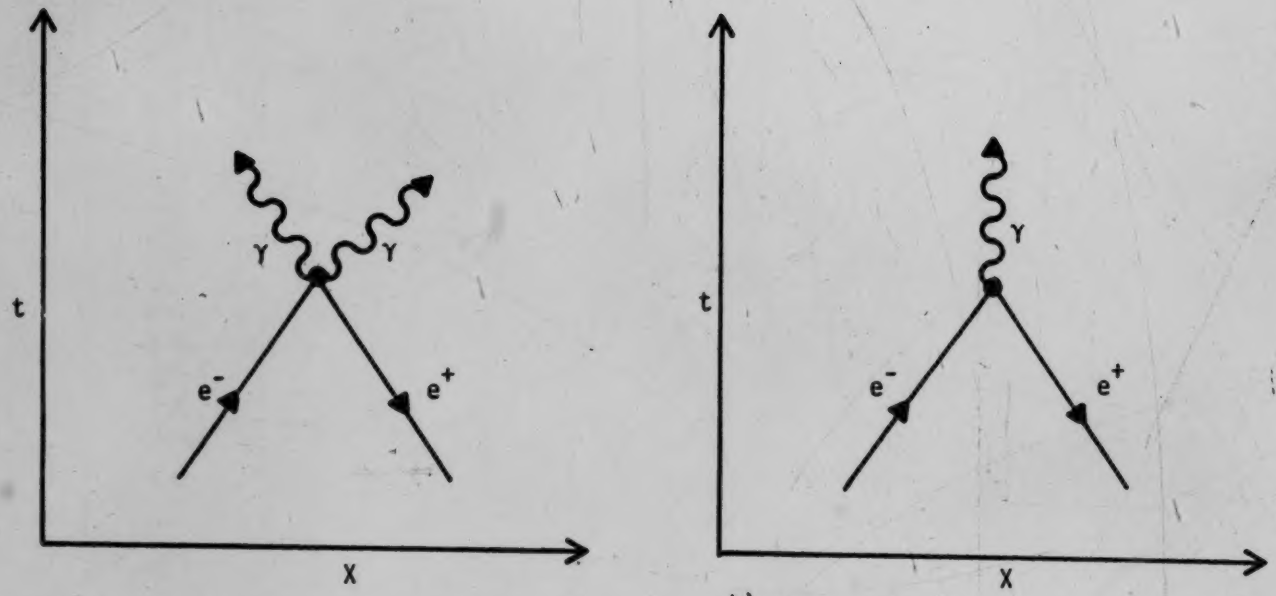
t
γ
γ
e⁻
e⁺
X
t
γ
e⁻
e⁺
X

a) b)

Figure #23. Feynman diagrams of positron annihilation.

considered to be at rest when undergoing annihilation then two photons, each with $h\nu = m_o c^2$, will be produced travelling in opposite directions. In Fig.#23(b) an electron moving forward in time is scattered by a single photon into a positron moving backward in time. This is the case of a positron annihilating with an electron that is tightly bound to a nucleus. The one-photon annihilation is in general much less probable that the two-photon annihilation. At its greatest probability, which occurs in high Z elements, the one-photon annihilation occures less than 20% as often as does two-photon annihilation. Multiple photon(3 or more) annihilation also occur, but at a much lower probability (1/370) than that of two-photon annihilation(14).

### 2.2.6 Electronic Range

Consider a monoenergetic beam of electrons incident upon a flat slab of material. The statistical nature of the scattering and energy loss processes dictate that there will be a distribution of depths in the absorber over which the incident electrons will have lost all of their energy. As well there will be a distribution of energies which the electrons will possess at any given depth. This energy distribution is referred to as energy straggling and the distribution of penetration depths is referred to as range straggling. Thus there is no well defined range of electrons in a medium. It is, however, convenient to define a mean range, or continuous-slowing-down-approximation(csda) range, based on the assumption of continuous energy loss given by the total stopping power. This mean range is then

$$R = \int_0^{E_o} \frac{1}{S_{TOT}} dE \qquad [2,48]$$

# III The Production of Radiation for Medical Use

## 3.1 Cobalt 60 Radiation

$\gamma$-rays emitted in the decay of radioactive isotopes is an important source of radiation used in medicine. Prior to 1951 the only isotope employed in the production of radiation for medical use was Radium. Radium, as a source, suffered from the two major drawbacks of producing very low intensity radiation and being prohibitively expensive. In 1951 high activity $^{60}$Co sources were produced in a Canadian nuclear reactor and the first radiotherapy employing $^{60}$Co as its source was constructed in Saskatchewan. $^{60}$Co with a half life of 5.26 years is produced by neutron activation of naturally occuring $^{59}$Co. The decay scheme of $^{60}$Co is shown in Fig.#24. $^{60}$Co decays with a probability of 99.88% by emission of a $\beta^-$ with a maximum energy of 0.315MeV to form an excited state of $^{60}$Ni. This excited state of $^{60}$Ni decays rapidly by emission of two $\gamma$- rays of energies 1.1732 and 1.3325MeV respectively in cascade. $^{60}$Co also decays with a probability of 0.12% by emission of a $\beta^-$ with a maximum energy of 1.4847MeV to form the lower excited state of $^{60}$Ni which then rapidly decays by the emission of a 1.3325MeV $\gamma$-ray. The two $\gamma$-rays of energy 1.1732 and 1.3325MeV, with relative

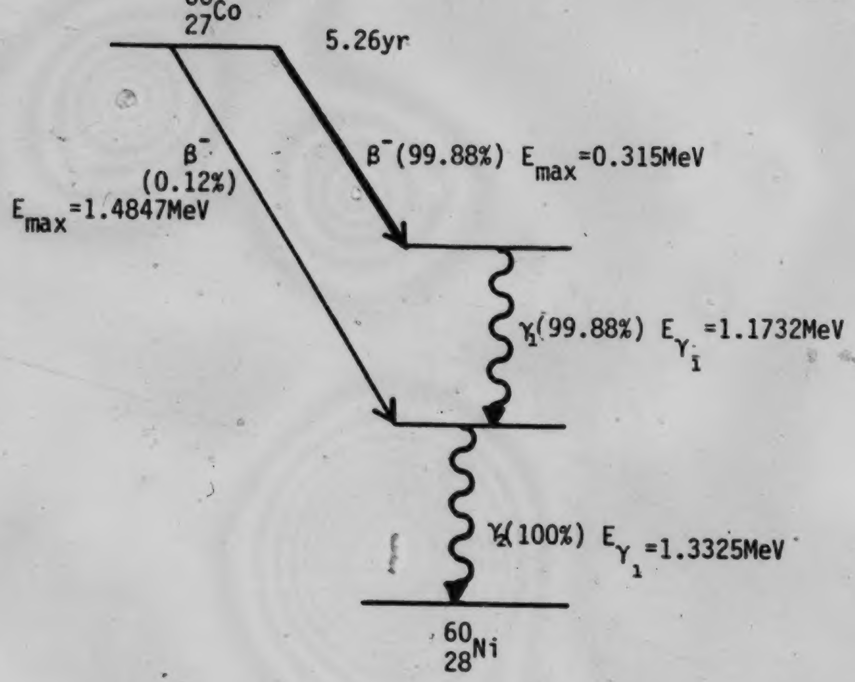
$^{60}_{27}Co$
5.26yr
$\beta^-$ (0.12%)
$E_{max}$=1.4847MeV
$\beta^-$(99.88%) $E_{max}$=0.315MeV
$\gamma_1$(99.88%) $E_{\gamma_1}$=1.1732MeV
$\gamma_2$(100%) $E_{\gamma_1}$=1.3325MeV
$^{60}_{28}Ni$

Figure #24. The decay scheme of $^{60}Co$.

intensities of 99.88% and 100% respectively, provide the radiation used in $^{60}$Co therapy and the pair are usuallt treated as a single photon of 1.25MeV.

The $^{60}$Co source is encapsulated in two stainless steel welded containers which are surrounded by a high Z shielding material, such as tungsten, on all sides except for the window through which the γ-rays are to be emitted. The source is placed near the center of a lead filled steel container which serves as the head of the treatment device. To provide the γ-ray beam for treatment the source is positioned inside the head at an opening which serves as a radiation port to volumes external to the head. Three such methods of source exposure are illustrated in Fig.#25. In Fig.#25(a) the source is positioned on a wheel which may be rotated through 180° to expose the source. In Fig.#25(b) the source is stationary and a wheel containing a portion of the port may be rotated through 90° to expose the source. In Fig.#25(c) the source is mounted on a drawer constructed of a high atomic number material which slides, usually by means of air pressure, horizontally to expose the source. The beam size is determined by a set of collimators which form the end of the radiation port. The field thus produced will have an attendant penumbra due in part to the small but finite size of the source.

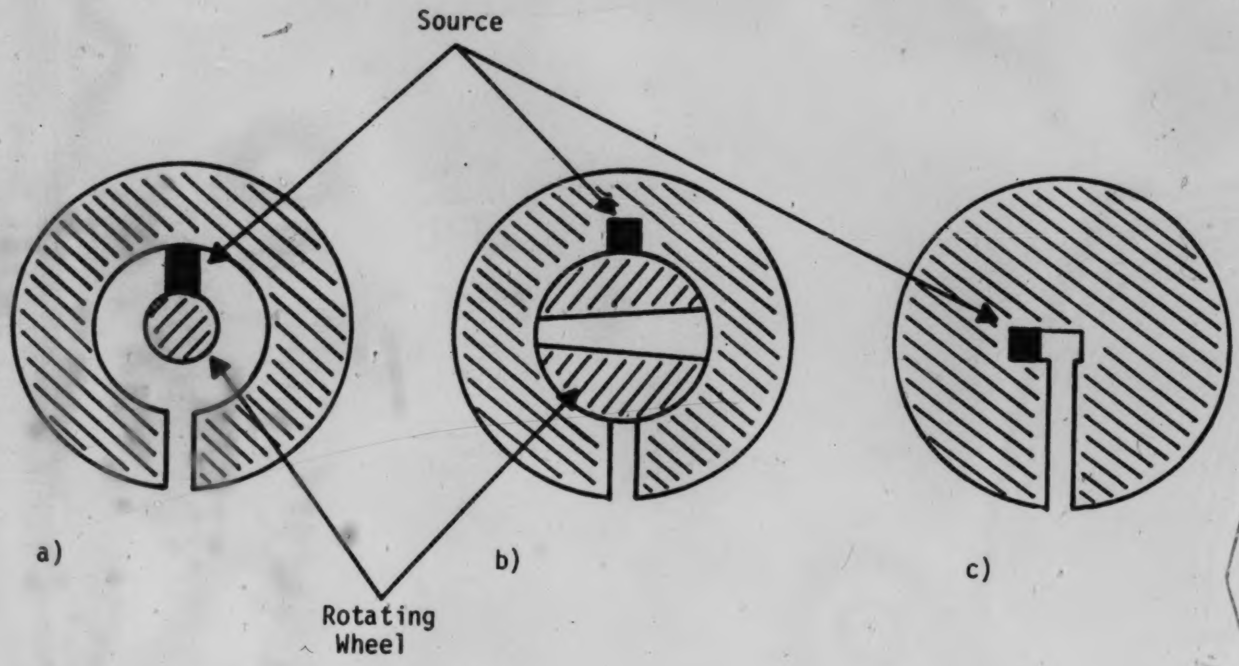
Source
a)
b)
c)
Rotating
Wheel

Figure #25. Three methods of $^{60}$Co source exposure.

## 3.2 Medical Linear Accelerators

### 3.2.1 Major Components

The major components of a modern linear accelerator are shown in Fig.#26. In this structure microwaves are employed to accelerate electrons to high energies. The accelerated electrons are directed onto a target where they produce Bremsstrahlung photons and the Bremsstrahlung photons so produced are used in radiotherapy treatment.

The microwave power supply consists of either a magnetron or a klystron. Klystrons can produce higher power outputs of microwaves than can magnetrons and as a result magnetrons are usually found on lower energy linear accelerators. The microwave power generated by either the magnetron or klystron is transported by means of a wave guide to the accelerator structure. The accelerator structure is a microwave resonant cavity and provides the environment wherein electrons may be accelerated to high energies by means of their interaction with microwaves. The bending magnet deflects the electrons emergent from the accelerator structure towards a target, if X-ray production is desired. The rest of the treatment head contains beam modifying and monitoring devices.

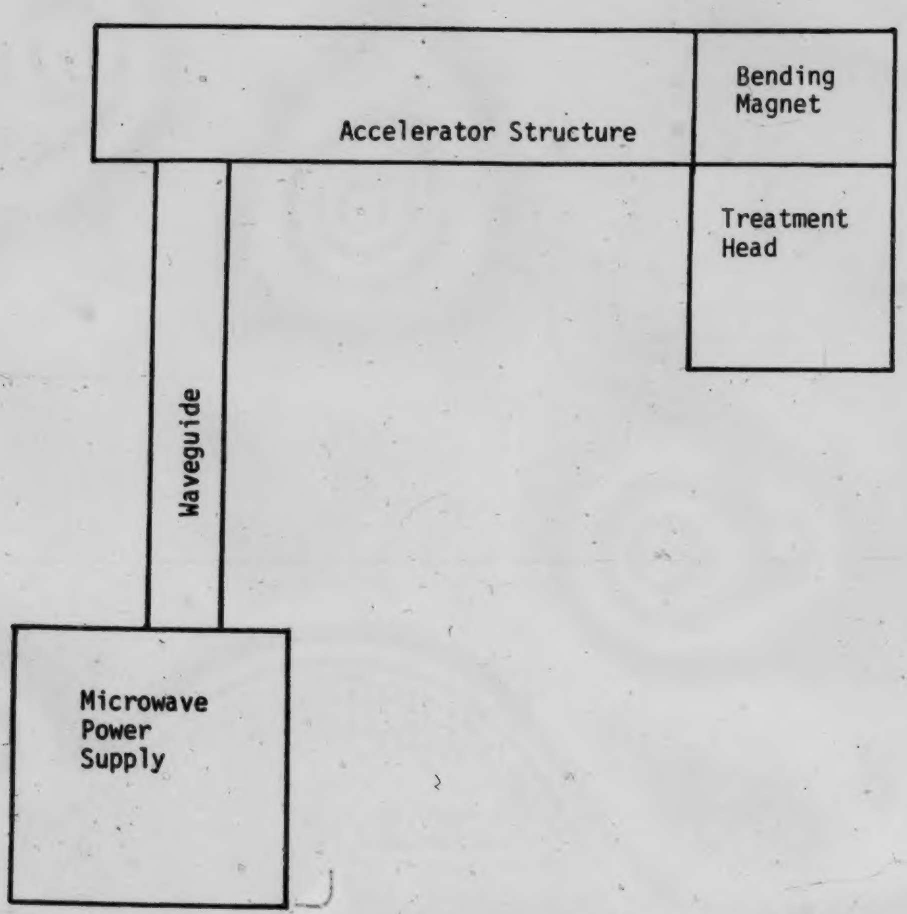
Accelerator Structure
Bending Magnet
Treatment Head
Waveguide
Microwave Power Supply

Figure #26. Major components of a linear accelerator.

### 3.2.2 Principles of Operation

#### 3.2.2.1 Microwave Power Supplies

Magnetrons are sources of microwave radiation which have a planar cylindrical geometry as shown in Fig.#27. The magnetron consists of a cylindrical central cathode separated from a clyindrical outer anode by a vacuum. A constant magnetic field is applied normal to the plane of geometry as shown and a pulsed electric field is applied radially inward from anode to cathode. Electrons generated by thermionic emission from the cathode are accelerated toward the anode and travel in spiral paths due to the applied magnetic field. The spiral motion of the electrons induces oscillating charge distributions of microwave frequency in the poles of the anode. These oscillating charge distributions create the desired oscillating electric fields of microwave frequency between the poles of the anode as shown.

The basic principles of a klystron are shown in Fig.#28. The klystron of Fig.#28 consists of two microwave resonance cavities connected by a drift tube. Electrons emitted by thermionic emission from the cathode are accelerated into the first microwave cavity, called the buncher cavity, and there encounter

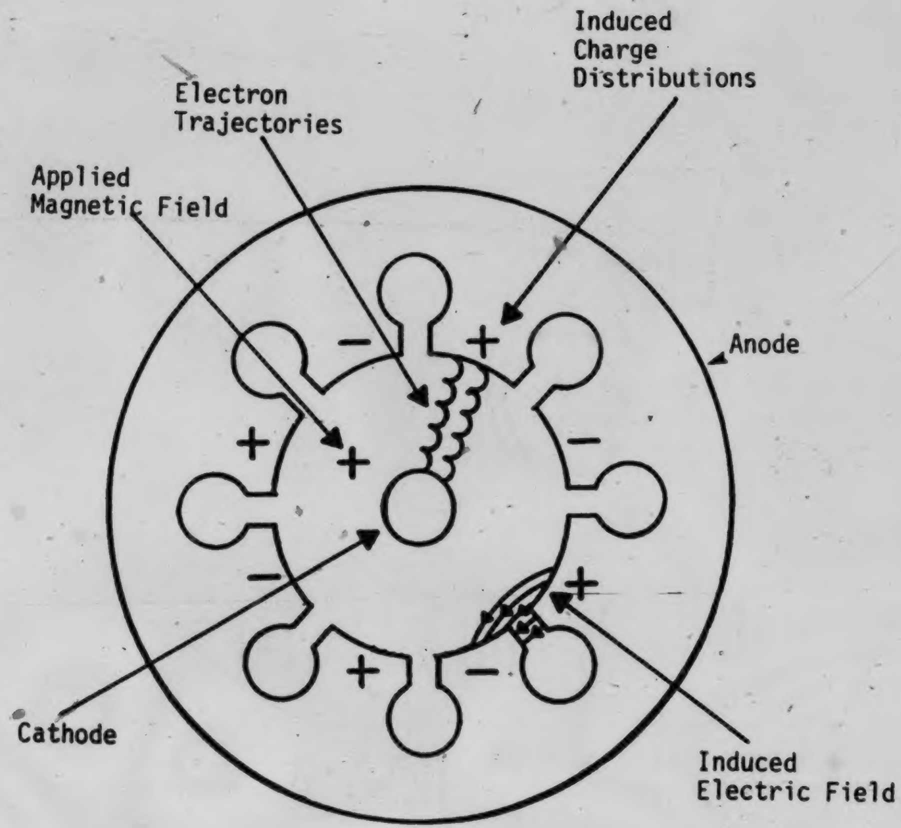
Induced
Charge
Distributions
Electron
Trajectories
Applied
Magnetic Field
Anode
Cathode
Induced
Electric Field
+
−
+
−
+
+
−
+
−
+
−

Figure #27. A cross sectional view of a magnetron.

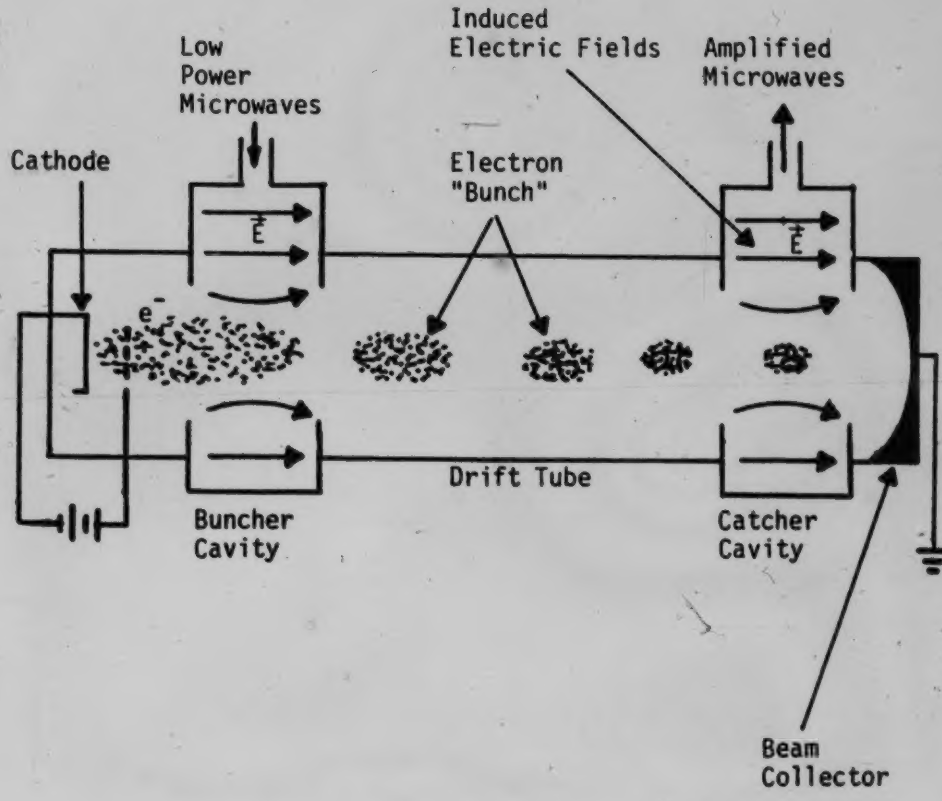
Induced
Electric Fields
Low
Power
Microwaves
Amplified
Microwaves
Cathode
Electron
"Bunch"
$\vec{E}$
$\vec{E}$
$e^-$
Drift Tube
Buncher
Cavity
Catcher
Cavity
Beam
Collector

Figure #28. The basic principles of a klystron.

alternating electric fields created by a high stability low power microwave source which energizes the cavity. The alternating electric field encountered by the electrons in this cavity serve to velocity modulate the electrons prior to their entry into the drift tube. In traveling from the buncher cavity to the second cavity, called the catcher cavity, the electrons will form discrete bunches or groups as the electrons with higher velocities "catch up" to those with lower velocities. Magnetic fields, not shown in Fig.#28, serve to focus and confine the electron beams as they traverse the length of the klystron. Upon entering the catcher cavity the electron bunches create large induced charges in the cavity walls which, according to Lenzs law, create strong electric fields which act to retard the motion of the electrons. Since the electrons arrive in the catcher cavity in bunches(ie: pulsed) the induced electric fields created between the cavity walls will be oscillatory in nature with the same frequency of the low power microwaves used to energize the buncher cavity. A large portion of the kinetic energy of the electrons entering the catcher cavity is converted into microwave power thus greatly amplifying the microwave power used to energize the buncher cavity. The electrons exiting the catcher cavity with greatly reduced energy are collected by the electron beam collector which serves as

✓

a dump to remove electrons from the system.

#### 3.2.2.2 The Waveguide

The high power microwaves produced by either the magnetron or the klystron are transported to the accelerator structure by means of a system of pipes called the waveguide. These pipes(often referred to as plumbing) are pressurized with an insulating gas, such as Freon or Sulphur hexafluoride, to increase the dielectric strength of the guide and hence increase its power handling capacity. The pressurized waveguide is separated from the evacuated magnetron or klystron and evacuated accelerator structure by ceramic or glass windows which readily transmit microwaves.

Also included in the waveguide structure is a device called a circulator which acts as a microwave diode. The circulator therefore allows transmission of microwave power in only one direction, from microwave power source to accelerator structure, thus eliminating feedback from the accelerator structure to the magnetron or klystron.

#### 3.2.2.3 The Accelerator Structure

The accelerator structure, or accelerator waveguide, consists of a large number of evacuated cylindrical microwave resonance cavities connected along their central axis as shown in Fig.#29. The operation of each microwave resonance cavity in the structure is the reverse of the catcher cavity in the klystron in that microwave energy in the cavity is converted into kinetic energy of electrons in the cavity.

There are two kinds of accelerator structures: travelling wave and standing wave. Both structures accelerate electrons which have been bunched into groups in a manner similar to that of the klystron.

The basic principles of a travelling wave accelerator are illustrated in Fig.#29. Microwaves enter the first cavity from the waveguide and propagate along the length of the waveguide, setting up alternating electric fields inside the resonance cavities, and are absorbed in a load at the end of the waveguide to prevent reflection. A group(bunch)of electrons is injected into the first cavity when the electric field is as shown in Fig.#29(a) and is accelerated. If the size of each cavity is chosen such that the group velocity(velocity of energy flow) of the microwaves in each cavity is matched to the velocity of the accelerating electrons in that cavity then the group of electrons in the first cavity will enter the second cavity half a cycle later, as in Fig#29(b), and again be

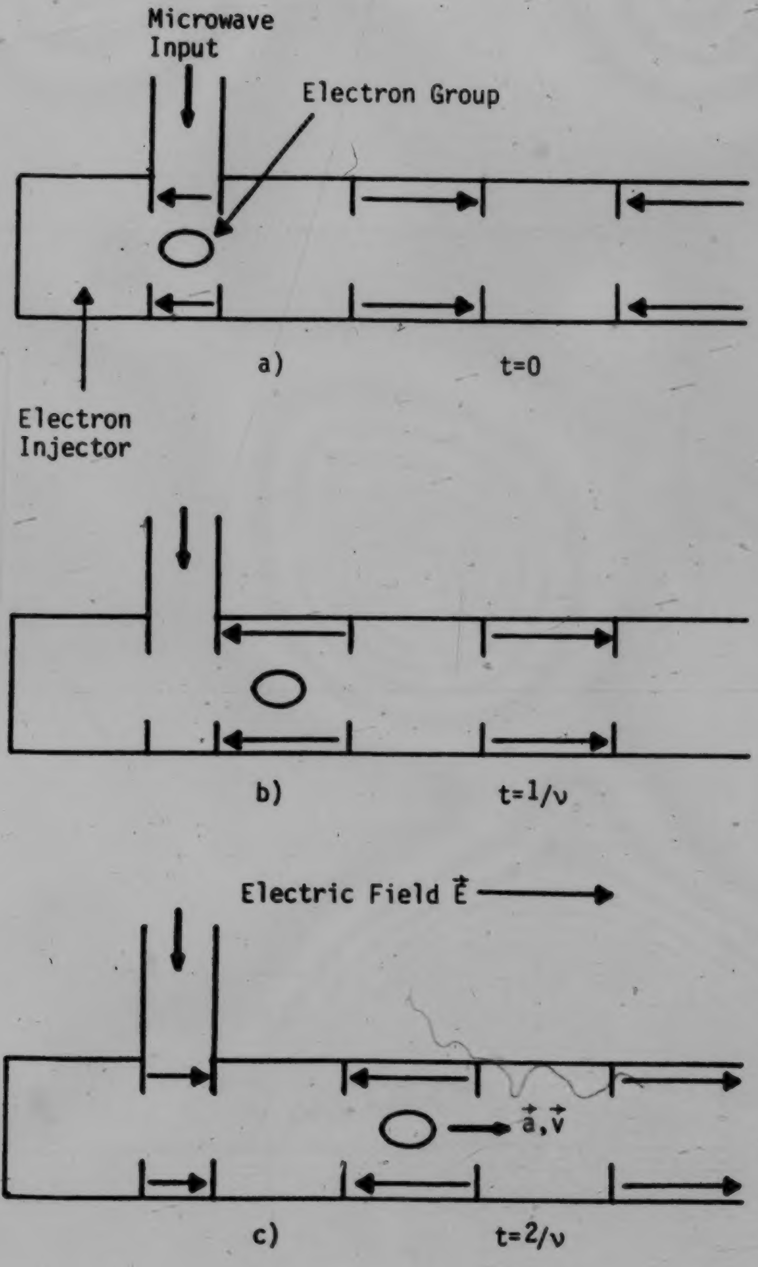
Microwave Input
Electron Group
a)
t=0
Electron Injector
b)
t=1/ν
Electric Field $\vec{E}$
$\vec{a},\vec{v}$
c)
t=2/ν

Figure #29. The basic principles of a traveling wave accelerator.

accelerated. After another half cycle the group of electrons in the second cavity will enter the third cavity,Fig.#29(c), and be further accelerated. This process is repeated as the group of electrons is accelerated along the length of the waveguide.

The basic principles of a standing wave accelerator are illustrated in Fig.#30. As was the case with the travelling wave accelerator, microwaves enter the first cavity from the waveguide and propagate the length of the waveguide. Unlike the travelling wave structure, however, the microwaves are reflected at the end of the waveguide to propagate back down the length of the waveguide, thus creating standing waves. The nodes and antinodes of the electric field of these standing waves will occur in distinct cavities in the waveguide. This allows the removal of the nodes, which provide no acceleration, from the electron beam path by moving the node cavities off axis as is shown in Fig.#30. Such a configuration is called side-coupled and permits greater flexibility and optimization in waveguide construction and performance. Reflection of the microwaves rather than absorption by a load at the end of the waveguide also results in greater energy efficiency. Most present day accelerator structures, including those used at the Cross Cancer Institute, are of the standing wave type.

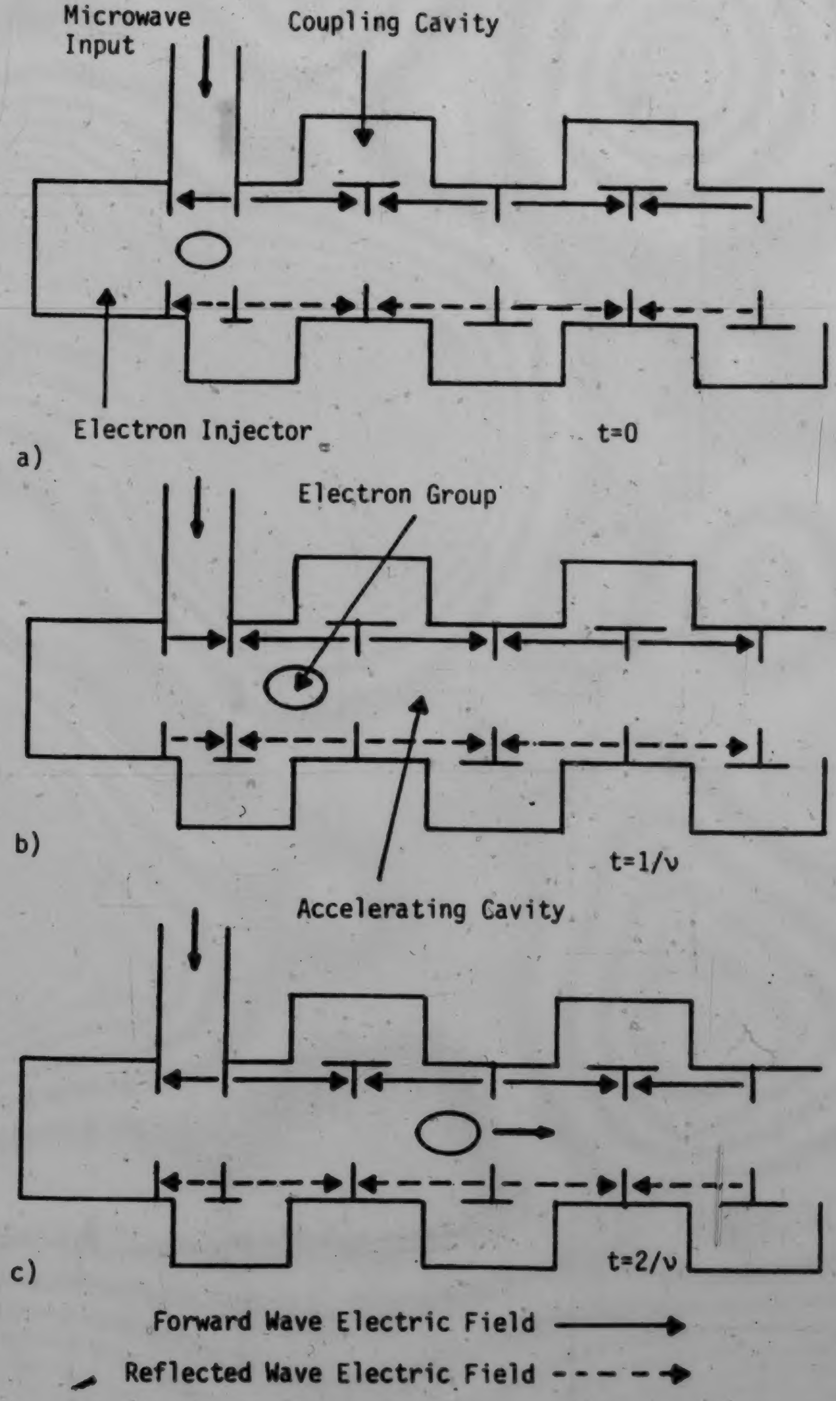
Microwave Input
Coupling Cavity
Electron Injector
a)
t=0
Electron Group
b)
t=1/ν
Accelerating Cavity
c)
t=2/ν
Forward Wave Electric Field ⟶
Reflected Wave Electric Field - - - →

Figure #30. The basic principles of a standing wave accelerator.

Again consider an electron group injected into the first cavity of a standing waveguide when the electric field is as shown in Fig.#30(a). Under these conditions the electron group will be accelerated. If the cavity sizes are chosen such that the phase velocity of the standing wave matches the velocity of the electron group as it is accelerated over the length of the waveguide then the electron group will enter the second cavity half a cycle later, as shown in Fig.#30(b), and again be accelerated. After another half cycle the electron group will enter the third chamber, as in Fig.#30(c), and again be accelerated. This process is repeated as the electron group is accelerated along the length of the waveguide.

### 3.2.2.4 The Bending Magnet

It is often desirable to direct the electron beam from the accelerator structure perpendicular to the axis of the accelerator. This may be achieved by bending the electron beam through 90° by means of a magnetic field but it is more often bent through 270° by an achromatic bending magnet as shown in Fig.#31. The reason behind use of the 270° achromatic bending magnet lies in the finite velocity distribution of the electrons in the electron group emerging from the accelerator. The radius of curvature r of an electron with total energy E in a

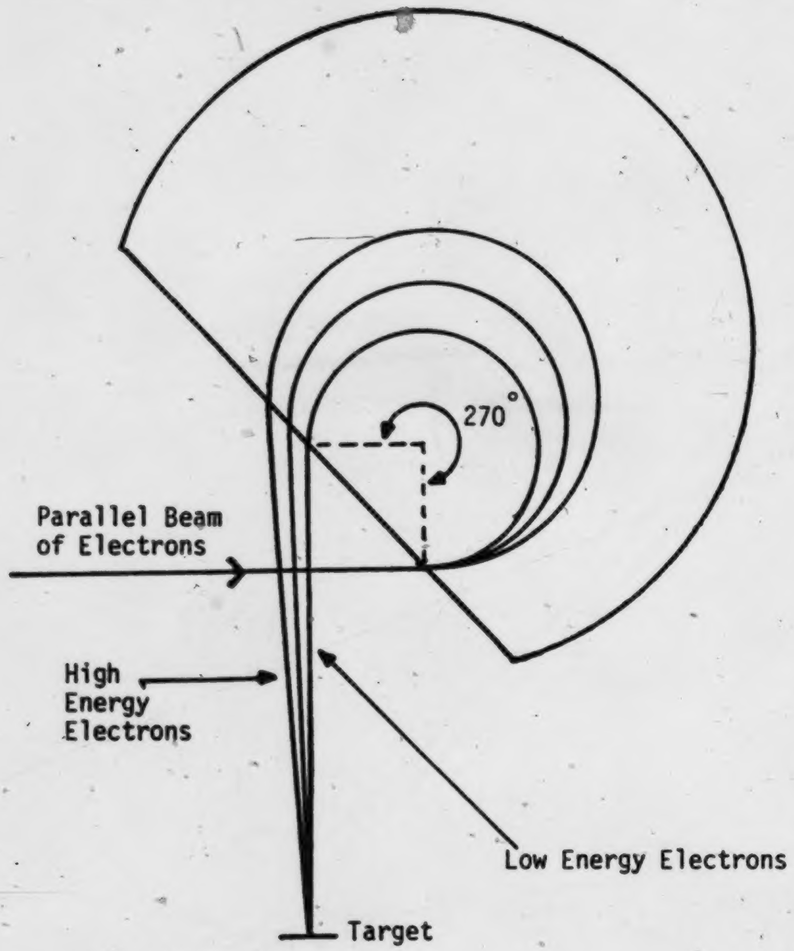
270°
Parallel Beam of Electrons
High Energy Electrons
Low Energy Electrons
Target

Figure #31. A 270° achromatic beam bending magnet.

uniform magnetic field B is given by

$$r = \frac{m_o c}{eB}\left(\frac{E^2}{m_o^2 c^4} - 1\right)^{\frac{1}{2}} \qquad [3.1]$$

Thus a collimated beam of electrons with a finite energy distribution will emerge divergent upon being bent through 90° by a uniform magnetic field. Such a divergent beam would require a larger than desired target size resulting in a larger than desired beam penumbra and give rise to a spectrum of x-ray energies.

An achromatic bending magnet provides a solution to this problem by generating a magnetic field which increases as a function of radial distance from the center of the magnetic field. Thus electrons entering this field with higher than average energy will have a larger than average radius of curvature where they will be subject to a greater bending force. Electrons with lower than average energy will experience the opposite effect. The net effect, as shown in Fig.#31, is to focus all electrons to a single point where the target may be placed to provide a small photon source with an attendent small penumbra.

### 3.2.2.5 The Treatment Head

The principle components of a typical treatment head are illustrated in Fig.#32. The beam of high energy electrons emergent from the accelerator and deflected by the bending magnet are incident upon a high Z target, such as tungsten, yielding bremsstrahlung photons which are highly forward peaked in intensity. Because the x-ray beam is forward peaked, a "flattening" filter is placed in the beam to flatten the X-ray field such that the beam intensity is relatively uniform over the cross sectional area of the beam. This flattening filter also tends to harden the beam, in that lower energy photons will be attenuated to a greater extent than will be higher energy photons. A low Z material is placed after the target to serve as an electron absorber which removes electrons emergent from the target from the beam.

A multiplate ion chamber is also placed in the beam. This allows monitoring of the dose rate, integral dose, and field symettry which are important for accurate dose delivery in a patient. A thin field light mirror placed in the beam as shown allows an off axis light source to optically illuminate the field on a given surface in the beam.

A primary collimator serves to limit the maximum field size at a given distance from the source. The actual field size employed is further defined by an

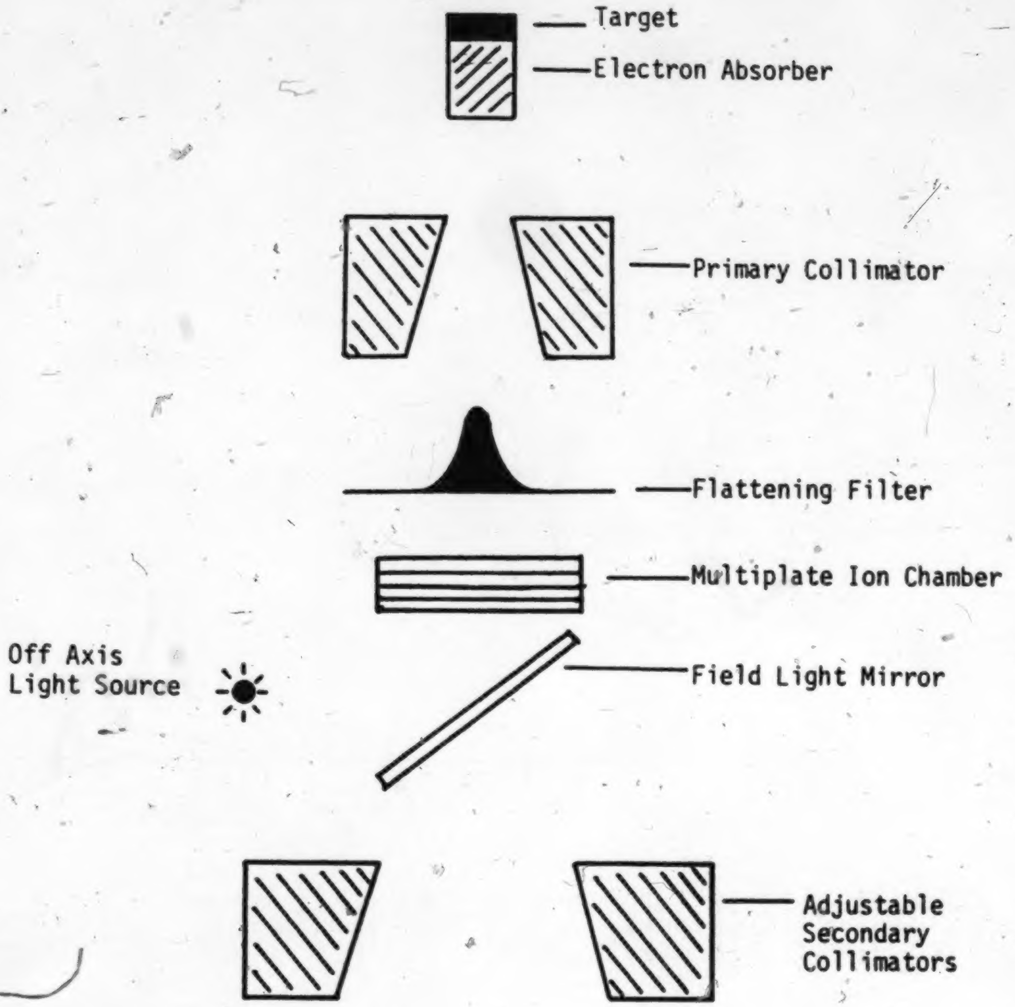
Target
Electron Absorber
Primary Collimator
Flattening Filter
Multiplate Ion Chamber
Off Axis
Light Source
Field Light Mirror
Adjustable
Secondary
Collimators

Figure #32. The principle components of a treatment head adjustable secondary collimator system. The secondary collimators are callibrated in terms of the field defined at a fixed source to surface distance(SSD). The edge of the field being defined to be that location where the absorbed dose falls to 50% of the dose along the central axis of the beam.

# IV DOSIMETRY

## 4.1 Energy Transfer

### 4.1.1 Basic Concepts

In radiotherapy a quantity of great interest is that of the absorbed dose. The absorbed dose from a beam of incident radiation is defined as being the energy absorbed from the radiation beam per unit mass of absorbing medium.

$$\text{Absorbed dose: } D = \frac{\Delta E_{ab}}{\Delta m} \qquad [4.1]$$

The SI unit for absorbed dose is the Gray(Gy) and is defined as

$$1\text{Gy} = 1\text{J/kg} \qquad [4.2]$$

An obsolete unit which is still used is the "rad", which is defined as

$$1\text{rad} = 100\text{erg/g} \qquad [4.3]$$

and hence

$$1\text{Gy} = 100\text{rad} \qquad [4.4]$$

### 4.1.2 KERMA

An x-ray photon will interact with the medium through which it passes, transferring some or all of its energy(depending on the type of interaction) to an electron of the medium or an electron-positron pair created by pair or triplet production, and these charged particles will in turn lose their energy as they travel from their point of origin. This energy loss takes the form of energy deposited in the medium via ionization and excitation of matter in the volume surrounding the particle's track and reradiation of photon energy via bremsstrahlung and positron annhilation quanta. Thus energy transfered to the medium by a photon at an interaction site is not necessarily equal to the energy absorbed at that point. To describe this process a quantity, called the KERMA, has been defined as the mean energy transferred per photon to electrons(or positrons) per unit mass.

$$\text{KERMA: } K = \frac{\Delta E_{tr}}{\Delta m} \qquad [4.5]$$

If a beam of photons of fluence is incident upon a thin slab of material of thickness x then the kerma will be

$$K = \Phi\left(\frac{\mu}{\rho}\right)\bar{E}_{tr} \qquad [4.6]$$

The units of KERMA are the same as those of absorbed dose. The word KERMA is an acronym for Kinetic Energy

Released in the Medium.

### 4.1.3 Electronic Equilibrium

Consider a non-divergent photon beam of fluence $\Phi$ incident normal to a flat slab of thickness L, as shown in Fig.#33, where $\mu$ is the linear attenuation coefficient of the beam in the slab material. If $L \ll \mu^{-1}$ then the photon fluence at depth $d \ll L$ in the slab is

$$\Phi = \Phi_o e^{-\mu d} = \Phi_o \left(1 - \frac{\mu d}{1!} + \frac{(\mu d)}{2!} - \frac{(\mu d)}{3!} + \dots\right) \qquad [4.7]$$

and hence to a first approximation photon attenuation may be ignored. Then in any given interval of depth $\delta d_i$ the KERMA will be

$$K = \Phi_o \left(\frac{\mu}{\rho}\right) \bar{E}_{tr} \qquad [4.8]$$

If n electrons are assumed to be set in motion at the beginning of the interval then they will lose(and hence deposit to the medium) an energy of $nS_{ion}\,\delta d_i$ in transiting the interval according to the continuous slowing down approximation if no bremsstrahlung is created. The energy deposited will be less than the KERMA and hence one has

$$K = nS_{ion}\delta d_i \neq 0 \qquad [4.9]$$

In the second interval the electrons set in motion in

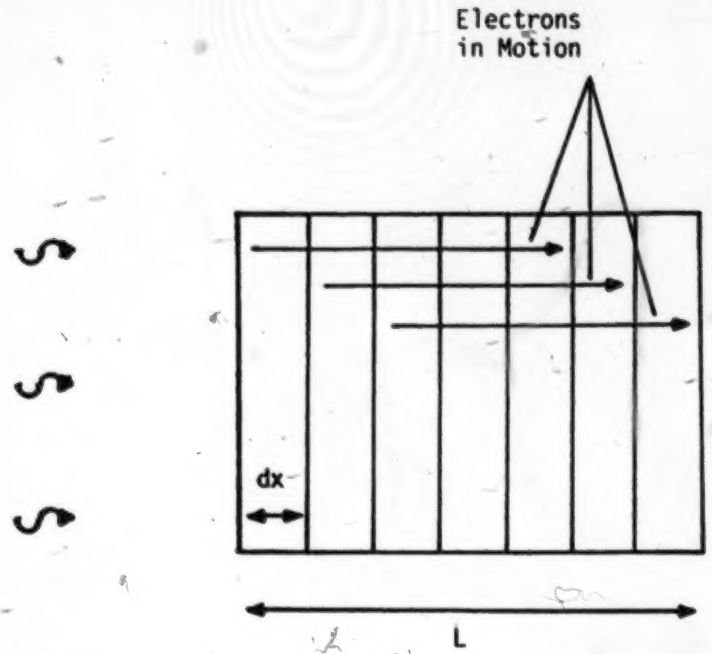
Electrons
in Motion
dx
L

Figure #33. A non-divergent photon beam incident normal to a flat slab of absorber material.

the first interval will lose an energy of $nS_{ion}\delta d$ and hence

$$K - 2nS_{ion}\delta d_i < K - nS_{ion}\delta d_i \qquad [4.10]$$

For any depth d<R, where R is the c.s.d.a range of electrons in the medium, one has

$$K - \sum_1^n nS_{ion}\delta d_i < K - \sum_1^{n-1} nS_{ion}\delta d_i \neq 0 \qquad [4.11]$$

For the case of $d = \sum_1^N \delta d_i = R$ the electrons originally set in motion in the first interval will have been completely stopped at the end of the N^th^ interval and hence will not contribute to the (N+1)^th^ interval. Thus one has

$$K - \sum_1^N nS_{ion}\, d_i = K - nS_{ion} \sum_1^N \delta d_i = K - nS_{ion}\, R \qquad [4.12]$$

If $S_{rad} = 0$ then

$$K - nS_{ion}R = 0 \qquad [4.13]$$

and for all intervals d for which d>R one has

$$K = nS_{ion}\, R \qquad [4.14]$$

This condition is called electronic(or charged particle) equilibrium as it exists in regions where the net energy transported into a region by electrons is equal to the net energy transported out of the same region by electrons. When this is the case then the absorbed dose is equal to the KERMA

$$D = \Phi_o \left(\frac{\mu}{\rho}\right) \overline{E}_{tr} \qquad [4.15]$$

If f is the fraction of the KERMA which is reradiated as bresstrahlung then equation [4.15] becomes

$$D = \Phi_o \left(\frac{\mu}{\rho}\right) \overline{E}_{tr} (1-f) \qquad [4.16]$$

The region for which $K - \sum_{1}^{n} nS_{ion} \delta d_i < 0$ is called the build-up region. The above situation is illustrated in Fig.#34(a).

In the real world photon attenuation may not be ignored and equation [4.8] becomes

$$D = \Phi_o \left(\frac{\mu}{\rho}\right) e^{-\mu d}\, \overline{E}_{tr} \qquad [4.17]$$

and $K - nS_{ion}R = 0$ at only one specific depth, called the equilibrium depth, which is less than the mean electron range R. In this case the energy deposited is less than the KERMA for depths less than the equilibrium depth and the energy deposited is greater than the KERMA for depths greater than the equilibrium depth. This situation is illustrated in Fig.#34(b).

## 4.2 Cavity Theory

In order to measure the absorbed dose at a given

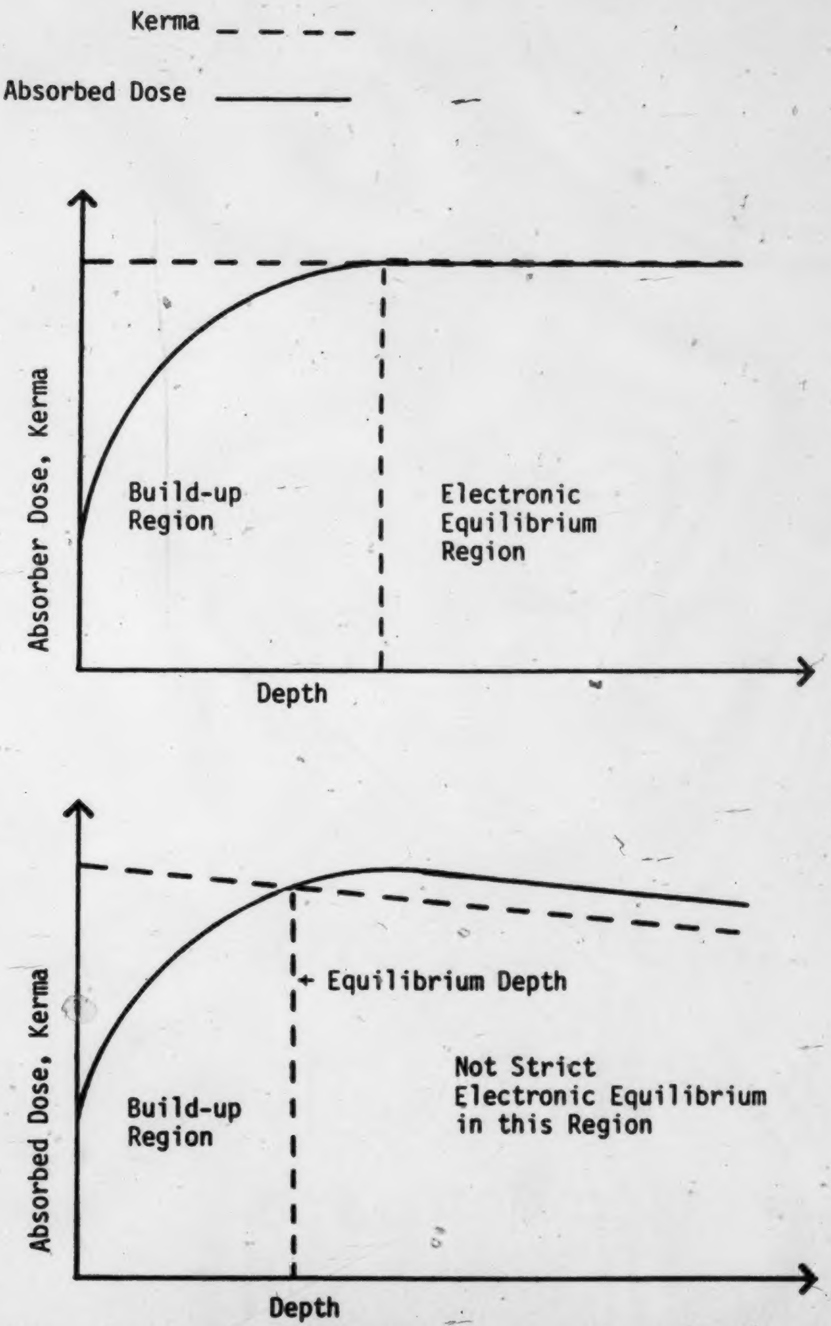

Figure #34. Variation of absorbed dose and kerma with depth in an absorber. In (a) no photon attenuation occurs. In (b) photon attenuation is taken into account.

point in a medium one must insert a measuring device into the medium. The measuring device thus inserted creates a discontinuity in the absorbing medium and this discontinuity is refered to as a "cavity". The relationship between the absorbed dose as measured by the measuring device and that which would occur if the measuring device were not inserted in the medium is the subject of cavity theory.

The Bragg-Gray formulation of cavity theory makes the following assumptions:

a) the size of the cavity is small in that its dimensions are much less than the range of secondary electrons in the medium.

b) the introduction of the cavity to the medium does not perturb the medium's spectrum of secondary electrons.

c) photon attenuation is negligible over the dimensions of the cavity, and hence secondary electrons in the cavity are due to photon interactions in the medium surrounding the cavity.

d) the primary photon fluence in the region surrounding the cavity from which secondary electrons generated in the medium may enter the cavity is isotropic.

e) secondary electrons lose energy

continuously according to the c.s.d.a approximation.

With these assumptions consider the small cavity in the medium of Fig.#35. If the secondary electron spectrum $\Phi_e$ of the medium is monoenergetic then the dose in the cavity is

$$D_c = \frac{S}{\rho}\bigg|_c \Phi_e \qquad [4.18]$$

and the dose that would be absorbed by the medium, if the cavity were replaced by medium, is

$$D_m = \frac{S}{\rho}\bigg|_m \Phi_e \qquad [4.19]$$

and hence

$$\frac{D_m}{D_c} = \frac{(S/\rho)_m}{(S/\rho)_c} = S_c^m = \left(\frac{1}{S_c^m}\right)^{-1} \qquad [4.20]$$

where $S_c^m$ is the ratio of the stopping power of the medium to that of the cavity. Now if the secondary electrons created in the medium by photon interactions all possess the same initial energy $E_o$ they will then lose energy to the medium according to the c.s.d.a and a spectrum of electron energies will be "seen" by the cavity. Under conditions of electronic equilibrium the spectrum of electrons thus generated may be approximated according to

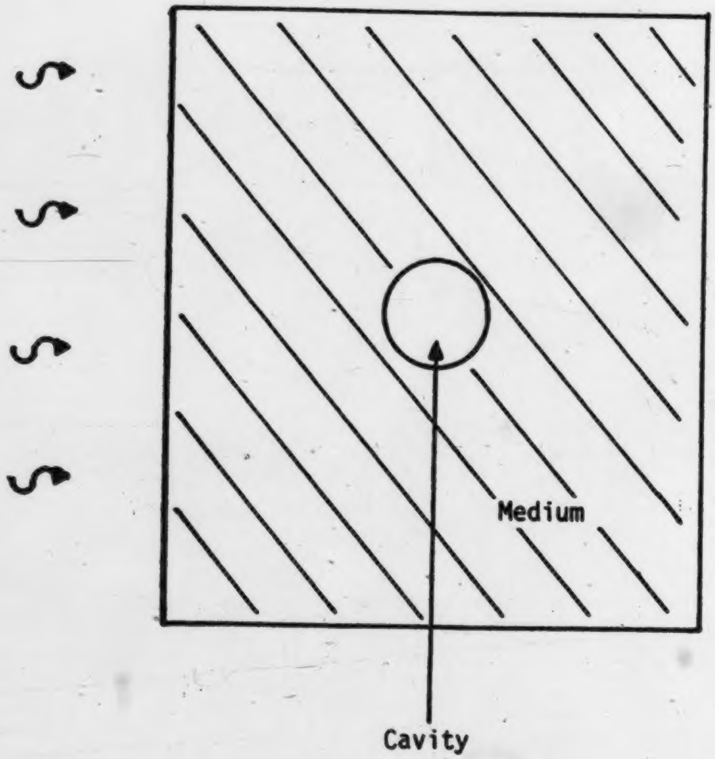
Medium
Cavity

Figure #35. A small cavity in a medium.

$$\Phi_e'(E_\circ) = \frac{1}{\frac{1}{\rho}\left[\frac{dE}{dx}\right]_m} n_e = \frac{1}{\left.\frac{S}{\rho}\right|_m} n_e \qquad [4.21]$$

where $n_e$ =number of electrons per gram of medium material. The dose to the cavity then becomes

$$D_c = \int_0^{E_\circ} \Phi_e'(E_\circ) \left.\frac{S}{\rho}\right|_c dE = \int_0^{E_\circ} \frac{(S/\rho)_c}{(S/\rho)_m} n_e \, dE$$

and [4.22]

$$\frac{D_c}{D_m} = \frac{\int_0^{E_\circ} \frac{(S/\rho)_c}{(S/\rho)_m} dE}{\int_0^{E_\circ} \frac{(S/\rho)_m}{(S/\rho)_m} dE} = \frac{\int_0^{E_\circ} \frac{(S/\rho)_c}{(S/\rho)_m} dE}{\int_0^{E_\circ} dE} = \frac{1}{S_c^m}$$

where $1/S_c^m$ = the inverse of the ratio of the mass stopping powers of the medium to that of the cavity averaged over the c.s.d.a electron spectrum.

If the secondary electrons do not all have the same initial energy $E_\circ$ then $1/S_c^m$ must be averaged over the spectrum of initial electron energies $\Phi_e''(E_\gamma, E_\circ)$

$$\frac{\bar{\bar{1}}}{S_c^m} = \frac{\int_0^{E_{max}} \Phi_e''(E_\gamma, E_\circ) \frac{\bar{1}}{S_c^m} dE_\circ}{\int_0^{E_{max}} \Phi_e''(E_\gamma, E_\circ) dE_\circ} \qquad [4.24]$$

And this must be in turn averaged over the spectrum of initial photon energies $\Phi_\gamma(E_\gamma)$

$$\frac{\bar{\bar{\bar{1}}}}{S_c^m} = \frac{\int_0^{E_{max}} \Phi_\gamma(E_\gamma) \frac{\bar{\bar{1}}}{S_c^m} dE_\gamma}{\int_0^{E_{max}} \Phi_\gamma(E_\gamma) dE_\gamma} \qquad [4.25]$$

Thus one has

$$\frac{D_c}{D_m} = \frac{\bar{\bar{\bar{1}}}}{S_c^m} = \left(\bar{\bar{\bar{S}}}_c^m\right)^{-1}$$

or

$$D_m = \bar{\bar{\bar{S}}}_c^m D_c \qquad [4.26]$$

The ratio $\bar{\bar{\bar{S}}}_c^m$ is often refered to as the "average stopping power ratio". The effect of δ-ray production has been taken into account by Spencer and Attix by employing the restricted stopping power $\Delta L$ in place of the stopping power S and averaging over the electron spectrum from a minimum electron energy Δ to Emax.

In order to make the measuring cavity more versatile it is often surrounded by a wall of material of sufficient thickness such that electronic equilibrium is established in the wall. Thus electrons incident upon the cavity originate in the wall material and one has

$$D_{wall} = \overset{\equiv}{S}{}_c^m D_c$$

and

$$\frac{D_w}{D_m} = \frac{(\mu_{en}/\rho)_{wall}}{(\mu_{en}/\rho)_m} \qquad [4.27]$$

where $\mu_{en}/\rho$ is the mass energy absorption coefficient. One therefore has

$$D_m = \overset{\equiv}{S}{}_c^m \frac{(\mu_{en}/\rho)_m}{(\mu_{en}/\rho)_{wall}} A_{eq} D_c \qquad [4.28]$$

where $A_{eq}$ is a correction factor for the perturbation of photon fluence resulting from the presence of the cavity and its wall.

Hence if one can measure the absorbed dose in the cavity then one can determine the absorbed dose to the volume of medium displaced by the cavity.

## 4.3 Methods of Photon Dosimetry

### 4.3.1 Ionizational Methods

#### 4.3.1.1 Standard Air Chamber

Dosimetry by ionizational methods involves measurement of the quantity of ionization produced in a cavity and the subsequent calculation of the absorbed dose in the medium in the absence of the cavity. In the case of the standard air chamber the medium and cavity are composed of the same material, air. In a standard air chamber, as shown in Fig.#36, a narrow x-ray beam passes through the center of the chamber. A large potential difference maintained between the upper and lower collection plates serves to remove ions produced in the active volume V and reduce recombination of these ions, such that they may be collected by the upper and lower collection plates. Guard electrodes on either side of the lower collection plate serve to reduce edge effects associated with the electric field. Upper and lower collection plates are separated by a distance of greater than twice the range of secondary electrons generated in order that only ions produced by the secondary electrons will be collected. The dimensions of the chamber required to establish electronic equilibrium are such that photon attenuation becomes significant for photon energies above 3MeV and hence standard air

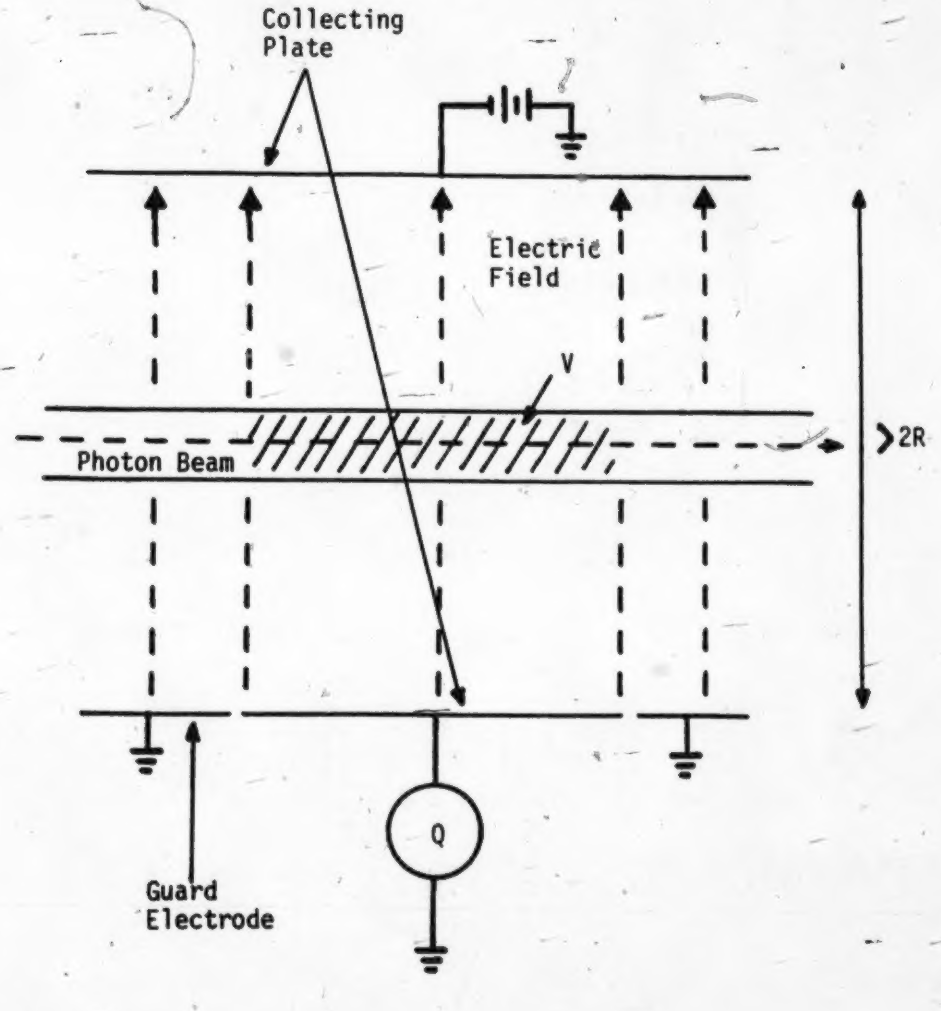
Collecting Plate
Electric Field
V
Photon Beam
2R
Q
Guard Electrode

Figure #36. Schematic representation of a standard air chamber.

chambers are not used for energies above that energy.

Assuming saturation, or the complete collection of all ions, one may define a quantity X, called exposure, as the amount of charge dQ generated in a mass dm

$$X = \frac{dQ}{dm} \qquad [4.29]$$

when all of the secondary electrons generated by photons in mass dm of air have been brought to rest. The unit of exposure is the roentgen, R, and is defined as

$$1R = 2.58X10^{-4} \text{ C/kg of air} \qquad [4.30]$$

It is found that the average energy required to cause a single ionization in a gas is constant over a large range of gas pressures and electron energies and hence one may determine the absorbed dose at a point from the exposure measured at that point. For air the average energy W required for one ionization is

$$W = 33.85 \frac{\text{eV}}{\text{ion pair}} = 33.85 \text{ J/Coulomb} \qquad [4.31]$$

Thus the absorbed dose in air becomes

$$D_{air} = W_{air} \frac{Q_{air}}{m_{air}} = W_{air} X_{air} \qquad [4.32]$$

where the mass of air is determined from a knowledge of the density of air in the measuring volume V.

### 4.3.1.2 Practical Ion Chambers

Standard air chambers are used for calibration in standards labs while much smaller "air-wall" ion chambers are more practical for routine radiation measurements. Such an air-wall ion chamber consists of a small air filled cavity containing a central electrode and bounded by an outer electrode. Surrounding the cavity is a wall of material with x-ray absorption and scattering properties very similar to that of air but of a much higher density than air. The high density of the wall allows electronic equilibrium to be established within much smaller dimensions than that of the standard air chamber. Special compositions of plastic usually serve as the wall material. With the small size of the cavity the electron spectrum seen by the cavity is that of the wall and hence equation [4.28] applies.

By careful choice of parameters, the "air-wall" chamber can be constructed such that its response to photon energies is very close to that of the standard air chamber. One may thus calibrate an air-wall chamber by comparison with a standard air chamber to produce an exposure calibration factor Nx(hν). This calibration factor may then be used to determine the exposure X measured by the air-wall chamber in terms of the charge q collected by the chamber electrodes.

$$X = N_X(h\nu)f(q) \qquad [4.33]$$

where f(q) represents the meter reading of the device which measures the charge collected. Build-up caps may be added to the outside of the air-wall to extend the use of the chamber to higher energies.

#### 4.3.1.3 Solid State Detectors

The basic underlying principle of solid state detectors is the same as that of gas-filled ionization chambers: the production of the equivalent of ion pairs by radiation interacting with the material of the detector. A simplified semiconductor detector consists of a block of semiconductor material across which is applied an electric potential via electrodes attached to opposite faces of the block. By means of this applied potential the ion pairs produced in the semiconductor block are converted directly into an electronic pulse which may be amplified and analysed by suitable electronic equipment so as to determine the energy and fluence of the incident ionizing radiation. Of available semiconductor materials, silicon is the most commonly used material of diode detectors which are employed in charged particle dosimetry, while germanium is the prefered material of ion-drifted detectors which are employed in x-ray dosimetry.

### 4.3.1.4 Thermoluminescent Detectors (TLD)

A thermoluminescent material is one in which many of the electrons, or their hole counterparts, which are produced upon the passage of ionizing radiation through the material while at a normal operating temperature, become trapped at lattice imperfection sites in the material. A thermoluminescent material which is suitable for dosimetry purposes is one in which the probability that these trapped electrons or holes will remain trapped is high if the material remains at or below a specific operating temperature, but, upon raising the temperature of the material the probability of electron or hole escape increases. Those electrons or holes which escape their lattice traps return to stable energy states in the lattice by the emission of visible light. This emitted light may be measured and can be plotted as a function of the temperature of the material. The resulting "glow curve" will exhibit one or more peaks which correspond to different energies of the different traps in the lattice. By means of suitable calibration, the absorbed dose of the material may then be determined as a function of the total light emitted in part or all of the glow curve, or the relative height of one or more of the particular peaks in the curve.

### 4.3.2 Actinometry

Actinometry, or chemical dosimetry, is the process by which the absorbed dose is determined by the chemical change produced in an appropriate medium due to exposure to radiation. This method of dosimetry is good even in a non-homogeneous radiation field as it produces an average dose value. The actinometer stands as a secondary standard in that it must be calibrated in some absolute manner. To qualify as a good actinometer the chemical change or yield produced by radiation must be independent of: the dose rate or total dose; moderate changes in pH, temperature, and concentration of reactants; the presence of trace amounts of impurity; and the nature and energy of radiation. In addition, no pre- or post-irradiative reactions should occur in the system and the absorbing properties of the actinometer should be as close to those of the medium which is irradiated.

#### 4.3.2.1 The Fricke Dosimeter

No universal actinometer has yet been developed but the most comonly used over the dose range of 1 to 500Gy is the Fricke dosimeter. Other actinometers provide measurement over the range from 10 to 100MGy, but none give as reliable results as does the Fricke dosimeter.

In the Fricke solution Fe(2+) ions(in an acid solution) are converted into Fe(3+) ions upon irradiation, and the amount of Fe(3+) produced, G(Fe(3+)) (the number of Fe(3+) ions produced per 100eV of energy absorbed by the system), is measured spectrophotometrically. The value of G(Fe(3+)) is much lower when oxygen is absent from the solution than when it is present and hence the amount of oxygen present in the solution, as well as the Fe(3+) concentration, sets an upper limit on the dose which may be measured. For a 0.001M ferrous sulphate solution this upper limit is about 400Gy. By raising the concentration of ferrous sulphate to 0.05M it is possible to extend the useful dose range to about 10kGy, but this requires extra oxygen which is often provided by bubbling oxygen continuously into the solution, but G(Fe(3+)) tends to be non-linear in this extended range. There is also a general decrease in G(Fe(3+)) with increasing LET and hence the measured dose is not independent of radiation energy. The Fricke dosimeter consists of two basic parts: the chemical solution, and the container for the chemicals called the reaction cell.

#### 4.3.2.2 Film Dosimetry

Another important actinometer is photographic film. The use of photographic film in dosimetry employs the use of a radiation-sensitive material, photographic emulsion, which consists of microscopic grains, silver halide crystals, dispersed in gelatin. This emulsion forms a thin layer on a suitable film. When radiation is absorbed in an individual grain a "latent image" is formed. This latent image is the physical condition which facilitates the reduction of the grain to elemental silver under the action of chemical development more rapidly than those grains which have not absorbed radiation. After development the film is fixed, whereby the unaffected silver bromide is removed from the film leaving behind the developed grains of elemental silver. Thus areas of the film exposed to radiation will be dark. The concentration or density of silver grains being a measure of the absorbed dose. The concentration of silver grains can be determined by measuring the optical density of the film with a densitometer. As the optical density of the film is a function of the development procedure the development procedure must be carefully controlled.

Film dosimetry finds use in rapid determination of the pattern of radiation distribution, personnel monitors, and a number of other applications where a high degree of accuracy is not required. The practical range of sensitivity of film as a dosimeter extends from about 10cGy to the kGy range and even up to the MGy range(with special processing techniques).

### 4.3.3 Calorimetry

If no chemical changes occur then the energy absorbed by an irradiated system can all appear as heat. If a chemical reaction does occur then the calorimetric method of dosimetry is inaccurate as a chemical reaction can either evolve heat(exothermic reaction) or absorb heat(endothermic reaction). The great advantage of calorimetry dosimetry is that energy deposition by irradiation is measured directly whereas other methods of dosimetry rely on secondary processes. The employment of secondary processes necessitates the use of conversion factors based on a physical interpretation of the absorption processes employed. No secondary conversion factors are required to relate the energy absorbed in a medium from ionizing radiation to the heating of that medium and hence calorimetry stands as the most direct method of dosimetry.

The basic principle of calorimetry dosimetry is that a suitable material is placed in an irradiation position and the resulting temperature rise of the material is measured during irradiation. The material which is to act as the absorber(core) of the calorimeter is placed inside an insulating jacket and a shield which is in turn contained in a large thermally controled mass called a buffer. The core, jacket, shield, and buffer are composed of the same material and are thermally isolated from one another so that the temperature of each can be measured and controlled. If the core, jacket, shield, and buffer are brought into thermal equilibrium with each other then the temperature of the core, jacket, and shield will increase at a uniform rate as radiation is absorbed. With the buffer being maintained at a constant temperature then the rise in temperature of the core, jacket, and shield can be measured and, if the mass and specific heat of each component is accurately known, thus the energy input due to irradiation can be readily determined from the rise in temperature of the core- jacket- shield system. In ~~doing so~~ corrections for wall effects and heat loss during measurement must be made, but with proper design these corrections can be minimized. Carbon, lead, and water are the most widely used absorber materials in calorimetry.

Due to limitations imposed by temperature control and measurement, the lower limit of measurable dose by calorimetry is about 10cGy. Since calorimetry involves the total absorption of radiation energy, calorimetry dosimeters are to a high degree independent of the energy of the radiation, but there is some dose dependence due to unknown chemical effects which do not appear as heat. Calorimetry finds great use in the calibration of other dosimeters.

## 4.4 Dosimetric Functions

Of prime concern in radiotherapy is the absorbed dose in tissue in an irradiated volume. To this end much experimental work has been performed with materials which absorb and scatter radiation in as similar a manner as possible to tissue. Such materials are called phantoms. The requirements of a phantom, as set out by the ICRU, are that it be "a volume of tissue-equivalent material, usually large enough to provide full scatter conditions for the beam being used..." where a tissue equivalent material is "a material whose absorption and scattering properties for a given irradiation simulate, as nearly as possible, those of a given biological material, such as soft tissue, muscle, bone, or fat.(15)

The absorbed dose at any point in a phantom is the result of two components. The first component is the dose due to primary radiation and the second component is the dose due to scattered radiation. Both the dose due to primary radiation and the dose due to scattered radiation are functions of the physical parameters of the radiation beam and the parameters of the physical geometry. For the irradiated phantom in Fig.#37 the dose to a given point at a depth d below the phantom surface is

$$D(d,Wd,F,h\nu) = D_0 e^{-\mu(h\nu)d} \; S(d,Wd,F,h\nu) \qquad [4.34]$$

where Wd is the field width at depth d, F is the distance from the radiation source to the phantom surface, $h\nu$ is the (characteristic) energy of the radiation beam, and $\mu(h\nu)$ is the linear attenuation coefficient of the beam. With this in mind certain relations have been developed to describe the absorbed dose as a function of these parameters.

### 4.5.1 Tissue-Air Ratio

One such important relation is the tissue-air ratio. The tissue-air ratio is defined as the ratio of the dose absorbed at a given point in a phantom to that of the dose absorbed by a small volume of phantom material just sufficient to establish electronic equilibrium at the same measurement point. This

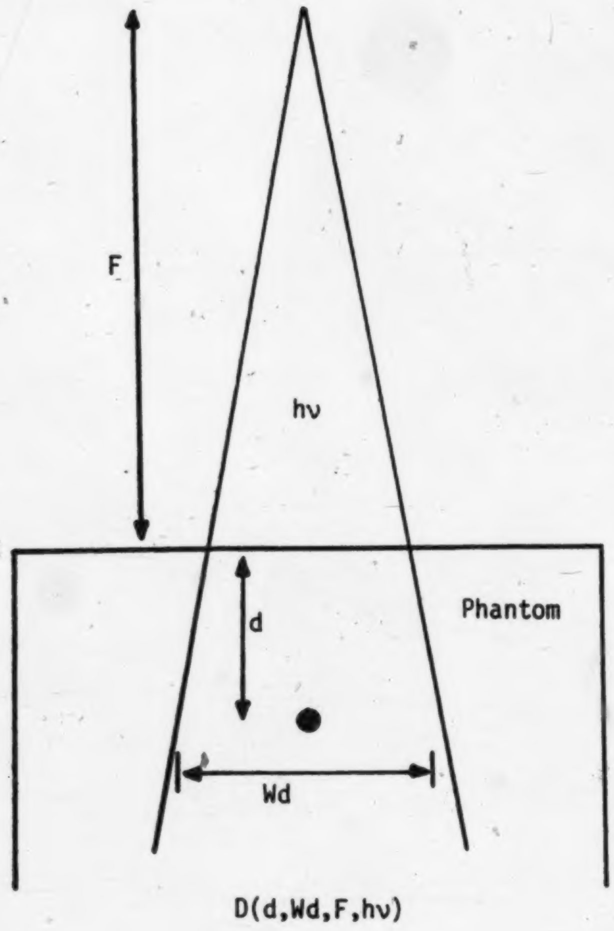
F
hν
d
Phantom
Wd
D(d,Wd,F,hν)

Figure #37. Basic geometry for dosimetric functions.

situation is illustrated in Fig.#38 and may be expressed mathematically as

$$TAR(d,Wd,h\nu) = \frac{D(d,Wd,F,h\nu)}{D'(d,Wd,F,h\nu)} \qquad [4.35]$$

The tissue-air ratio is thus a description of the dose due to the attenuated primary beam plus the dose due to scatter within the phantom.

In the special case where the depth d in the phantom equals the equilibrium thickness dmax for that phantom, the tissue-air ratio is written as

$$TAR(d_{max},Wd_{max},F,h\nu) = B(d_{max},Wd_{max},h\nu) \qquad [4.36]$$

$$= \frac{D(d_{max},Wd_{max},F,h\nu)}{D'(d_{max},Wd_{max},F,h\nu)}$$

and is refered to as the backscatter factor as it gives the increase in dose resulting from the backscatter radiation from the phantom.

### 4.5.2 Scatter-Air Ratio

The scatter-air ratio is a function derived from the tissue-air ratio which yields the amount of dose due to scatter in a phantom. The scatter-air ratio is defined as

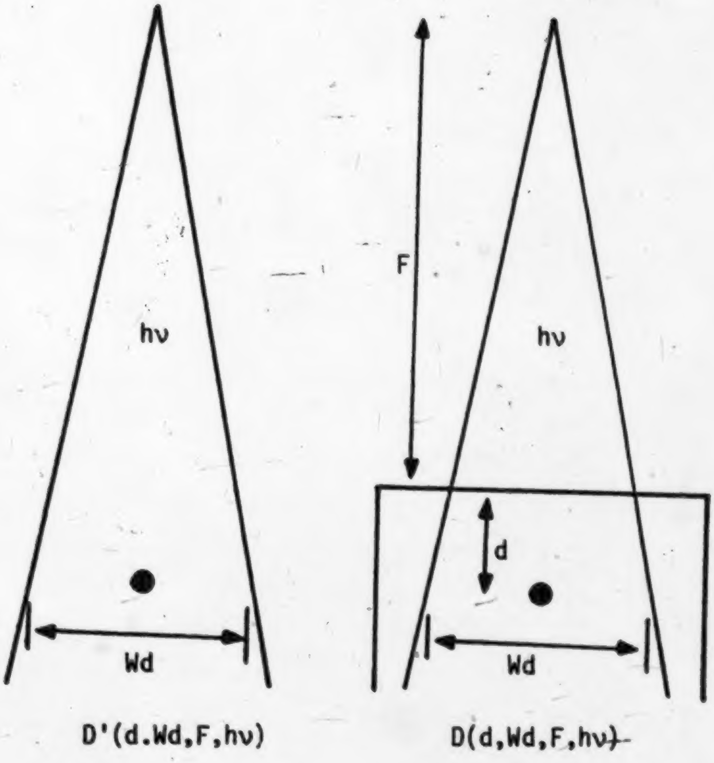
hν
Wd
D'(d.Wd,F,hν)
F
hν
d
Wd
D(d,Wd,F,hν)

Figure #38. Tissue Air Ratio (TAR) geometry.

$$SAR(d.Wd,h\nu) = TAR(d,Wd,h\nu) - TAR(d,Wd=0,h\nu) \qquad [4.37]$$

where TAR(d,Wd=0,hν) is the extrapolated tissue-air ratio for a field of zero size and thus is due to the attenuated primary beam only. The difference between the finite field size TAR and the zero size field size TAR at the same depth yields the dose due to scattered radiation alone from within the phantom.

### 4.5.3 Tissue-Phantom Ratio

At high energies the thickness of phantom material just sufficient to ensure electronic equilibrium as required by the definition of the tissue-air ratio introduces non-negligible photon attenuation and thus invalidates the definition of the TAR at these energies. In place of the TAR at high energies a quantity refered to as the tissue-phantom ratio is employed. The tissue-phantom ratio is defined as the ratio of the dose at a depth d in a phantom to that at a reference depth dr in the phantom such that, as shown in Fig.#39, both points of measurement are located the same distance from the radiation source. The tissue-phantom ratio is thus written as

$$TPR(d,dr,Wd,h\nu) = \frac{D(d,Wd,F,h\nu)}{D(dr,Wd,F,h\nu)} \qquad [4.38]$$

In the special case where the reference depth dr is

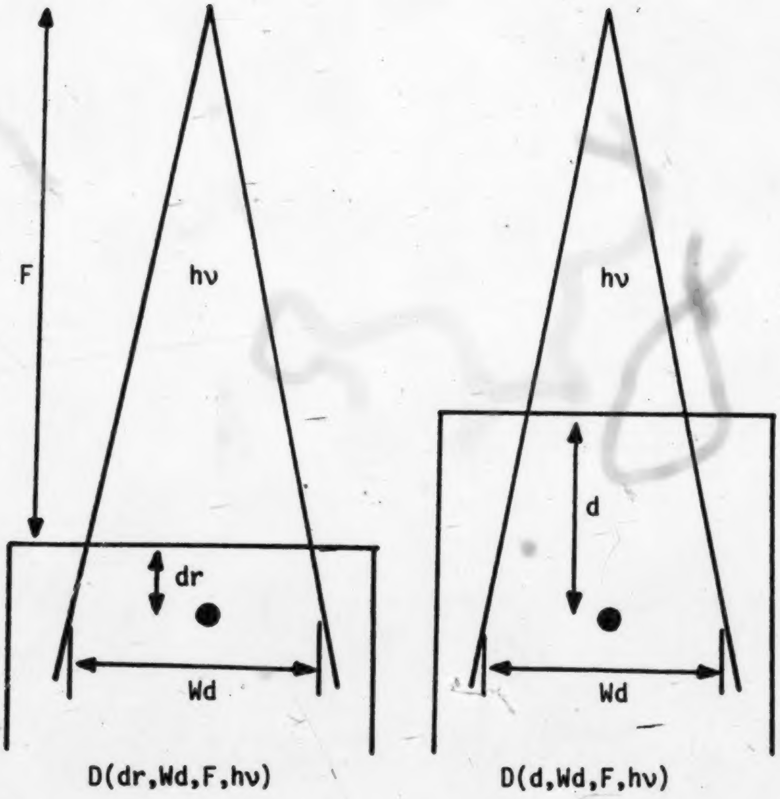
F
hν
hν
dr
d
Wd
Wd
D(dr,Wd,F,hν)
D(d,Wd,F,hν)

Figure #39. Tissue Phantom Ratio (TPR) geometry.

taken to be dmax, the depth of maximum absorbed dose, the tissue-phantom ratio is refered to as the tissue-maximum ratio and is written as

$$TMR(d,dmax,Wd,h\nu) = \frac{D(d,Wd,F,h\nu)}{D(dmax,Wd,F,h\nu)} \qquad [4.39]$$

### 4.5.4 Percentage Depth Dose

The percentage depth dose is a function which relates the dose at a given depth d in a phantom to that at a reference depth dr, as shown in Fig.#40, in terms of a percentage of the dose at the reference depth. The percentage depth dose may be written as

$$PDD(d,Wdr,F,h\nu) = \frac{D(d,Wdr,F,h\nu)}{D(dr,Wdr,F,h\nu)} \times 100\% \qquad [4.40]$$

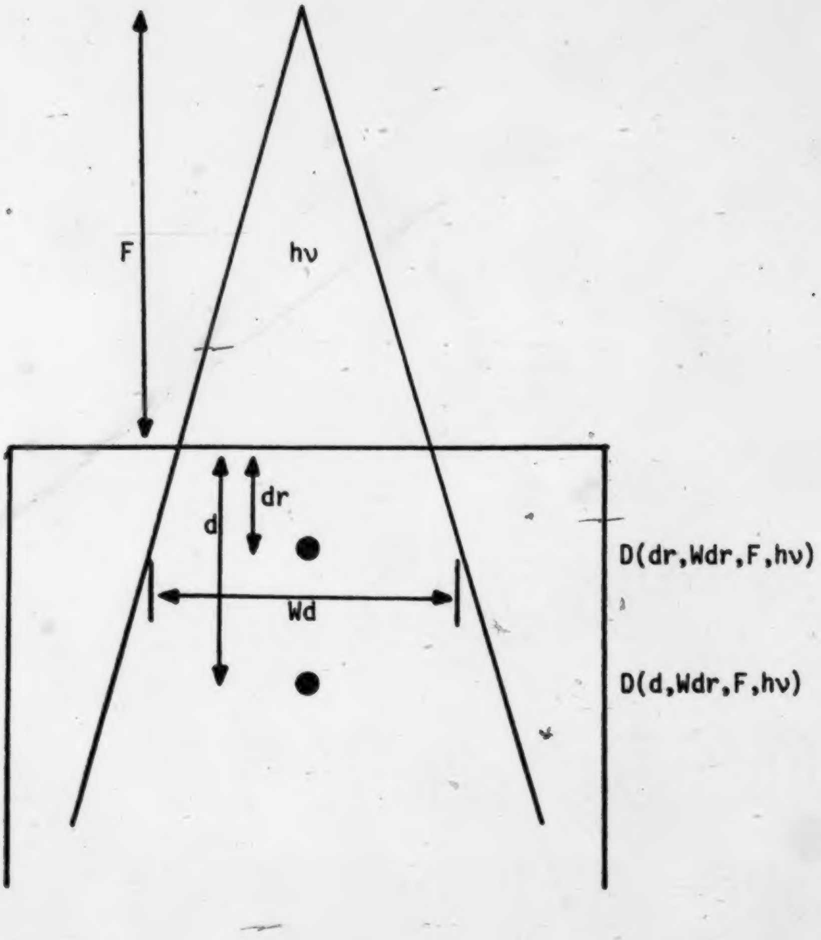
F
hν
dr
d
Wd
D(dr,Wdr,F,hν)
D(d,Wdr,F,hν)

Figure # 40. Percentage Depth Dose (PDD) geometry.

# V RETRACTED TISSUE COMPENSATORS

C

## 5.1 Introduction

Consider an x-ray beam incident normal to the surface of a homogeneous phantom as shown in Fig.#41. If one were to plot the absorbed dose which would be measured at a depth d in the phantom as a function of that depth then one would obtain a plot such as is shown in Fig.#42. Such a plot is characterized by a dose which rises rapidly as depth increases from a relatively low (but finite) dose at zero depth to a maximum dose at some depth and then decreases almost exponentially as depth is increased further. The depth at which the maximum dose occurs is referred to as dmax. The region between the surface and dmax is referred to as the "build-up" region, as it is the region in which conditions are building up toward the establishment of maximum dose at dmax. The existence of this build-up region below the surface of the phantom is of distinct advantage in the treatment(with high energy x-rays) of tumors located below the skin surface in that the outer layers of the skin are spared from a high dose. This effect, called skin sparing, has been shown to be clinically desirable(16). The clinical benefits of skin sparing are "undesirable only when the region to be treated includes the skin or superficial tissue"(17).

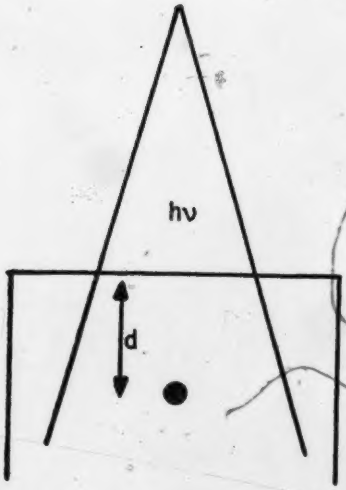

Figure #41. An x-ray beam incident normal to the surface of a homogeneous phantom.

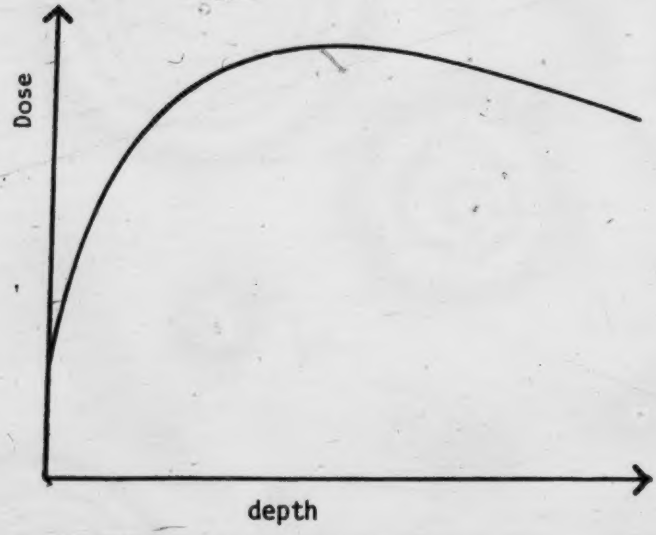

Figure #42. A plot of dose as a function of depth for the geomerty of figure #41.

If one now considers points in the phantom which receive the same dose one may generate a set of isodose contours. In two dimensions, for an x-ray beam incident normal to the flat surface of a homogeneous phantom these isodose curves are of the form shown in Fig.#43. The dose represented by each curve is referenced(as a percentage) to the dose received at some reference point which is often the dose received at depth dmax. Such isodose curves, along with other dosimetric functions, find much use in the planning of radiotherapy treatments. These isodose curves, which provide a picture or map of the pattern of the dose distribution in a particular plane of a phantom may be easily generated(in the case of a homogeneous phantom) by scanning a probe, such as a diode, by remote control across the beam at different depths in a water phantom.

The surface of a patient rarely, if ever, presents a flat surface to an incident x-ray beam. With this in mind, consider the phantom of Fig.#44 which presents a curved surface to the incident x-ray beam. The solid isodose curves shown are those that would result from the surface curvature. The distortion to the isodose curves resulting from the surface curvature is clearly seen when the solid isodose curves are compared to the dashed isodose curves which would result if the beam were incident normal to the flat dashed surface S'. The

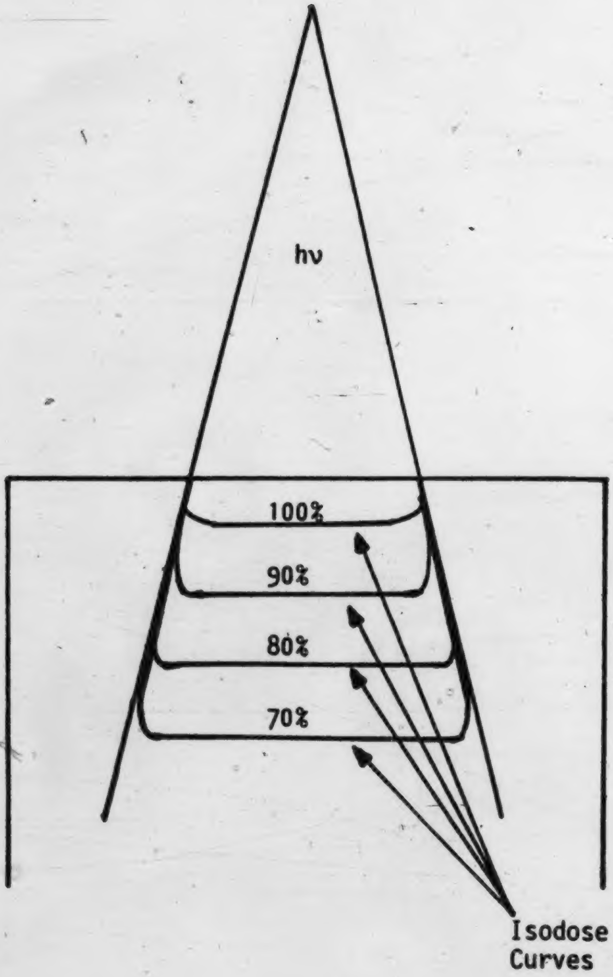
hν
100%
90%
80%
70%
Isodose
Curves

Figure #43. Isodose curves in a homogeneous phantom with a flat surface.

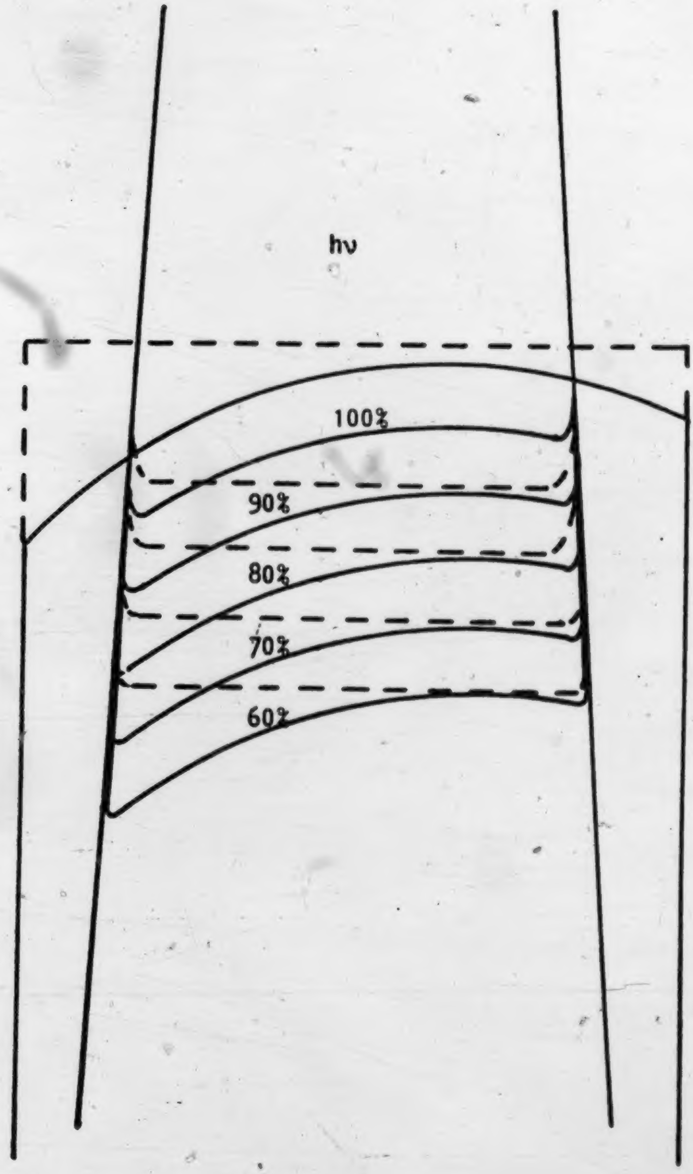
hν
100%
90%
80%
70%
60%

Figure #44. Isodose curves in a homogeneous phantom with a curved surface.

distortion in the isodose distribution resulting from surface contour would be more acute in regions of high surface irregularity such as the head and neck where treatment of the lower head, the neck, and the upper thorax may be comtemplated.

There exist a number of occasions in which it is desirable to have the isodose curves unaltered by the patient's surface contour. This is of particular benefit when one wishes to deliver a uniform dose to a tumor volume which underlies an irregular surface, and also when the combination of two or more beams are employed to deliver a uniform dose to a tumor volume. One simple method of eliminating the alteration of dose due to patient surface contour is to fill in the "missing tissue" in the air gaps with external bolus (tissue like material) as illustrated in Fig.#45.

In Fig.#45(a) an x-ray beam is incident upon the sloping surface of a phantom and, as the resulting isodose curves show, a nonuniform dose will be delivered across the target volume. With the placement of bolus on the surface of the phantom such that the x-ray beam is now incident normal to a flat surface, as shown in Fig.#45(b), the alteration of the isodose curves which resulted from the surface contour of the phantom are eliminated and a relatively uniform dose is delivered

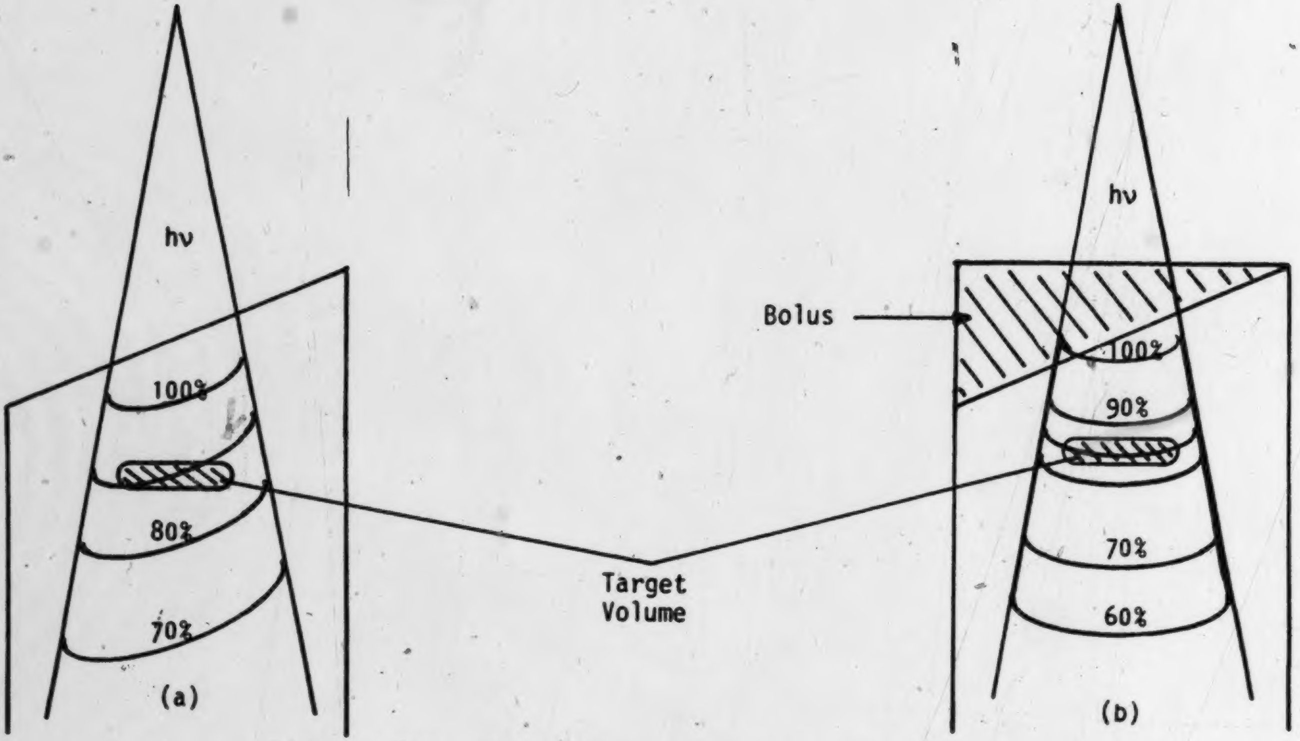
hν
100%
80%
70%
(a)
Target
Volume
hν
Bolus
100%
90%
70%
60%
(b)

Figure #45. The effect of bolus on isodose curves. a) Isodose curves without bolus. b)Isodose curves with bolus on the phantom surface.

across the area normal to the beam in the target volume. The use of bolus in high energy radiotherapy treatment has as a disadvantage the loss of skin sparing. This is lost due to the occurrence of the buildup region within the bolus volume rather than under the surface of the skin, and thus a much higher surface dose is delivered than without the bolus present.

A simple solution to the loss of skin sparing resulting from the employment of bolus is to retract the bolus away from the surface of the patient in the direction of the beam. Such retracted bolus is referred to as a tissue compensator. The result of retraction of the tissue compensator is a restoration of partial skin sparing. This effect is illustrated in Fig.#46. In Fig.#46(a) the tissue compensator rests flush with the surface of the phantom and a relatively high dose is delivered to the phantom surface. In Fig.#46(b) the compensator is retracted away from the surface of the phantom in the direction of the beam and partial skin sparing is restored. The restoration of partial skin sparing with compensator retraction results from the introduction of an air gap between the compensator and phantom. The existence of this air gap reintroduces the existence of a buildup region below the phantom surface. The restoration of skin sparing is only partial due to the dose to the phantom surface resulting from electrons

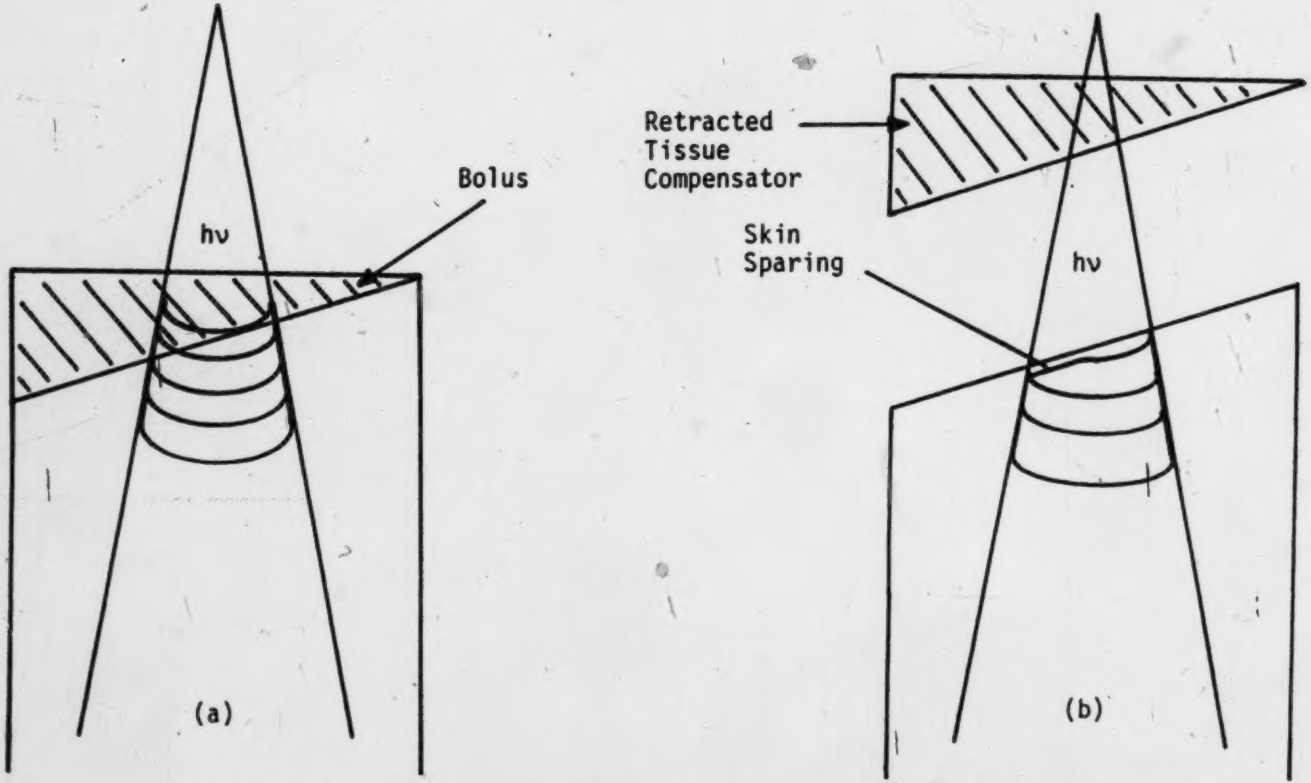
Bolus
hν
(a)
Retracted
Tissue
Compensator
Skin
Sparing
hν
(b)

Figure #46. Restoration of partial skin sparing by compensator retraction. a)Relatively high dose to phantom surface with compensator unretracted. b)Relatively low dose to phantom surface with compensator retracted.

and low energy photons scattered from the compensator. Thus the degree to which skin sparing is restored increases as the retraction distance increases since the fluence of scattered electrons and photons from the compensator at the phantom surface will decrease with increasing retraction distance.

This retraction introduces a complication in the determination of dose at depths below the surface of the patient. The complication is that the dose at any particular depth is altered by the retraction process relative to that which occurs with the bolus flush against the surface of the patient and the alteration thus produced varies with depth.

The use of tissue compensators was first proposed by Ellis(18) in 1959 and since that time numerous papers have appeared on the subject. Tissue compensators have been employed to compensate for the irregular surface contour of the body(19,20,21,22), oblique incidence of the beam(23), variations in scatter and SSD for large fields(24), and inhomogeneities occuring inside the body(25,26). Any given compensator may be employed to compensate for any or all of these effects at one time.

The design of tissue compensators is both simple and elegant, but suffers from a major drawback. This drawback is the fact that a tissue compensator can easily correct for the missing primary beam attenuation which would occur if the body presented a flat surface to the x-ray beam or primary attenuation differences created by inhomogeneities inside the body, but compensating for the deviations in scattered radiation is much more difficult. The contribution to the dose at any given point in a phantom or body resulting from scattered radiation is dependent upon a number of factors such as primary photon energy, the type of material of which the phantom is composed, the depth and position of the point in the phantom, and the size of the beam. It is thus impossible to design a simple compensator in a simple manner such that correct compensation will be achieved at all points in the phantom. The scatter contribution to dose has been dealt with in the design of compensators in terms of empirically determined effective attenuation coefficients(27,28,29,30,31) and thickness ratios (32,33). The compensator may thus be designed to provide optimum compensation over the volume of interest(34) or to provide precise compensation at one particular depth. It would appear that the majority of authors have chosen to achieve precise compensation at one particular depth while accepting the resulting errors created at other depths. Such errors can be substantial. Wilks and Casebow have shown that for a $^{60}$Co x-ray beam of field size 12X12cm$^2$ at 100 cm SSD, correct compensation at a depth of 5cm below a water phantom surface results in errors of up to ±3% for depths up to 8cm and errors of up to ±10% for depths up to 15cm(35).

A number of materials have been employed in the construction of compensators, including wax, plastics, and metals. Of these, lead seems to be the most popular material in the literature for compensator construction. The vertical dimensions of a compensator constructed of a non-unit density material must be expanded or contracted in proportion to the ratio of that material's linear attenuation coefficient to that of tissue.

Three main techniques are employed in the design and fabrication of tissue compensators: (i) fabrication based on a particular method of surface topography measurements; (ii) fabrication based on the dose distribution obtained upon irradiating a film by passing the beam through the patient; (iii) and fabrication based on density distribution information of the body obtained by means of CT scanning. Surface measurement techniques were the first to be employed and of these methods a mechanical rod box was first employed to map the surface topography of the area to be irradiated(36,37,38). A modified version of this technique is presently in use at the Cross Cancer

Institute. Non-mechanical surface measuring techniques have been developed using photogrammetry(39,40,41,42,43, 44). These techniques determine the surface topography from photographs taken of the patient. Such surface measurement techniques suffer from two drawbacks. First, such techniques, by their very nature, do not yield information regarding internal tissue inhomogeneities, and secondly the surface contour of a patient may change under treatment conditions, eg. such as if a patient is turned over for anterior and posterior parallel-opposed ports. In such a case body parts display a tendency to migrate downward in each position thus shifting the surface topography.

The design of compensators from portal films is extensively reported in the literature(45,46,47,48,49). In this technique port films are scanned to determine the density encountered by each primary ray path through the volume to be irradiated. These densities are then used to compensate midline doses for parallel opposed ports. The limitation of such a technique is the inability to distinguish the positions of varying density along any single path ray.

Finally, compensator design based on density distribution information provided by CT scans is potentially the most accurate method due to the large volume of information that CT scans are capable of providing. These possibilities have been explored by a few authors(50,51) but this technique suffers from the drawbacks of high cost and the limited availability of CT scanners.

As mentioned earlier compensation is achieved at only one depth(due primarily to scattering) errors in compensation will occur for all other depths in any particular arrangement. These errors have been investigated for wax compensators by Jackson(52) who has concluded that "large retraction distances, while reducing skin contamination, may lead to serious depth dose errors unless the wax is thin....If the error is thought to be excessive it may be reduced by the choice of a smaller retracting distance, though at the expense of increased skin dose. The technique is evidently most suitable for small fields where adequate skin protection can be achieved with a small retracting distance and the consequent depth dose errors are also small. With large fields it may be possible to compromise between skin dose and depth dose errors by reducing the retraction distance, but in certain instances it may well be concluded, especially if the wax is thick, that the errors are unacceptable"(52).

The majority of published work on compensators has been carried out at $^{60}$Co energies while very little has been reported concerning higher energies. Jackson(52) has examined both $^{60}$Co and 4MV energies and Thomas(53) has examined energies up to 16MV, but as recently as 1985 Huang et al states that "published quantitative information about scattered photons from beam-modifying filters is lacking"(54).

## 5.2 Experimental Parameters

### 5.2.1 Experimental Setup

The alteration of both surface dose and dose at depth for high energy x-ray beams resulting from compensator retraction was measured for points along the central beam axis. The experimental setup employed is shown diagramatically in Fig.#47. The phantom, as well as one set of compensators employed, were constructed of approximately tissue-equivalent opaque white polystyrene which has an electron density of $3.50X10^{23}$ el/cm$^3$ and a mass density of 1.08g/cm$^3$. The opaque white polystyrene used here is derived from clear polystyrene$(C_8H_8)n$ by the addition of a fine particulate filler of titanium dioxide($TiO_2$)(3.7% by weight) which improves the tissue equivalence of polystyrene for low energy photons ($E(\gamma)<0.1MeV$) and high energy photons($E(\gamma)>10MeV$(55). In all cases the phantoms consisted of blocks of

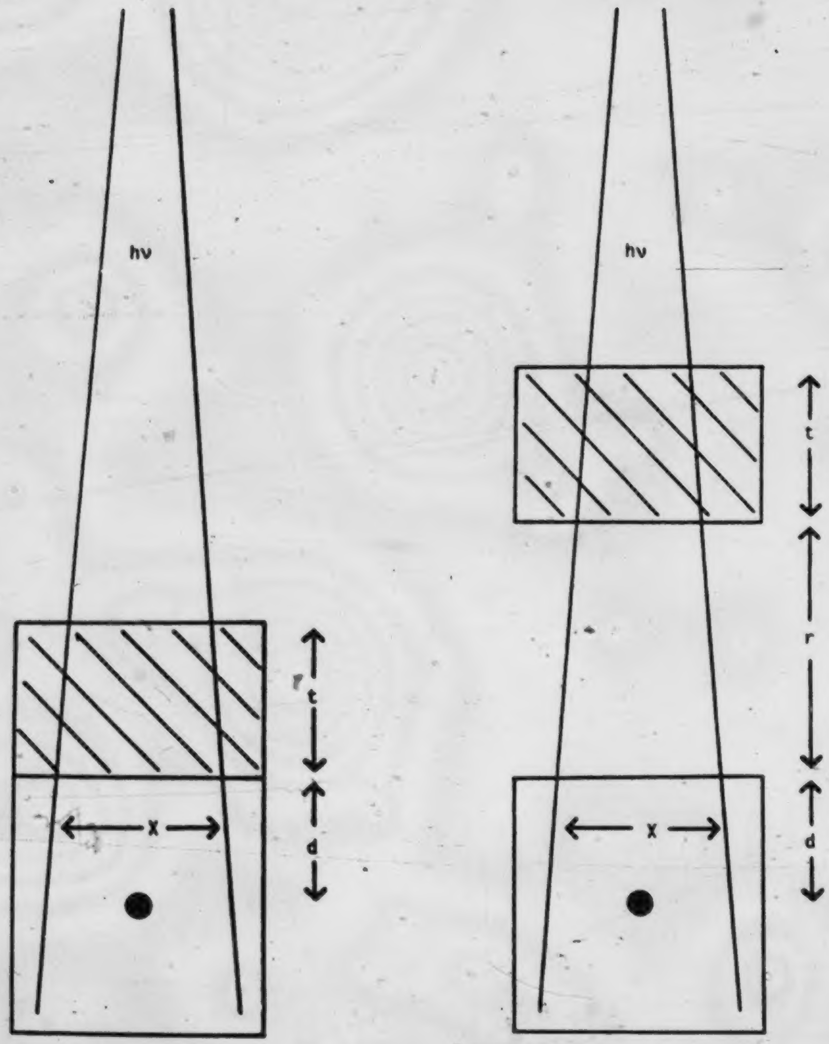
hν
hν
t
d
x
t
r
d
x

Figure #47. Diagramatic representation of the experimental setup polystyrene which presented a cross-sectional area of $25X25 cm^2$ to the incident beam. The other set of compensators were constructed of lead(electron density= $2.707X10^{24}$ el/cm$^3$ and mass density of 11.36g/cm$^3$).

The "compensators" employed consisted of uniform thickness slabs of polystyrene and lead, with thicknesses of 2, 4, and, 7 cm for polystyrene and 1.75, 3.5, and, 6.25 mm for lead. The thickness of the polystyrene compensators was chosen in accordance with the work of Jackson(52) and the thicknesses of lead were chosen to correspond approximately to those of polystyrene by means of the ratio of the densities of lead to polystyrene. Exact correspondence was not achieved due to the fact that the lead compensators were constructed by laminating available thicknesses of sheet lead(the milling of these laminates to more precise thicknesses was not possible).

A Capintec thin window parallel plate ionization chamber was used to obtain surface dose measurements. The ionization chamber was inserted into a slot in the surface of the phantom such that its window was centered at the beam axis flush with the phantom surface. The system was initially exposed with the compensator flush on the phantom surface and then retracted in the beam direction. The fluence rate and time of exposure was held constant throughout. The ratio of retracted to zero-retraction surface dose was thus determined and plotted as a function of retraction distance for retraction distances up to 30cm. This procedure was carried out for both the three polystyrene compensator thicknesses and the three lead compensator thicknesses with field sizes of $5X5cm^2$, $10X10cm^2$, and, $20X20cm^2$ and beam qualities of $^{60}Co$, 6MV, and, 15MV.

A similar procedure was carried out in the determination of the alteration of dose at depth resulting from the retraction process. Depth was defined with respect to the phantom surface. For these measurements a Capintec Farmer Replacement Chamber and its corresponding buildup cap, which fit snugly into holes bored into the phantom at various depths, was employed. All measurements were made along the central beam axis to determine the ratio of retracted to zero retraction dose for retraction distances up to 30cm. The results were plotted. This procedure was carried out for depths up to 13cm and for both the three polystyrene and lead compensator thicknesses with field sizes of $5X5cm^2$, $10X10cm^2$, and, $20X20cm^2$, and beam qualities of $^{60}Co$, 6MV, and 15MV.

In all cases the phantom surface was located at the machine isocenter, which provided a source to surface distance(SSD) of 80cm for $^{60}$Co and 100 cm for both 6MV and 15MV. The measurement depth was taken to be located along the central axis of the probe. Field sizes were determined at the phantom surface. Maximum retraction distances of 25cm in the case of $^{60}$Co and 30cm for both 6MV and 15MV were determined by the limitations in available space between the phantom surface located at the machine isocenter and the particular machine head.

### 5.2.2 Radiation Sources

#### 5.2.2.1 Cobalt 60

The source of the $^{60}$Co $\gamma$-rays employed in this work is a Theratron 780 Cobalt 60 teletherapy unit with an SAD(source to axis distance) of 80cm . The $^{60}$Co source is exposed by means of a source drawer which is operated by compressed air. The actual source employed is a 1.75cm diameter standard source which had an activity of 7518 curies of $^{60}$Co and provided an exposure rate of 127.8 roentgens per minute at one meter distance when measured on March 3, 1983.

#### 5.2.2.2 6MV

The source of 6MV x-rays employed in this work is a 6MV Siemens Mevatron 67 medical linear accelerator with an SAD of 100cm. This accelerator employs a standing wave waveguide which provides an electron beam of 3mm diameter with energies up to 6MeV. This electron beam is bent through 270° to strike a tungsten target and the x-ray field produced is flattened by a brass flattening filter. The primary collimator provides a maximum field size of 35X35cm$^2$ at the isocenter. With an electron beam energy of 6MeV the x-rays produced form a spectrum which ranges in energy from a few keV up to 6MeV and is thus refered to as a 6MV x-ray beam. The energy of the 6MV beam is defined as providing a depth dose of (67±2)% when measured at 10cm depth in water for a 10X10cm$^2$ field defined at the water surface at 100cm SSD. The depth of maximum dose is 1.5±0.2cm as measured in water for a 10X10cm$^2$ field at 100cm SSD. The effective energy of the 6MV beam is approximately 2MeV.

The waveguide is powered by a 2MW(peak) magnetron operating at a frequency of 2.998GHz. The waveguide operates in a pulsed mode and delivers a constant 200 cGy per minute.

#### 5.2.2.3 15MV

The source of 15MV x-rays employed in this work is a 15MV Siemens Mevatron 77 medical linear accelerator with an SAD of 100cm. This accelerator employs a standing wave waveguide which provides an electron beam of less than 3mm diameter with energies up to 18MeV. This electron beam is deflected through 270° to strike a tungsten target and the x-ray field produced is flattened by a stainless steel flattening filter. The primary collimator provides a maximum field size of $40X40cm^2$ at 100cm from the target(100cm SSD). This accelerator provides an x-ray beam of 15MV x-rays which is comprised of a spectrum of x-rays ranging in energy from a few keV to 15MeV. The energy of the 15MV beam is defined as providing a depth dose of (77±2)% when measured at 10cm depth in water for a $10X10cm^2$ field defined at the water surface at 100cm SSD. The depth of maximum dose is 3.0±0.2cm as measured in water for a $10X10cm^2$ field at 100cm SSD. The effective energy of the 15MV beam is approximately 5MeV.

The waveguide is powered by a 7MW(peak) klystron operating at a frequency of 2.998MHz. The waveguide operates in a pulsed mode and delivers a constant dose rate of 300 cGy per minute.

### 5.2.3 Dosimetry Devices

Surface dose measurements were carried out with a Capintec PS033 thin window parallel plate ionization chamber having an effective collection diameter of 16mm and an electrode spacing of 2.4mm. The entrance window of the chamber has a thickness of 0.5mg/cm$^2$ of aluminized polyethylene terephthalate(PET-Al).

Dose at depth measurements were carried out with a Capintec PR-06c air equivalent plastic Farmer Replacement ionization chamber with an effective volume of 0.6ml. The chamber has a diameter of 7mm and length of 22mm and an air equivalent plastic wall of 50mg/cm$^2$ thickness. In all measurements the chamber was used with its $^{60}$Co buildup cap.

Both ionization probes were used in conjunction with a Capintec Model 192 Digital exposure meter which supplied a collection voltage of 300 volts to the probes. The accuracy and consistency of the dose meter is stated by the manufacturer to be better than 1%.

## 5.3 Experimental Results

Experimental uncertainties in all dose measurements were determined by making each measurement a number of times and determining the standard deviation of these measurements. The standard deviations thus determined were found to be consistent over a number of determinations of the same measurement performed on different days. Propagation of error was determined using the formulas for standard error. The depth of dose for depth measurements was taken to be the central axis of the probe. All geometrical measurements were performed with an accuracy of±1mm or better, with ±1mm taken as the error in measurements unless stated otherwise.

### 5.3.1 Alteration of Surface Dose

The motivation behind retraction of tissue compensators away from the skin surface is the decrease in skin or surface dose obtained. This decrease in skin dose amounts to either full or partial restoration of skin sparing. The alteration of surface dose resulting from the retraction process was measured with the thin window ionization chamber(with the window of the chamber flush with the phantom surface) for polystyrene compensators of 2, 4, and, 7cm thickness and lead compensators of 1.75, 3.5, and, 6.25mm thickness for retraction distances ranging from 0 to 30cm and field sizes of 5X5, 10X10, and, 20X20cm$^2$ and beam qualities of $^{60}$Co, 6MV, and, 15MV. The results obtained for the 4cm polystyrene compensator and the 3.5mm lead compensator are not presented as they yield results intermediate between the other thicknesses and provide little additional information. The measured dose was normalized to the dose at zero retraction unless otherwise stated.

The alteration of surface dose is shown in figures #48 to #51 for $^{60}Co$ photons, figures #54 to #57 for 6MV photons, and figures #60 to #63 for 15MV photons. In all cases the relative surface dose exhibits a pronounced decrease for moderate retraction distances, followed by varying degrees of leveling out as retraction distance is increased further. Examination of these plots reveals the alteration of surface dose to be a function of compensator thickness, field size, compensator material, energy of the incident photons, and retraction distance.

In order to ascertain the relative merit of using lead compensators as compared to polystyrene compensators, with regard to the actual surface dose received by the phantom from each compensator material, the surface dose from each compensator material was measured. This data is presented in the form of a plot of the percentage ratio of the surface dose from Pb to that from polystyrene for compensators of corresponding thickness(1.75mm Pb/2cm poly) and (6.25mm Pb/7cm poly) and is shown in figures #52 and #53 for $^{60}Co$ photons, figures #58 and #59 for 6MV photons, and figures #64 and #65 for 15MV photons. With the exception of the 20X20cm$^2$ field at 15MV the ratio of [dose Pb/dose poly] is seen to decrease rapidly for small retraction distances, go through a minimum, and then increase as retraction distance is increased further. The 20X20cm$^2$ field at

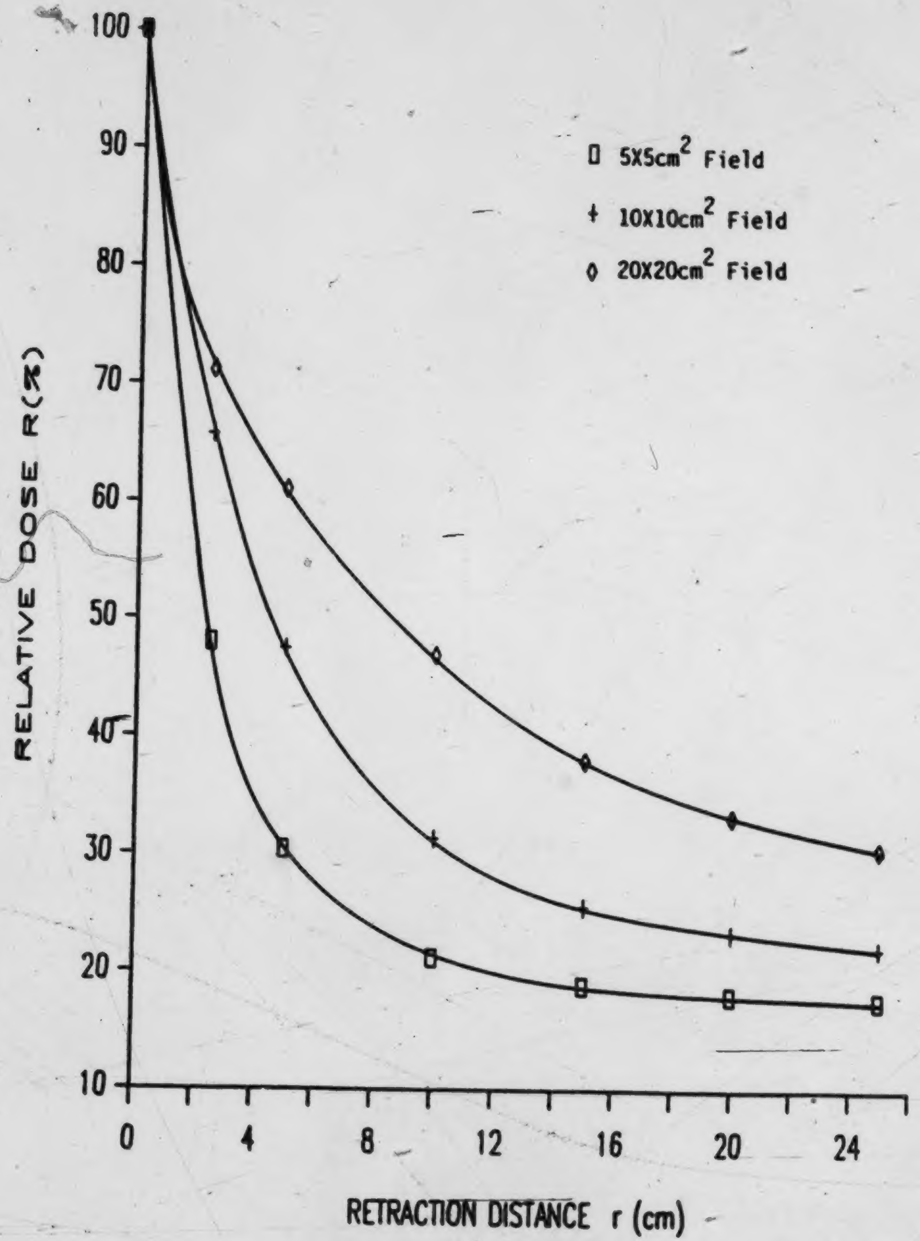

Figure #48. A plot of relative dose R(%) at the surface as a function of retraction distance r for a Pb compensator of 1.75mm thickness.
($E(\gamma)$=$^{60}$Co)

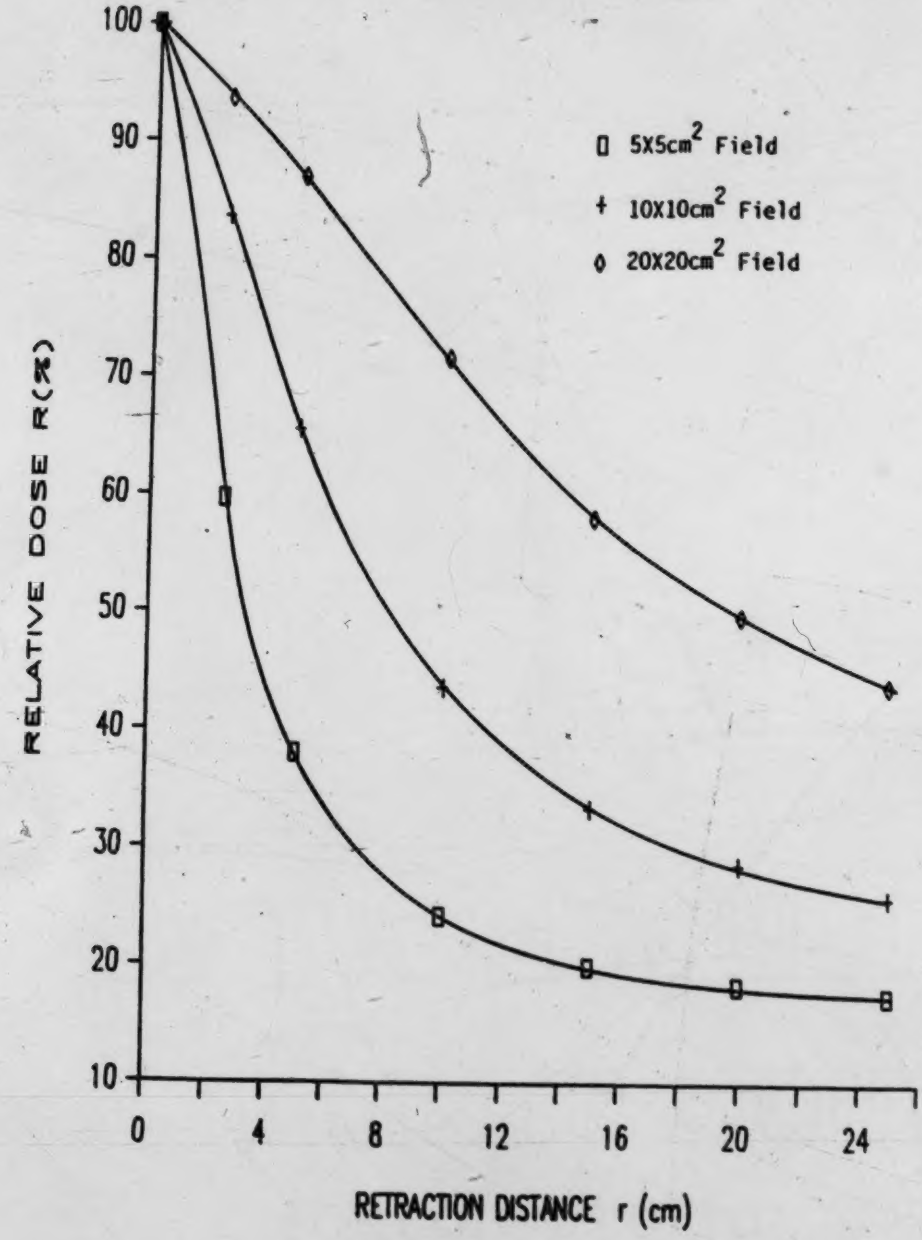

**Figure #49.** A plot of relative dose R(%) at the surface as a function of retraction distance r for a Polystyrene compensator of 2cm thickness.

(E(γ)= $^{60}$Co)

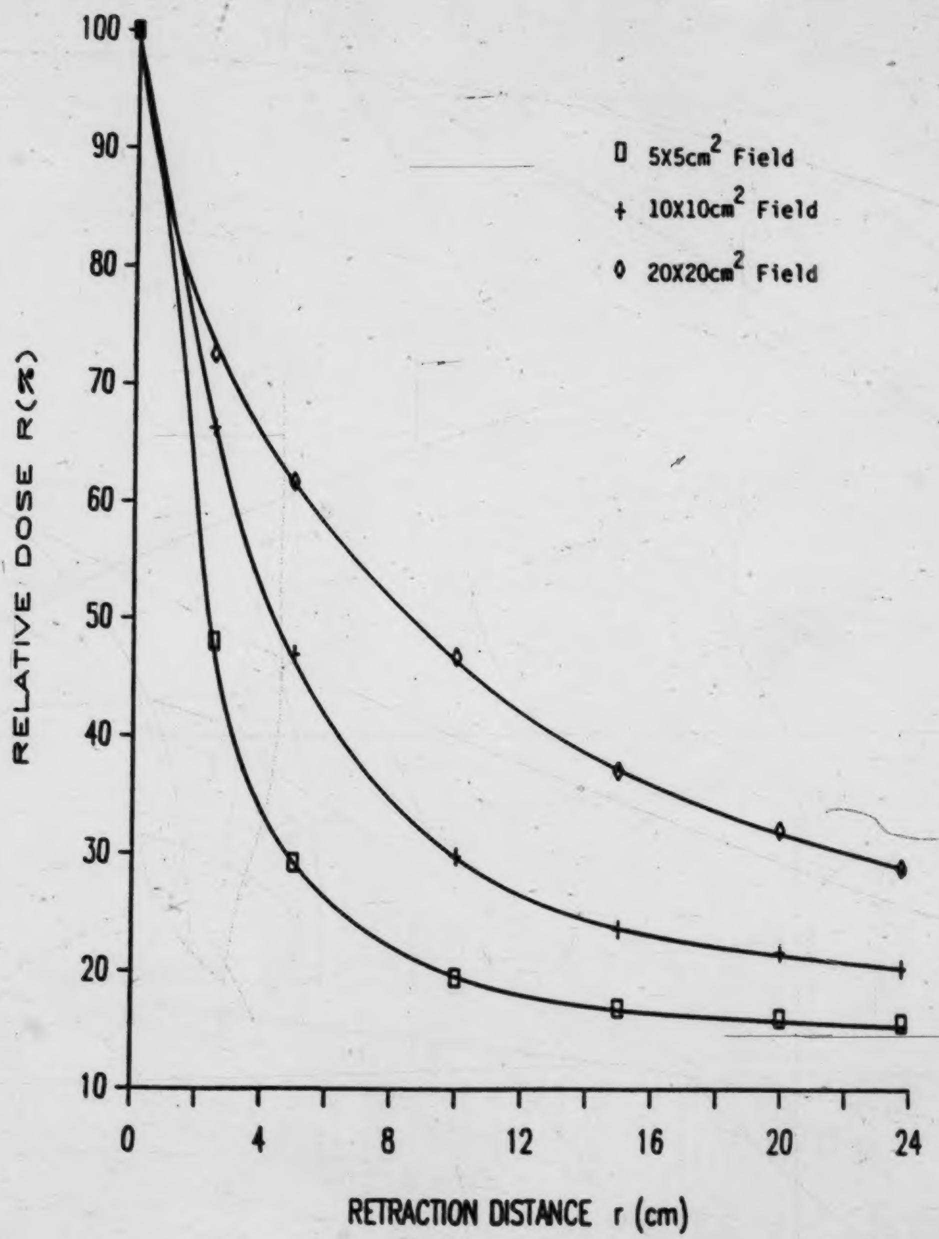

Figure #50. A plot of relative dose R(%) at the surface as a function of retraction distance r for a Pb compensator of 6.25mm thickness. (E( $\gamma$)= $^{60}$Co)

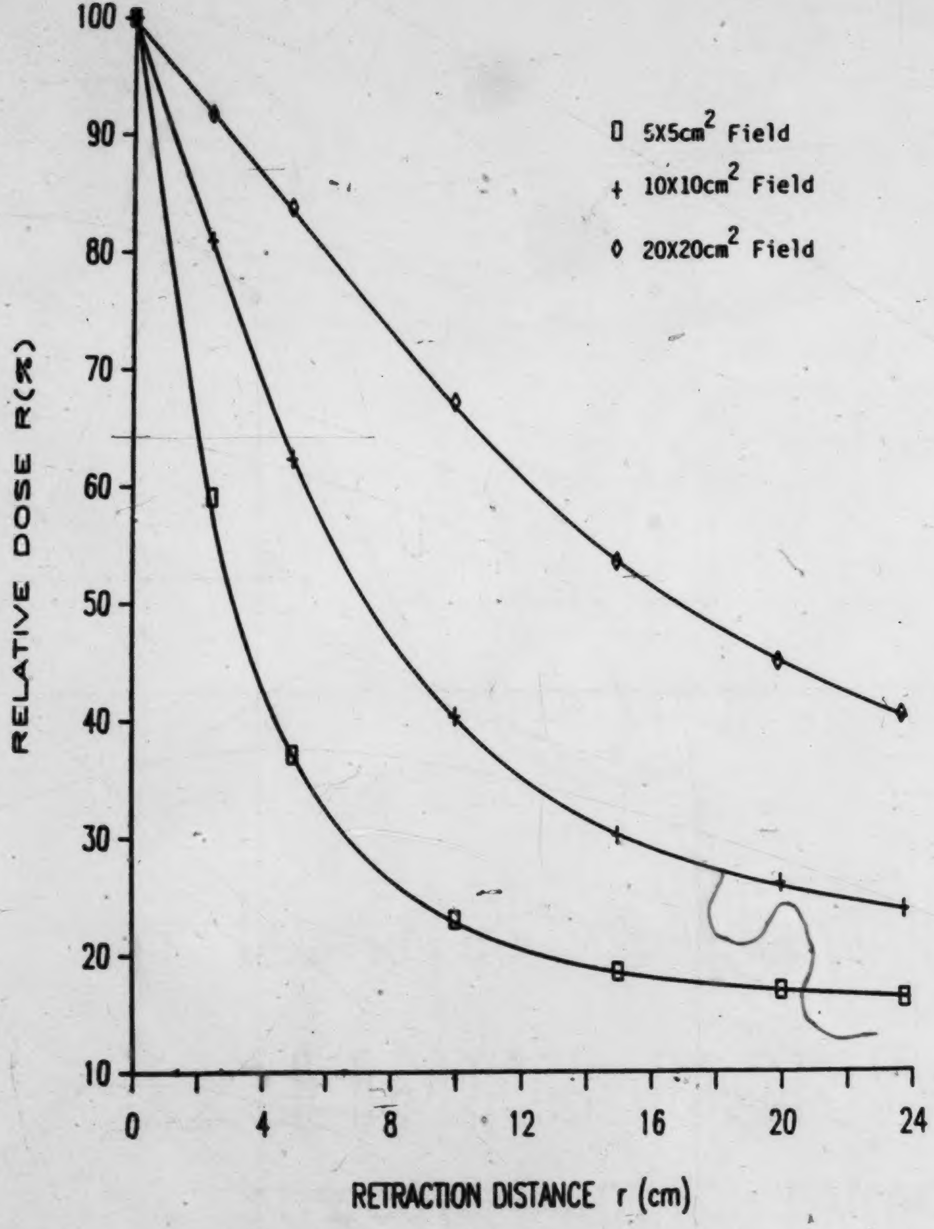

**Figure #51.** A plot of relative dose R(%) at the surface as a function of retraction distance r for a Polystyrene compensator of 7cm thickness.

(E(γ)-$^{60}$Co)

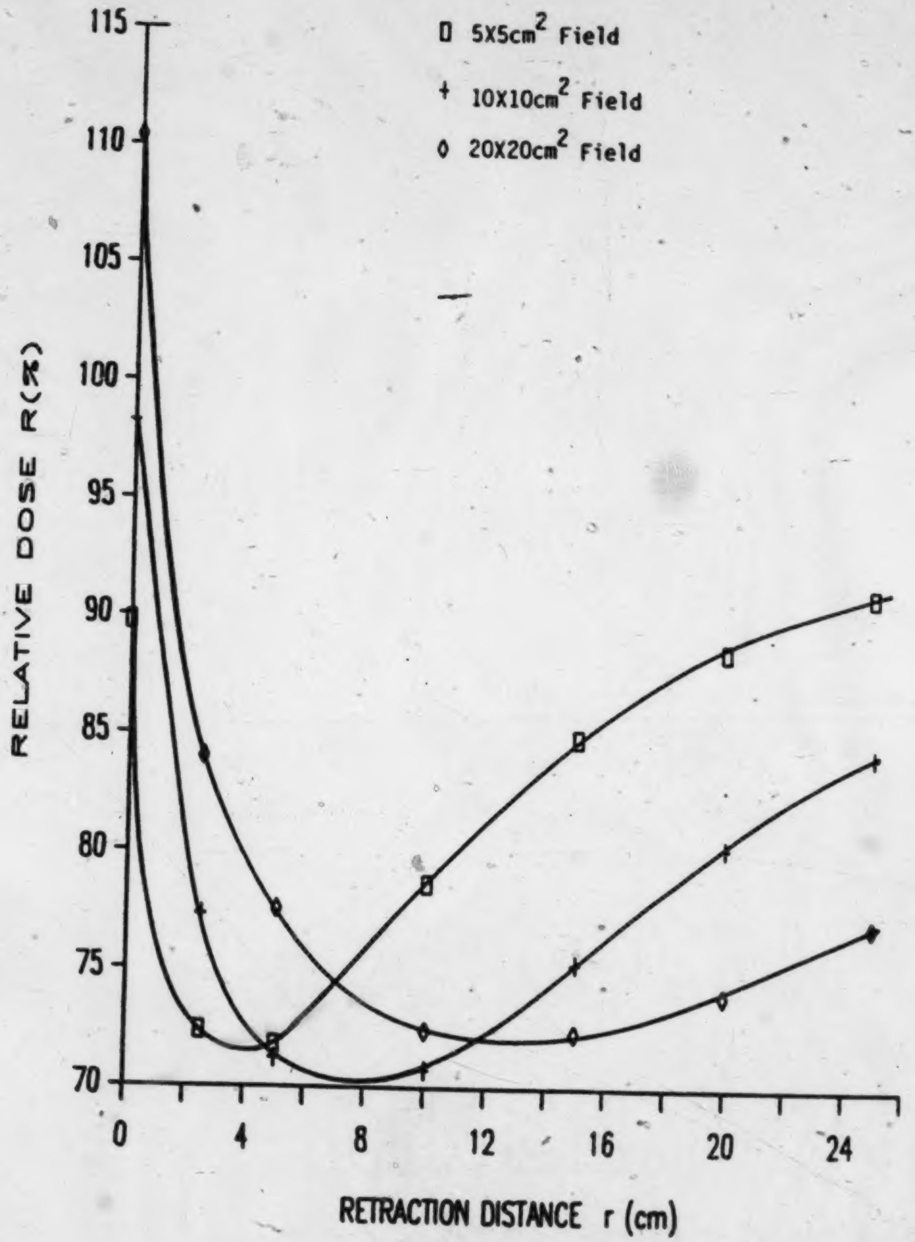

Figure #52. A plot of the ratio of [dose Pb/dose Poly] at the surface as a function of retraction distance for a Pb compensator of 1.75mm thickness and a polystyrene compensator of 2cm thickness.

($E(\gamma) = {}^{60}Co$)

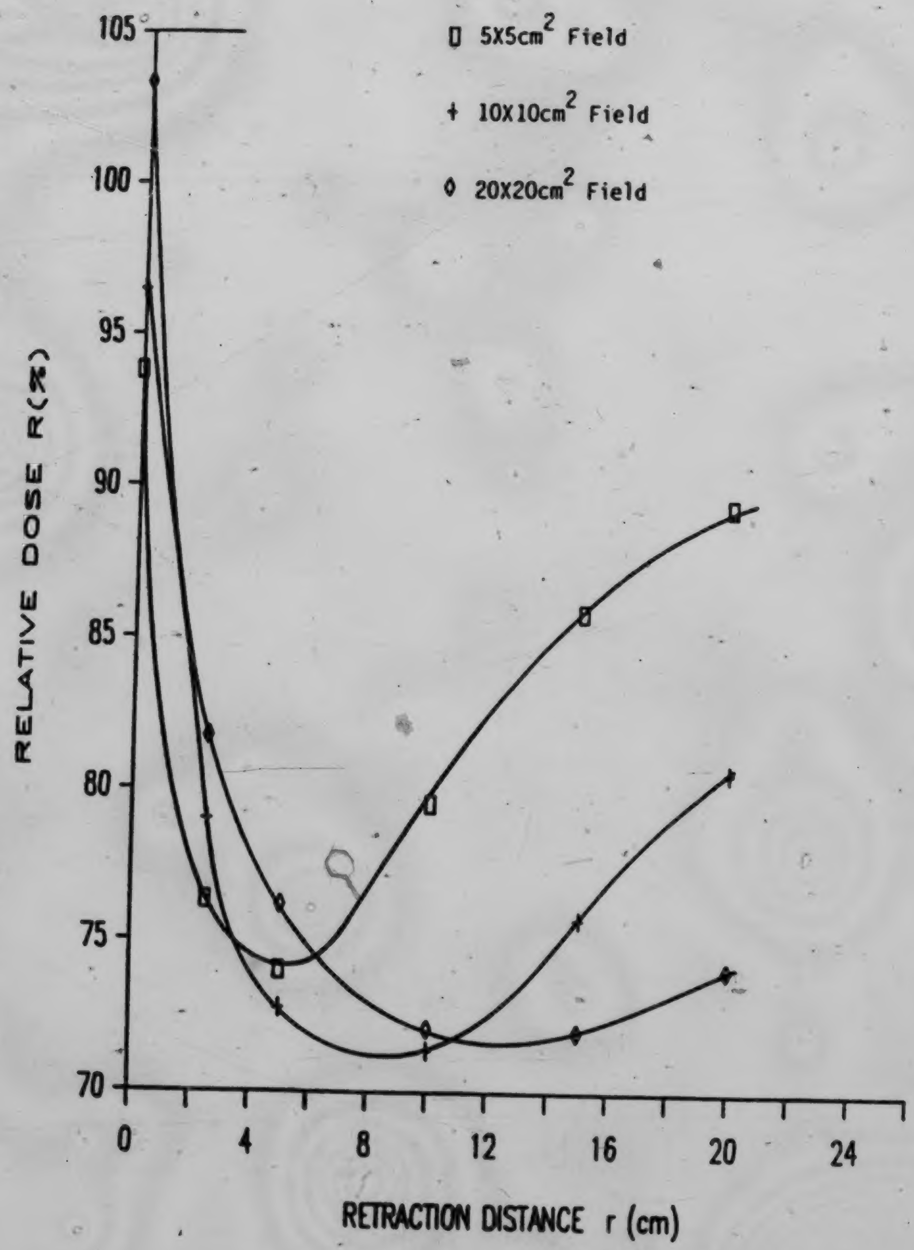

**Figure #53.** A plot of the ratio of [dose Pb/dose Poly] at the surface as a function of retraction distance for a Pb compensator of 6.25mm thickness and a polystyrene compensator of 7cm thickness.
$(E(\gamma)={}^{60}Co)$

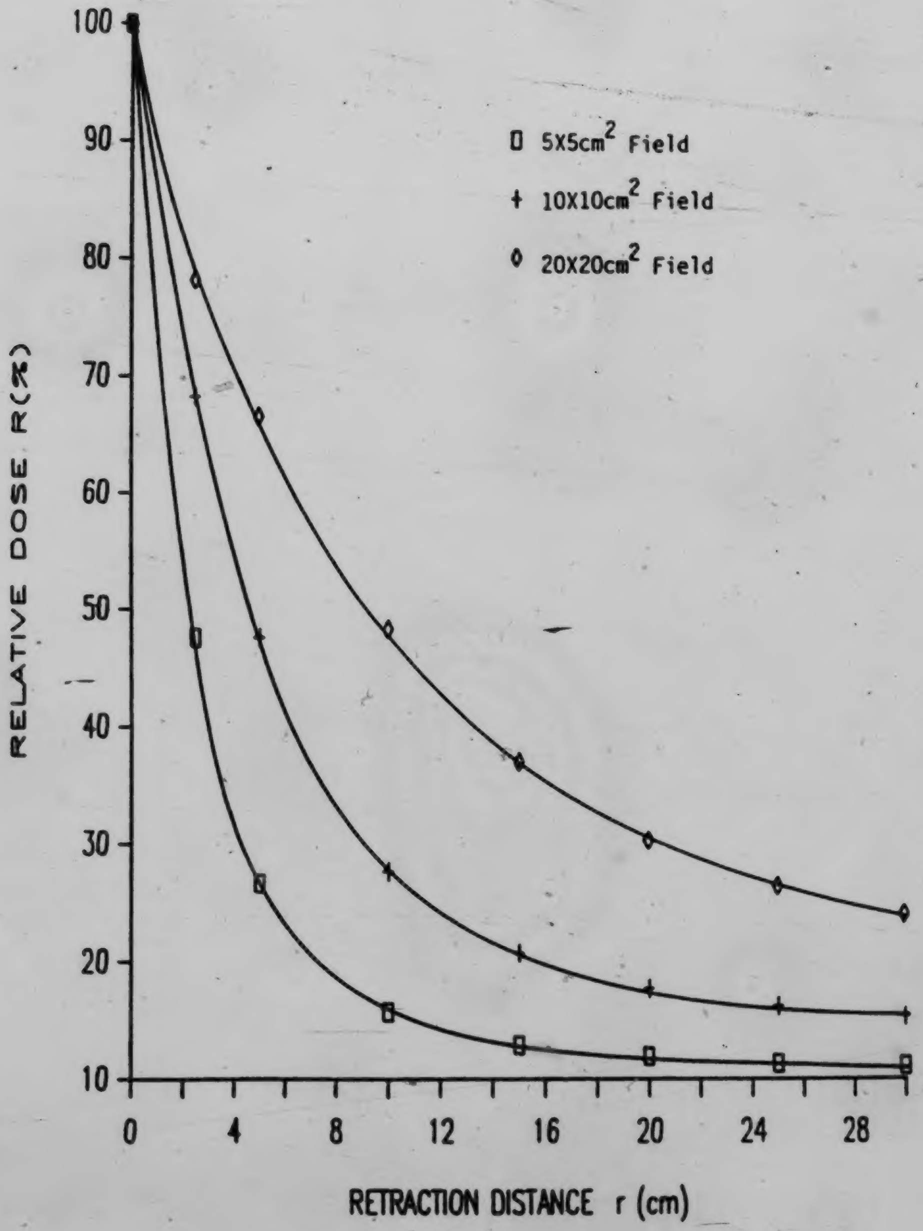

**Figure #54.** A plot of relative dose R(%) at the surface as a function of retraction distance r for a Pb compensator of 1.75mm thickness.
(E(γ)=6MV)

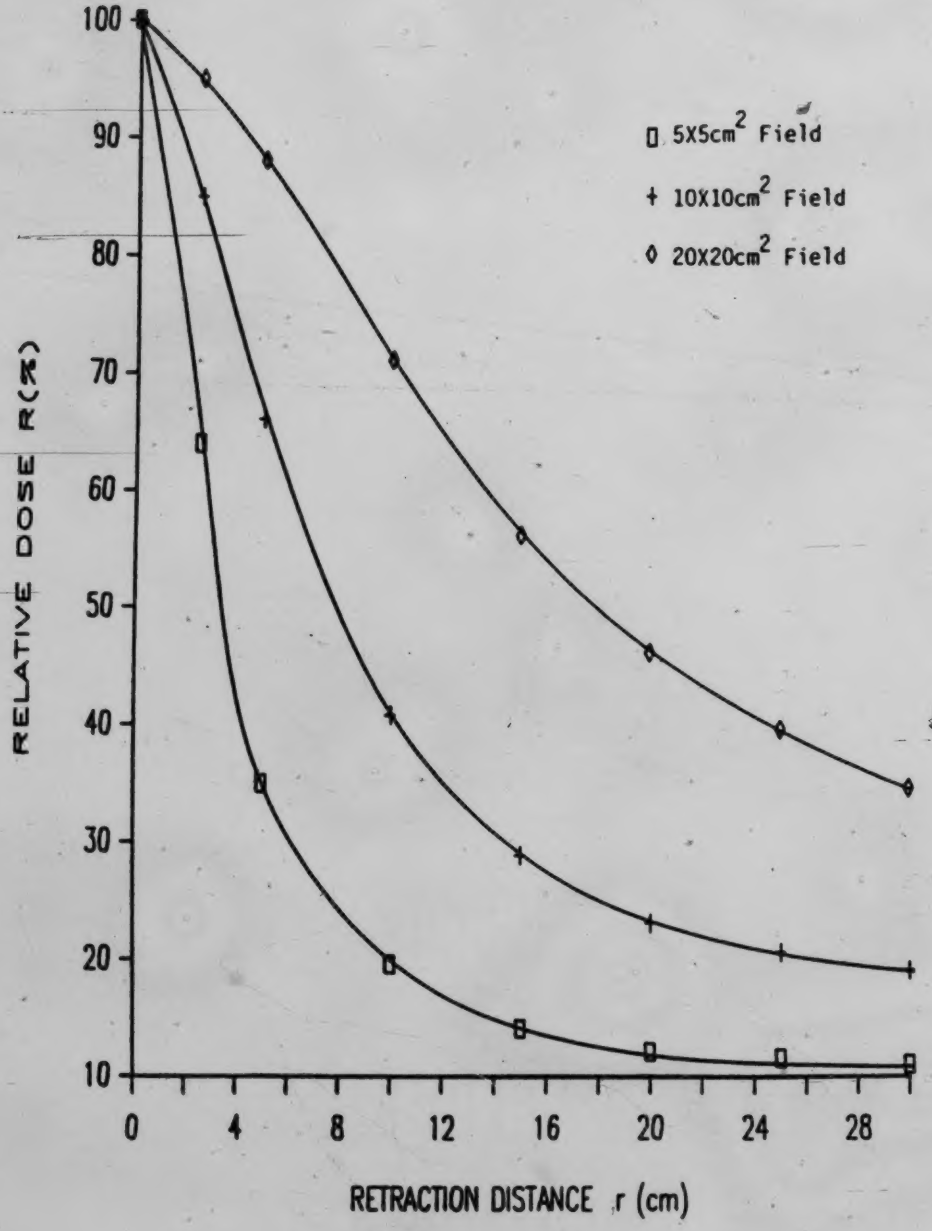

**Figure #55.** A plot of relative dose R(%) at the surface as a function of retraction distance r for a Polystyrene compensator of 2cm thickness. (E( γ)=6MV)

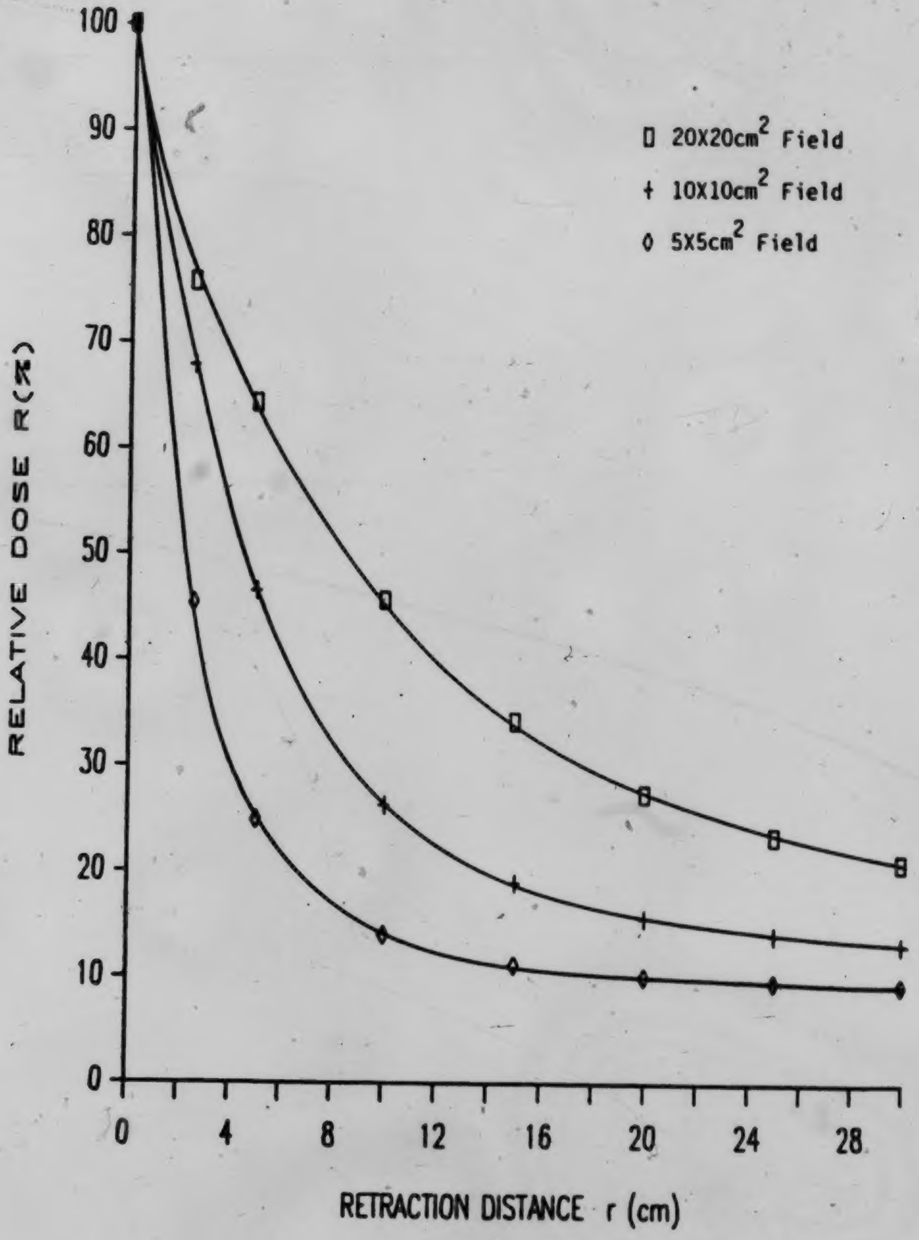

**Figure #56. A plot of relative dose R(%) at the surface as a function of retraction distance r for a Pb compensator of 6.26mm thickness. (E(γ)=6MV)**

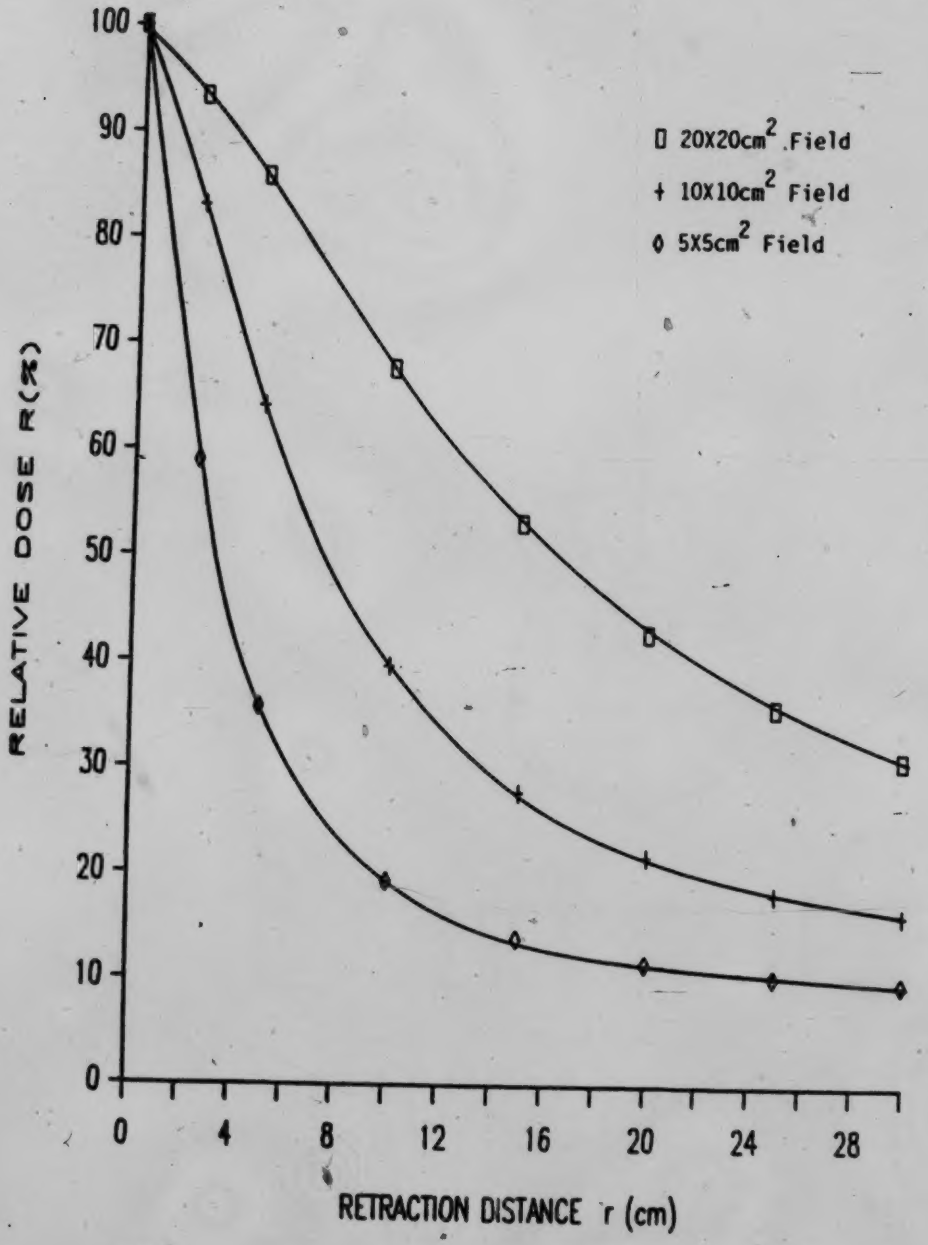

Figure #57. A plot of relative dose R(%) at the surface as a function of retraction distance r for a Polystyrene compensator of 7cm thickness. (E(γ)=6MV)

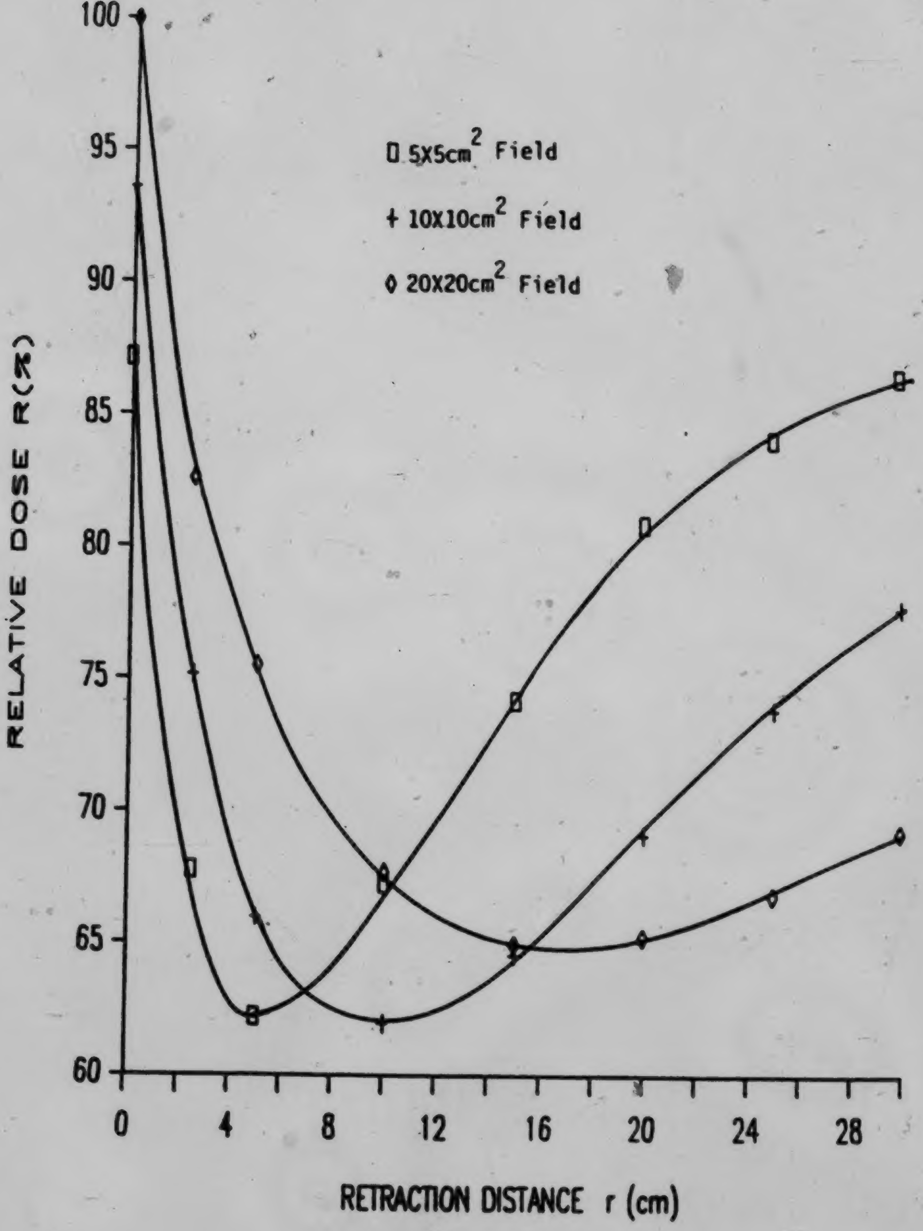

Figure #58. A plot of the ratio of [dose Pb/dose Poly] at the surface as a function of retraction distance for a Pb compensator of 1.75mm thickness and a polystyrene compensator of 2cm thickness. (E(γ)=6MV)

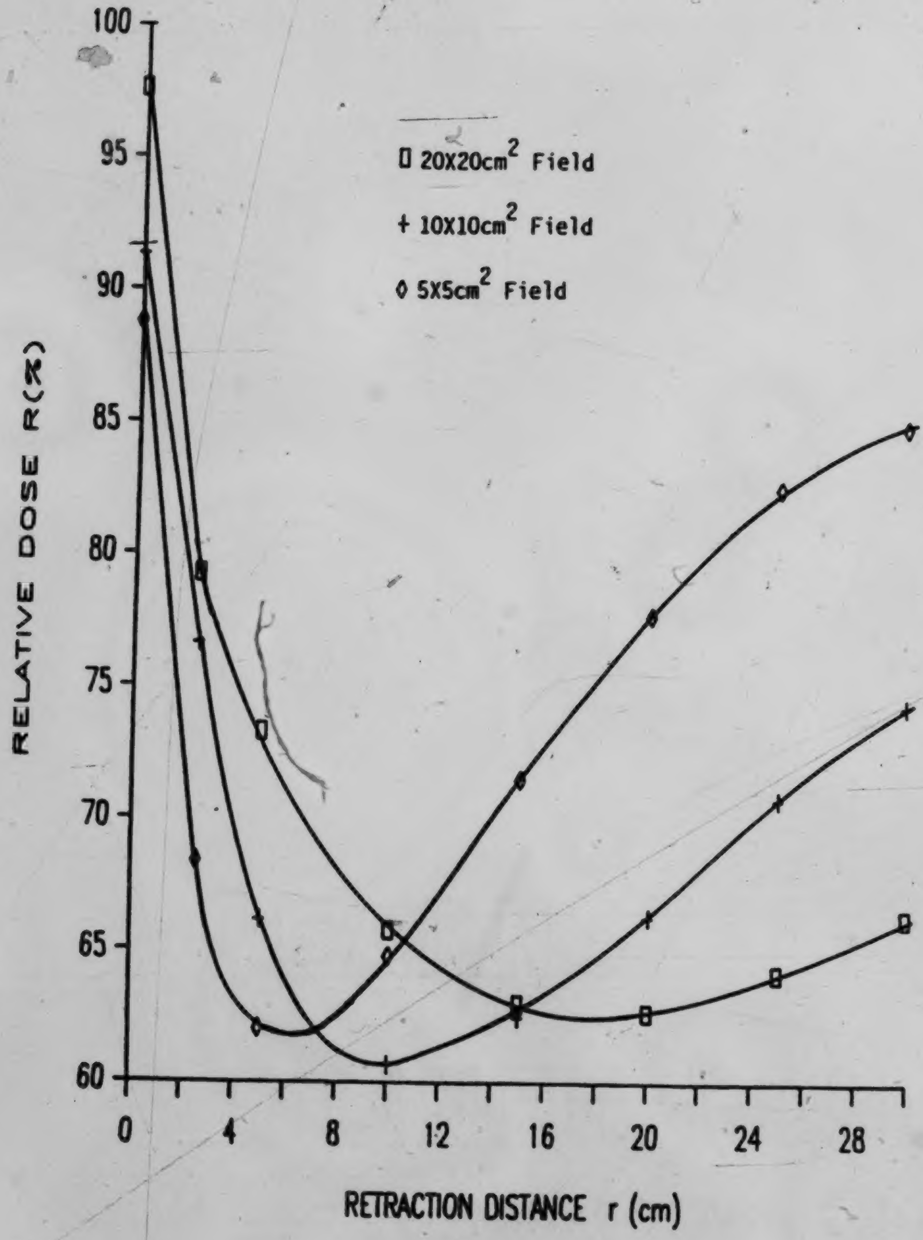

**Figure #59.** A plot of the ratio of [dose Pb/dose Poly] at the surface as a function of retraction distance for a Pb compensator of 6.25mm thickness and a polystyrene compensator of 7cm thickness. (E(γ)=6MV)

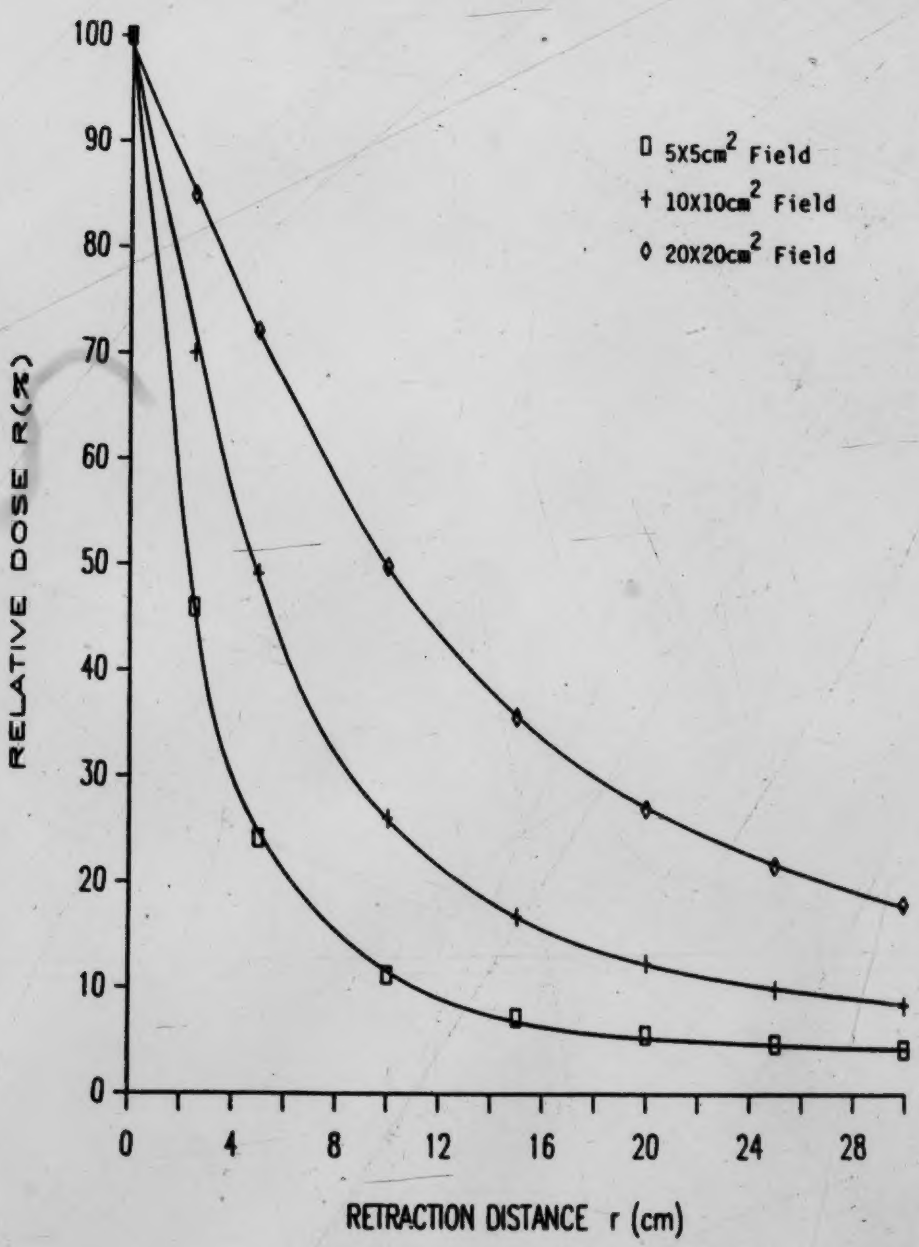

**Figure #60.** A plot of relative dose R(%) at the surface as a function of retraction distance r for a Pb compensator of 1.75mm thickness. (E(γ)=15MV)

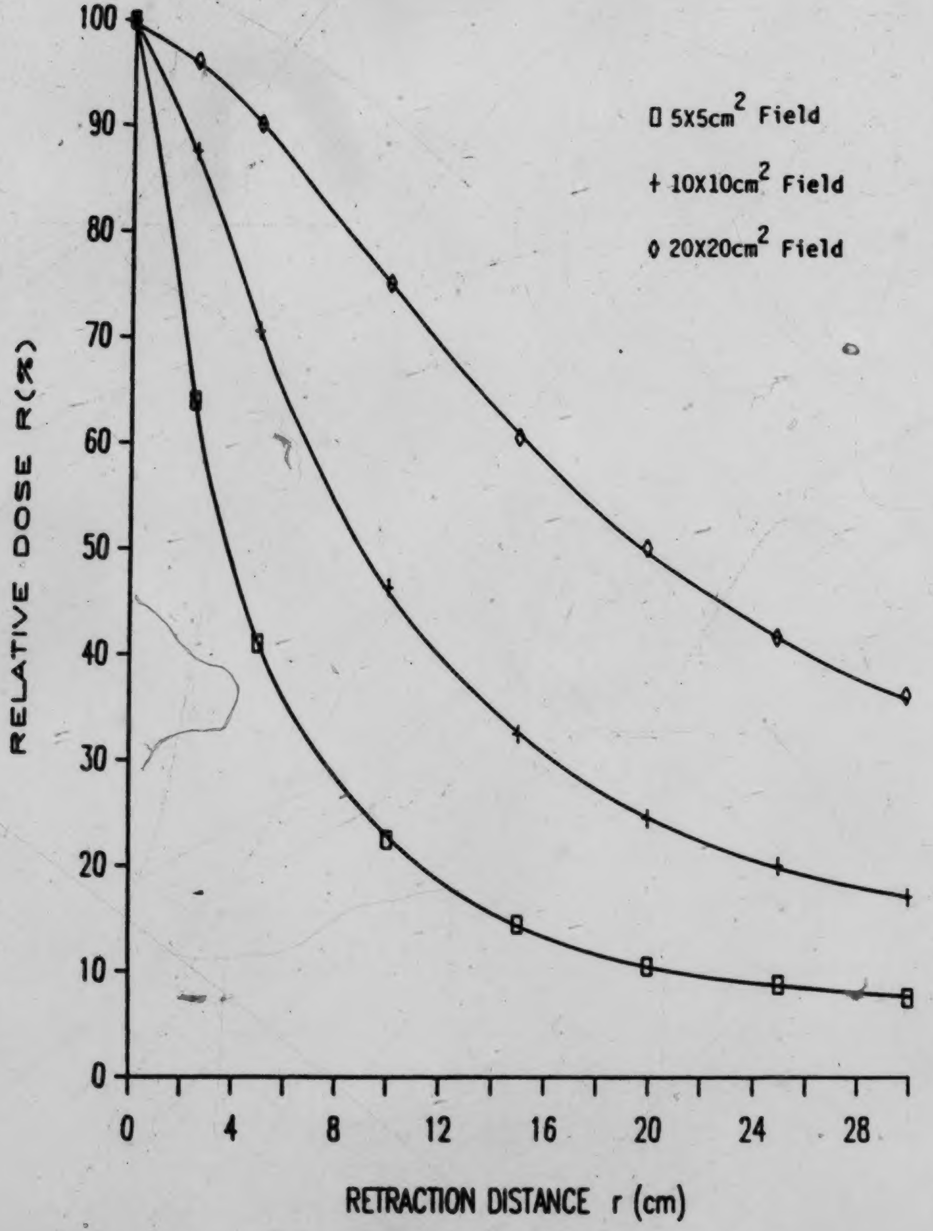

Figure #61. A plot of relative dose R(%) at the surface as a function of retraction distance r for a Polystyrene compensator of 2cm thickness. (E(γ)=15MV)

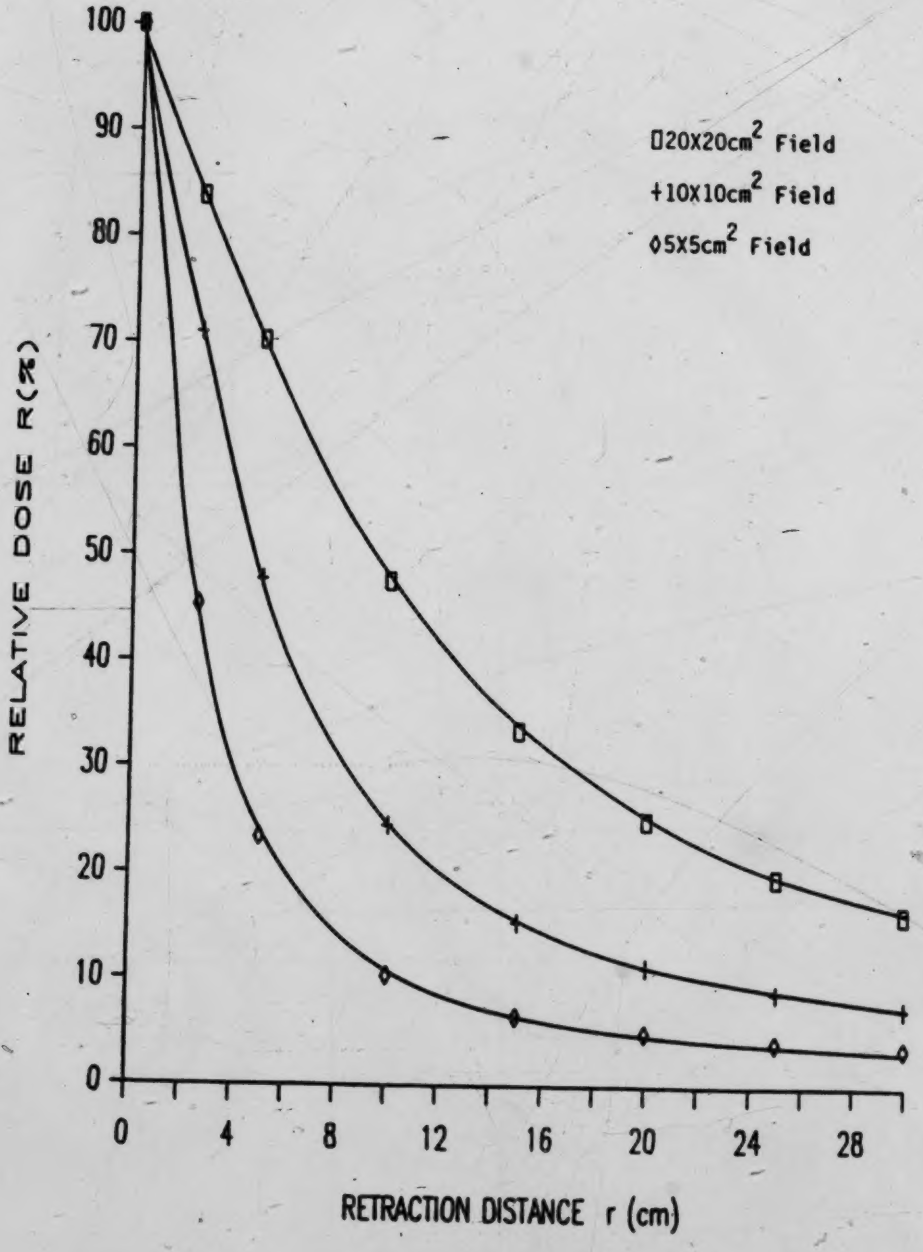

Figure #62. A plot of relative dose R(%) at the surface as a function of retraction distance r for a Pb compensator of 6.25mm thickness. (E(γ)=15MV)

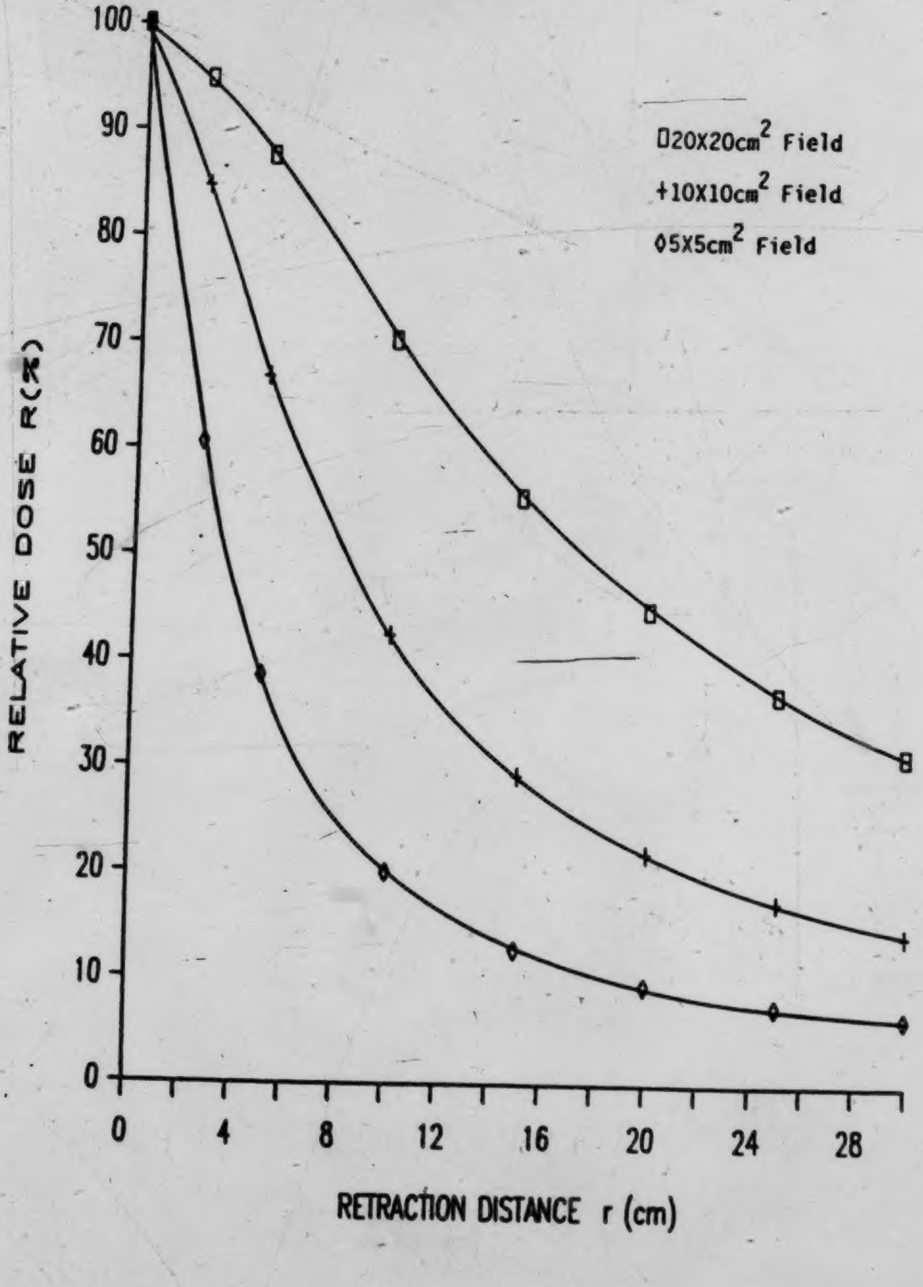

Figure #63. A plot of relative dose R(%) at the surface as a function of retraction distance r for a Polystyrene compensator of 7cm thickness. (E($\gamma$)=15MV)

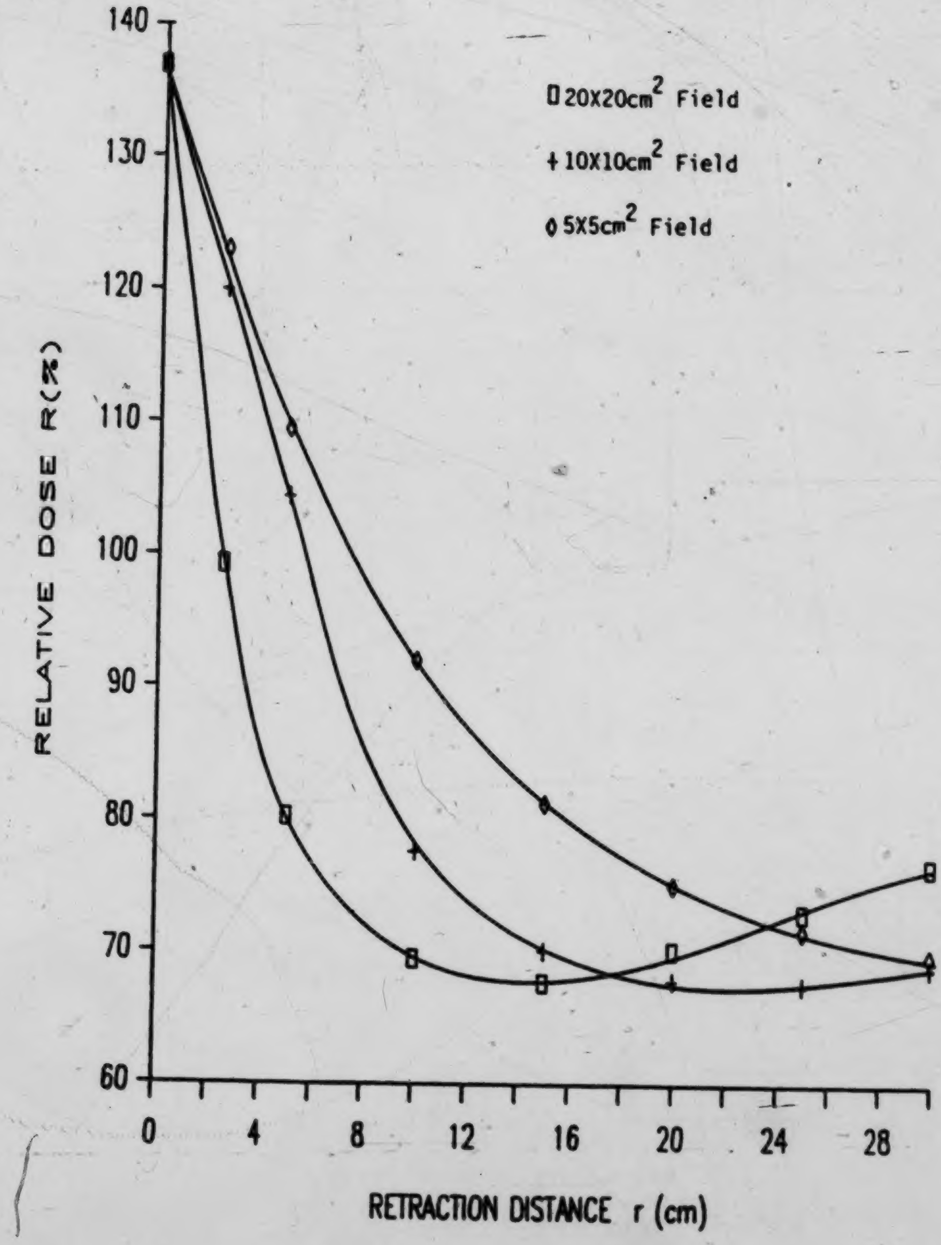

**Figure #64.** A plot of the ratio of [dose Pb/dose Poly] at the surface as a function of retraction distance for a Pb compensator of 1.75mm thickness and a polystyrene compensator of 2cm thickness. ($E(\gamma)$=15MV)

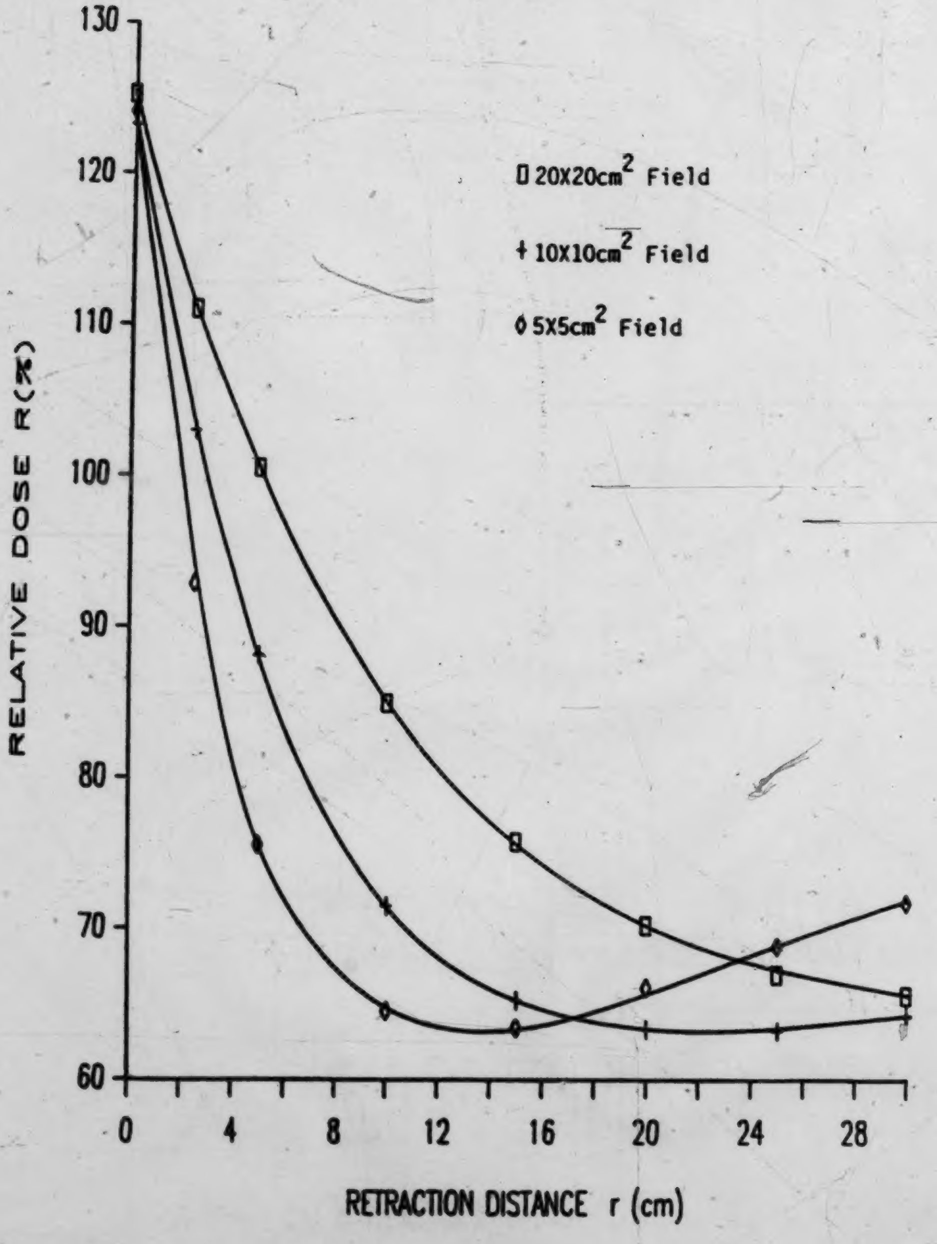

**Figure #65.** A plot of the ratio of [dose Pb/dose Poly] at the surface as a function of retraction distance for a Pb compensator of 6.25mm thickness and a polystyrene compensator of 7cm thickness. (E(γ)=15MV)

15MV does not exhibit a minimum over the range of retraction distances employed. As with relative surface dose, the ratio of [dose Pb/dose poly] is seen to be a function of compensator thickness, field size, energy of the incident photons, and retraction distance.

### 5.3.1.1 Analysis

From the above, the alteration of surface dose is seen to be a function of retraction distance, field size, compensator thickness, compensator material, and the energy of the x-ray beam. The following general observations apply:

a) retraction distance
  i) surface dose decreases as retraction distance increases
b) field size
  i) magnitude and rate of decrease of surface dose is inversely related to field size in that the largest and most rapid relative decrease(as a function of retraction distance) occurs for the smallest field size and vice versa for the largest field size
  ii) The ratio of [dose Pb/dose poly] is larger for larger field sizes at zero retraction

c) compensator thickness
    i) magnitude of relative decrease is greater for thicker compensators
    ii) the ratio of [dosePb/dose poly] is larger for thinner compensators
d) compensator material
    i) rate of decrease is greater for lead
    ii) magnitude of relative reduction is greater for lead
e) photon energy
    i) magnitude of relative reduction is greater for higher energies
    ii) the ratio of [dose Pb/dose poly] at zero retraction for the same thickness of Pb and poly for a given field size is least for 6MV, higher for $^{60}$Co, and largest for 15MV

To make sense of these many dependencies consider the arrangement of Fig.#66 where the surface dose is measured by the detector of area A. The surface dose will be due to backscatter from the phantom plus forward scattered photons from the compensator plus forward scattered electrons from the compensator. Of these three, the dose due to scattered electrons will dominate. Of the electrons generated in the compensator only those generated between z=0 and z=dmax will have a sufficient range to reach the detector. Consider the

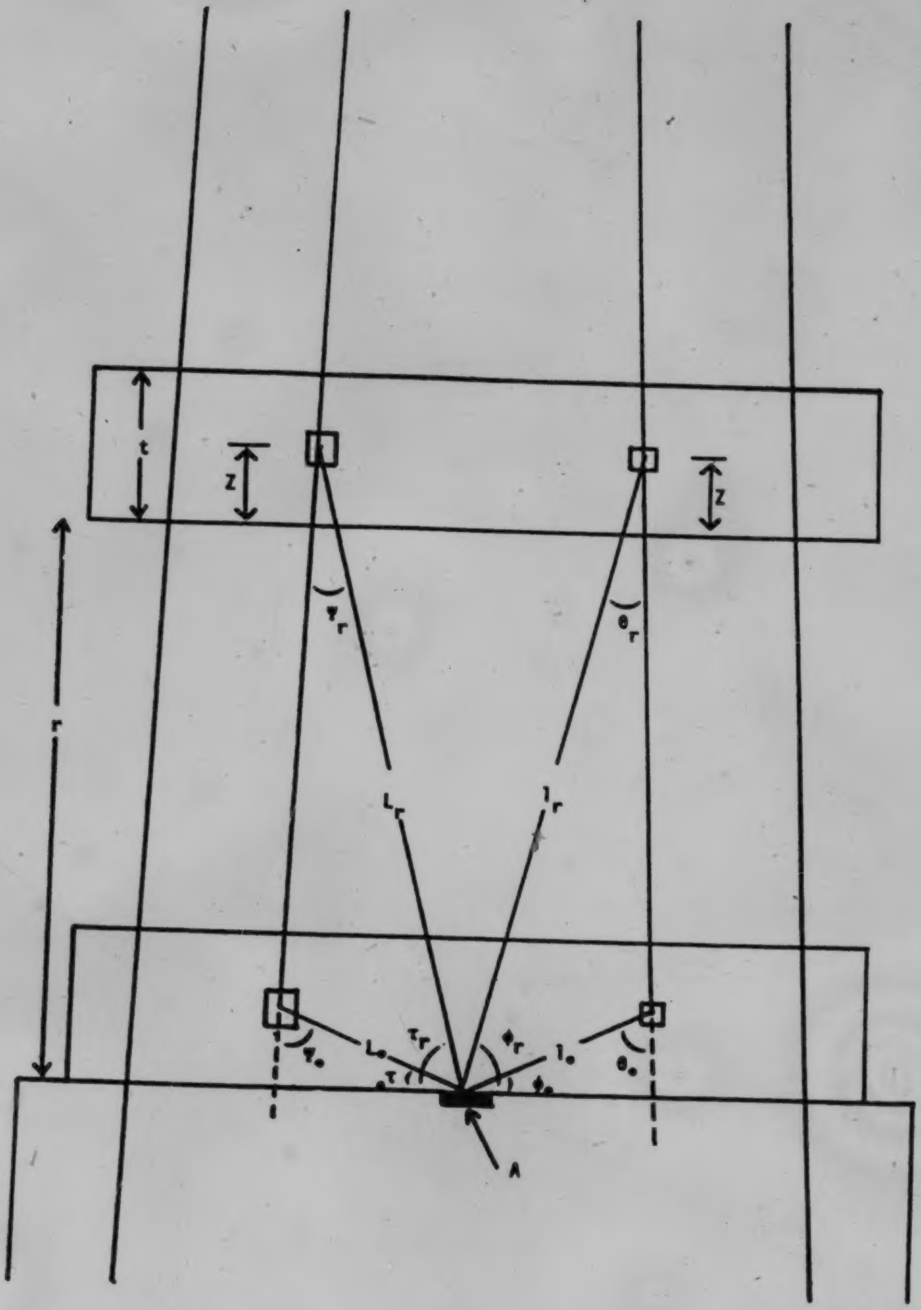
t
Z
Z
r
Ψr
θr
Lr
lr
Ψo
Lo
τr
τ
φr
lo
θo
φo
A

Figure #66. Surface dose due to scattered electrons and photons from the compensator.

electrons scattered from the compensator at zero retraction toward the detector. Let a photon from the point source be incident in the volume element $dV_e$ and let $(dN_e/d\Omega)(\theta_\circ h\nu)$ be the fractional number of secondary electrons scattered into unit solid angle at an angle $\theta_\circ$. The solid angle $d\Omega$ subtended by the detector at the volume element $dV_e$ will be $A\sin\phi_\circ/l_\circ^2$ where $l_\circ$ is the distance from the volume element $dV_e$ to the detector. The number of the electrons reaching the detector will be reduced by a factor $R(l_\circ, \theta_\circ)$ due to electron attenuation in the compensator. The fractional number of electrons incident upon the detector from the scattering volume $dV_e$ will then be

$$dN_e \propto \frac{dN_e}{d\Omega}(\theta_\circ, h\nu)\frac{A\sin\phi_\circ}{l_\circ^2}\, R(l_\circ, \theta_\circ) \qquad [5.1]$$

Also consider the photons scattered from the compensator toward the detector. Let a photon from the point source be incident in the photon scattering volume element $dV_e$ located, as shown in Fig.#66, in the compensator and let $(dN_p/d\Omega)(\Psi_\circ, h\nu)$ be the fractional number of photons scattered into unit solid angle at an angle $\Psi_\circ$. The solid angle $d\Omega'$ formed by the detector with volume element $dV_p$ will be $A\sin\pi_\circ/L_\circ^2$ where $L_\circ$ is the distance from the volume element $dV_p$ to the detector. The number of photons reaching the detector will be reduced by a factor $A(L_o, \Psi_o)$ due to photon attenuation in the compensator. Thus the number of scattered photons incident upon the detector will be

$$dn_p \propto \frac{dN_p}{d\Omega}(\Psi_o, h\nu)\frac{A\sin\tau_o}{L_o^2}\, A(L_o, \Psi_o) \qquad [5.2]$$

Now upon compensator retraction an air gap is introduced between the compensator and the phantom. As the range of electrons in air is of the order of 1000 times that in polystyrene or lead and the linear attenuation coefficient of photons in air is of the order of 1000 times less than that in lead or polystyrene then the effect of the air gap on electron and photon attenuation may be safely ignored for the retraction distances of up to 30cm employed.

At a retraction distance r the fractional number of electrons and photons incident upon the detector become

$$dN_e \propto \frac{dN_r}{d\Omega}(\theta_r, h\nu)\frac{A\sin\phi_r}{l_r^2}\, R(l_r, \theta_r) \qquad [5.3]$$

and

$$dN_p \propto \frac{dN_p}{d\Omega}(\Psi_r, h\nu)\frac{A\sin\tau_r}{L_r^2} A(L_r, \Psi_r) \qquad [5.4]$$

respectively.

If the scattering mechanism for both electrons and photons is that of Compton scattering then both $(dN_e/d\Omega)(\theta_r, h\nu)$ and $(dN_p/d\Omega)(\Psi_r, h\nu)$ will be forward peaked and will increase as retraction distance increases since $\theta_r$ and $\Psi_r$ decrease with increasing r. The rate of decrease of $\theta_r$ and $\Psi_r$ is greater the farther the scattering volumes are located from the central beam axis.

The majority of scattered electrons which reach the detector will originate from scattering volumes located closer and closer to the bottom of the compensator as the distance of the scattering volume from the central beam axis increases due to the finite range of the electrons. For scattering volumes at the same distance from the central axis the scattering angle will range from a maximum scattering angle at the bottom of the compensator to a mimimum scattering angle for points deeper inside the compensator. The smaller the retraction distance the closer to the compensator bottom the scattering volume must be to contribute electrons to the detector. At zero retraction distance the contribution from scattering volumes located a distance farther than the range of electrons in the compensator will be effectively zero, even from scattering points on the very bottom of the compensator as $\sin\phi_o=0$ for bottom elements at zero retraction. Thus for retraction distances smaller than a critical retraction distance the solid angle $A\sin\phi_r/l_r^2$ will increase as retraction distance increases for scattering volumes at or near the bottom of the compensator. This critical retraction distance will be greater the farther the scattering volume is located from the central beam axis and the closer the scattering volume is to the bottom of the compensator. For all retraction distances greater than the critical retraction distance for a particular scatering volume the solid angle decreases. The rate of decrease of the solid angle will be less the farther the scattering volume is located from the central beam axis and the the closer it is located to the compensator bottom.

Thus from the above one would expect the relative dose at the surface to decrease as retraction distance increases and that the reduction rate should be greatest for small fields as larger field sizes will contribute scattered electrons from volume elements farther from the beam axis for which the rate of change of the solid angle is less and the rate of change of the scattering angle is greater. This being the case then for any given retraction distance the magnitude of the reduction in relative surface dose should be greatest for the smallest field.

The observation that the ratio of [dose Pb/dose poly] at zero retraction is larger for larger field sizes may be explained by examining the scattering angles for both electrons and photons in the corresponding compensators. As the range of electrons is greater in polystyrene than in lead the range of scattering angles for electrons will be greater in polystyrene than in lead. The same maximum scattering angle of $\theta_o$=90 exists for both lead and polystyrene(at zero retraction distance) but the minimum scattering angle for points off the central beam axis is less for polystyrene than for lead. A smaller scattering angle (assuming Compton scattering) gives a larger scattering cross section and, all other factors being equal, a higher dose. This minimum scattering angle for polystyrene converges to that of lead the farther the scattering volume is located from the central beam axis and hence the ratio of [dose Pb/dose poly] will increase for scattering volumes which are farther and farther from the central beam axis(ie. larger fields). Thus the ratio of [dose Pb/dose poly] will be larger for larger field sizes. This effect is compounded by a similar argument concerning the minimum scattering angle(which occurs at the top of the compensator) for photon scattering volumes in polystyrene and lead which lie off the central beam axis.

Comparing compensators of the same material but of different thickness, there should be no difference in relative dose alteration due to the dose due to scattered electrons as the range of electrons is the same in both compensators. The difference then arises from differences in backscatter from the phantom and forward scattered photons from the compensator. The compensator of larger thickness will scatter more photons into the phantom and thus give a larger surface dose due to backscatter. As well the dose due to forward scattered photons from the compensator will be larger for the thicker compensator. The increased dose from backscatter and forward scattered photons results from the greater scattering mass of the thicker compensator as long as the increase due to increased mass is greater than the effect of self attenuation caused by the increased mass. This is the case for the thicknesses of compensator employed here. The increased dose is also due to the smaller minimum scattering angle for photons for off axis scattering volumes in the thicker compensator. The ratio of the scattering mass remains constant as retraction distance increases but the minimum scattering angles of the thick compensator approach those of the thin compensator(at the same retraction distance) as retraction distance increases. Thus the relative dose reduction for thick compensators should be greater than for thin compensators as is observed. This effect will be greater for the polystyrene than for the lead as the change in minimum photon scattering angle for the lead compensators will be much less than for the polystyrene compensators when comparing thicker to thinner. Thus the ratio of [thick dose/thin dose] will be greater for polystyrene than for lead and hence the ratio of [dose Pb/dose poly] will be greater for thinner compensators as is the case.

The location of the mean scattering volume element(that scattering volume element which, if all the mass of the compensator were located in it, would give the same scatter at the detector as does the entire compensator) for lead will be closer to the detector than that of the corresponding thickness polystyrene compensator due to the smaller dimensions and smaller range of electrons for lead. Thus the rate of change of the solid angle of the mean scattering volume as retraction distance increases will be greater for lead than for polystyrene and hence both the rate and the magnitude of the relative decrease in surface dose will be greater for lead than for polystyrene.

The energy dependence of the magnitude of relative surface dose reduction can be understood in terms of the fact that Compton scattered electrons and photons become more forward peaked as the incident photon energy increases. Thus as beam energy increases scattered photons and electrons from points closer to the central beam axis will become more and more dominant while scatter from points farther from the beam axis will decrease. For the same reason that at a given energy the smallest field will exhibit the greatest reduction in relative dose, the same field size will exhibit the greatest reduction in relative surface dose for the highest incident photon energy.

Finally, at zero retraction the ratio of [dose Pb/dose poly] for the same field size and same thickness of Pb and polystyrene compensators is observed to be the smallest for 6MV, larger for $^{60}$Co, and greatest for 15MV. The explanation for this observation lies in the components of the total cross section for both polystyrene and lead at the three different energies. The total and constituent components of the cross sections for polystyrene and lead are listed in table #2. At all three energies the ratio of Compton cross section for lead to the Compton cross section for polystyrene is a constant at [illegible].75 and hence the ratio of [dose Pb/dose poly] due to compton scattering does not change with energy. At $^{60}$Co energies the Pb compensator will produce a higher surface dose than at 6MV due to its the greatly increased photoelectric cross section and at 15MV the lead compensator will produce a higher surface dose due to the larger pair and triplet

| | Cross Section ($cm^2/g$) | | | | | |
|---|---|---|---|---|---|---|
| Interaction | $^{60}Co$ | | 6MV | | 15MV | |
| | Poly | Pb | Poly | Pb | Poly | Pb |
| Compton | $4.12X10^{-2}$ | $4.62X10^{-2}$ | $4.75X10^{-2}$ | $3.54X10^{-2}$ | $2.69X10^{-2}$ | $1.99X10^{-2}$ |
| Photoelectric | $9.68X10^{-7}$ | $1.19X10^{-2}$ | $3.99X10^{-7}$ | $5.13X10^{-3}$ | $1.17X10^{-7}$ | $2.97X10^{-4}$ |
| Pair & Triplet | ——— | ——— | $3.05X10^{-4}$ | $4.93X10^{-3}$ | $2.02X10^{-3}$ | $2.12X10^{-2}$ |
| Total | $6.12X10^{-2}$ | $5.81X10^{-2}$ | $4.78X10^{-2}$ | $4.55X10^{-2}$ | $2.90X10^{-2}$ | $4.24X10^{-2}$ |

Table #2. Cross sections for polystyrene and lead at $^{60}Co$, 6MV, and 15MV.

production cross section. The ratio of the pair production cross section to the Compton cross section for lead at 15MV is 1.07 while the ratio of the photoelectric cross section to compton cross section for lead at $^{60}$Co is 0.26 and hence the surface dose from the lead compensator at $^{60}$Co will be larger than at 6MV and even larger at 15MV. The increase in dose due to the photoelectric effect at $^{60}$Co and pair and triplet production at 15MV is much less for polystyrene and hence the ratio of [dose Pb/dose poly] at zero retraction will be highest for 15MV, intermediate for $^{60}$Co, and lowest for 6MV if all other parameters remain the same.

### 5.3.2 Alteration of Dose at Depth

The retraction of the compensator away from the phantom in the direction of the beam has been shown to yield significant reductions in surface dose for all compensator materials, compensators thicknesses, field sizes, and incident photon energies. The retraction process also alters the dose at depth in the phantom. The alteration in dose at depth along the central beam axis was measured using the Farmer Replacement ionization chamber. The depth of measurement was defined as the depth of the central axis of the ionization chamber below the phantom surface. These measurements were carried out for polystyrene compensators of 2, 4, and, 7cm thickness and lead compensators of 1.75, 3.5, and, 6.25mm thickness for retraction distances ranging from 0 to 30 cm and field sizes of 5X5, 10X10, and, 20X20cm$^2$ and beam qualities of $^{60}$Co, 6MV, and, 15MV. The depth of measurement ranged from 4 to 13cm. The results obtained for the 4cm polystyrene compensator and the 3.5mm lead compensator are not presented as they yield results intermediate between those results obtained for the compensators of greater and lesser thickness of that material and thus yielded little additional information. The measured doses have been normalized to the dose at a given depth for zero retraction distance.

The alteration of relative dose at depth is shown in figures #67 to #74 for $^{60}$Co photons, figures #75 to #82 for 6MV photons, and figures #83 to #90 for 15MV photons. The dependencies seen are more complicated than those at the surface. In particular the dose due to any one given field size can, at times, be greater than that for one or both of the other field sizes, and at other times be less than either one or both of the other two field sizes. The points where the dose due to one field becomes less than that due to another field(the cross over points) are seen to vary form one set of parameters to another. Over all the alteration in relative dose at depth is seen to be a function of field size,

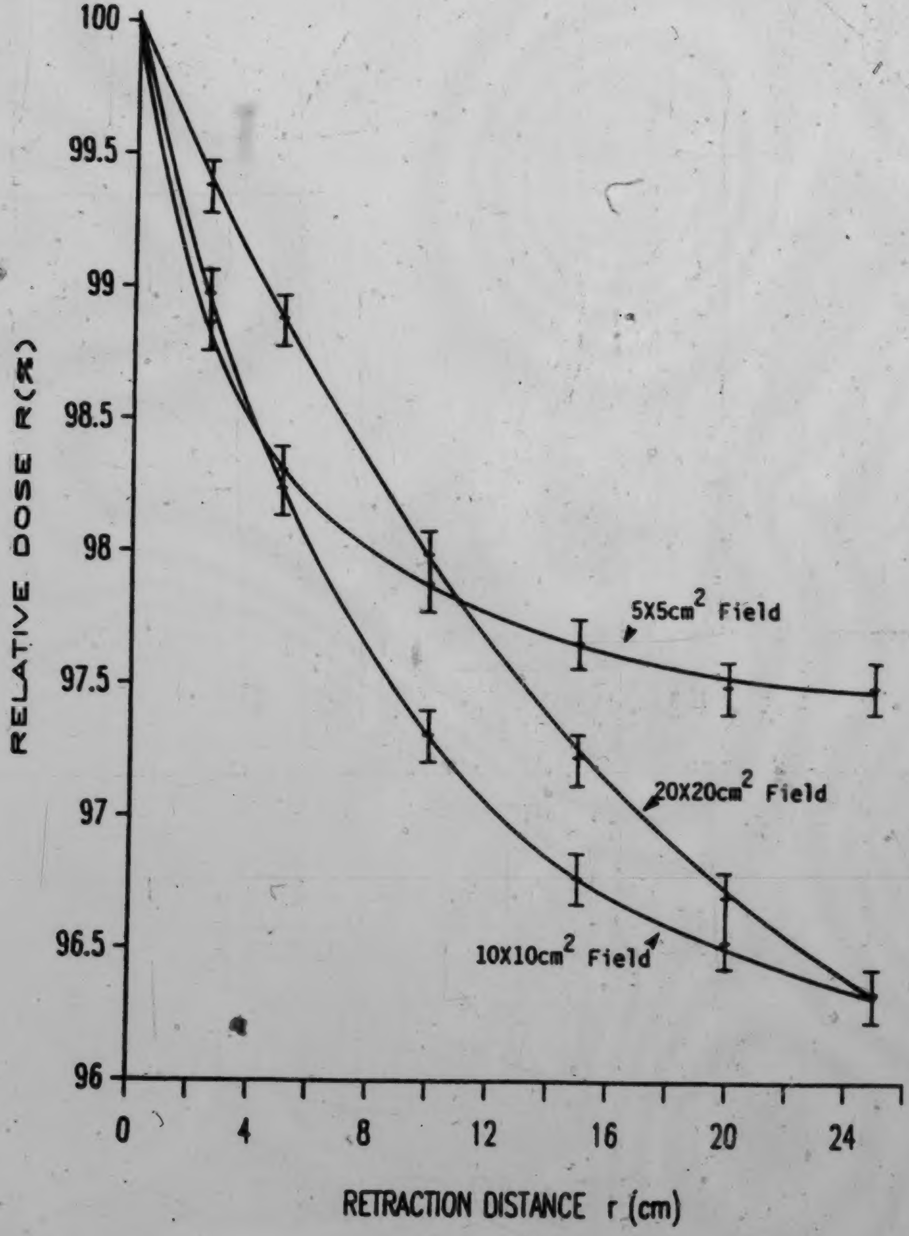

Figure #67. A plot of relative dose R(%) at 4cm depth as a function of retraction distance r for a Pb compensator of 1.75mm thickness. (E(γ)=$^{60}$Co)

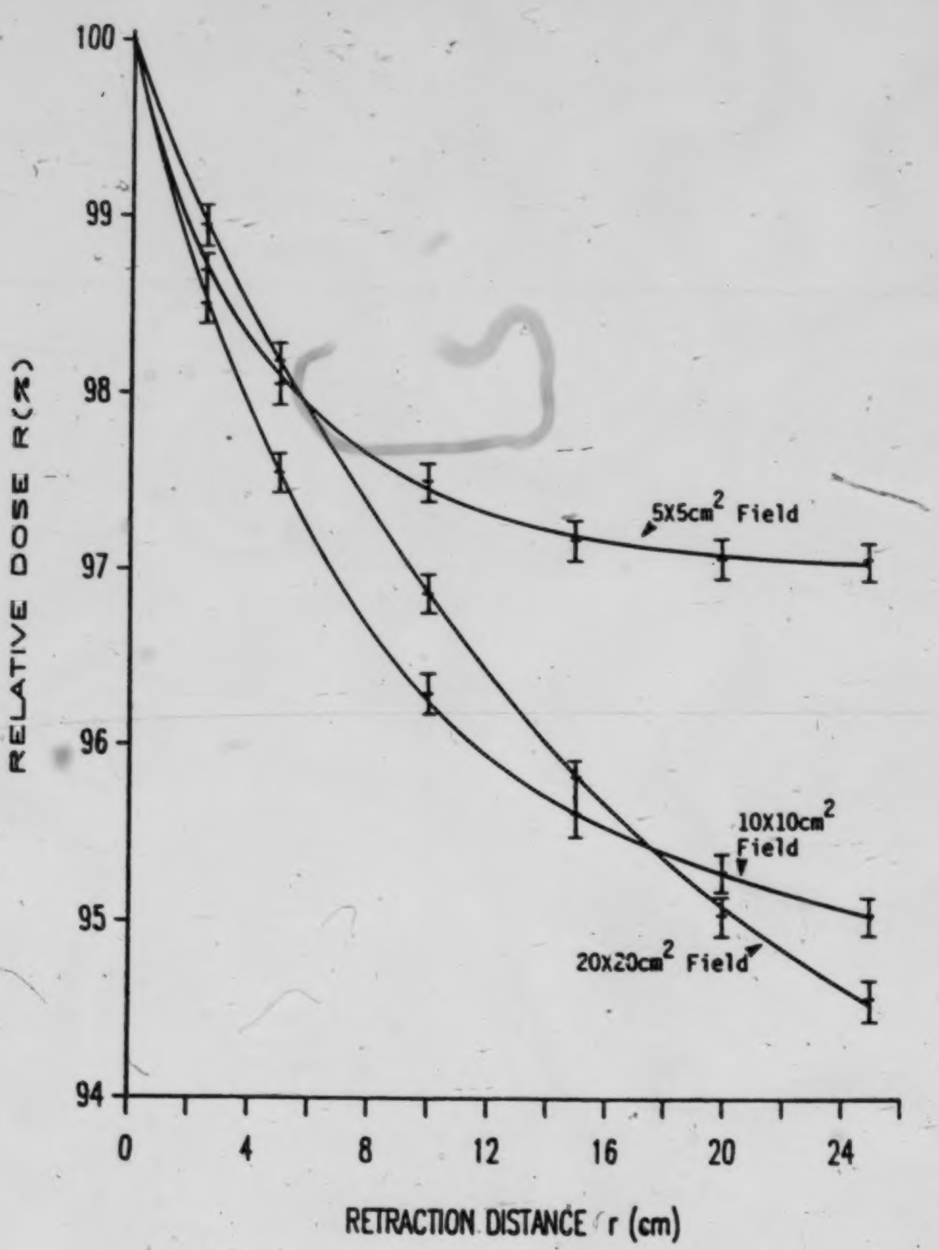

Figure #68. A plot of relative dose R(%) at 4cm depth as a function of retraction distance r for a polystyrene compensator of 2cm thickness

$(E(\gamma)={}^{60}Co)$

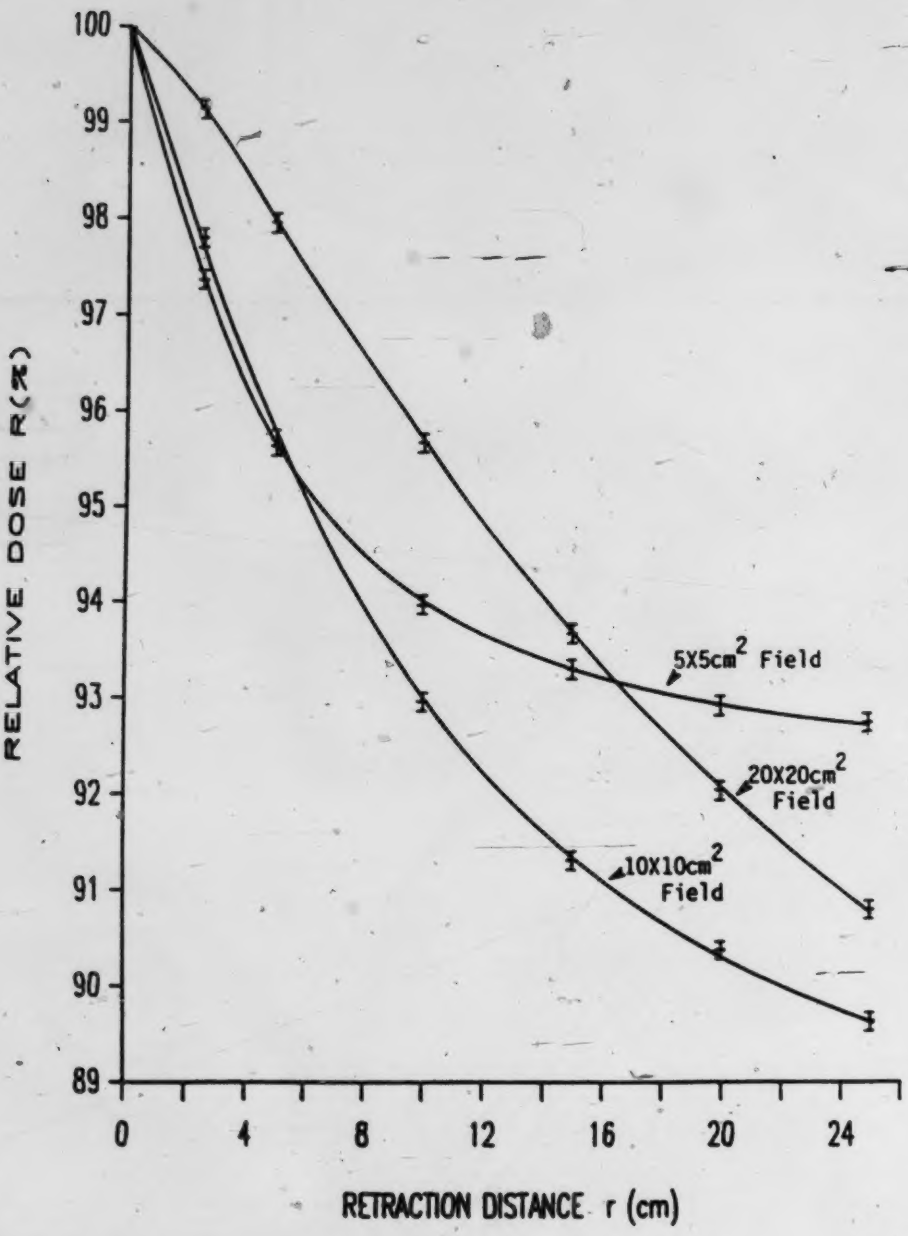

Figure #69. A plot of relative dose R(%) at 4cm depth as a function of retraction distance r for a Pb compensator of 6.25mm thickness. ($E(\gamma)={}^{60}Co$)

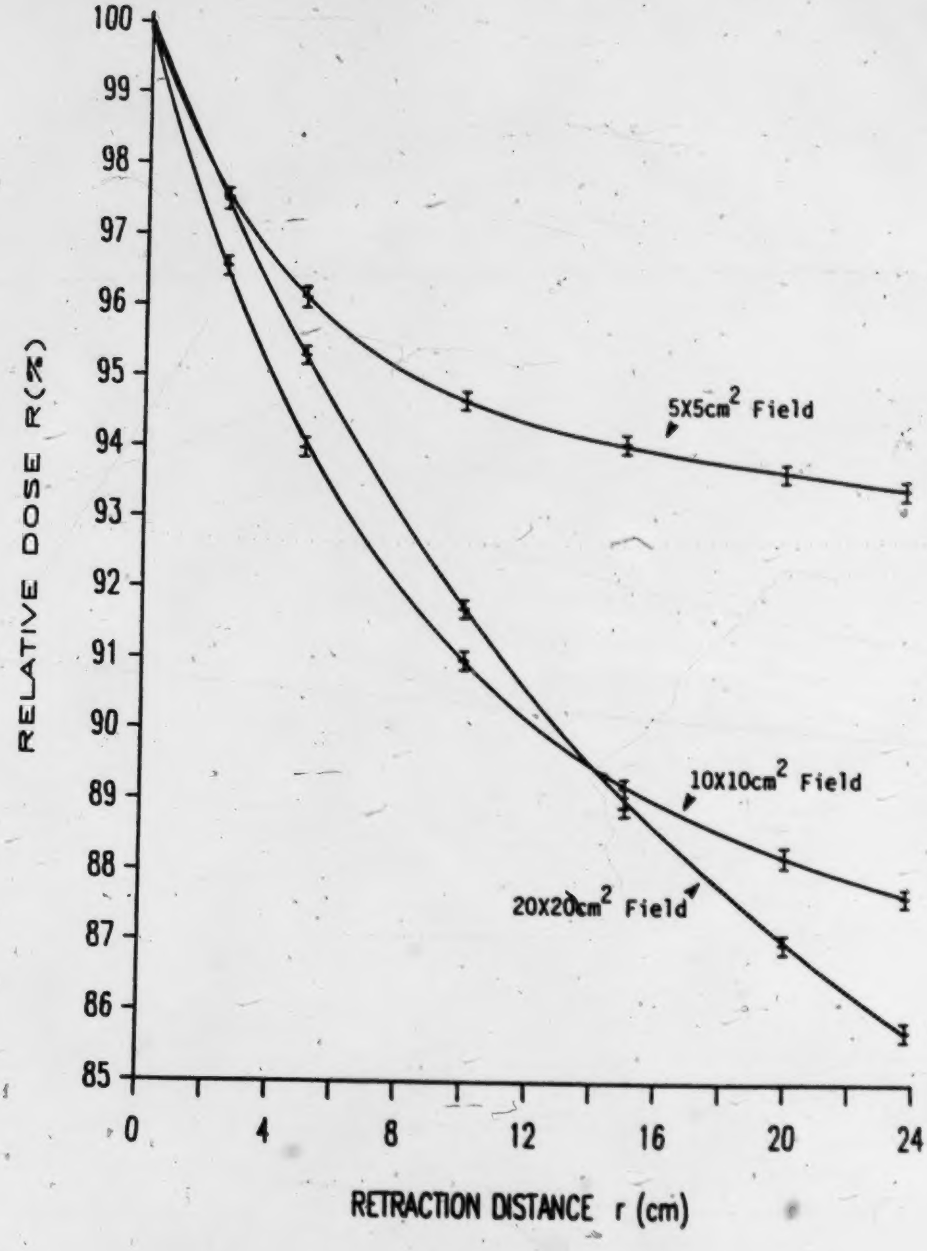

Figure #70. A plot of relative dose R(%) at 4cm depth as a function of retraction distance r for a polystyrene compensator of 7cm thickness

(E(γ)=$^{60}$Co)

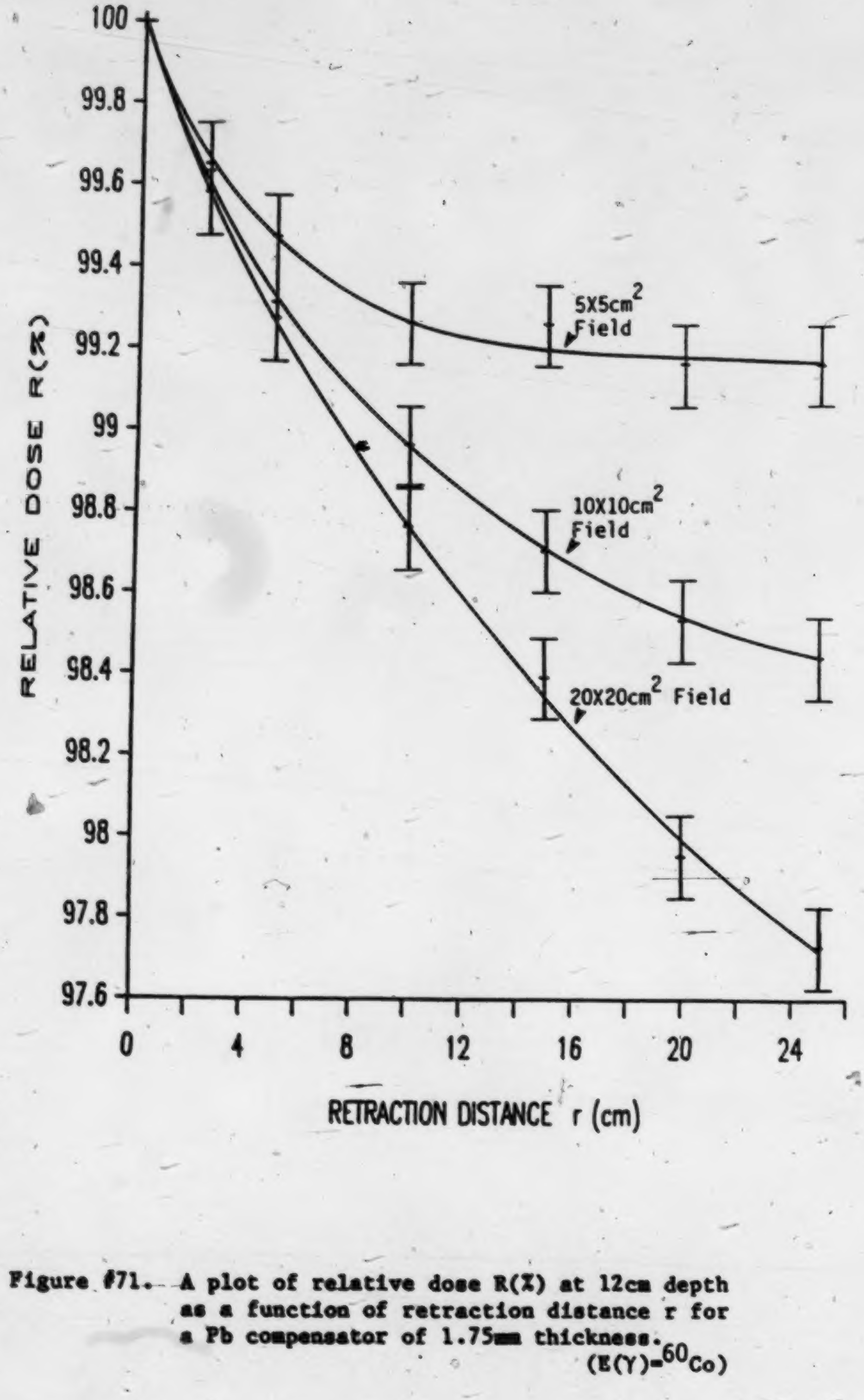

Figure #71. A plot of relative dose R(%) at 12cm depth as a function of retraction distance r for a Pb compensator of 1.75mm thickness. $(E(\gamma)={}^{60}Co)$

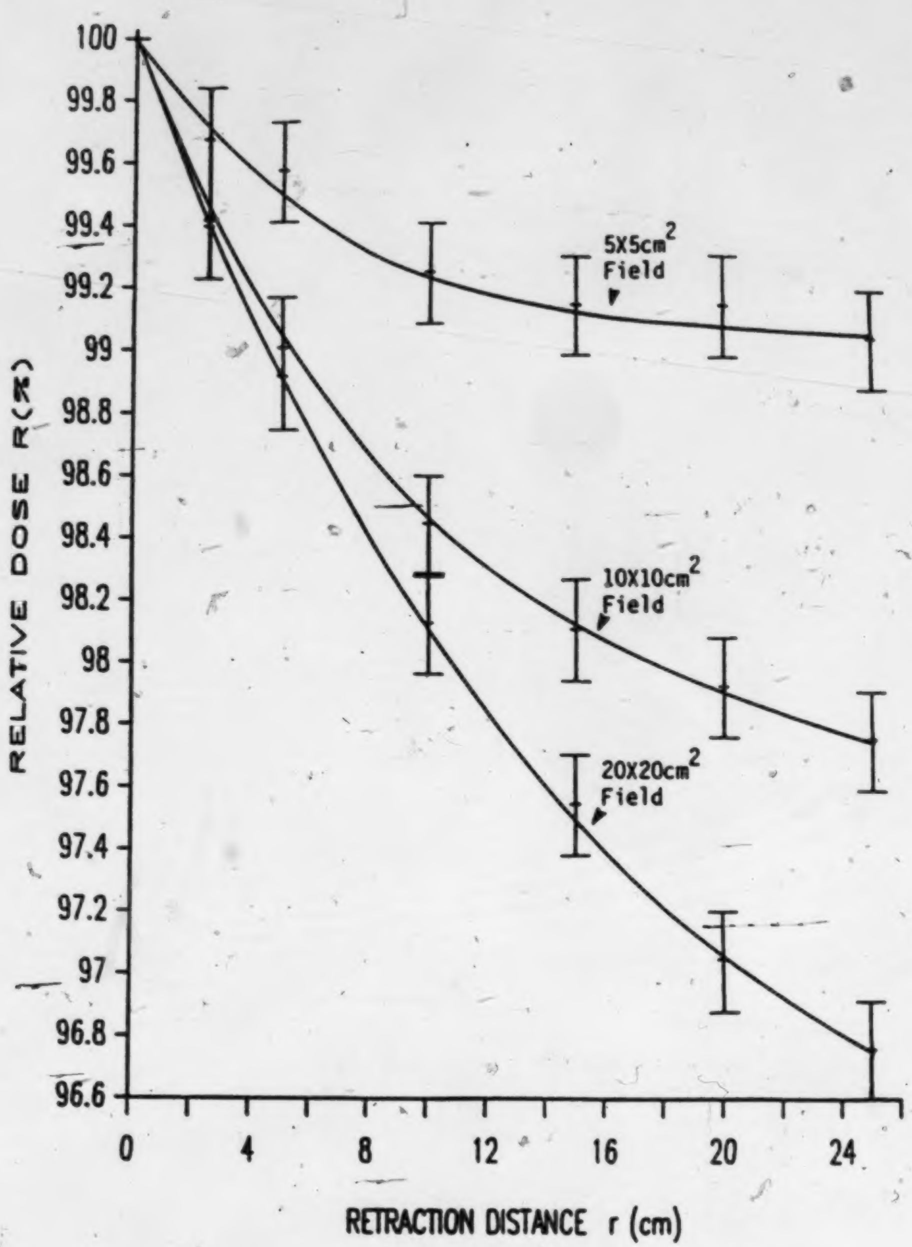

**Figure #72.** A plot of relative dose R(%) at 12cm depth as a function of retraction distance r for a polystyrene compensator of 2cm thickness

($E(\gamma)={}^{60}Co$)

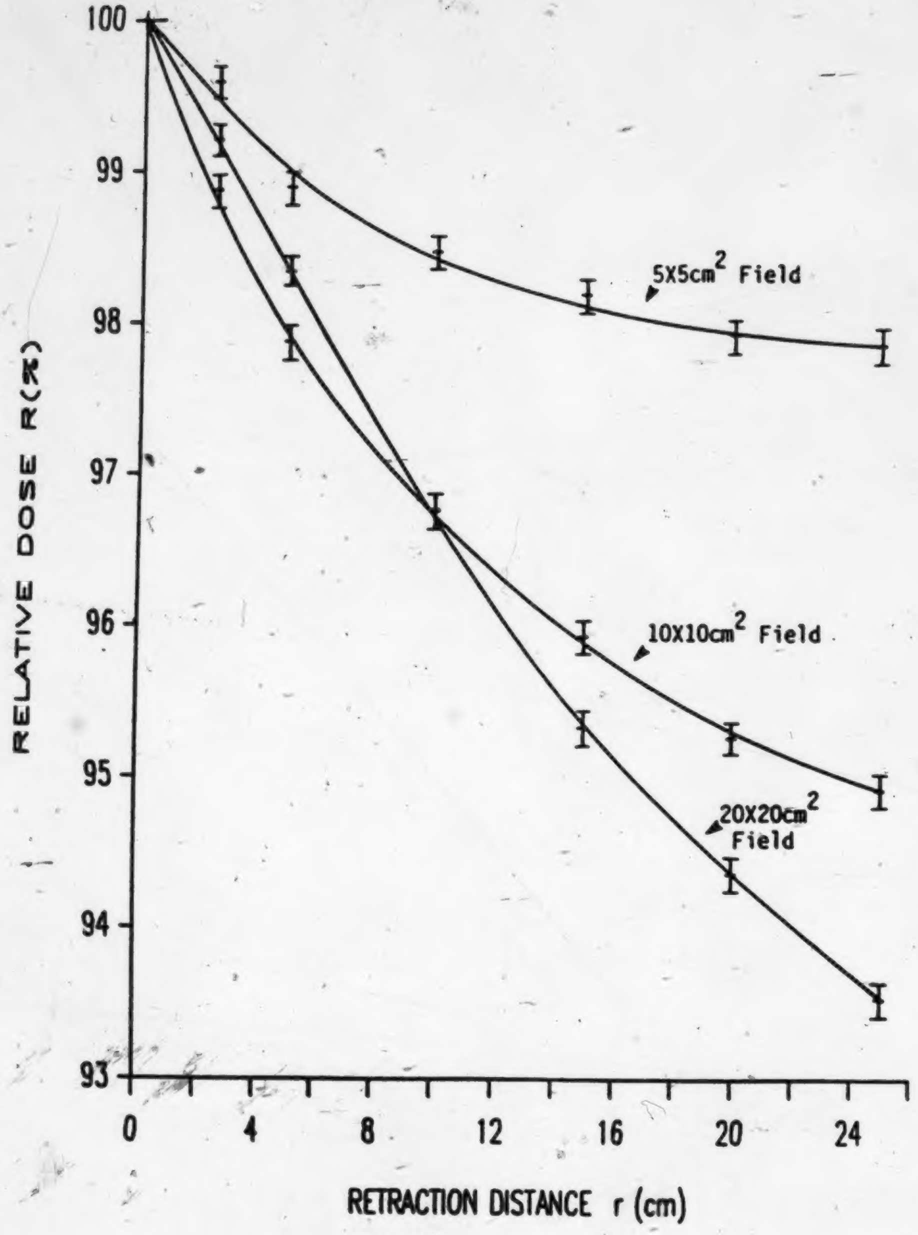

Figure #73. A plot of relative dose R(%) at 12cm depth as a function of retraction distance r for a Pb compensator of 6.25mm thickness. (E(γ)=$^{60}$Co)

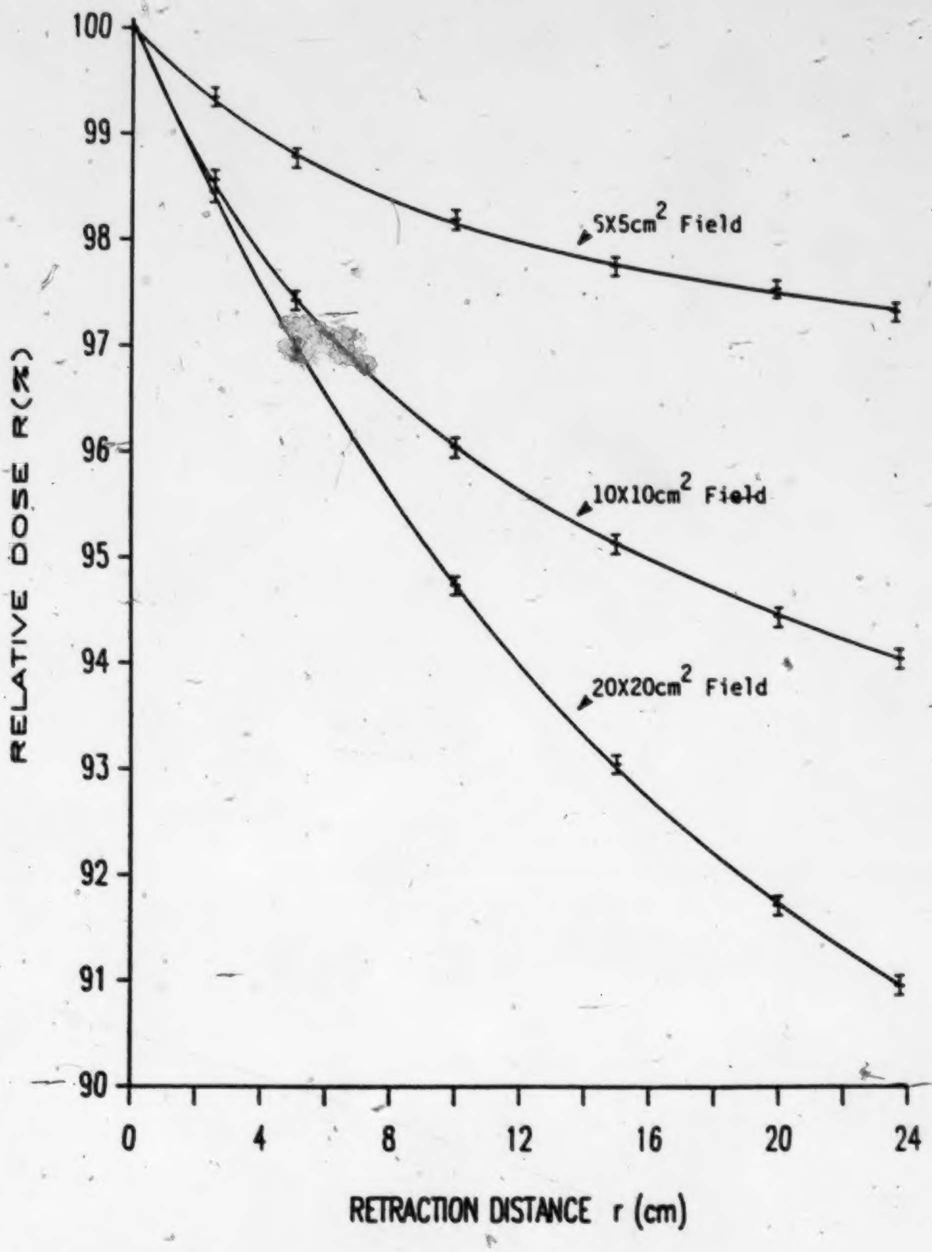

Figure #74. A plot of relative dose R(%) at 12cm depth as a function of retraction distance r for a polystyrene compensator of 7cm thickness ($E(\gamma)={}^{60}Co$)

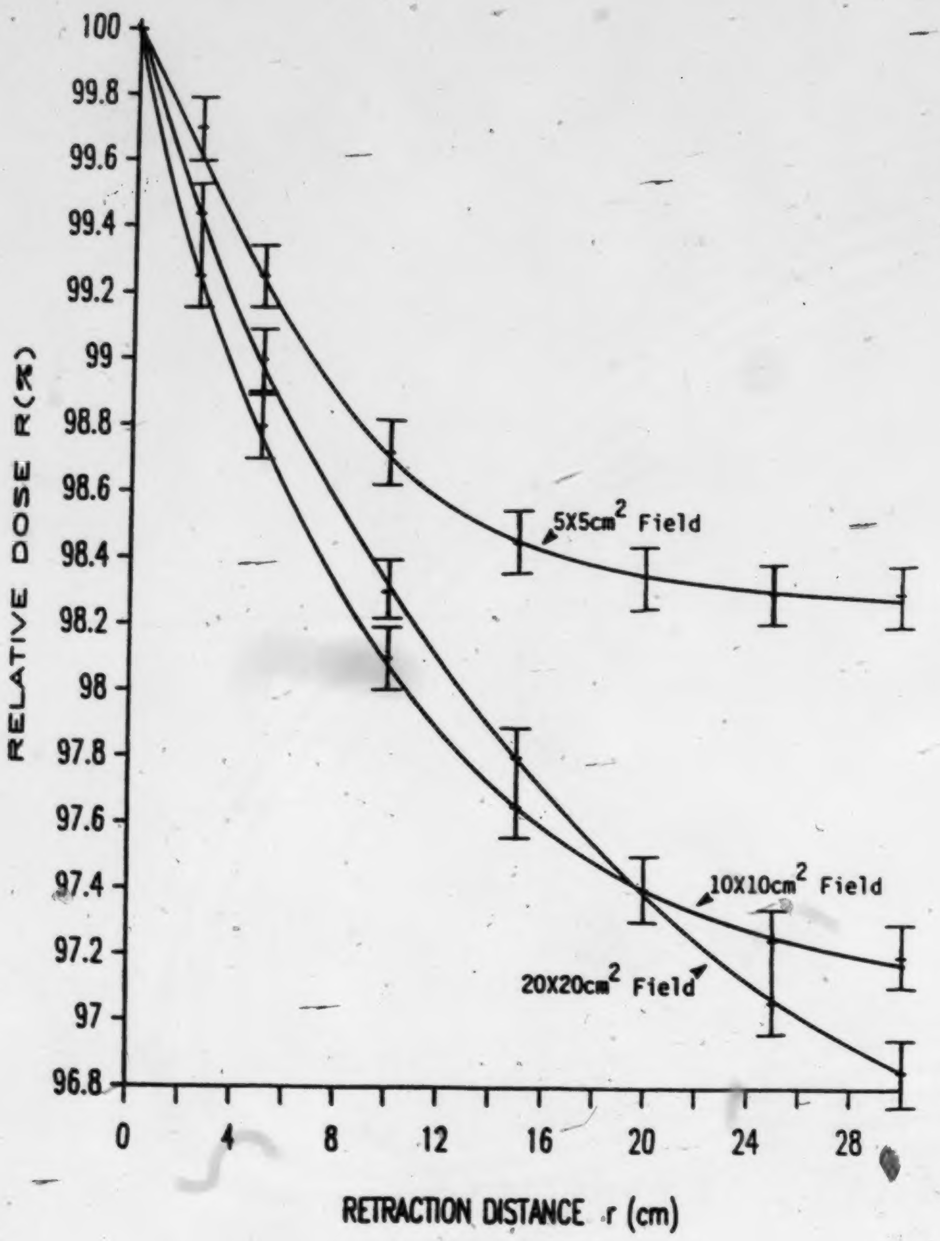

Figure #75. A plot of relative dose R(%) at 4cm depth as a function of retraction distance r for a Pb compensator of 1.75mm thickness. (E(γ)=6MV)

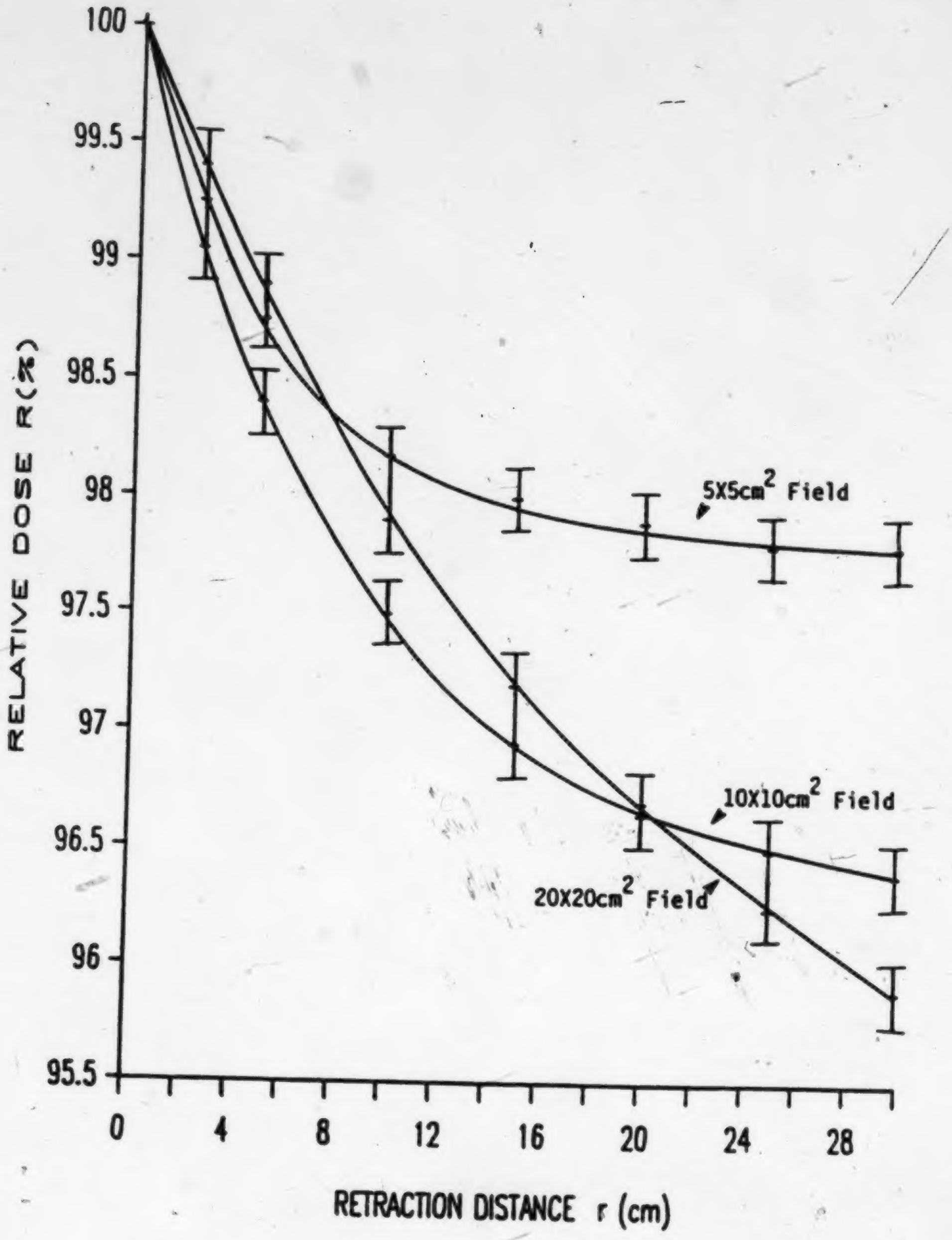

Figure #76. A plot of relative dose R(%) at 4cm depth as a function of retraction distance r for a polystyrene compensator of 2cm thickness (E(γ)=6MV)

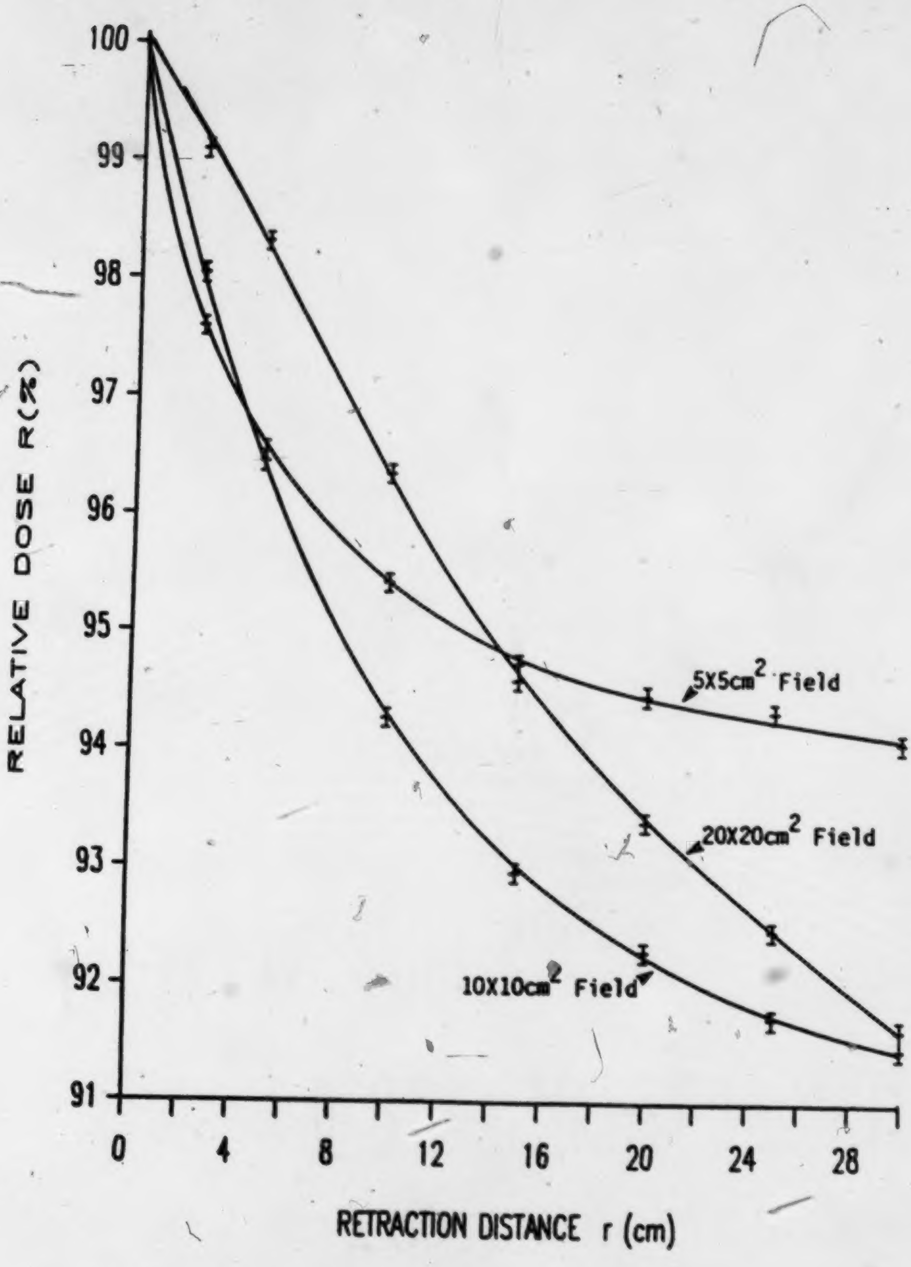

Figure #77. A plot of relative dose R(%) at 4cm depth as a function of retraction distance r for a Pb compensator of 6.25mm thickness. (E(γ)=6MV)

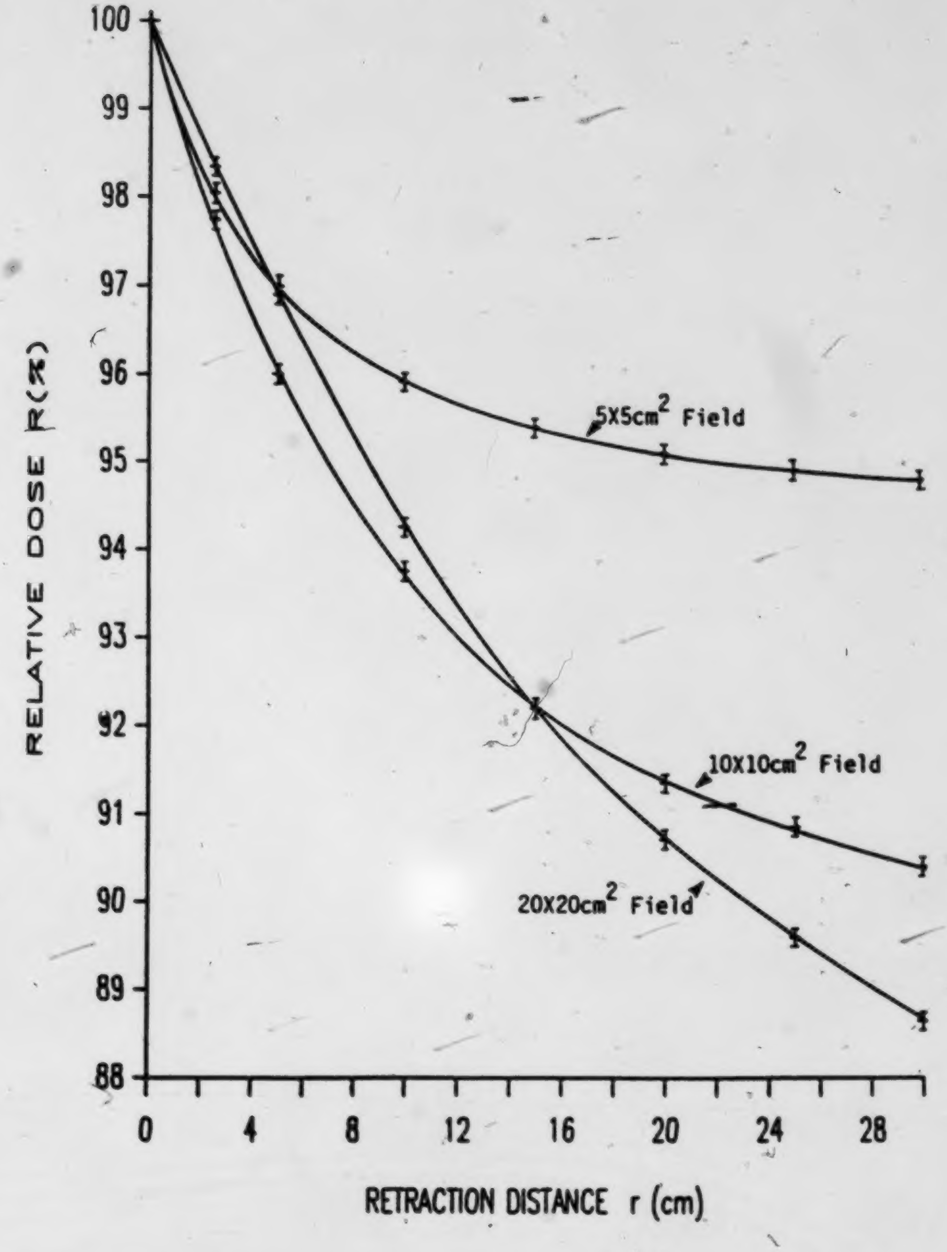

Figure #78. A plot of relative dose R(%) at 4cm depth as a function of retraction distance r for a polystyrene compensator of 7cm thickness (E(γ)=6MV)

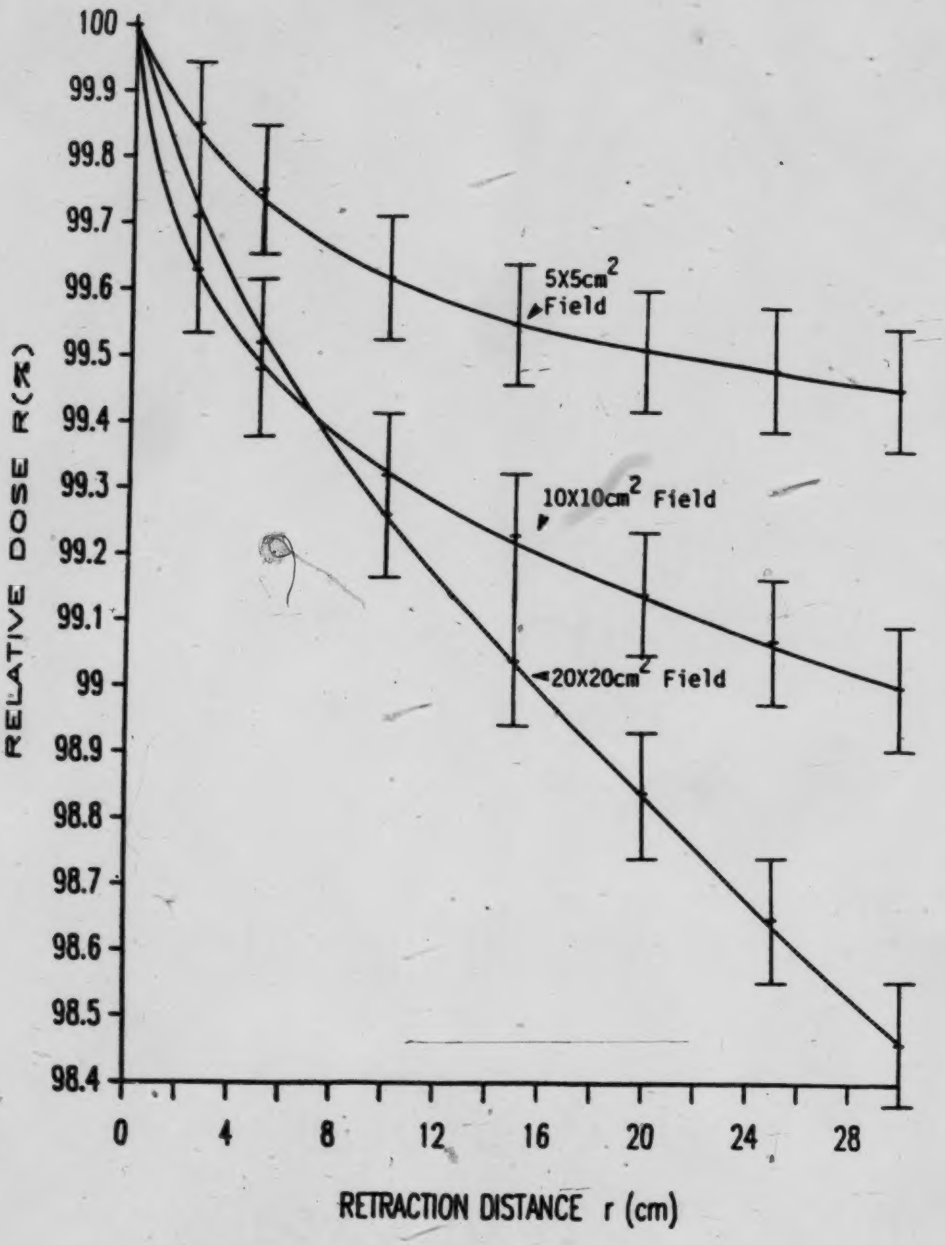

**Figure #79.** A plot of relative dose R(%) at 13cm depth as a function of retraction distance r for a Pb compensator of 1.75mm thickness. (E(γ)=6MV)

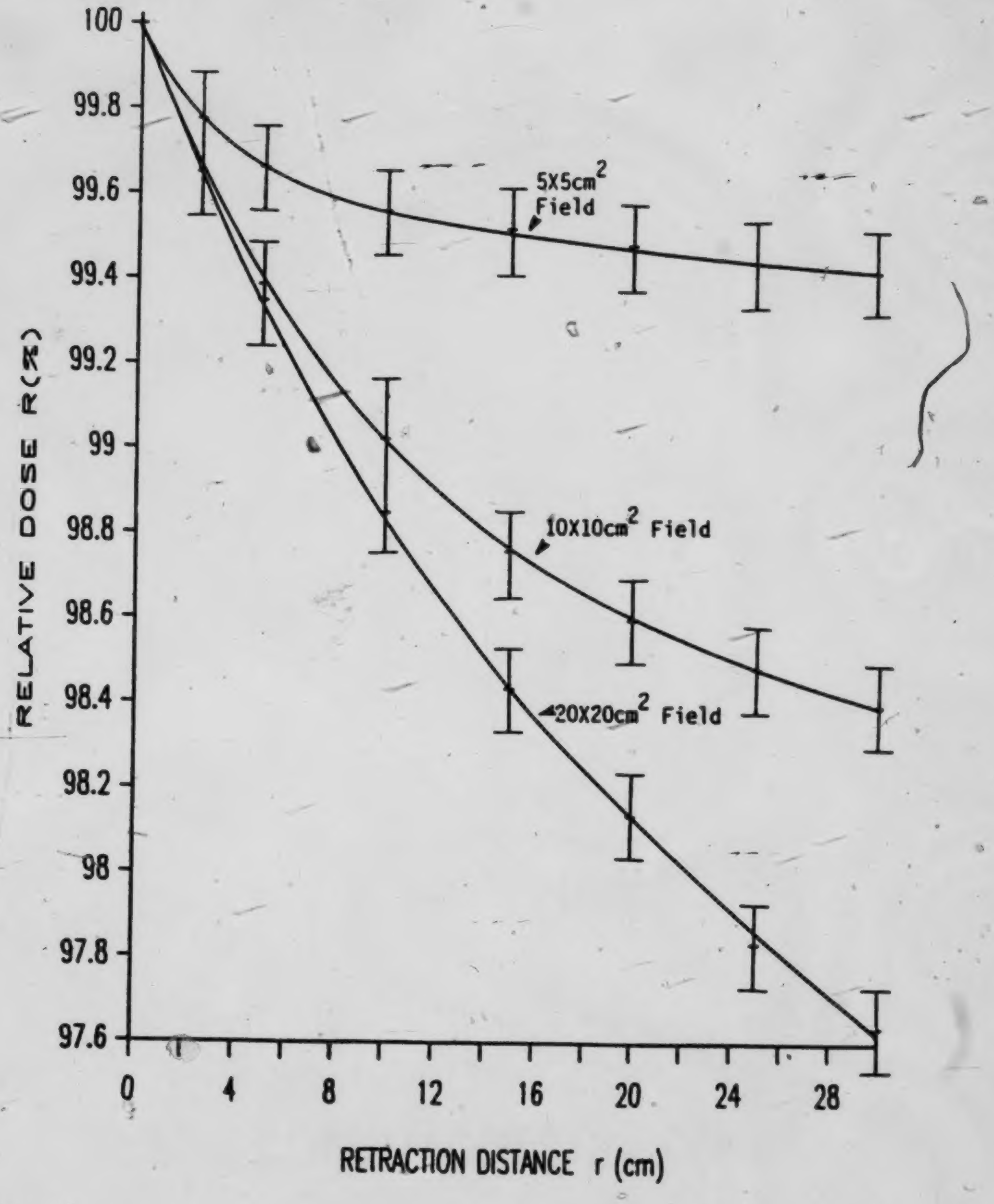

**Figure #80.** A plot of relative dose R(%) at 13cm depth as a function of retraction distance r for a polystyrene compensator of 2cm thickness (E(γ)=6MV)

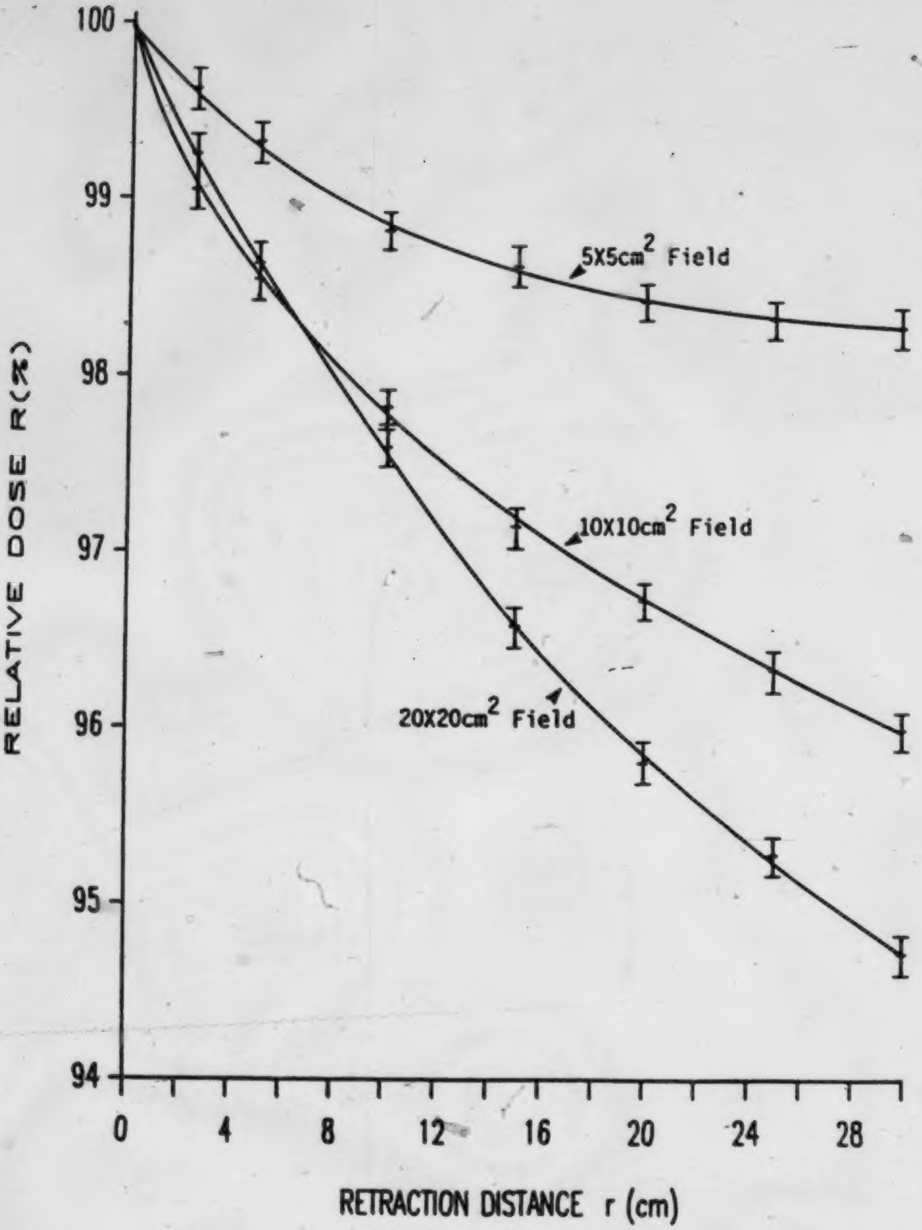

**Figure #81.** A plot of relative dose R(%) at 13cm depth as a function of retraction distance r for a Pb compensator of 6.25mm thickness. (E(γ)=6MV)

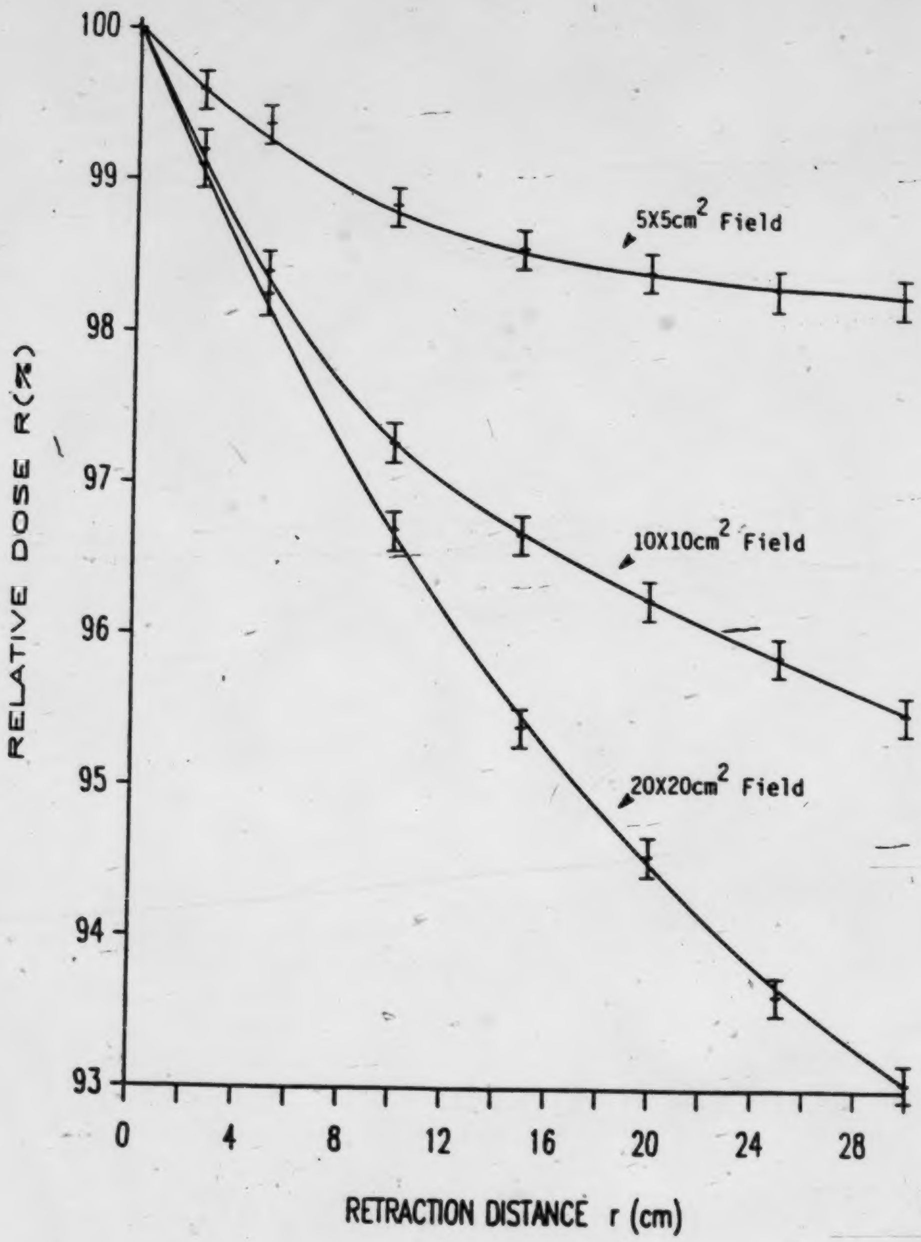

Figure #82. A plot of relative dose R(%) at 13cm depth as a function of retraction distance r for a polystyrene compensator of 7cm thickness (E(γ)=6MV)

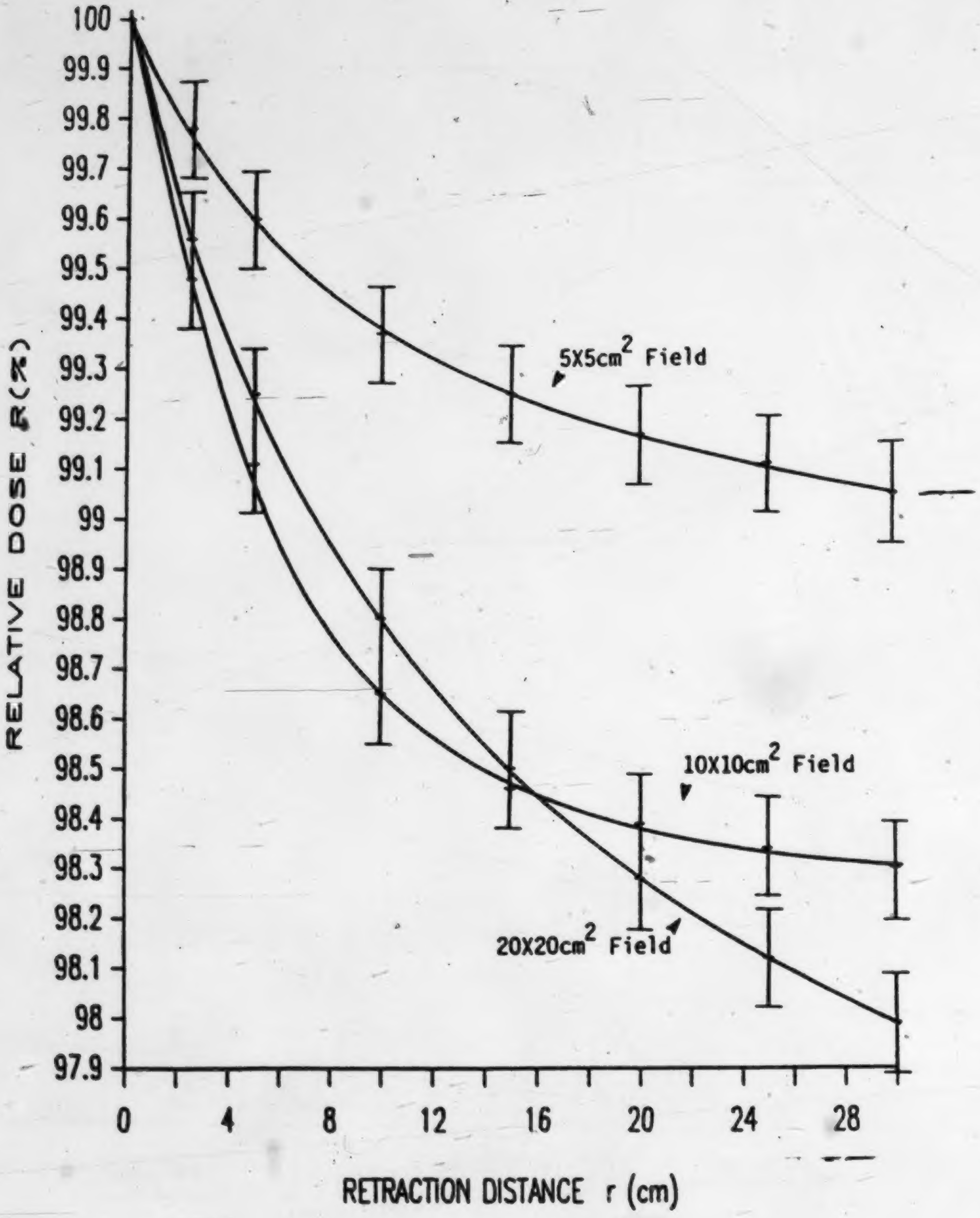

**Figure #83.** A plot of relative dose R(%) at 6cm depth as a function of retraction distance r for a Pb compensator of 1.75mm thickness. (E(γ)=15MV)

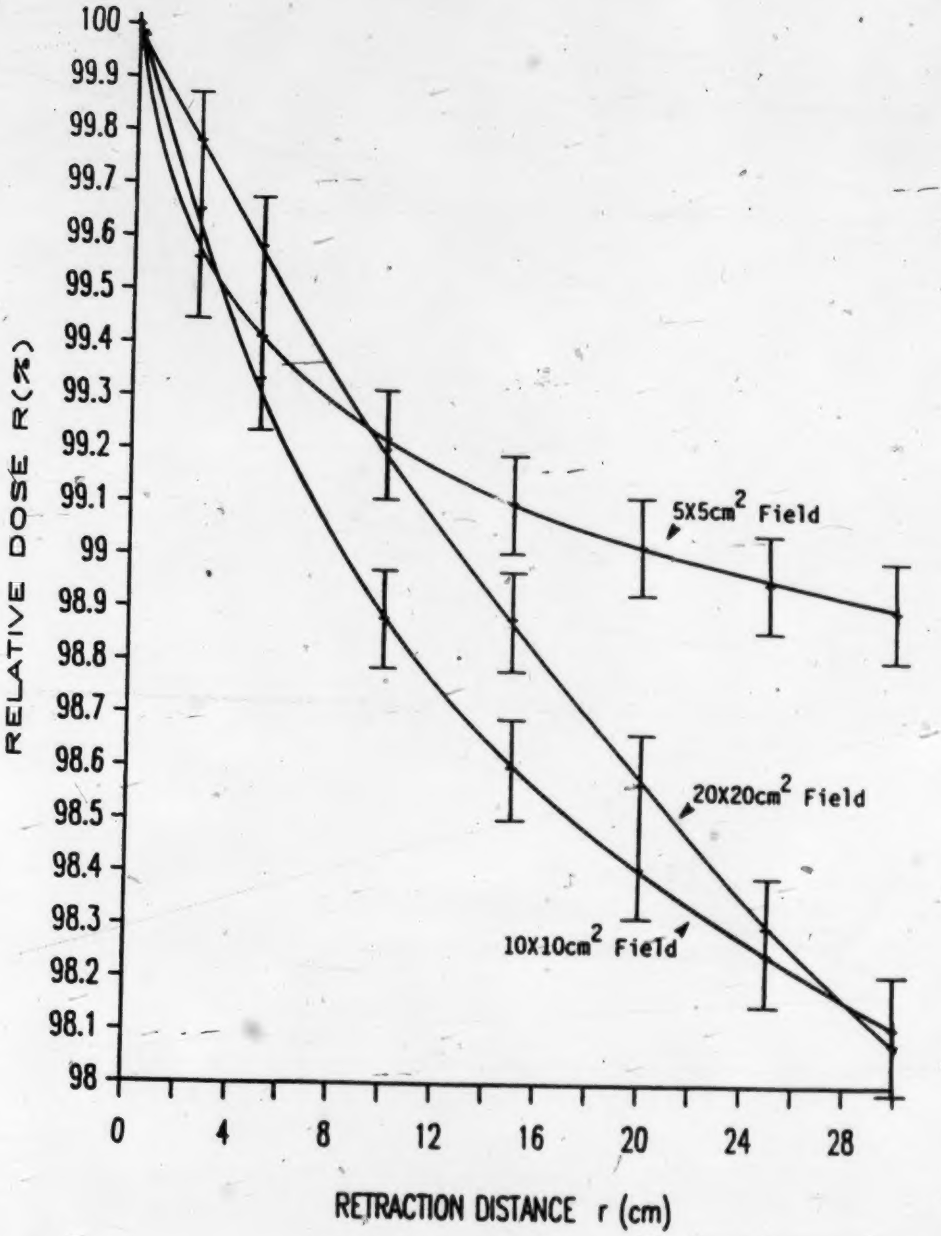

**Figure #84.** A plot of relative dose R(%) at 6cm depth as a function of retraction distance r for a polystyrene compensator of 2cm thickness ($E(\gamma)=15MV$)

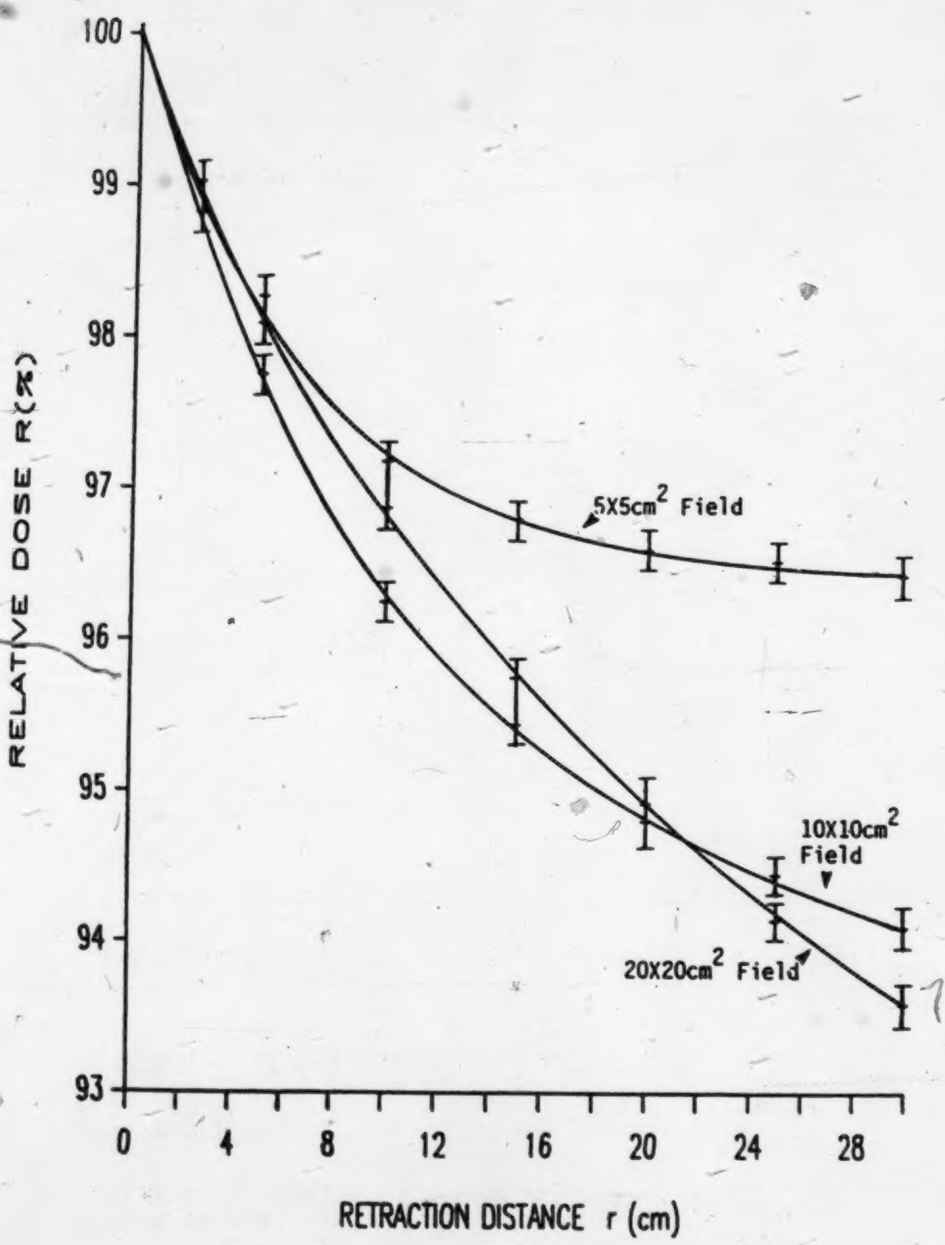

**Figure #85.** A plot of relative dose R(%) at 6cm depth as a function of retraction distance r for a Pb compensator of 6.25mm thickness. (E(γ)=15MV)

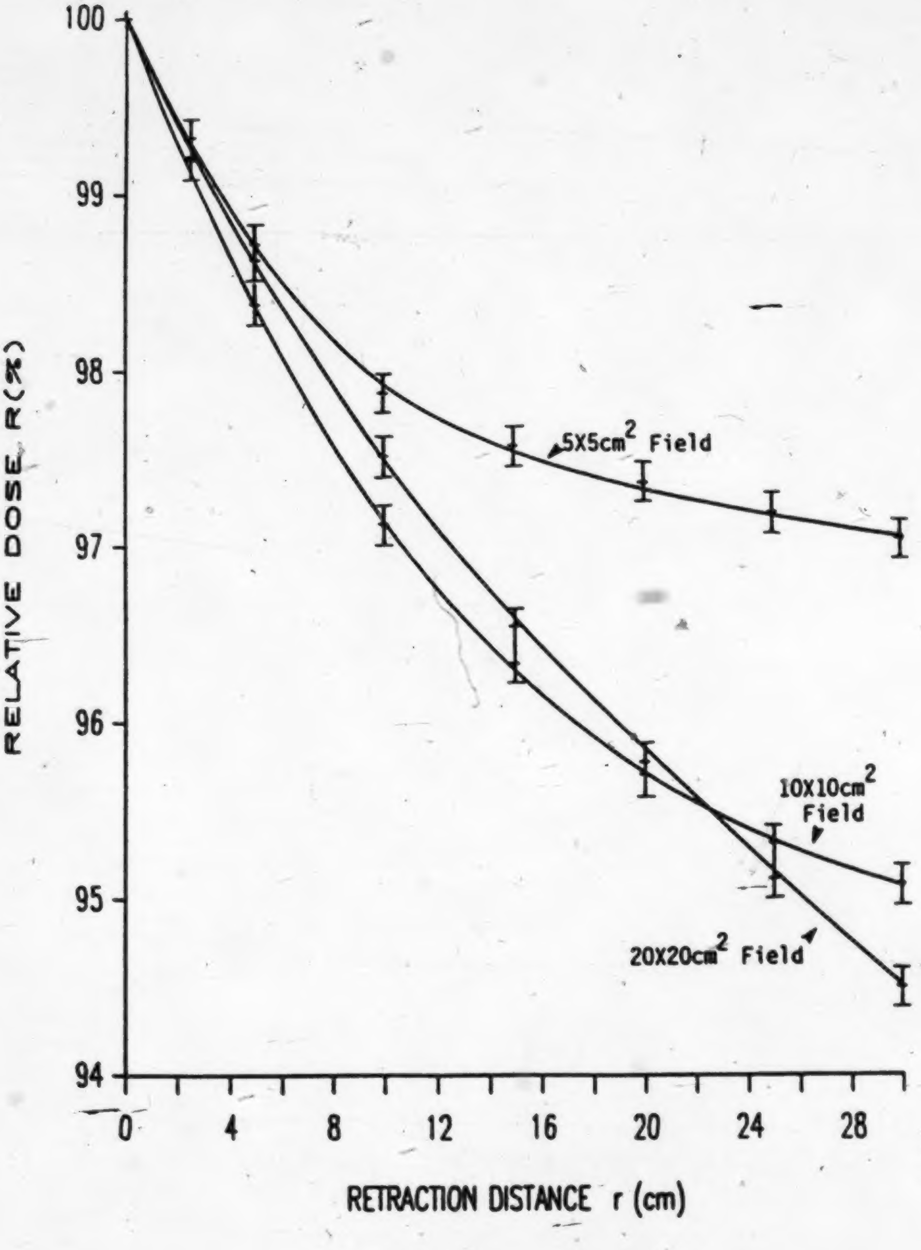

Figure #86. A plot of relative dose R(%) at 6cm depth as a function of retraction distance r for a polystyrene compensator of 7cm thickness (E(γ)=15MV)

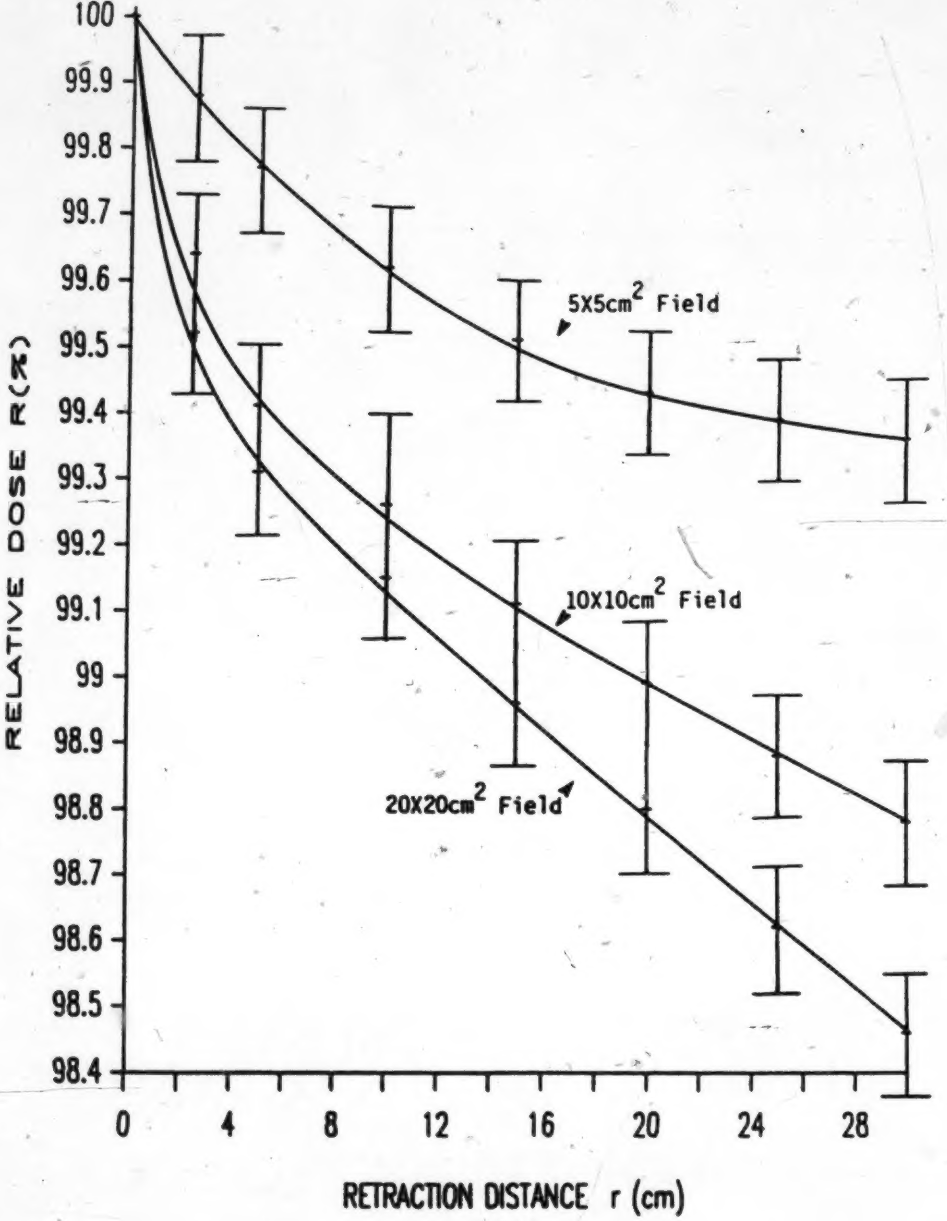

Figure #87. A plot of relative dose R(%) at 12cm depth as a function of retraction distance r for a Pb compensator of 1.75mm thickness. (E(γ)=15MV)

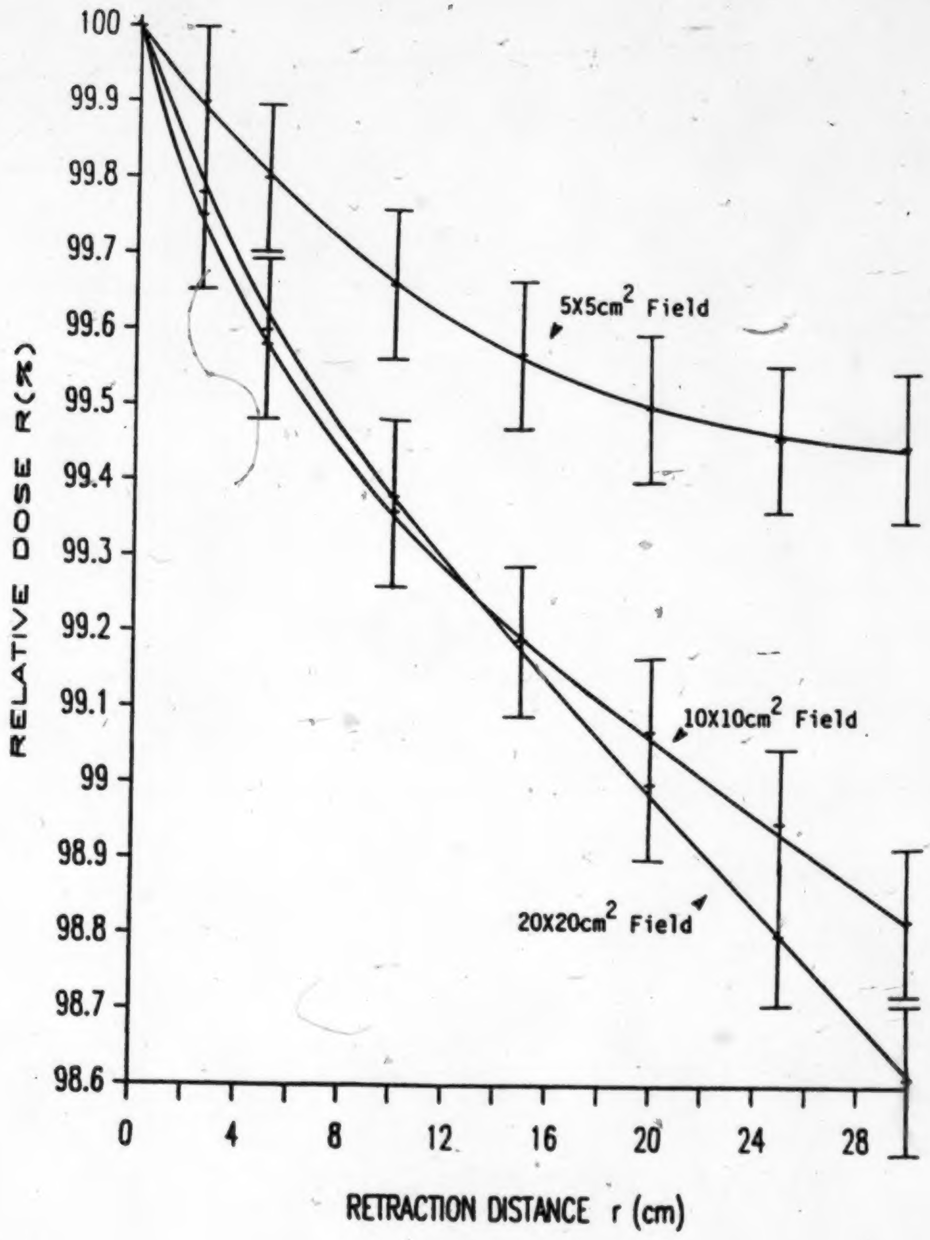

**Figure #88.** A plot of relative dose R(%) at 12cm depth as a function of retraction distance r for a polystyrene compensator of 2cm thickness (E(γ)=15MV)

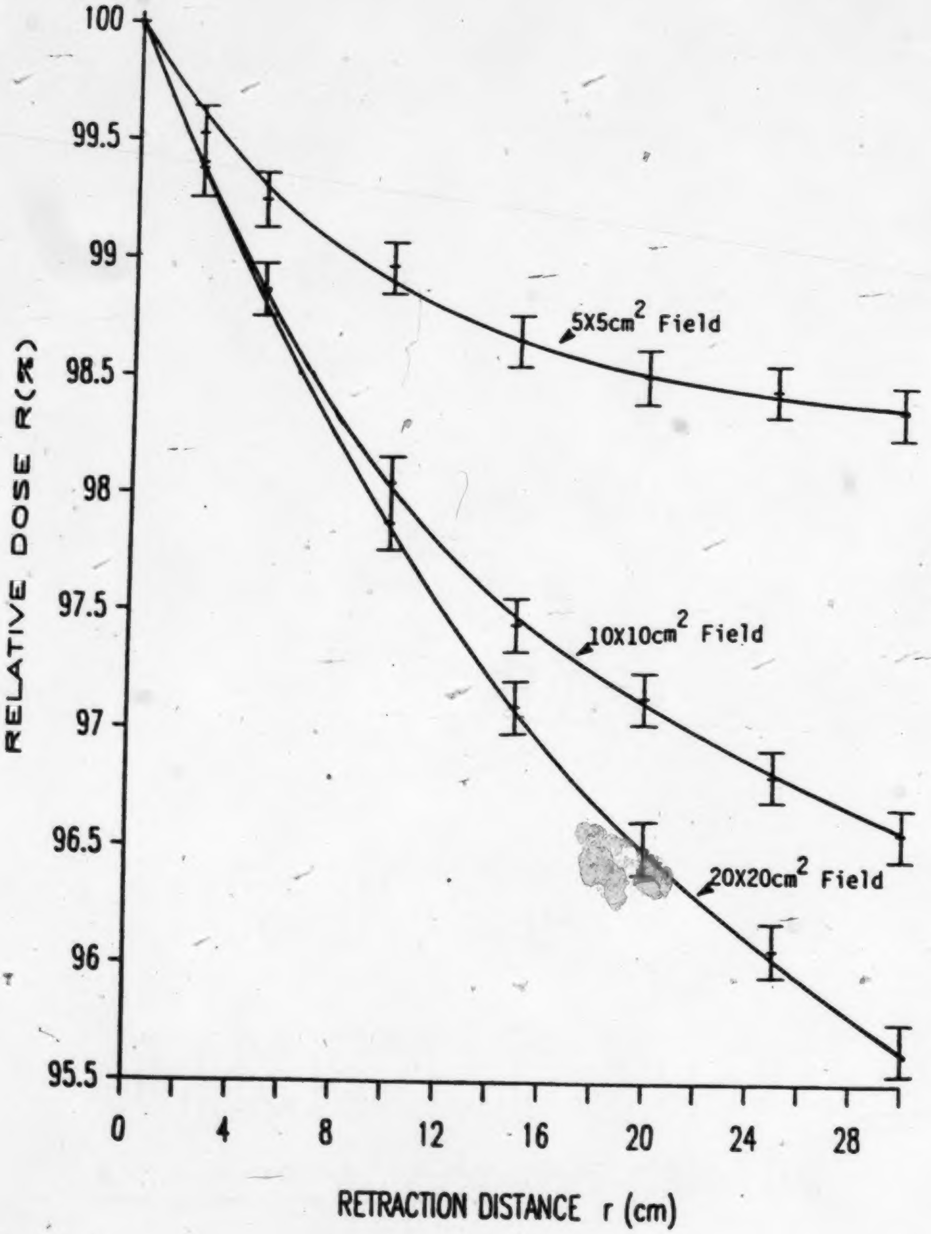

**Figure #89.** A plot of relative dose R(%) at 12cm depth as a function of retraction distance r for a Pb compensator of 6.25mm thickness. ($E(\gamma)$=15MV)

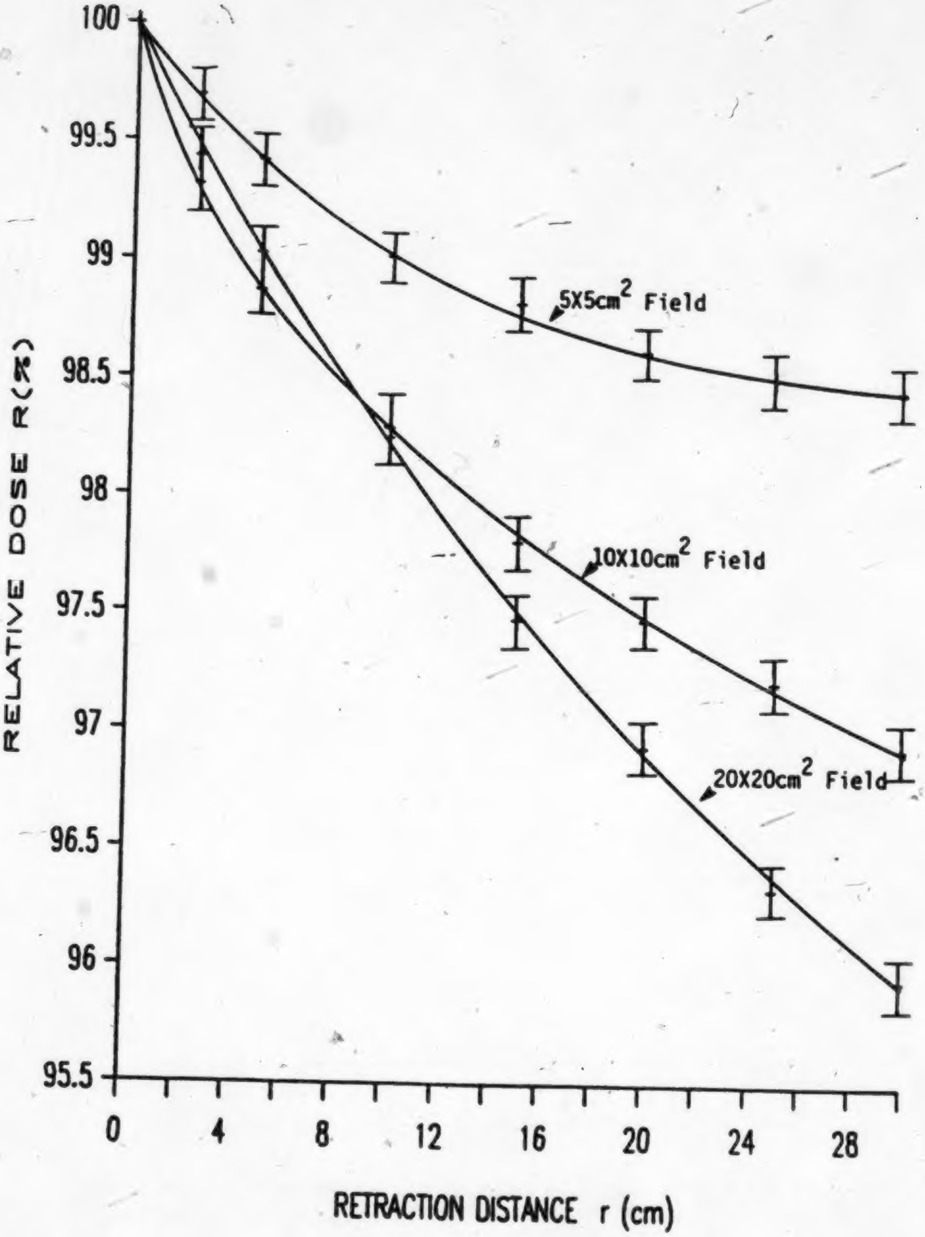

**Figure #90.** A plot of relative dose R(%) at 12cm depth as a function of retraction distance r for a polystyrene compensator of 7cm thickness (E(Y)=15MV) compensator thickness, compensator material, depth of measurement, energy of the incident photons, and retraction distance.

### 5.3.2.1 Analysis

In general it can be seen that the alteration in relative dose at depth is a function of retraction distance, field size, compensator thickness, depth, compensator material, and energy of the incident x-ray beam according to the following:

a) retraction distance
    i) relative dose decreases as retraction distance increases in all cases
b) field size
    i) the $5X5cm^2$ field exhibits the smallest magnitude of reduction and the greatest degree of plateauing out at large retraction distances
    ii) the $10X10^2$ and $20X20cm^2$ fields both exhibit greater reductions than the $5X5cm^2$ field at large retraction distances
    iii) if the trends exhibited between 0 and 30cm retraction distance continue beyond 30cm retraction distance, one would predict that the greatest reduction occurs for the largest field size at very large retraction

distances

c) compensator thickness

   i) both the rate and magnitude of reduction are greatest for the thickest compensator when comparing compensators of the same material

d) depth

   i) both the rate and magnitude of reduction are greatest for the smallest depth and least for the largest depth

   ii) the cross over points occur at larger retraction distances for smaller depths

e) compensator material

   i) at $^{60}$Co and 6MV polystyrene gives greater or equal(within experimental error) reductions than lead except for the 5X5cm$^2$ field at 4cm depth. The amount by which the reduction is greater for polystyrene is smaller at 6MV than at $^{60}$Co. At 15MV lead gives consistently greater reductions than does polystyrene.

   ii) at $^{60}$Co and 6MV the cross over points occur at greater retraction distances for lead than for the comparative thickness polystyrene compensator. At 15MV the cross over points occur at greater or equal (within experimental error) retraction distances for polystyrene.

  - ii) for compensators of the same material the cross over points occur at greater retraction distances for the thinnest polystyrene compensator and the thickest lead compensator

- f) energy
  - i) the energy dependencies as listed above
  - ii) the magnitude and rate of reduction decreases as the energy of the incident x-ray beam increases for the same field size, depth, compensator thickness, and compensator material

Since relative dose is seen to decrease under all circumstances as retraction distance increases, it would seem reasonable to conclude that the main factor in dose reduction is the increase in retraction distance. The dependencies on field size, compensator thickness, compensator material, depth, and incident photon energy would thus be seen as secondary modifications to the primary dependence on retraction distance.

To explain these many dependencies consider the compensator and phantom arrangement of Fig.#91. In this model only Compton scattering will be considered, and of

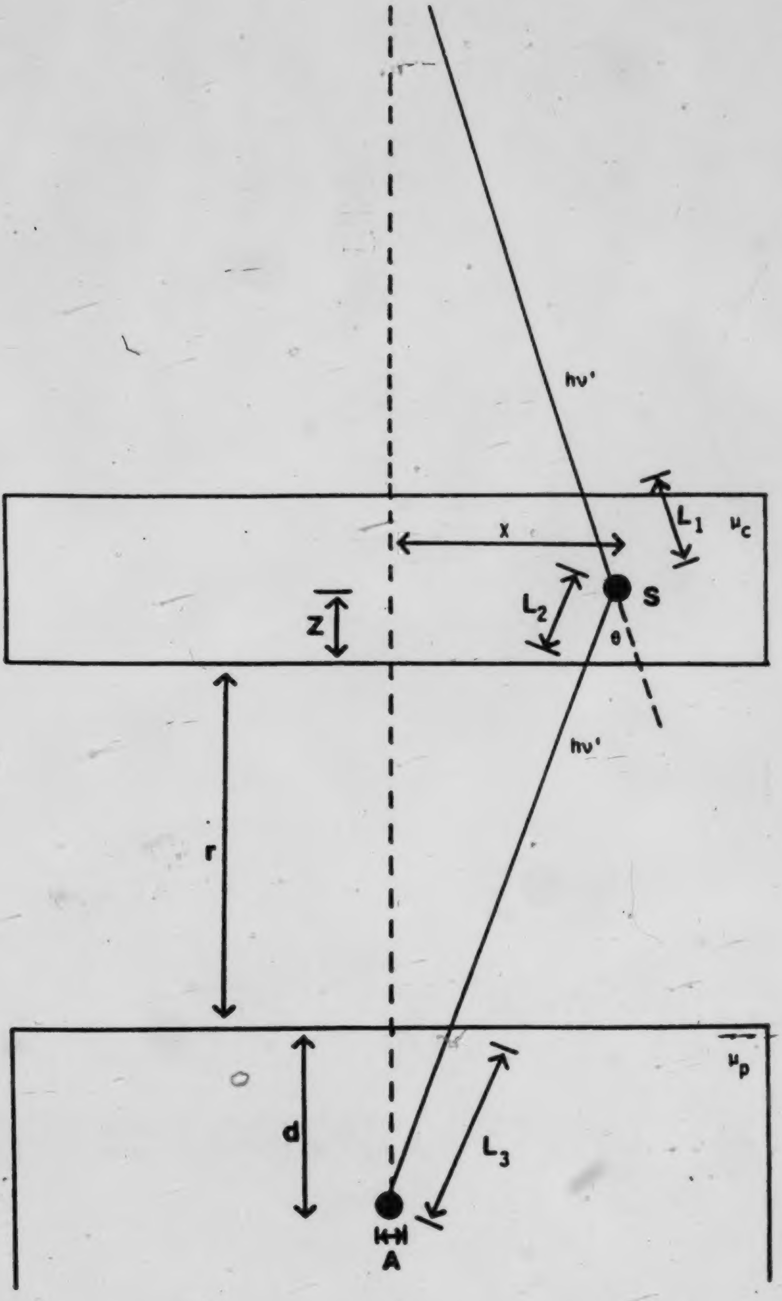
hν'
$L_1$
$\mu_c$
X
S
$L_2$
Z
θ
hν'
r
$\mu_p$
d
$L_3$
A

Figure #91. The dose at a depth d in a phantom due to a single scattering point in a retracted compensator.

that only first order Compton scattering from a single point in the compensator. The photons scattered by this point will be detected in the phanton by a spherical detector at a depth sufficient to ensure the existance of electronic equilibrium. The dose due to the attenuated primary beam along with scatter originating within the phantom will be ignored. In Fig.#91 let n incident photons of energy hν undergo compton scattering at point S in the compensator. A fraction of these photons will be scattered through an angle θ toward the measurement point P in the phantom where they are measured by a probe of cross-sectional area A. In reaching point S in the compensator the incident photons will have been attenuated by an amount

$$e^{-\mu_c(h\nu)L_1} \qquad [5.4]$$

where $\mu_c(h\nu)$ is the linear attenuation coefficient of photons of energy hν in the compensator and $L_1$ is the primary ray path length of the incident photons in the compensator. At point S a number of incident photons will be scattered through an angle θ into unit solid angle dΩ toward the measurement point P according to the Klein-Nishina cross section formula

$$\frac{d_e\sigma}{d\Omega}(\theta,h\nu) = \frac{r_o^2}{2}\,\frac{1+\cos^2\theta}{[1+\alpha(\cos\theta)]^2} + \frac{\alpha^2(1-\cos\theta)^2}{[1+\alpha(1-\cos\theta)]^3}\;\frac{\text{cm}^2}{\text{el sr}} \qquad [5.5]$$

where $r_o = 2.81794 \times 10^{-15}$m is the classical radius of the electron and $\alpha = h\nu/m_o c^2$ where $m_o$ is the rest mass of an electron.

The solid angle dΩ subtended at S by the measuring probe of cross sectional area A will be

$$d\Omega = \frac{A}{(d+r+z)^2 + x^2} \qquad [5.6]$$

and the energy $h\nu'$ of the photons scattered through angle θ toward the probe will be

$$h\nu' = \frac{h\nu}{1+\alpha(\cos\theta)} \qquad [5.7]$$

These scattered photons will be attenuated in the compensator by an amount

$$e^{-\mu_c(h\nu')L_2} \qquad [5.8]$$

where $\mu_c(h\nu')$ is the linear attenuation coefficient of photons of energy $h\nu'$ in the compensator and $L_2$ is the ray path length of these scattered photons in the compensator. These scattered photons will also be attenuated in the phantom by an amount

$$e^{-\mu_p(h\nu')L_3} \qquad [5.9]$$

where $\mu_p(h\nu')$ is the linear attenuation coefficient of photons of energy $h\nu'$ in the phantom and $L_3$ is the ray path length of these scattered photons in the compensator.

Since all measurements were performed at a depth greater than d then electronic equilibrium will exist for all photon energies and the absorbed dose DS measured by the probe at point P due to these scattered photons will be

$$DS = \Phi_s \left.\frac{\mu}{\rho}\right|_{h\nu'} \bar{E}_{ab}(h\nu') \qquad [5.10]$$

where $\Phi_s$ is the fluence of scattered photons of energy $h\nu'$ at point P, $\mu/\rho|_{h\nu'}$ is the mass attenuation coefficient for photons of energy $h\nu'$, and $\bar{E}_{ab}(h\nu')$ is the average energy absorbed from a photon of energy $h\nu'$.

Thus the dose measured at P resulting from the n incident photons at point S in the compensator will be

$$DS = \Phi \frac{d_e\sigma}{d\Omega}(\theta,h\nu) \frac{A}{(d+r+z)^2+x^2} \rho_e dl \left.\frac{\mu}{\rho}\right|_{h\nu} \bar{E}_{ab}(h\nu') \qquad [5.11]$$

$$\times \left( e^{-\mu_c(h\nu)L_1} \, e^{-\mu_c(h\nu')L_2} \, e^{-\mu_p(h\nu')L_3} \right)$$

where $\rho_e$ is the electronic density of the compensator and dl is the linear dimension of the infinitesimal scattering volume surrounding S in the beam direction.

As retraction distance increases two primary changes take place. First, the solid angle decreases and second, the scattering angle also decreases. From these two effects arise all of the other changes which take place due to scattered dose as retraction distance increases. These changes may be categorized as follows:

1) a decrease in solid angle causes a decrease in the dose due to scatter
2) a decrease in scattering angle θ causes:
    a) an increase in the scattering cross section $\frac{d_e\sigma}{d\Omega}(\theta,h\nu)$ and hence an increase in the scattered photon fluence at P
    b) a decrease in the attenuation path lengths $L_1$, $L_2$ , and $L_3$ and hence an increase in scattered photon fluence at P
    c) an increase in scattered photon energy which in turn causes:
        i) a decrease(in general) in the linear attenuation coefficients $\mu_c(h\nu')$ and $\mu_p(h\nu')$ of the scattered photons in both the compensator and the phantom and hence an increase in the scattered photon fluence at P. The linear attenuation coefficient in lead actually rises for energies above ~4MeV and thus in this range an

increase in scattered photon energy would act to decrease the scattered photon fluence at P

ii) a decrease(except for Pb above 4Mev) in the mass attenuation coefficient of the scattered photons at P and hence this would act to decrease the dose at P due to scattered photons

iii) an increase in the overall energy absorbed $\bar{E}_{ab}$ at P and hence this acts to increase the absorbed dose due to scattered photons at P

There are thus a number of competing factors which act to change the dose at P due to first order scattering in the compensator from the point S. To properly determine the dose at P due to scattering in the compensator, equation [5.11] would have to be integrated over the irradiated volume of the compensator and first and higher order scattering would have to be taken into account in both the compensator and the phantom. Also the dose due to scattered photons from the compensator arising from other mechanisms such as fluorescence, bremsstrahlung, and positron annihilation should be considered. Such a calculation is described later, using Monte Carlo methods(see section 5.5).

In order to see more clearly the functional dependence of relative dose on the factors of retraction distance, field size, depth, compensator thickness, compensator material, and incident photon energy, consider the following simplified 2-dimensional pedagogic model as illustrated in in Fig.#92. Consider first-order scattering only and allow the volume of the compensator irradiated by the 5X5cm$^2$ field to be treated as if all of the scattered photons generated in this volume originated at one point, $S_5$ located at midplane in in the compensator half way between the central beam axis and the edge of the 5x5cm$^2$ field. A 10X10cm$^2$ field will irradiate the same volume as the 5X5cm$^2$ field plus the additional volume between the outer edge of the 5X5cm field and the outer edge of the 10X10cm$^2$ field. Allow the scatter due to this extra volume for the 10X10cm field to be treated as if it all originated at the point $S_{10}$ located at midplane in the compensator half way between the outer edge of the 5X5cm$^2$ field and the outer dege of the 10X10cm$^2$ field. Also allow the extra scatter from the 20X20cm$^2$ field to be treated as if it all originated at the point $S_{20}$ located at midplane in the compensator half way between the outer edge of the 10X10cm$^2$ field and the outer edge of the 20X20cm$^2$ field.

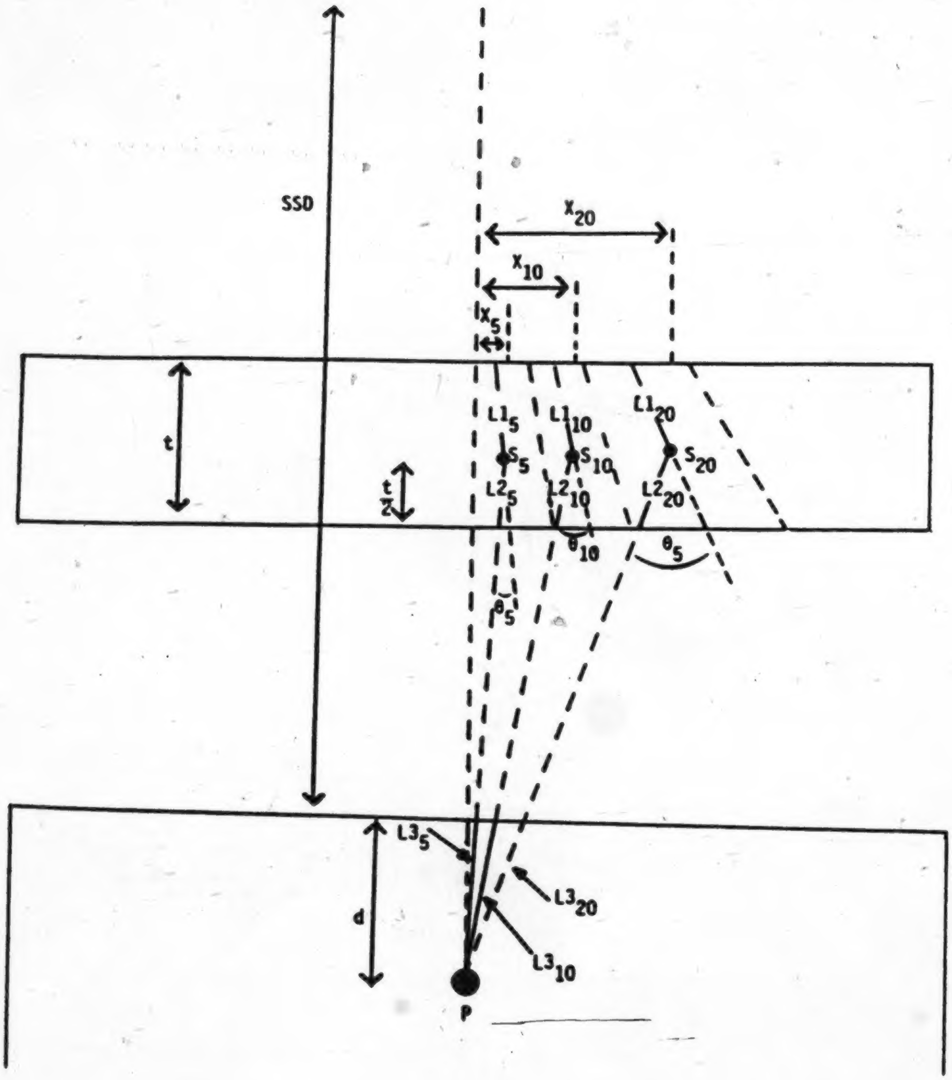
SSD
X20
X10
X5
t
t/2
L15
L110
L120
S5
S10
S20
L25
L210
L220
θ10
θ5
θ5
L35
L320
L310
d
P

Figure #92. Diagramatic representation of the Pedagogic model.

In Fig.#92 $L1_5$, $L1_{10}$, and $L1_{20}$ are the ray path lengths of incident photons in the compensator which will be scattered at points $S_5$, $S_{10}$, and $S_{20}$ respectively. The scattered photons from points $S_5$, $S_{10}$, and $S_{20}$ which reach the measuring point P will be scattered through angles $\theta_5$, $\theta_{10}$, and $\theta_{20}$ respectively. These scattered photons from points $S_5$, $S_{10}$, and $S_{20}$ will be attenuated in the compensator as they follow ray paths $L2_5$, $L2_{10}$, and $L2_{20}$ respectively. In the phantom these scattered photons from points $S_5$, $S_{10}$, and $S_{20}$ will be attenuated as they follow ray paths $L3_5$, $L3_{10}$, and $L3_{20}$ respectively. The measuring point P is a distance d below the phantom surface which is a distance SSD from the point source of x-rays. The compensator has a thickness of t.

The dose measured at P along the central beam axis for irradiation by a $5X5cm^2$ field will consist of the dose due to primary photons attenuated by the compensator plus scatter from the primary beam in the phantom plus scatter from point $S_5$ in the compensator. For flat slab compensators such as are used here the scatter in the phantom will be unaltered by compensator retraction and thus for the purpose of simplification the dose due to scatter in the phantom will be considered as a constant component of the total dose. Thus the dose $D_5$ at point P for a $5X5cm^2$ field will consist of the dose due to primary attenuated photons plus dose due to scattered photons from point $S_5$ in the compensator. The dose $D_{10}$ at P for a $10X10cm^2$ field will consist of the dose due to primary attenuated photons plus the dose from scattered photons from point $S_5$ plus the dose due to the extra scattered photons from point $S_{10}$. Likewise the dose at P for a $20X20cm^2$ field will consist of the dose due to primary attenuated photons plus the dose due to scattered photons originating from points $S_5$, $S_{10}$, and $S_{20}$. If the photon fluence on the phantom surface in the absence of the compensator is Φ and the probe at P presents a unit cross sectional area to the beam then with the compensator present the dose at P due to primary attenuated photons will be

$$D(Prim) = \Phi \frac{\mu}{\rho} \bar{E}_{ab}(h\nu)e^{-\mu_c(h\nu)t}\ e^{-\mu_p(h\nu)d}\ \frac{(SSD)^2}{(SSD+d)^2} \qquad [5.12]$$

where $\mu_c(h\nu)$ and $\mu_p(h\nu)$ are the linear attenuation coefficients of the incident photons in the compensator and phantom respectively.

The number of photons incident on the compensator area irradiated by the $5X5cm^2$ field will be

$$N_5 = \Phi 5^2 = 25\Phi \qquad [5.13]$$

and the number of photons incident on the the extra areas irradiated by the $10X10^2$ and $20X20cm^2$ fields will be

$$N_{10} = \Phi(10^2-5^2) = 75\Phi = 3N_5$$

$$N_{20} = \Phi(20^2-10^2) = 300\Phi = 12N_5 \qquad [5.14]$$

respectively. Thus the dose at P due to scatter from $S_5$ at a retraction distance r will be

$$DS_5(r) = 25\Phi \frac{d_e\sigma}{d\Omega}(\theta_5,h\nu) \frac{\rho_e t}{(d+r+t/2)^2+X_5^2} \left.\frac{\mu}{\rho}\right|_{h\nu'} \overline{E}_{ab}(h\nu') \qquad [5.15]$$

$$\times \left( e^{-\mu_c(h\nu)L1_5} e^{-\mu_c(h\nu')L2_5}\, e^{-\mu_p(h\nu')L3_5} \right]$$

and the dose at P due to scatter from $S_{10}$ and $S_{20}$ will be

$$DS_{10}(r) = 75\Phi \frac{d_e\sigma}{d\Omega}(\theta_{10},h\nu) \frac{\rho_e t}{(d+r+t/2)^2+X_{10}^2} \left.\frac{\mu}{\rho}\right|_{h\nu'} \overline{E}_{ab}(h\nu')$$

$$\times \left( e^{-\mu_c(h\nu)L1_{10}}\, e^{-\mu_c(h\nu')L2_{10}}\, e^{-\mu_p(h\nu')L3_{10}} \right] \qquad [5.16]$$

$$DS_{20}(r) = 300\Phi \frac{d_e\sigma}{d\Omega}(\theta_{20},h\nu) \frac{\rho_e t}{(d+r+t/2)^2+X_{20}^2} \left.\frac{\mu}{\rho}\right|_{h\nu'} \overline{E}_{ab}(h\nu')$$

$$\times \left( e^{-\mu_c(h\nu)L1_{20}}\, e^{-\mu_c(h\nu')L2_{20}}\, e^{-\mu_p(h\nu')L3_{20}} \right]$$

respectively where $\rho_e$ is the electronic density of the compensator.

Thus the dose at P will be

$$\begin{aligned} DP_5(r) &= D(prim) + DS_5(r) \\ DP_{10}(r) &= D(prim) + DS_{10}(r) \qquad [5.17] \\ DP_{20}(r) &= D(prim) + DS_{20}(r) \end{aligned}$$

for the 5X5, 10X10, and 20X20cm$^2$ fields respectively, and the relative dose at a given retraction distance will be

$$R_5(r) = \frac{DP_5(r)}{DP_5(r=0)} = \frac{D(prim)+DS_5(r)}{D(prim)+DS_5(r=0)} \qquad [5.18]$$

$$R_{10}(r) = \frac{DP_{10}(r)}{DP_{10}(r=0)} = \frac{D(prim)+DS_5(r)+DS_{10}(r)}{D(prim)+DS_5(r=0)+DS_{10}(r=0)} \qquad [5.19]$$

$$R_{20}(r) = \frac{DP_{20}(r)}{DP_{20}(r=0)} = \frac{D(prim)+DS_5(r)+DS_{10}(r)+DS_{20}(r)}{D(prim)+DS_5(r=0)+DS_{10}(r=0)+DS_{20}(r=0)} \qquad [5.20]$$

for the 5X5, 10X10, and 20X20cm$^2$ fields respectively.

Having thus reduced the compensator to 3 distinct scattering points it remains to analyse the manner in which the dose at P from these three points is altered by field size, compensator thickness, compensator material, depth, retraction distance, and energy of the incident photons. As discussed earlier the change in dose due to scatter arises from two main causes as retraction distance increases: the change in the solid angle subtended by the probe with respect to the point of scatter, and the change in scattering angle.

The following graphs help to visualize these effects. Fig.#93 is a plot of the Klein-Nishina cross section as a function of scattering angle for the three energies employed. The energy of $^{60}$Co is taken to be 1.25Mev and the effective or mean energies of the 6MV and 15MV beams are taken to be 2MeV and 5MeV respectively. Fig.#94 is a plot of the energy $h\nu'$ of a scattered photon as a function of scattering angle for the three energies. Fig.#95 and Fig.#96 are plots of the linear attenuation coefficients of polystyrene and lead respectively as a function of scattering angle for the three energies. Fig.#97 is a plot of the average energy absorbed $\bar{E}_{ab}$ as a function of scattering angle for polystyrene for the three energies and Fig.#98 is a plot of the product $\mu/\rho|_{h\nu}\,\bar{E}_{ab}(h\nu')$ of the mass attenuation coefficient and the average energy absorbed for polystyrene as a function of scattering angle.

Of all the factors involved only the reduction in solid angle and the decrease in mass attenuation

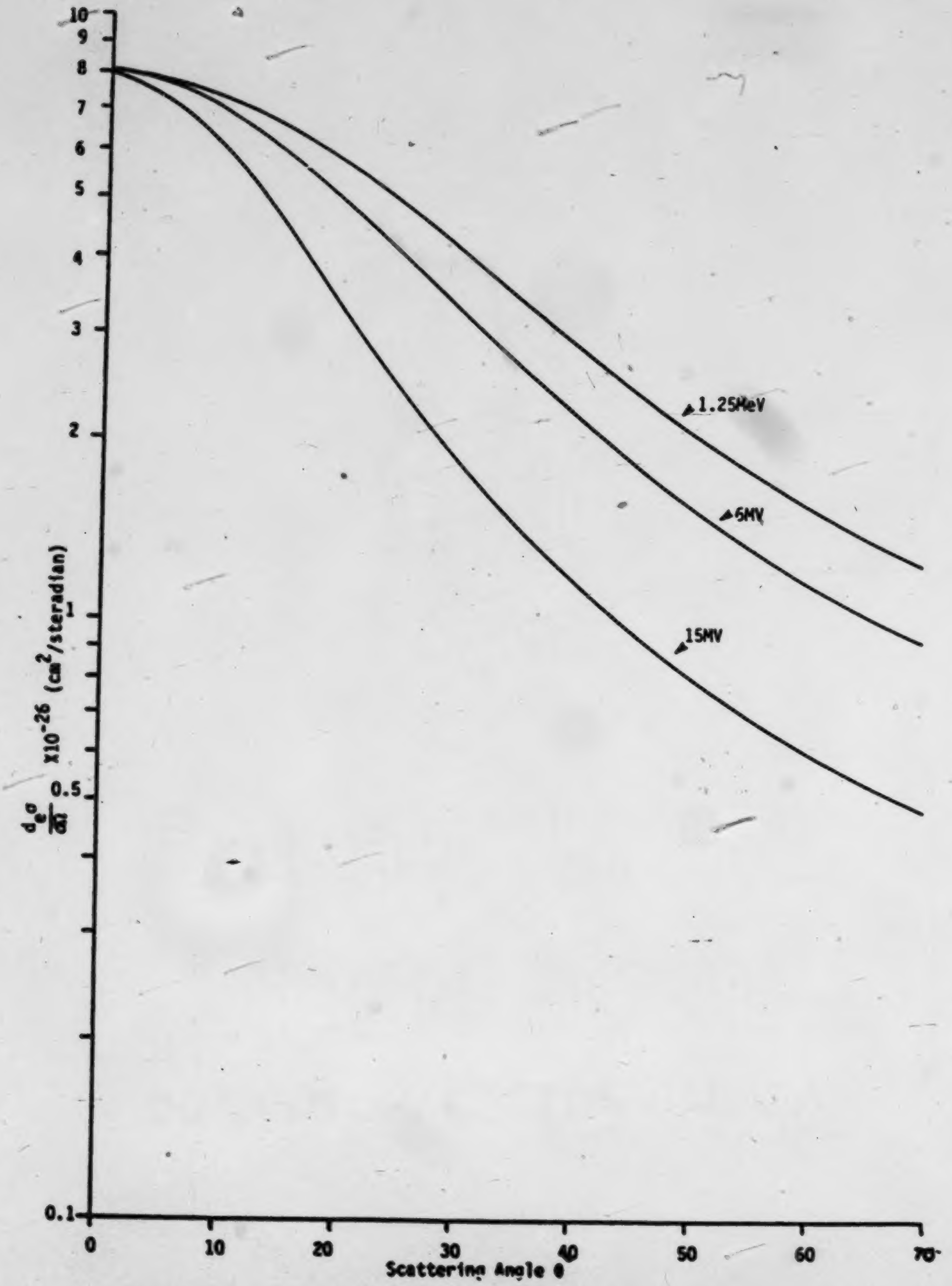

Figure #93. A plot of the Klein-Nishina cross section as a function of scattering angle for incident photon energies of $^{60}$Co 6MV, and 15MV.

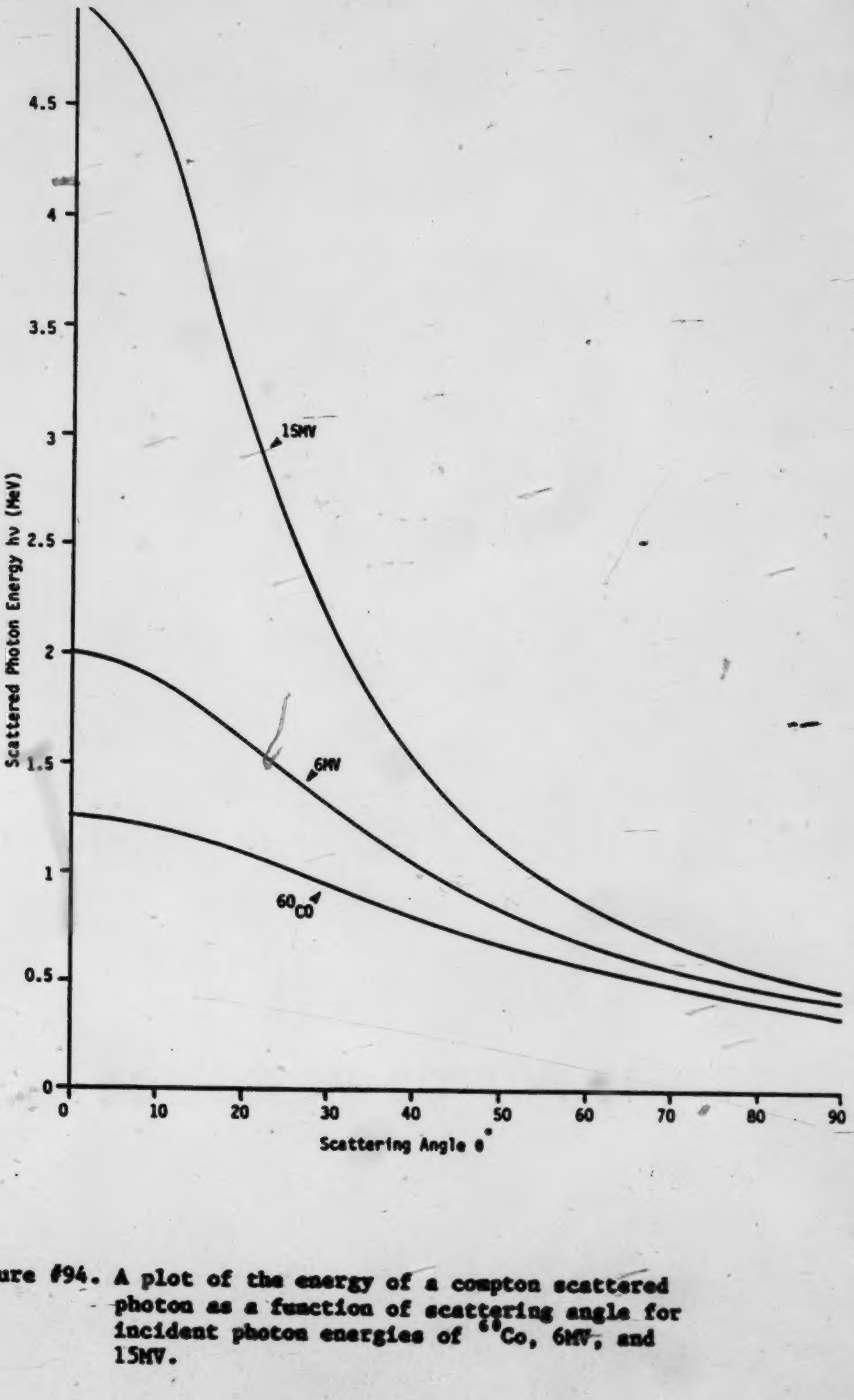

Figure #94. A plot of the energy of a compton scattered photon as a function of scattering angle for incident photon energies of $^{60}$Co, 6MV, and 15MV.

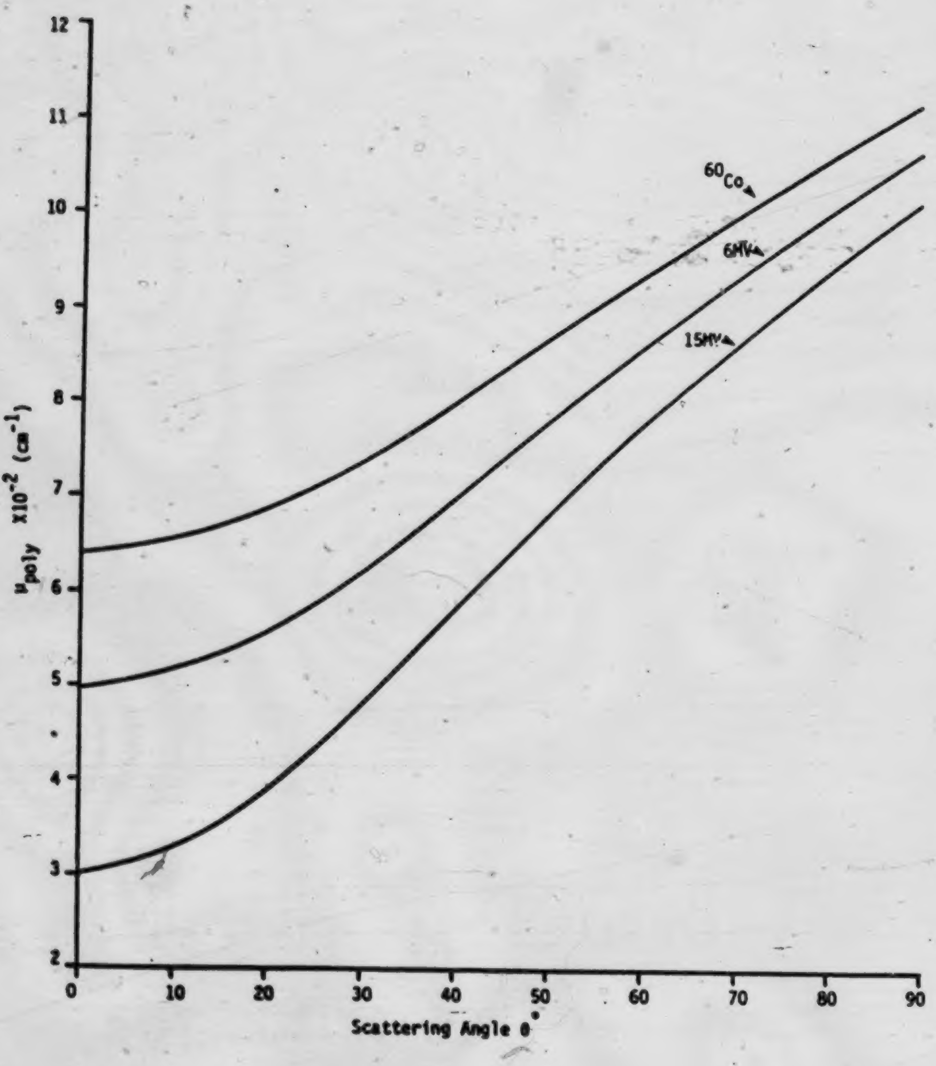

**Figure #95.** A plot of the linear attenuation coefficient of polystyrene as a function of photon scattering angle for incident photon energies of $^{60}$Co, 6MV, and 15MV.

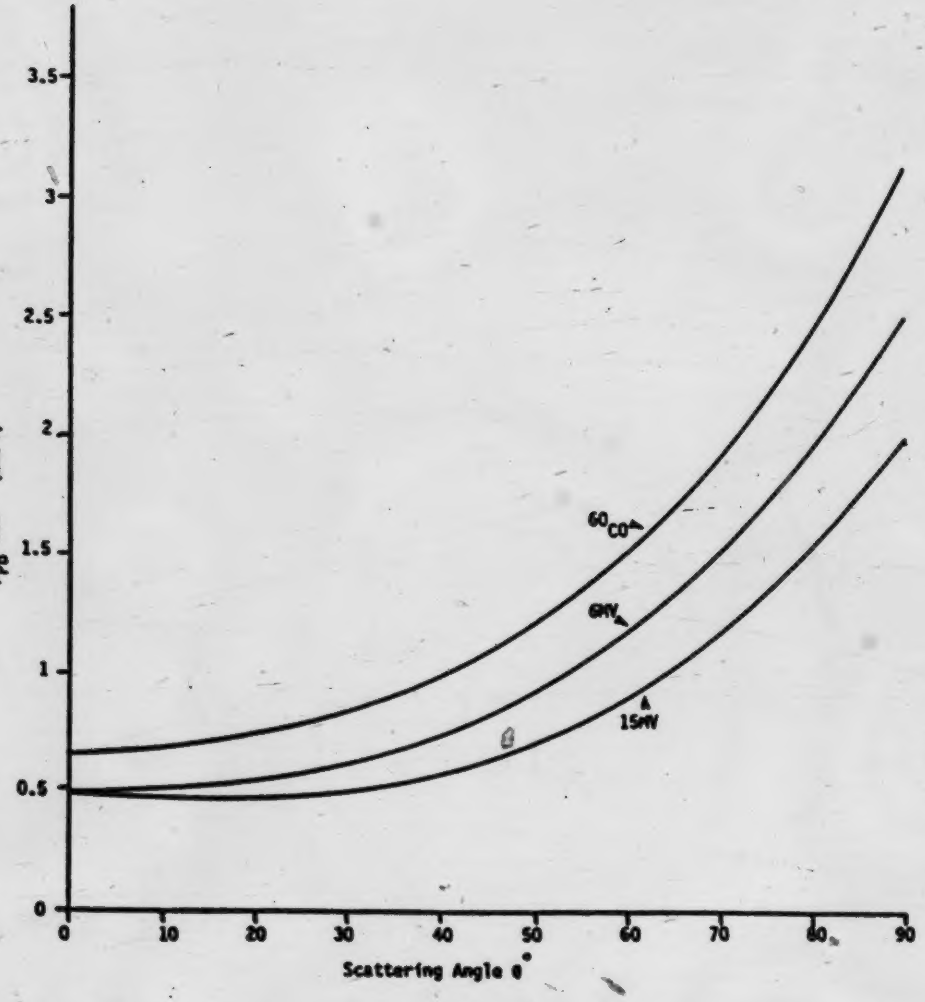

**Figure #96.** A plot of the linear attenuation coefficient of lead as a function of photon scattering angle for incident photon energies of $^{60}$Co, 6MV, and 15MV.

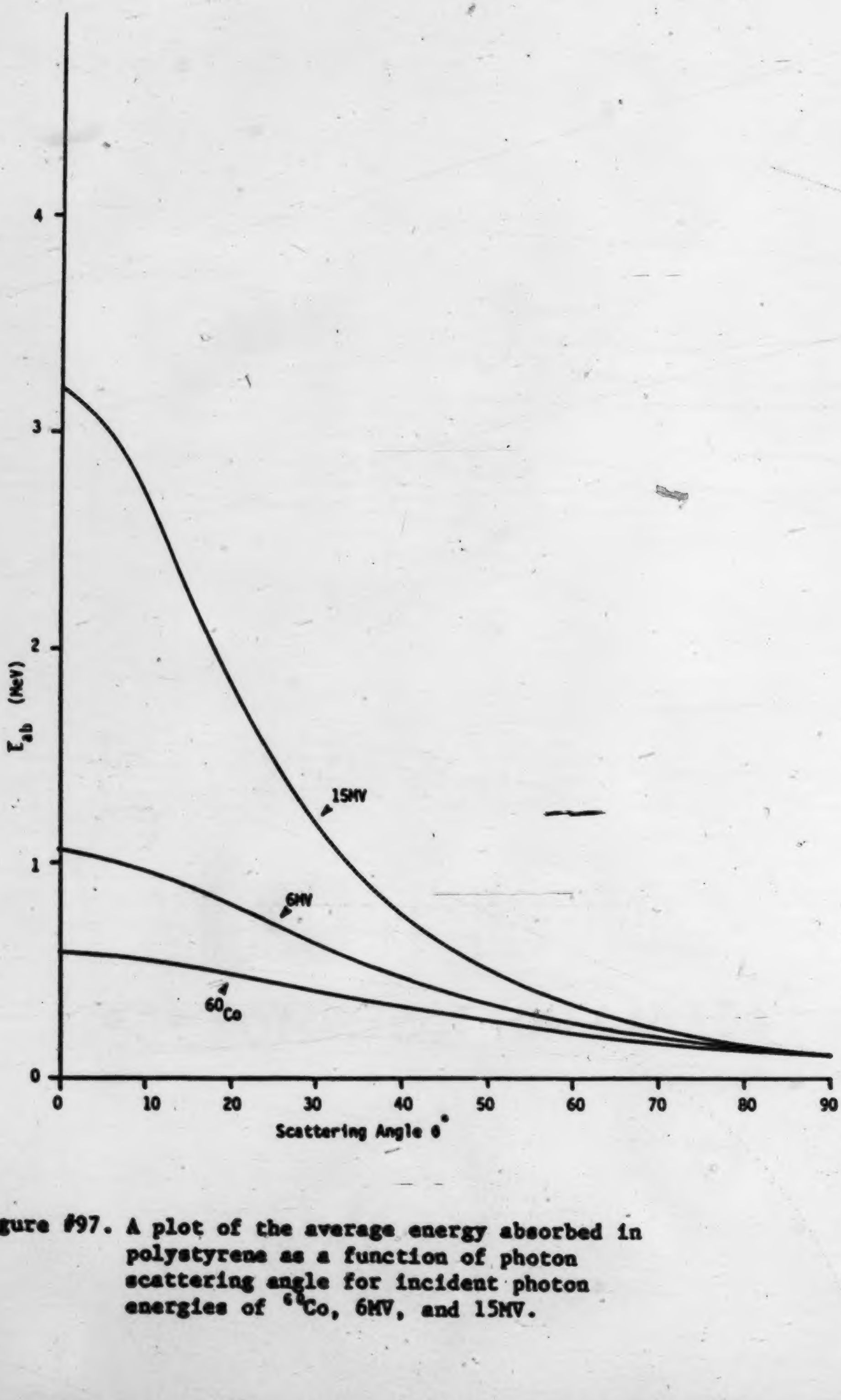

Figure #97. A plot of the average energy absorbed in polystyrene as a function of photon scattering angle for incident photon energies of $^{60}Co$, 6MV, and 15MV.

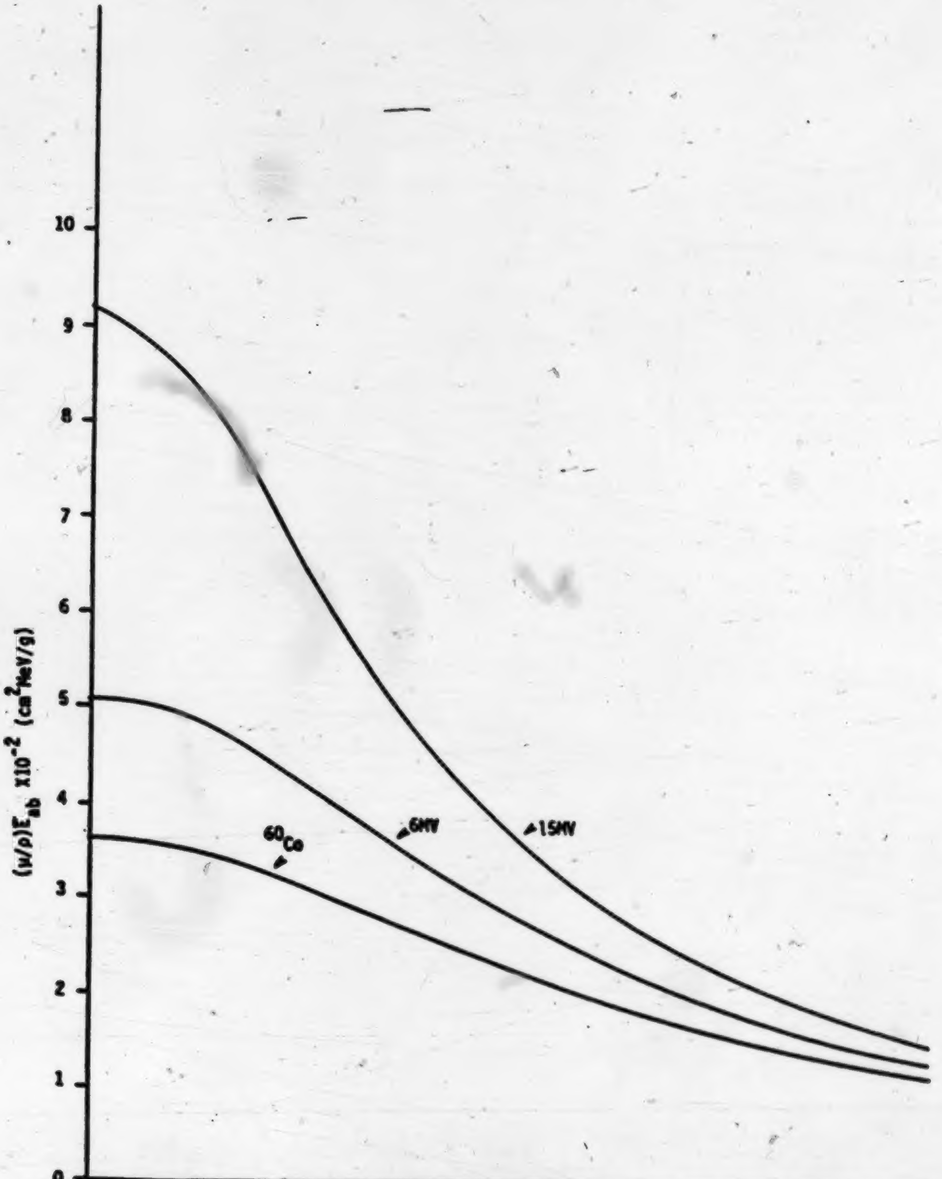

Figure #98. A plot of the product of the mass attenuation coefficient and the average energy absorbed in polystyrene as a function of photon scattering angle for incident photon energies of $^{60}$Co, 6MV, 15MV.

coefficient cause the relative dose to decrease as retraction distance increases. The product of the mass attenuation coefficient and the average energy absorbed increases as retraction distance increases, as Fig.#98 shows, and thus we will regard the solid angle as the only factor causing the dose due to scatter from the compensator to decrease as retraction distance increases. As experimental results clearly show, the relative dose always decreases as retraction distance increases and hence the other factors serve to modify the rate and magnitude of reduction at any given retraction distance.

The observation that if the general trends exhibited by the data continue for retraction distances larger than 30cm one would eventually observe the largest field size exhibiting the largest reduction in relative dose may be explained by examining equations 5.18, 5.19, and 5.20. These equations give the relative dose for each field size as

$$R_5(r) = \frac{DP_5(r)}{DP_5(r=0)} = \frac{D(prim)+DS_5(r)}{D(prim)+DS_5(r=0)}$$

$$R_{10}(r) = \frac{DP_{10}(r)}{DP_{10}(r=0)} = \frac{D(prim)+DS_5(r)+DS_{10}(r)}{D(prim)+DS_5(r=0)+DS_{10}(r=0)} \qquad [5.21]$$

and

$$R_{20}(r) = \frac{DP_{20}(r)}{DP_{20}(r=0)} = \frac{D(prim)+DS_5(r)+DS_{10}(r)+DS_{20}(r)}{D(prim)+DS_5(r=0)+DS_{10}(r=0)+DS_{20}(r=0)}$$

for the 5X5, 10X10, and 20X20cm$^2$ fields respectively. At very large retraction distances the solid angle for all three scattering points will be effectively zero and the scatter from each point reaching the probe at P will have been reduced to zero. This being the case one has

$$DS_5(r) = DS_{10}(r) = DS_{20}(r) = 0 \qquad [5.22]$$

and equations 5.21 become

$$R_5(r) = \frac{D(prim)}{D(prim)+DS_5(r=0)}$$

$$R_{10}(r) = \frac{D(prim)}{D(prim)+DS_5(r=0)+DS_{10}(r=0)+DS_{20}(r=0)} \qquad [5.23]$$

$$R_{20}(r) = \frac{D(prim)}{D(prim)+DS_5(r=0)+DS_{10}(r=0)+DS_{20}(r=0)}$$

and comparing equations 5.23 one finds

$$R_{20} < R_{10} < R_5 \qquad [5.24]$$

and thus at very large retraction distances one would expect to see the greatest reduction in relative dose for the largest field and the smallest reduction for the smallest field.

The reason that the largest field does not always exhibit the greatest reduction in relative dose for smaller retraction distances lies in the rate of change of the solid angle and both the magnitude and rate of change of the scattering angle of $S_{20}$. For a given depth the rate of change of the solid angle is greatest for $S_5$ and least for $S_{20}$ and this difference is greater for smaller retraction distances. Thus for small retraction distances the more rapidly decreasing solid angle for $S_5$ may cause the 5X5cm$^2$ field to exhibit a greater magnitude and rate of reduction in relative dose than that of the 20X20cm$^2$ field before leveling out at a smaller reduction than the 20x20cm$^2$ field. Whether this is seen or not depends on the relative magnitude of the rate of change of the solid angles, which is in turn dependent on the thickness of the compensators and the depth of measurement. The relative rate of reduction of the solid angle of $S_5$(or $S_{10}$ for that matter) in comparison to that of $S_{20}$ will be greatest for shallow depths and thinner compensators and hence one would expect that if cross over points do occur they will occur at greater retraction distances for shallower depths of measurement and thinner compensators.

This then explains the observed dependence of the cross over points on depth for both types of compensator materials and also the dependence of the cross over points on compensator thickness for the polystyrene compensators but not for the lead compensators. The opposite effect is observed for Pb in that the cross over points occur at larger retraction distances for the compensator of greater thickness. For lead the change between the solid angle for the scattering points of thicker and thinner compensators is much less than that for polystyrene compensators due to the much smaller thickness of the lead compensators. To understand the thickness dependence of the cross over points for lead one must consider the change in attenuation pathlength $L2_{20}$ for $S_{20}$ and $L2_5$ for $S_5$. Both $L2_5$ and $L2_{20}$ will decrease as retraction distance increases but $L2_{20}$ will decrease by a far greater amount due to the greater change in scattering angle for $S_{20}$ as compared to $S_5$. For a thicker Pb compensator the scattering angles are virtually the same as those for the thinner compensator and the magnitude of change of $L2_5$ and $L2_{20}$ for the thicker compensator will be proportionalely greater than for the thinner compensator. If the decrease in $L2_5$ is a and the decrease in $L2_{20}$ is b (where b>a always) in the thinner compensator then for a compensator which is c times as thick(for lead) the changes in in $L2_5$ and $L2_{20}$ will be ac and bc respectively.

If the path lengths $L2_5$ and $L2_{20}$ are $L2_5(r=0)$ and $L2_{20}(r=0)$ at zero retraction and $L2_5(r)$ and $L2_{20}(r)$ at a retraction distance r, then the ratio of retracted to non-retracted attenuation along each pathlength will be

$$\frac{e^{-\mu L_5(r)}}{e^{-\mu L_5(r=0)}} > 1$$

and [5.25]

$$\frac{e^{-\mu L_{20}(r)}}{e^{-\mu L_{20}(r=0)}} > 1$$

Since the change in $L2_{20}$ is b and the change in $L2_5$ is a and b>a then one has

$$\frac{e^{-\mu L_{20}(r)}}{e^{-\mu L_{20}(r=0)}} > \frac{e^{-\mu L_5(r)}}{e^{-\mu L_5(r=0)}} \qquad [5.25a]$$

and therefore

$$\frac{\left(\dfrac{e^{-\mu L_{20}(r)}}{e^{-\mu L_{20}(r=0)}}\right)}{\left(\dfrac{e^{-\mu L_5(r)}}{e^{-\mu L_5(r=0)}}\right)} > 1 \qquad [5.25b]$$

Now for the thicker compensator(c times thicker) equations [5.25] become

$$\frac{e^{-\mu c L_5(r)}}{e^{-\mu c L_5(r=0)}} > 1$$

and [5.26]

$$\frac{e^{-\mu c L_{20}(r)}}{e^{-\mu c L_{20}(r=0)}} > 1$$

$$\frac{e^{-\mu c L_{20}(r)}}{e^{-\mu c L_{20}(r=0)}} > 1$$

or

$$\left(\frac{e^{-\mu L_5(r)}}{e^{-\mu L_5(r=0)}}\right)^c > 1$$

and [5.26a]

$$\left(\frac{e^{-\mu L_{20}(r)}}{e^{-\mu L_{20}(r=0)}}\right)^c > 1$$

but

$$\left(\frac{e^{-\mu L_5(r)}}{e^{-\mu L_5(r=0)}}\right)^c > \frac{e^{-\mu L_5(r)}}{e^{-\mu L_5(r=0)}}$$

and [5.26b]

$$\left(\frac{e^{-\mu L_{20}(r)}}{e^{-\mu L_{20}(r=0)}}\right)^c > \frac{e^{-\mu L_{20}(r)}}{e^{-\mu L_{20}(r=0)}}$$

Thus for the thicker compensator, equation [5.25b] becomes

$$\frac{\left(\dfrac{e^{-\mu L_{20}(r)}}{e^{-\mu L_{20}(r=0)}}\right)^c}{\left(\dfrac{e^{-\mu L_5(r)}}{e^{-\mu L_5(r=0)}}\right)^c} = \left(\frac{\dfrac{e^{-\mu L_{20}(r)}}{e^{-\mu L_{20}(r=0)}}}{\dfrac{e^{-\mu L_5(r)}}{e^{-\mu L_5(r=0)}}}\right)^c \qquad [5.26c]$$

Therefore one has

$$\left(\frac{\dfrac{e^{-\mu L_{20}(r)}}{e^{-\mu L_{20}(r=0)}}}{\dfrac{e^{-\mu L_{5}(r)}}{e^{-\mu L_{5}(r=0)}}}\right)^{c} > \left(\frac{\dfrac{e^{-\mu L_{20}(r)}}{e^{-\mu L_{20}(r=0)}}}{\dfrac{e^{-\mu L_{5}(r)}}{e^{-\mu L_{5}(r=0)}}}\right)$$

and thus the magnitude of change in the attenuation along path length $L2_{20}$ as compared to that along $L2_5$ will be greater in the thicker compensator than the in the thinner compensator. This will decrease the rate of dose reduction for $S_{20}$ as compared to that of $S_5$ in the thicker compensator much greater than in the thinner compensator and thus the cross over points will occur at greater retraction distances for the thicker lead compensator.

This effect exists for the polystyrene compensators as well but it is masked by the much greater difference between the solid angles and the scattering angles for $S_5$ and $S_{20}$ for thicker and thinner polystyrene compensators. The effect of the much greater difference in scattering angles for $S_{20}$ in the polystyrene compensators can be seen by examining Fig. #93, #94 , #95, #96, #97, and #98. The smaller scattering angle for S at zero retraction in the thicker polystyrene compensator means a smaller increase in $d_e\sigma/d\Omega$ , a smaller increase in the energy of the scattered photons, a smaller decrease in the linear attenuation coefficients $\mu_c(h\nu')$ and $\mu_p(h\nu')$ and a smaller increase in the product of $(\mu/\rho)\bar{E}_{ab}$ and hence a more rapid relative decrease in the dose from $S_{20}$ for the thicker polystyrene compensator as opposed to that for the thicker lead compensator.

The overall effect of the larger magnitude and rate of reduction of the scattering angle for the larger field size is also evident from examination of figures #93-98. The larger change(and greater rate of change) in the scattering angle for the larger field size causes a larger relative increase in cross section and energy of scattered photons and the product $(\mu/\rho)\bar{E}_{ab}$ and also a greater decrease in attenuation path length and linear attenuation coefficients of the scattered photons. All these factors act to lessen the rate of relative dose reduction as retraction distance increases to a greater extent for larger fields in comparison to smaller fields. The magnitude of this effect depends on the actual angles involved which in turn depend on measurement depth and compensator thickness.

For a given field size, depth, energy, and compensator material it is observed that a thicker compensator will exhibit a greater reduction in relative dose at a given depth than will a thinner compensator of the same material. The dose DP(r) at point P from any field size will consist of the dose D(prim) due to attenuated primary photons plus the dose DS(r) due to scatter at a given retraction distance r. Thus the relative dose at any given retraction distance r to that at zero retraction distance r=0 will be

$$R(r) = \frac{DP(r)}{DP(r=0)} = \frac{D(prim)+DS(r)}{D(prim)+DS(r=0)} \qquad [5.28]$$

and

$$D(prim) > DS(r=0) > DS(r) \qquad [5.29]$$

As the thickness of the compensator increases the dose due to primary photons will decrease due to increased primary attenuation in the thicker compensator. Differentiating with respect to t one has

$$\frac{d(D(prim))}{dt} < 0 \qquad [5.30]$$

The increased scattering mass of the thicker compensator will tend to increase the scatter dose as more scattered photons will be produced but this will be tempered or overcome(depending on the thickness and the scattering angle) by the increased attenuation of both the primary and scattered photons due to the greater attenuation pathlengths in the thicker compensator. For the thicknesses involved in this work the scatter does increase as thickness increases and thus one has

$$\frac{d(DS(r))}{dt} > 0 \qquad [5.31]$$

and due to the difference in solid angles

$$\frac{d(DS(r=0))}{dt} > \frac{d(DS(r)}{dt} \qquad [5.31]$$

and also

$$\frac{d(D(prim))}{dt} > \frac{d(DS(r=0)}{dt} \qquad [5.32]$$

due to solid angle and the competing factors of increased scatter mass and increased attenuation in the compensator.

Upon differentiating [5.28] with respect to thickness t and collecting terms one has

$$\begin{aligned} &\frac{d(D(prim))}{dt}\,[DS(r=0)-DS(r)] \\ &+ D(prim)\left(\frac{d(DS(r))}{dt}-\frac{d(DS(r=0))}{dt}\right) \qquad [5.33] \\ &+ DS(r=0)\left(\frac{d(DS(r))}{dt}\right) - DS(r)\left(\frac{d(DS(r=0))}{dt}\right) \end{aligned}$$

The first term in [5.33] is negative and the second term in negative if r>0 and zero if r=0. Now consider the last two terms

$$DS(r=0)\left(\frac{d(DS(r))}{dt}\right) - DS(r)\left(\frac{d(DS(r=0))}{dt}\right) \leq \frac{d(DS(r=0))}{dt}\,[DS(r=0)-DS(r)] \qquad [5.34]$$

and one may write

$$\begin{aligned} &\frac{d(D(prim))}{dt}\,[DS(r=0)-DS(r)] \\ &+ D(prim)\left(\frac{d(DS(r=0))}{dt} - \frac{d(DS(r=0))}{dt}\right) \qquad [5.35] \\ &+ DS(r=0)\left(\frac{d(DS(r))}{dt}\right) - DS(r)\left(\frac{d(DS(r=0))}{dt}\right) \\ &< \left(\frac{d(D(prim))}{dt} + \frac{d(DS(r=0)}{dt}\right)[DS(r=0)-DS(r)] \\ &+ D(prim)\left(\frac{d(DS(r))}{dt} - \frac{d(DS(r=0))}{dt}\right) \end{aligned}$$

but

$$\frac{d(D(prim))}{dt} < 0$$

and

$$\frac{d(D(prim))}{dt} > \frac{d(DS(r=0)}{dt}$$

and hence

$$\frac{d(D(prim))}{dt} + \frac{d(DS(r=0))}{dt} < 0$$

and thus the numerator is negative for all values of retraction distance. This then gives for equation [5.28]

$$\frac{dR}{dt} < 0 \qquad [5.36]$$

and thus the relative reduction in dose increases as compensator thickness increases.

It is also observed that both the rate and magnitude of relative dose reduction is greater for smaller depths and least for the largest depths. This effect may be explained by observing that the solid angle of any scattering point is greatest for the smallest depth and also that the distance from that scattering point to the probe is the smallest for the smallest depth. The larger the solid angle at zero retraction and the smaller the distance from the scattering point to the measuring point the greater the magnitude and rate of reduction of the solid angle will be for any given field size, compensator thickness, compensator material, depth, and energy of incident photons. Thus the smaller the depth the greater the rate and magnitude of the relative reduction in dose will be for any given set of parameters.

For $^{60}$Co and 6MV the polystyrene compensators give greater than or equal(within experimental error) reductions in relative dose than do their comparative thickness lead compensators except for the 7cm polystyrene compensator and the 6.25mm lead compensator at 4cm depth for the 5X5cm$^2$ field. The reasons for this may be seen readily by considering the solid angles of both compensators in this situation. The distance from $S_5$ to P for the polystyrene compensator will be approximately 1.7 times the distance from $S_5$ to P for the lead compensator and thus the solid angle for $S_5$ in lead is almost 3 times greater than the solid angle for $S_5$ in polystyrene. Thus in this case the relative dose reduction for lead will be greater than for polystyrene while in all other situations the solid angles for the lead scattering points are much closer to those of polystyrene and the smaller scattering angles for polystyrene give it the greatest reduction in relative dose for $^{60}$Co and 6MV.

Finally, a number of energy dependencies are seen. The clear trend for all three energies is such that both the rate and magnitude of relative dose reduction decreases as the energy of the incident photons increases. The reasons for this are seen by examining figures #93 to #98. The larger energy gives a greater increase in cross section, scattered photon energy, average energy absorbed $\overline{E}_{ab}$ , and the product $(\mu/\rho)\overline{E}_{ab}$ as retraction distance increases and also a larger reduction in linear attenuation coefficient for polystyrene as retraction distance increases. All of these factors act to reduce both the rate and magnitude of relative dose reduction and stem from the fact that the higher the energy of the incident photons the more forward peaked will be the scattered photons produced by Compton scatter.

The magnitude of decrease of the linear attenuation coefficient of lead as retraction distance increases is, as shown in Fig.#96, greatest for the lowest energy and least for the highest energy. This is opposite to the energy dependence of the linear attenuation coefficient of polystyrene. Thus the reduction in rate and magnitude of relative dose reduction for lead compensators is less than that for polystyrene compensators as energy increases and the amount by which polystyrene exhibits a greater reduction than the comparative thickness lead compensator will decrease with increasing energy. The reduction in relative dose for the lead compensators will become greater than that for polystyrene at some energy and this is observed at 15MV where the reduction in relative dose for Pb is greater than that for the comparative thickness polystyrene compensators. For this reason, the polystyrene compensators will exhibit cross over points at larger retraction distances than their comparative thickness Pb compensators at 15MV. Further, the pair production cross section for lead is much greater than that for polystyrene at 15MV, as table #2 shows, and hence the lead compensator will give a comparatively larger dose due to bremsstrahlung and positron annihilation quanta than will polystyrene. This will tend to increase both the magnitude and rate of relative dose reduction as equations [5.18], [5.19], and [5.20] show.

## 5.4 Scatter and Attenuation

### 5.4.1 Quantitative Analysis of the Experimental Data

Referring again to the experimental data concerning the alteration of surface dose, as seen in figures #48 to #65, the reduction in surface dose can be quite large for even moderate retraction distances. At the maximum retraction distance obtainable under experimental conditions the reduction ranges from a minimum of 56% at 25cm retraction for a 20X20cm$^2$ field and a 2cm polystyrene compensator at $^{60}$Co to a maximum of 96% at 30cm retraction distance for a 5X5cm$^2$ field with a 6.25mm lead compensator at 15MV. Such substantial reductions in surface dose certainly justify the retraction of the compensator away from the surface of the patient when the intent is to reduce the surface dose.

When comparing the relative merits of using lead as opposed to polystyrene as a compensator material one sees that under certain conditions lead gives a larger surface dose than polystyrene and under other circumstances lead gives a smaller surface dose than does polystyrene.

When lead does give a larger surface dose than polystyrene it does so only for small retraction distances(<8cm) and for all retraction distances greater than 8cm the surface dose from lead is found to be less than that of polystyrene. The ratio of the dose from lead to that from polystyrene decreases as retraction distance is increased for small retraction distances, goes through a minimum, and then increases as retraction distance is increased further. The existence of these minima show that selection of material on the basis of achieving the optimum reduction in surface dose is retraction distance dependent.

The experimental data demonstrating the alteration in dose at depth is shown in figures #67 to #90. The magnitude of reduction in dose at depth resulting from the retraction process is seen to be much less than that of the surface dose. The maximum reduction for any given set of parameters occurs at the largest retraction distance obtainable and this maximum ranges in magnitude from a minimum of about 0.55% at depths of 12 and 13cm, for a 2cm polystyrene compensator at 15MV and a 1.75mm lead compensator at 6MV respectively, at 30cm retraction for a 5X5cm$^2$ field, to a maximum of about 14.25% at a depth of 4cm for a 7cm polystyrene compensator at 23.8cm retraction for a 20X20cm$^2$ field at $^{60}$Co. For a given compensator and field size the range in the magnitude of the alteration in dose can vary from as little as 0.3% over a range of depths from 6 to 12cm for a 5X5cm$^2$ field with 1.75mm lead compensator at 15MV to as much as 6.5% over a range of depths from 4 to 12cm for a 10X10cm$^2$ field with a 7cm polystyrene compensator at $^{60}$Co.

While the magnitude of alteration of dose at depth resulting from the retraction process is much less than that of the surface dose, it is nonetheless an alteration of significant magnitude to merit consideration in treatment planning if the goal of obtaining the greatest possible accuracy in dose delivery is to be achieved. For the depths and field sizes and compensator thicknesses and compensator materials and beam energies employed in this work, the error which would result from failing to take into account the alteration in dose at depth resulting from the retraction process can be as low as only about 0.5%, but it can also be as high as 14.25%. While an error of 0.5% may be acceptable, an error of 14% certainly is not if the ICRU recomendations as stated in Ch.1 are to be adhered to.

### 5.4.2 End Point Calculations

A simple "end-point" calculation may be employed to predict the maximum dose alteration which one may expect to obtain by the retraction process. Consider Fig.#99 in which three different geometries are irradiated by identical radiation beams. In the geometry of Fig.99(a) the absorbed dose is measured at a reference depth dr in the phantom. In Fig.#99(b) a compensator of thickness t rests on the surface of the phantom and the absorbed dose is measured at a depth d+t below the upper surface of the compensator-phanton combination. If both phantom and compensator are constructed of the same material and the measurements are made at the same distance from the source in both cases then the ratio of the absorbed dose D(d+t) of #99(b) to that of #99(a), D(dr), is the tissue phantom ratio TPR(d+t). In the geometry of Fig.#99(c) the compensator has been retracted a very great distance from the surface of the phantom such that the contribution to the measured dose from scatter originating in the compensator has effectively been

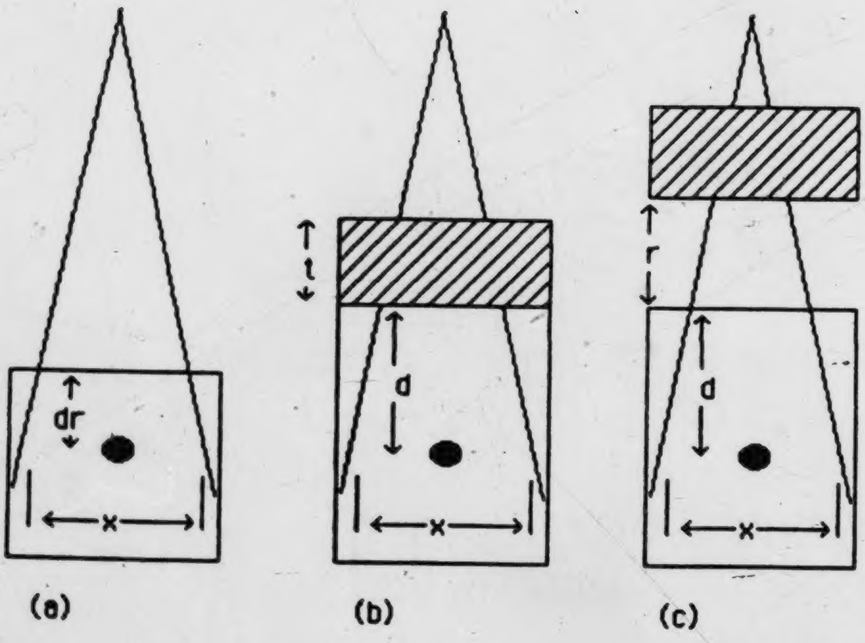
dr
x
(a)
t
d
x
(b)
r
d
x
(c)

Figure #99. Geometry of the "end point" calculations.

reduced to zero. The ratio of the absorbed dose D(d) in #99(c) to that of #99(a), D(dr), is then $TPR(d)e^{-\mu t}$, where $e^{-\mu t}$ is the attenuation of the primary beam by the compensator and $\mu$ is the narrow field linear attenuation coefficient of the compensator. Thus the ratio of the dose absorbed with the compensator retracted to a very great distance to that with the compensator resting on the phantom surface will be

$$\frac{TPR(d)e^{-\mu t}}{TPR(d+t)} \qquad [5.32]$$

The ratio thus generated by this "end point" calculation gives the maximum alteration in dose at depth which may be expected for large retraction distances(ie. ignoring radiation originating in the compensator).

These calculations were carried out for the polystyrene compensators employed in this work and the results are tabulated in tables #3, #4, and #5. For comparison purposes the experimentally measured dose reduction at the maximum retraction distance obtained is also tabulated along with the dose reduction predictions made by the Alberta treatment planning (ATP) system developed at the Cross Cancer Institute and the dose reduction predictions of the pedagogic model. The treatment planning and pedagogic model predictions are

| Depth | Field size | Compensator Material | Compensator Thickness | Experimental Reduction at 25cm Retraction | Reduction by End Point Calculation | Reduction by ATP at 25cm Retraction | Reduction by Pedagogic Model at 25cm Retraction |
|---|---|---|---|---|---|---|---|
| (cm) | (cm²) | (%) | (cm) | (%) | (%) | (%) | (%) |
| 4 | 5X5 | Pb | 0.175 | 2.5 | — | — | 3.2 |
| 4 | 5X5 | Poly | 2.0 | 2.95 | 3.55 | 4.6 | 4.0 |
| 4 | 5x5 | Pb | 0.625 | 7.25 | — | — | 8.85 |
| 4 | 5X5 | Poly | 7.0 | 6.6 | 8.0 | 12.1 | 8.6 |
| 4 | 10X10 | Pb | 0.175 | 3.65 | — | — | 3.85 |
| 4 | 10X10 | Poly | 2.0 | 4.95 | 5.25 | 6.4 | 5.2 |
| 4 | 10X10 | Pb | 0.625 | 10.4 | — | — | 11.45 |
| 4 | 10X10 | Poly | 7.0 | 12.5 | 13.1 | 17.15 | 12.6 |
| 4 | 20X20 | Pb | 0.175 | 3.7 | — | — | 3.3 |
| 4 | 20X20 | Poly | 2.0 | 5.4 | 6.7 | 7.85 | 4.45 |
| 4 | 20X20 | Pb | 0.625 | 9.2 | — | — | 9.3 |
| 4 | 20X20 | Poly | 7.0 | 14.5 | 18.85 | 22.5 | 11.3 |
| 12 | 5X5 | Pb | 0.175 | 0.86 | — | — | 0.7 |
| 12 | 5X5 | Poly | 2.0 | 0.95 | 1.9 | 3.1 | 0.9 |
| 12 | 5X5 | Pb | 0.625 | 2.2 | — | — | 2.25 |
| 12 | 5X5 | Poly | 7.0 | 2.7 | 6.1 | 10.5 | 2.4 |
| 12 | 10X10 | Pb | 0.175 | 1.6 | — | — | 1.6 |
| 12 | 10X10 | Poly | 2.0 | 2.25 | 3.3 | 4.4 | 2.15 |
| 12 | 10X10 | Pb | 0.625 | 5.1 | — | — | 5.1 |
| 12 | 10X10 | Poly | 7.0 | 6.1 | 10.0 | 14.6 | 5.9 |
| 12 | 20X20 | Pb | 0.175 | 2.3 | — | — | 6.2 |
| 12 | 20X20 | Poly | 2.0 | 3.25 | 5.1 | 6.2 | 2.6 |
| 12 | 20X20 | Pb | 0.625 | 6.5 | — | — | 5.7 |
| 12 | 20X20 | Poly | 7.0 | 9.3 | 15.5 | 19.9 | 7.4 |

Table #3. Comparison between experiment and end point calculations, ATP, and the Pedagogic model at $E(\gamma) = {}^{60}Co$.

| Depth | Field Size | Compensator Material | Compensator Thickness | Experimental Reduction at 30cm Retraction | Reduction by End Point Calculation | Reduction by ATP at 30cm Retraction | Reduction by Pedagogic Model at 30cm Retraction |
|---|---|---|---|---|---|---|---|
| (cm) | (cm$^2$) | (%) | (cm) | (%) | (%) | (%) | (%) |
| 4 | 5x5 | Pb | 0.175 | 1.7 | — | — | 2.7 |
| 4 | 5x5 | Poly | 2.0 | 2.2 | 2.45 | 2.5 | 3.5 |
| 4 | 5x5 | Pb | 0.625 | 5.9 | — | — | 8.65 |
| 4 | 5x5 | Poly | 7.0 | 5.2 | 6.5 | 7.05 | 7.9 |
| 4 | 10x10 | Pb | 0.175 | 2.8 | — | — | 3.15 |
| 4 | 10x10 | Poly | 2.0 | 3.6 | 4.05 | 4.15 | 4.25 |
| 4 | 10x10 | Pb | 0.625 | 8.55 | — | — | 9.8 |
| 4 | 10x10 | Poly | 7.0 | 9.6 | 11.35 | 12.25 | 10.8 |
| 4 | 20x20 | Pb | 0.175 | 3.2 | — | — | 2.7 |
| 4 | 20x20 | Poly | 2.0 | 4.1 | 5.45 | 5.5 | 3.75 |
| 4 | 20x20 | Pb | 0.625 | 8.4 | — | — | 8.2 |
| 4 | 20x20 | Poly | 7.0 | 11.3 | 12.45 | 16.9 | 9.65 |
| 13 | 5x5 | Pb | 0.175 | 0.55 | — | — | 0.55 |
| 13 | 5x5 | Poly | 2.0 | 0.56 | 1.35 | 1.55 | 0.75 |
| 13 | 5x5 | Pb | 0.625 | 1.75 | — | — | 1.9 |
| 13 | 5x5 | Poly | 7.0 | 1.75 | 5.45 | 6.5 | 2.05 |
| 13 | 10x10 | Pb | 0.175 | 1.0 | — | — | 1.25 |
| 13 | 10x10 | Poly | 2.0 | 1.6 | 2.55 | 2.8 | 1.75 |
| 13 | 10x10 | Pb | 0.625 | 4.0 | — | — | 4.25 |
| 13 | 10x10 | Poly | 7.0 | 4.5 | 8.15 | 9.45 | 4.9 |
| 13 | 20x20 | Pb | 0.175 | 1.56 | — | — | 1.45 |
| 13 | 20x20 | Poly | 2.0 | 2.36 | 3.8 | 4.06 | 2.06 |
| 13 | 20x20 | Pb | 0.625 | 5.3 | — | — | 4.6 |
| 13 | 20x20 | Poly | 7.0 | 6.96 | 12.5 | 13.5 | 6.05 |

Table #4. Comparison between experiment and end point calculations, ATP, and the Pedagogic model at $E(\gamma) = 6MV$.

| Depth | Field Size | Compensator Material | Compensator Thickness | Experimental Reduction at 30cm Retraction | Reduction by End Point Calculation | Reduction by ATP at 30cm Retraction | Reduction by Pedagogic Model at 30cm Retraction |
|---|---|---|---|---|---|---|---|
| (cm) | (cm²) | (%) | (cm) | (%) | (%) | (%) | (%) |
| 6 | 5x5 | Pb | 0.175 | 0.95 | — | — | 1.25 |
| 6 | 5x5 | Poly | 2.0 | 1.1 | 1.9 | 2.2 | 1.7 |
| 6 | 5x5 | Pb | 0.625 | 3.55 | — | — | 4.25 |
| 6 | 5x5 | Poly | 7.0 | 2.95 | 7.3 | 7.65 | 4.35 |
| 6 | 10x10 | Pb | 0.175 | 1.7 | — | — | 1.4 |
| 6 | 10x10 | Poly | 2.0 | 1.85 | 3.1 | 3.3 | 2.0 |
| 6 | 10x10 | Pb | 0.625 | 5.9 | — | — | 4.75 |
| 6 | 10x10 | Poly | 7.0 | 4.9 | 9.35 | 9.75 | 5.5 |
| 6 | 20x20 | Pb | 0.175 | 2.0 | — | — | 1.1 |
| 6 | 20x20 | Poly | 2.0 | 1.9 | 3.55 | 3.95 | 1.55 |
| 6 | 20x20 | Pb | 0.625 | 6.4 | — | — | 3.65 |
| 6 | 20x20 | Poly | 7.0 | 5.5 | 11.5 | 11.85 | 4.35 |
| 12 | 5x5 | Pb | 0.175 | 0.65 | — | — | 0.55 |
| 12 | 5x5 | Poly | 2.0 | 0.55 | 1.8 | 2.3 | 0.75 |
| 12 | 5x5 | Pb | 0.625 | 1.65 | — | — | 1.9 |
| 12 | 5x5 | Poly | 7.0 | 1.5 | 6.25 | 6.75 | 2.1 |
| 12 | 10x10 | Pb | 0.175 | 1.2 | — | — | 0.9 |
| 12 | 10x10 | Poly | 2.0 | 1.2 | 2.5 | 3.0 | 1.25 |
| 12 | 10x10 | Pb | 0.625 | 3.45 | — | — | 3.0 |
| 12 | 10x10 | Poly | 7.0 | 3.05 | 8.15 | 8.75 | 3.6 |
| 12 | 20x20 | Pb | 0.175 | 1.55 | — | — | 0.75 |
| 12 | 20x20 | Poly | 2.0 | 1.4 | 3.25 | 3.75 | 1.05 |
| 12 | 20x20 | Pb | 0.625 | 4.35 | — | — | 2.5 |
| 12 | 20x20 | Poly | 7.0 | 4.0 | 10.5 | 11.05 | 3.15 |

Table #5. Comparison between experiment and end point calculations, ATP, and the Pedagogic model at $E(\gamma)$ = 15MV.

discussed in the following sections.

As the 6MV and 15MV x-rays are comprised of a spectrum of photon energies, and the assignment of an effective or mean energy is approximate, the narrow field linear attenuation coefficients were not looked up in tables but rather were determined experimentally. Measurements of the linear attenuation coefficient of polystyrene were performed at 6 and 15MV for various field sizes and these attenuation coefficients are plotted in Fig.#100 and Fig.#101. The narrow beam linear attenuation coefficient for polystyrene was then determined by graphically extrapolating to zero field size as shown. The narrow field linear attenuation coefficients obtained for polystyrene are $\mu = (0.053 \pm 0.001)\ \mathrm{cm}^{-1}$ at 6MV and $(0.038 \pm 0.001)\ \mathrm{cm}^{-1}$ for 15MV.

It is to be expected that the dose reductions predicted by these end point calculations will be greater than the experimentally determined reductions due to the finite retraction distances employed. This is indeed the case as examination of tables #3, #4, and #5 show. The smallest difference between experimental and end point reductions occurs at a depth of 4cm for a $5\mathrm{X}5\mathrm{cm}^2$ field and 2cm thick polystyrene compensator at 6MV. The largest difference is observed at a depth of

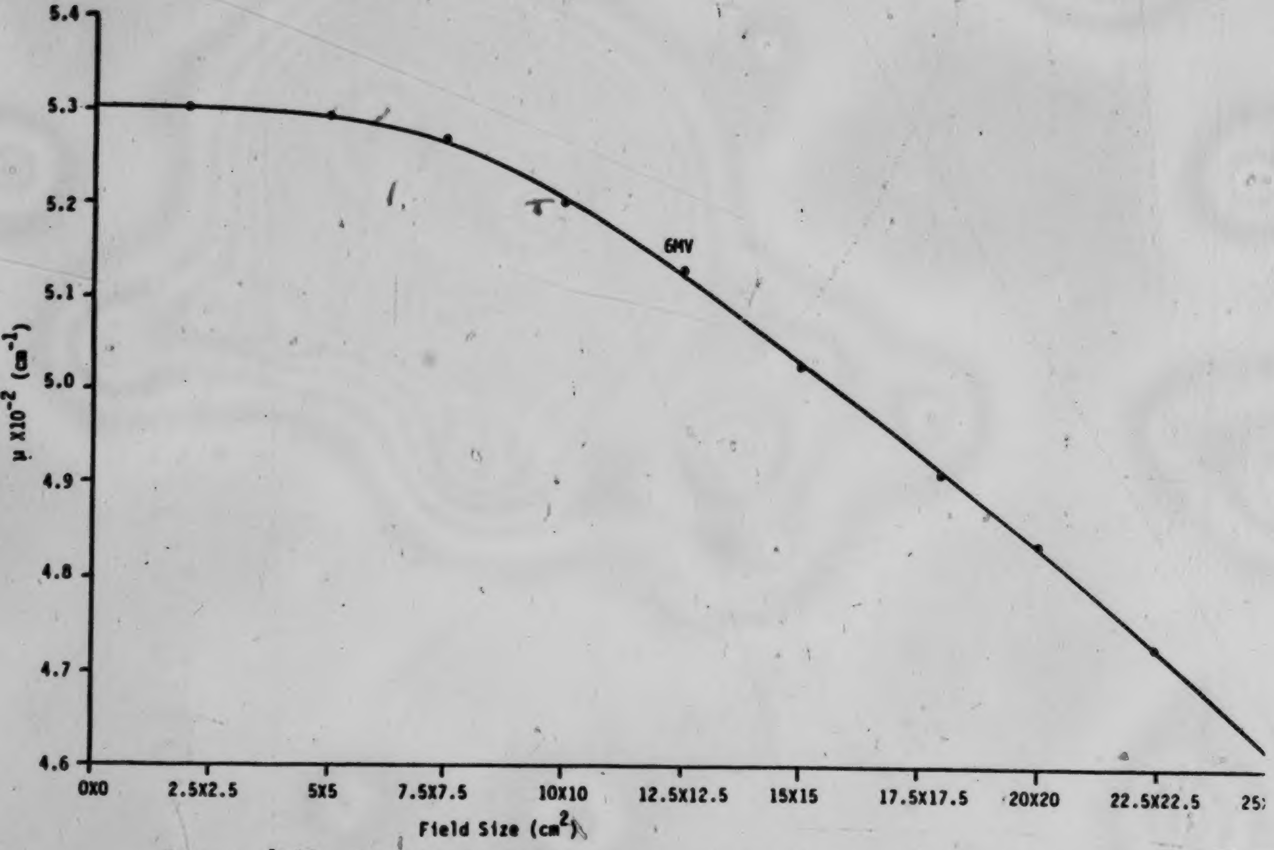

Figure #100. Graphical extrapolation of the zero field linear attenuation coefficient for polystyrene at 6MV.

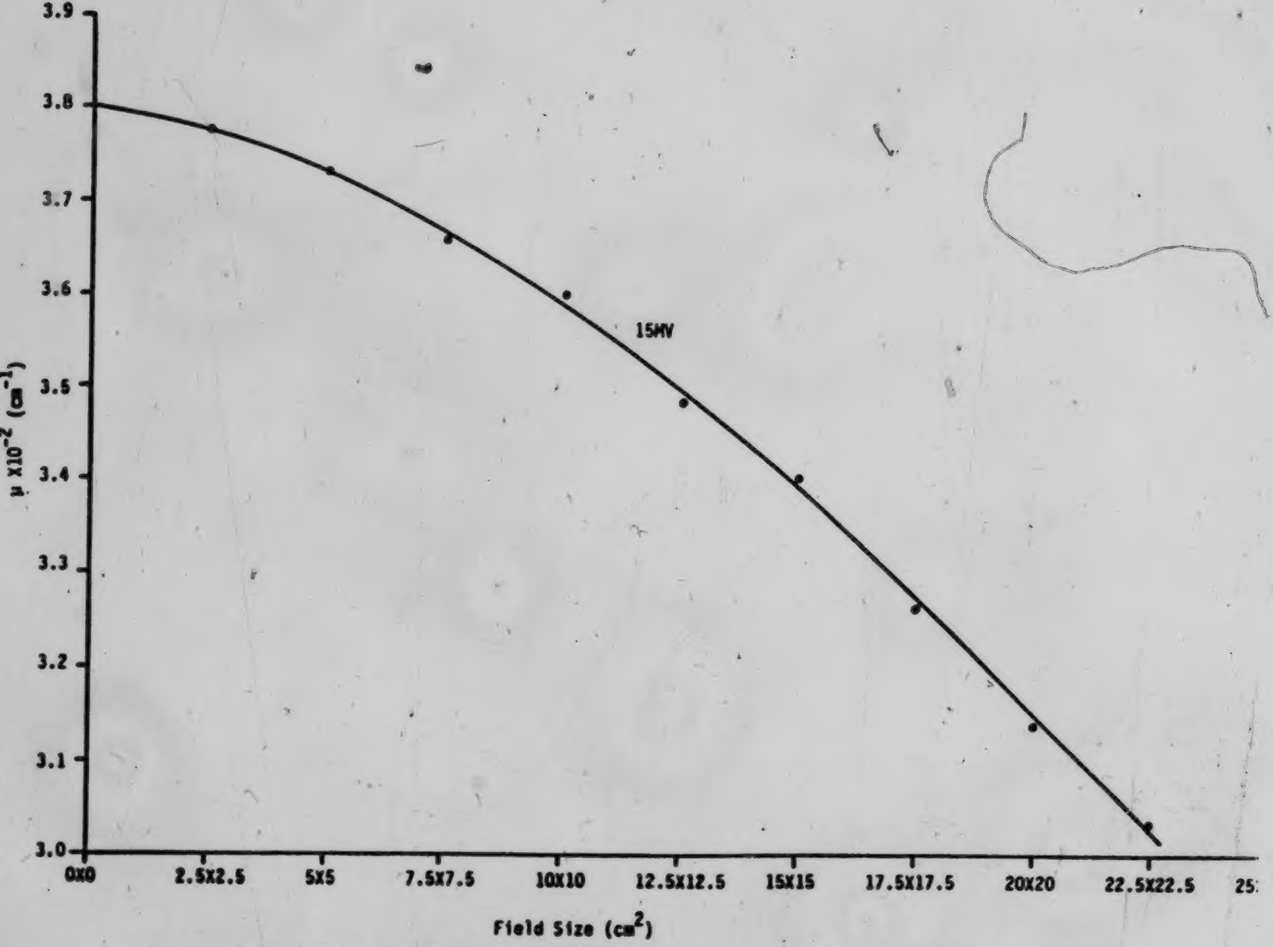

Figure #101. Graphical extrapolation of the zero field linear attenuation coefficient for polystyrene at 15MV.

12cm for a 20X20cm$^2$ field and 7cm polystyrene compensator at 15MV.

### 5.4.3 ATP Predictions

The Alberta treatment planning program ATP developed at the Cross Cancer Institute has an option for the insertion of a beam modifying device or a compensator into the beam. The basic concept of this program with regard to its treatment of compensators is shown in Fig.#102. A point P below the surface of a phantom will receive a dose due to primary radiation plus a dose due to scatter within the phantom plus a dose due to scatter from the compensator in the beam. The dose due to primary radiation will be dependent on the length of the primary ray path through both the phantom and the compensator. This ray path through a flat phantom will be least for points located on the central beam axis due to the divergence of the beam. The path length through the compensator will depend on the geometry of the compensator. The contribution to the dose from scatter originating in the phantom from portions of the beam whose ray paths have passed through thicker parts of the compensator will be less than from those whose ray paths have passed through thinner parts. On the other hand the contribution to the dose from compensator scatter will be greater for those portions

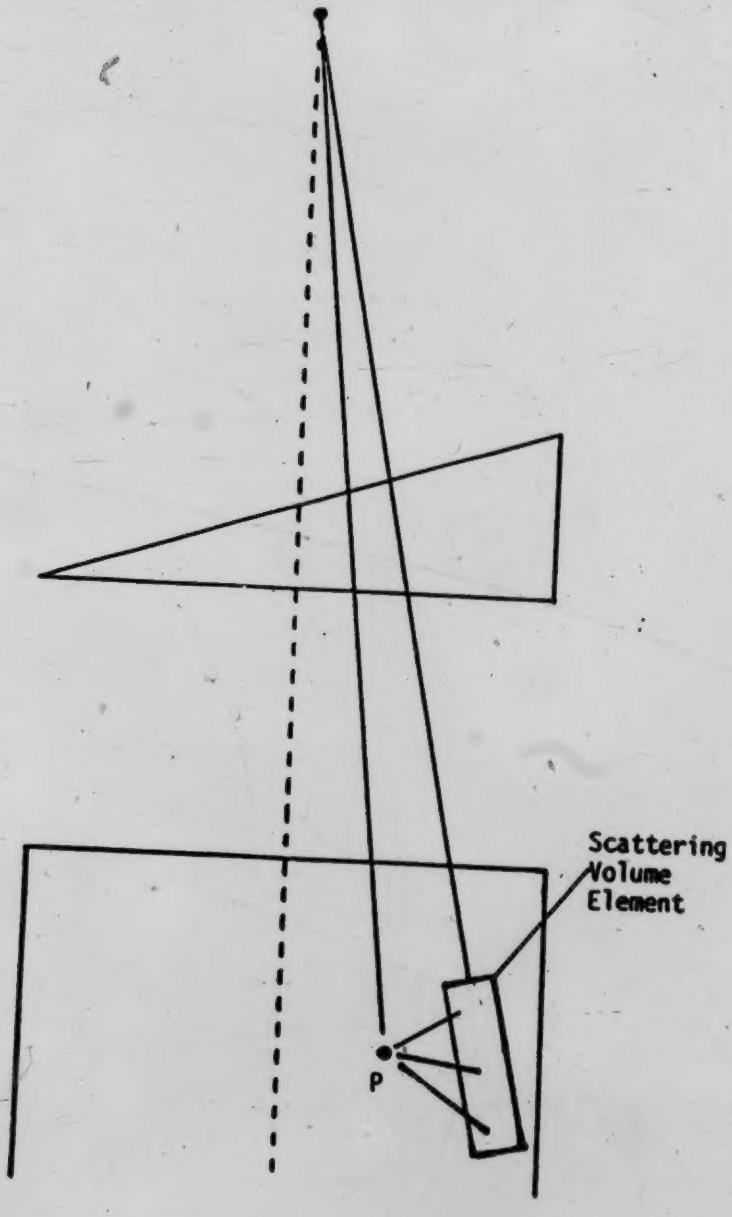
Scattering
Volume
Element
P

Figure #102. The treatment of retracted compensators by ATP.

of the beam whose ray paths pass through thicker parts of the compensator than those which pass through thinner parts. In order to take these two factors into account both the shape of the compensator and its distance of retraction from the phantom surface must be known.

ATP takes both the shape and retraction distance of the compensator into account with regard to the alteration of primary dose and the alteration of dose due to scatter arising in the phantom. The dose due to scatter arising from the compensator per se is not taken into account and the compensator is treated as a pure attenuator. Thus for points of measurement which lie along the central beam axis the only alteration in dose resulting from the retraction process, according to ATP, will be the alteration in scatter dose arising from within the phantom. If the compensator is specified to be bolus rather than a compensator the dose due to scatter from the compensator/bolus is taken into account, but this is only possible for zero retraction distance.

ATP predictions of the dose reduction at the maximum experimental retraction distance are tabulated in tables #3, #4, and #5. For all of these ATP predictions the compensator at zero retraction distance was treated as bolus. The attenuation coefficient of the compensator is a user-defined value and the values used were the extrapolated zero field values discussed in section 5.4.2. The ATP predictions for the magnitude of the dose reduction at the maximum experimental retraction distance are, as tables #3, #4, and #5 show, all greater than the actual experimental value. This is to be expected due to the fact that the dose arising from the retracted compensator was not considered. The reason for the ATP predictions being greater than the end point calculation predictions is not clear.

### 5.4.4 Pedagogic Model Predictions

The 2 dimensional pedagogic model of section 5.3.2.4 proved to be useful in understanding the manner in which the retraction process alters the dose at depth. This model has been generalized to 3 dimensions for the purpose of making numerical predictions concerning the magnitude of dose reduction resulting from the retraction process. The manner in which this was done is as follows. In order to take advantage of simplifications due to radial symmetry the square fields used experimentally were treated as circular fields. The radius of these circular fields was taken to be the radius of the circular "equivalent field" corresponding to each square field size. An equivalent field is defined as "that standard(ie circular or square) field which has the same central-axis depth dose characteristics as the given non-standard field."(55) The radii of the circular fields corresponding to the square fields of 5X5, 10X10, and 20X20cm$^2$ are 2.8, 5.6, and 11.1cm respectively. Having done this the scattering points $S_5$, $S_{10}$, and $S_{20}$ of the 2 dimensional model were each replaced by a thin scattering annulus located at midplane in the compensator. The radius of each scattering annulus was defined in the same manner as was the distance of points $S_5$, $S_{10}$, and $S_{20}$ with respect to the central beam axis. Equations [5.4] to [5.19] in conjunction with tabulated values of the mass attenuation coefficients and $\overline{E}_{ab}$ were used to predict the reduction in dose at depth for all of the experimental situations tested.

The predictions of the pedagogic model for the maximum experimental retraction distance are tabulated in tables #3, #4, and #5. Examining these tables shows that in the vast majority of cases the pedagogic model gives substantially better agreement with experiment than do either the end point calculations or ATP predictions. In only 6 out of 36 cases are the predictions of the pedagogic model worse than those of the end point calculations or ATP, and of these 6 times only 3 are worse than the ATP predictions. The pedagogic model also makes predictions for the case of lead compensators, which neither the end point calculations or ATP are capable of. In no case is the absolute discrepancy between experiment and the pedagogic model greater than ±3.2%.

All those cases in which the pedagogic model fails to give better agreement than either the end point calculations or ATP predictions occur at shallow depths at $^{60}$Co and 6MV. The pedagogic model represents a finite volume of scattering material which contains a large number of scattering points by a small set of scattering points. In reality a volume of scattering points will have scattering solid angles and scattering angles which will vary markedly over its volume, while the pedagogic model assigns a single scattering solid angle and scattering angle to such a volume. This fact stands as a major flaw in the model. This was done for the sake of simplicity but it would seem reasonable to conclude that a less arbitrary representation would yield better agreement between the model and experiment. The pedagogic model suffers , as well, from a number of other flaws, as no account is taken of scatter inside the phantom or the way in which the retraction of the compensator alters it, and other sources of scatter besides compton are not taken into account.

The pedagogic model also makes predictions of the dose reduction at all retraction distances as opposed to the end point calculations and , effectively, ATP. These predictions for retraction distances ranging from zero to 30 cm are presented in figures #103, #104, and #105 along with the actual experimental values for comparison. In order to avoid reproducing the entire data set only one representative set of pedagogic model results for each energy is provided.

## 5.5 Monte Carlo Modeling

The pedagogic model of section 5.4.4 produces results which are close to the experimental results. It does this in spite of its limitations, as discussed previously. In order to more faithfully model the experimental situation and take into account as many relevant factors as possible, a Monte Carlo modeling program was employed. The program employed was the EGS( Electron Gamma Shower) Monte Carlo code which was originally developed at Stanford University for the purpose of studying the cascade of charged particles and photons produced by high energy(up to 1GeV) cosmic rays. This code was modified for use at energies appropriate to medical physics by Dr. Dave Rogers et al of the National Research Council of Canada. Since that time the EGS code has found a wide range of applications and has undergone numerous updates and refinements. For the

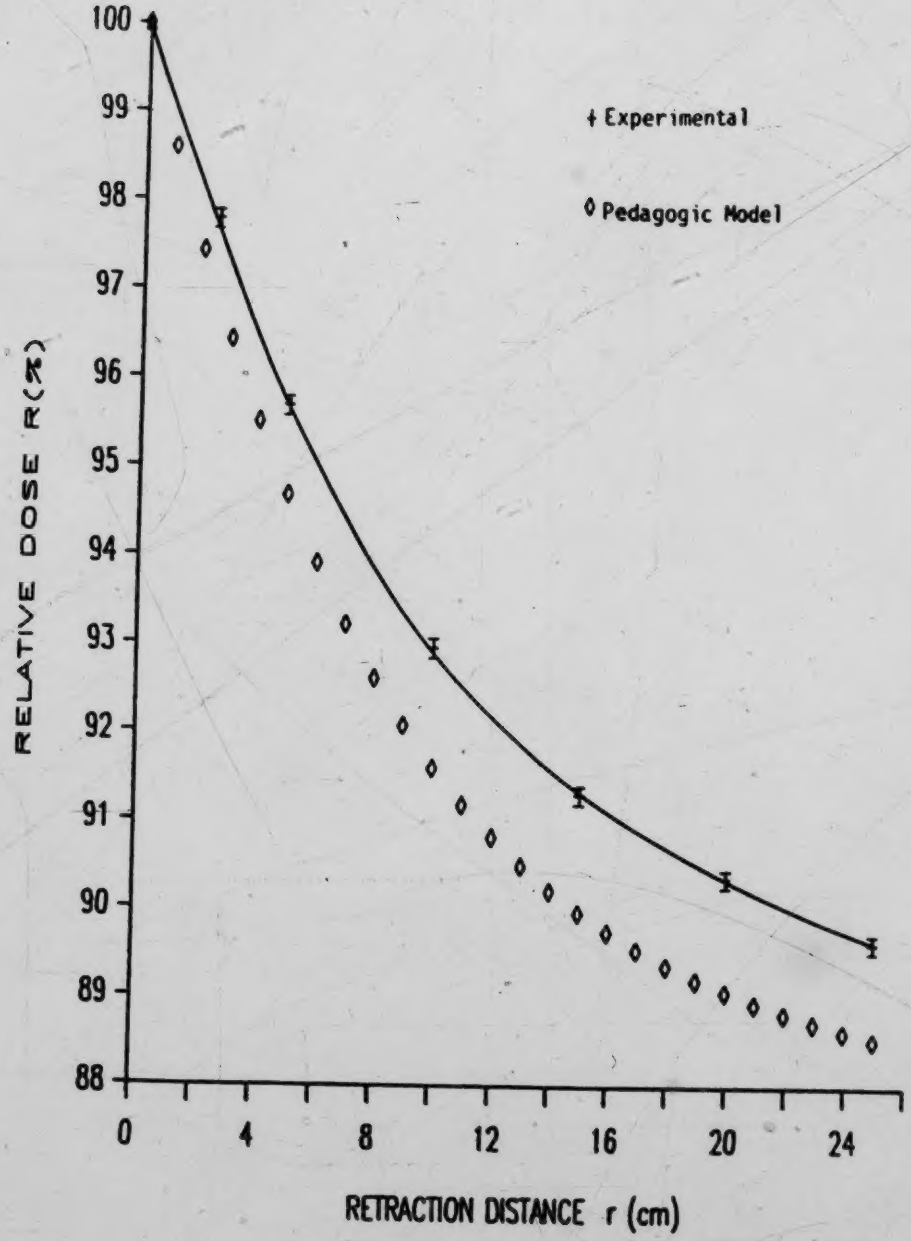

Figure #103. Comparison between experimental results and the Pedagogic model for a 10X10cm$^2$ field at 4cm depth for a Pb compensator of 6.25mm thickness.

$(E(\gamma)={}^{60}Co)$

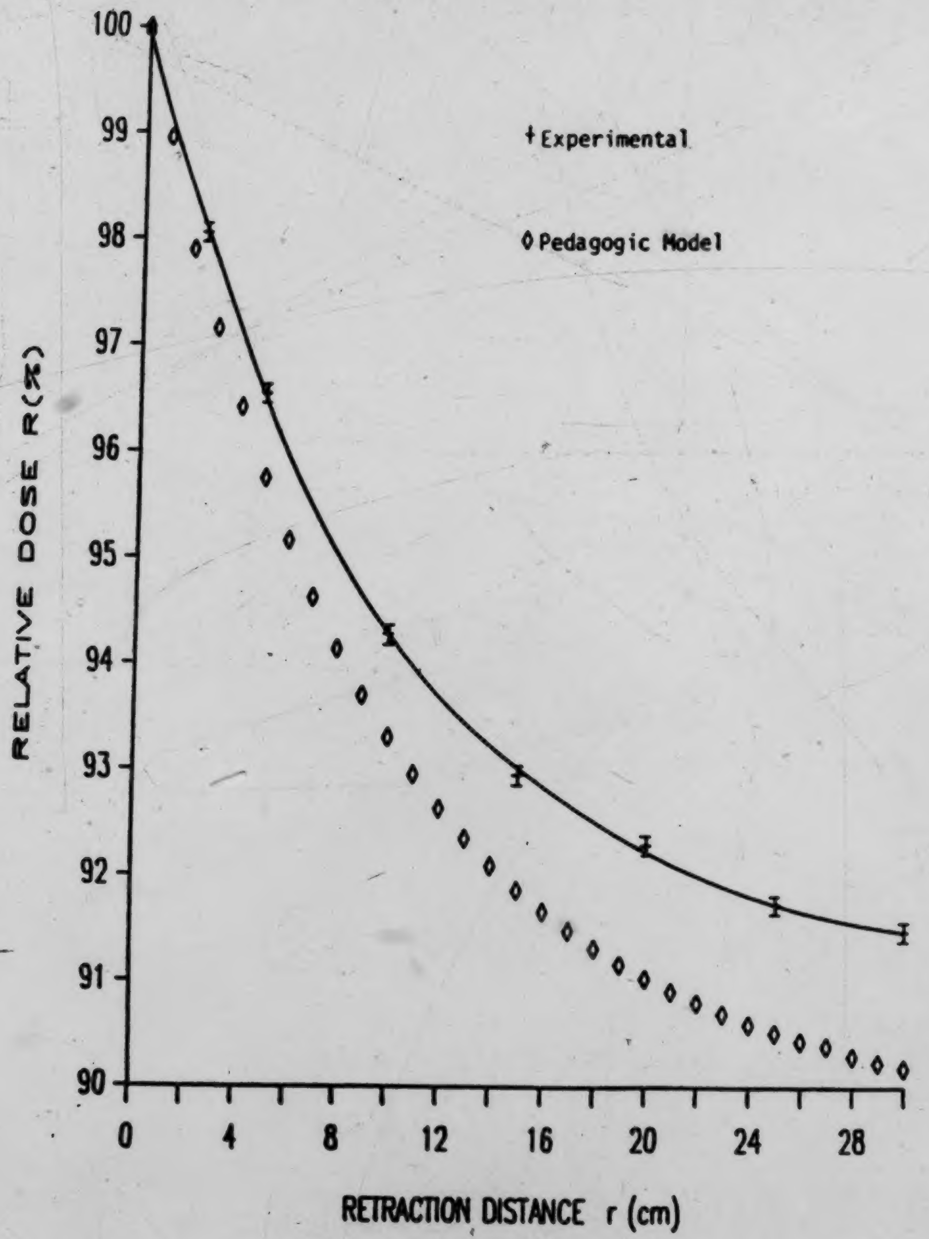

Figure #104. Comparison between experimental results and the Pedagogic model for a 10X10cm$^2$ field at 4cm depth for a Pb compensator of 6.25mm thickness. (E(γ)=6MV)

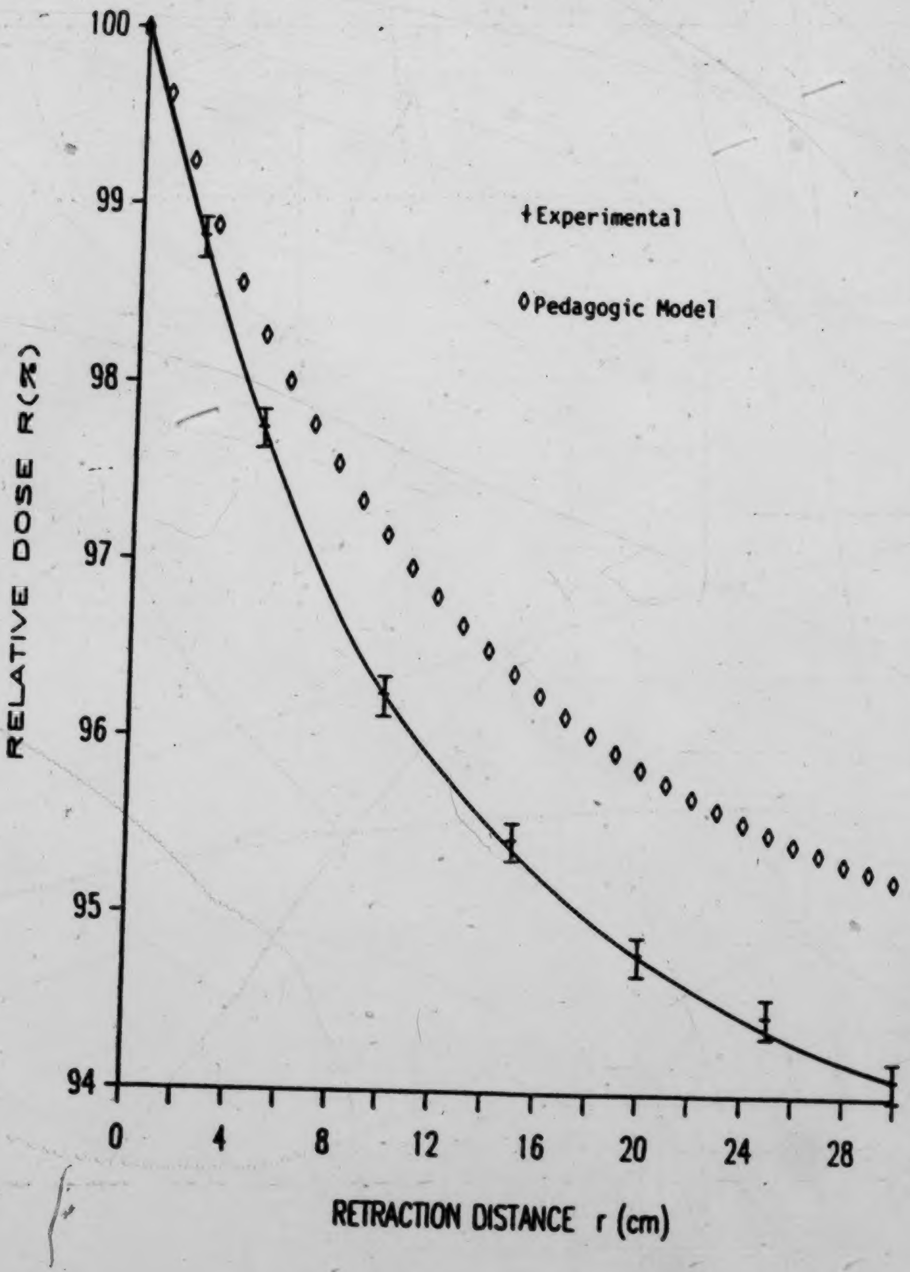

Figure #105. Comparison between experimental results and the Pedagogic model for a 10X10cm$^2$ field at 4cm depth for a Pb compensator of 6.25mm thickness. (E(γ)=15MV) results presented here, EGS version 4 was used.

EGS takes into account most of the physics required for the energies employed here. The photon interactions treated are Rayleigh scattering, photoelectric effect, Compton scattering, and pair and triplet production. The charged particle interactions treated are multiple scattering(according to Mollier's theory as formulated by Bethe), Moller scattering for electrons, Bhabha scattering for positrons, the continuous slowing down approximation, positron annihilation, and bremsstrahlung. The code lacks, among other things, general purpose routines to treat fluorescent x-rays, Auger electrons, and the binding effects in Compton scattering.

The EGS program was implemented to produce the reduction in relative dose at depth for a select number of experimental situations for comparison purposes. This was done mainly as a test of the usefulness of EGS as a research tool in this area.

### 5.5.1 EGS Results

The results obtained from the EGS program are presented in figures #106, #107, and #108. While the results of EGS do not always agree within experimental error with the experimental results, the agreement is

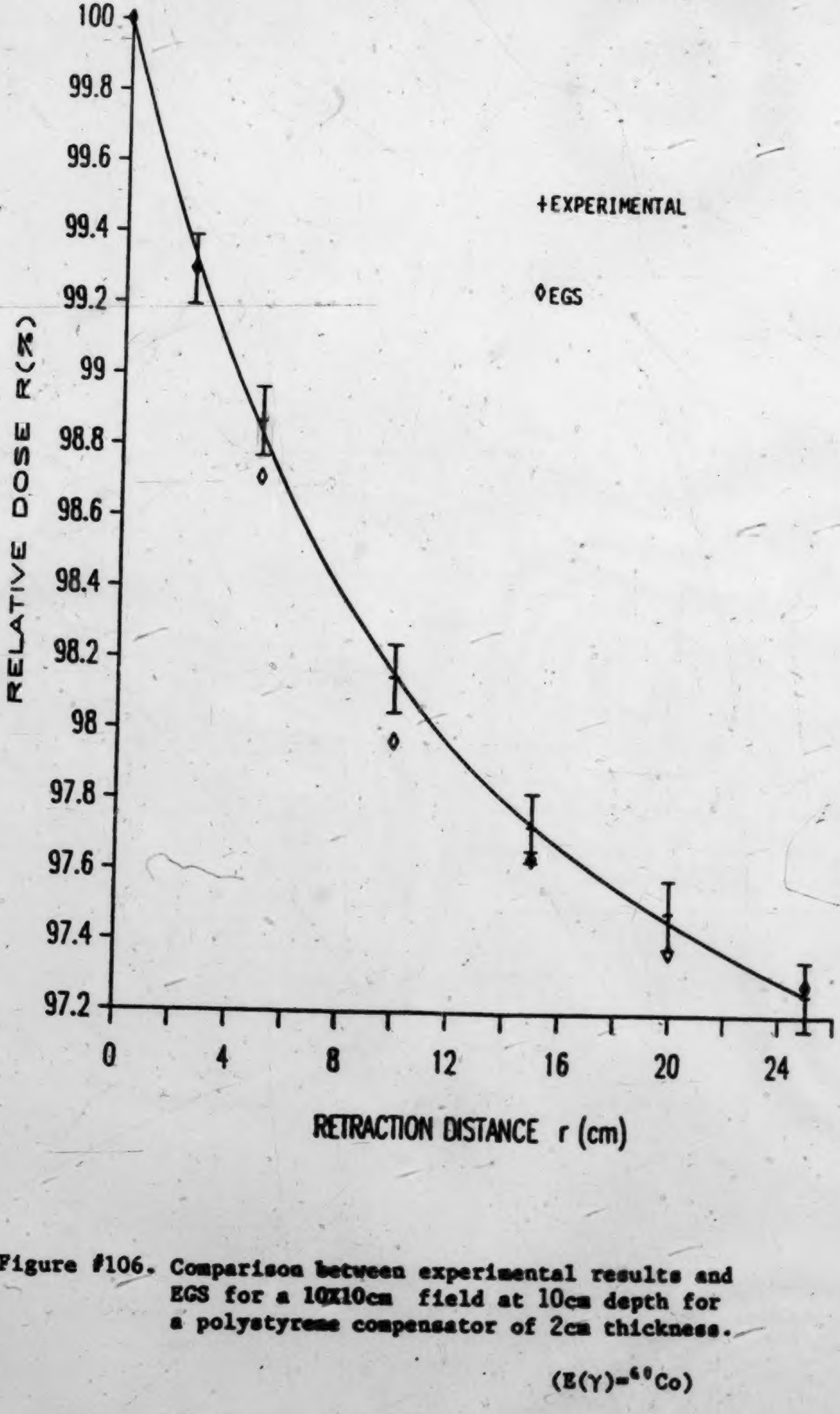

**Figure #106.** Comparison between experimental results and EGS for a 10X10cm field at 10cm depth for a polystyreme compensator of 2cm thickness.

($E(\gamma)={}^{60}Co$)

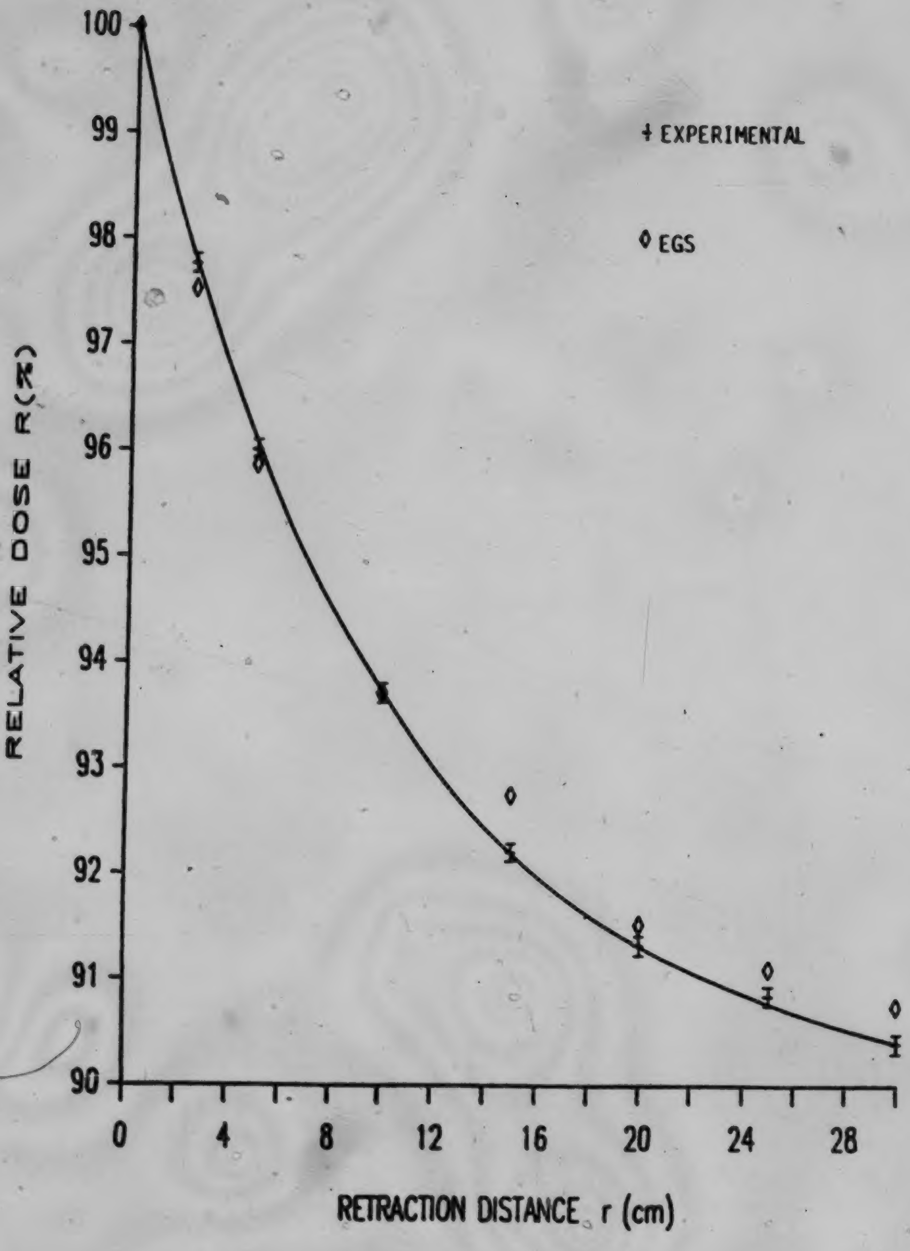

Figure #107. Comparison between experimental results and EGS for a 10X10cm field at 4cm depth for a polystyrene compensator of 7cm thickness. (E(γ)=6MV)

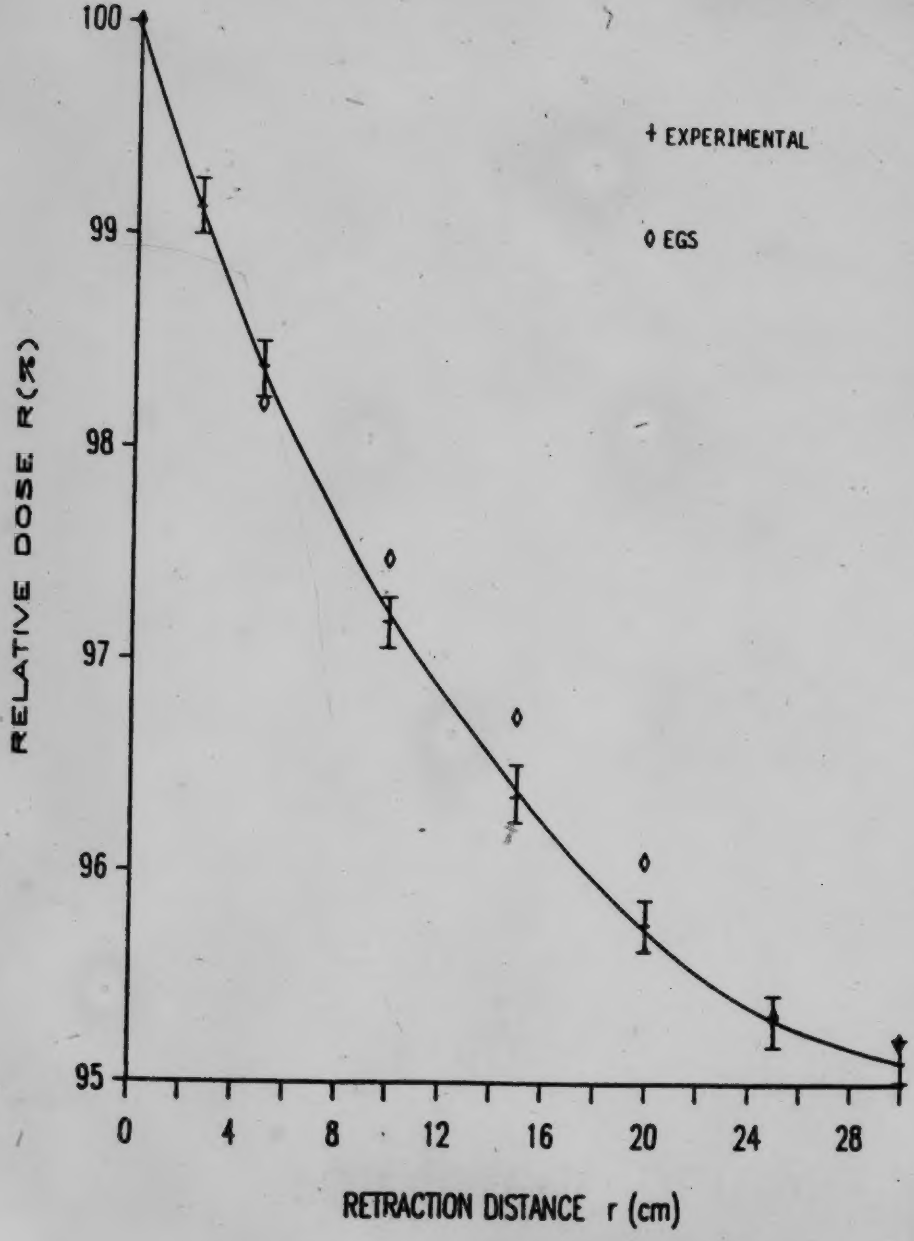

Figure #108. Comparison between experimental results and EGS for a 10X10cm field at 6cm depth for a polystyrene compensator of 7cm thickness. ($E(\gamma)$=15MV) very close. At $^{60}$Co, Fig.#106, the agreement is to better than ±0.2% while at 6MV and 15MV, Figs.#107 and #108 respectively, the difference between EGS and experiment is at no time greater than ±0.5%. This is far better agreement than the pedagogic model, but it comes at an inordinate cost in terms of computing time. Each EGS data point in figures #106, #107, and #108 required an average computation time of about 20 CPU hours on a VAX 11/780 computer. In comparison the entire data set of Fig.#103 produced by the pedagogic model required less than one minute to produce running on a home microcomputer. Thus while EGS produces by far the most accurate results, the production time required will most certainly limit EGS, in its present form, to the role of a research tool. EGS may indeed provide valuable information which will enable simpler and quicker methods of correctly predicting the alteration in dose at depth to be produced.

# VI CONCLUSIONS

The large magnitude of reduction in surface dose achieved at even moderate retraction distances justifies the retraction process in those cases in which skin sparing is desirable. The reduction in dose at depth which also results from the retraction process is not as great as that at the surface, but it is nonetheless of significant magnitude to merit consideration in most cases. Both the rate and magnitude of the reduction in dose at depth is a complicated function of retraction distance, field size, depth, compensator thickness, compensator material, and incident photon energy.

At the surface the largest reductions in dose are seen for the largest retraction distances, smallest field sizes, and highest energies. In contrast, the largest alterations in dose at depth occur for the largest retraction distances, larger field sizes, smallest depths, and lowest incident photon energies. The other factors of compensator thickness and compensator material alter the dose in a more complicated manner.

The actual magnitude of reduction varies from situation to situation depending on the particular parameters involved and failure to take into account the alteration in dose at a given depth due to compensator retraction can result in errors of up to about 14%. While such large errors do not occur in every situation, their possible existence calls for a more adequate treatment of this effect if a desired dose is to be delivered with the greatest degree of accuracy to a particular volume in the body.

# REFERENCES

(1) "Code of practice for x-ray therapy linear accelerators", Medical Physics, 2, 110-121, (1975).

(2) ICRU Report #24, Determination of Absorbed Dose in a Patient Irradiated by Beams of X or Gamma Rays in Radiotherapy Procedures, International Commision on Radiation Units and Measurements, Washington, D.C., 1976.

(3) Hubble, J.H., Photon Cross-Sections, Attenuation Coefficients, and Energy Absorption Coefficients from 10keV to 100GeV, NSRDA - NBS 29, U.S. Department of Commerce, 1969

(4) Ibid.

(5) Nelms, A.T., Graphs of the Compton Energy-Angle Relationship and the Klein-Nishina Formula from 10keV to 500ZMeV, N.B.S. Circular, 542, U.S. Department of Commerce, 1953.

(6) Ibid.

(7) Hubble, loc. cit.

(8) Ibid.

(9) Mott, N.F., Gonville, M.A., College, C., "The Polarization of Electrons by Double Scattering", Proceedings of the Royal Society of London, A135, 429-458, (1932).

(10) Goudsmit, G.A., and Saunderson, J.L., "Multiple Scattering of Electrons", Physical Review, 89, 24-29, (1953).

(11) Bethe, H,A., "Moliere's Theory of Multiple Scattering", Physical Review", 89, 1256-1266, (1953).

(12) Snyder, H., Scott, W.T., "Multiple Scattering of Fast Charged Particles", Physical Review, 76, 220-225, (1949).

## REFERENCES (CONT'D)

(13) Berger, M.J., and Seltzer, S.M., Evaluation of Collision Stopping Power of Elements and Compounds for Electrons and Positrons", International Journal of Applied RAdiation and Isotopes, 133, 1189-1218, (1982).

(14) Rich, J.A., "Experimental Evidence for the Three - Photon Annihilation of an Electron-Positron Pair", Physical Review, 81, 140-141, (1951).

(15) ICRU Report #24, Loc. cit.

(16) Burkell,C.C., Watson, T.A., Johns, H.E., Horsley, R.J., "Skin Effects of Cobalt 60 Telecurie Therapy", British Journal of Radiology, 27, 171-176, (1954).

(17) Hendee, W.R., Medical Radiation Physics, (Chicago: Year Book Medical Publishers, 1973), p 230.

(18) Ellis, F., Hall, E.J., Oliver, R., "A Compensator for Variations in Tissue Thickness for High Energy Beams", British Journal of Radiology, 32, 421-422, (1959).

(19) Hall, E.J., Oliver, R., "The use of Standard Isodose Distributions with High Energy Radiation Beams-The Accuracy of a compensator Technique in Correcting for Body Contours", British Journal of Radiology, 34, 43-52, (1961).

(20) Wilks, R.W., Casebow, M.P., Tissue compensation with lead for Cobalt 60 therapy", British Journal of Radiology, 42, 452-456, (1969).

(21) Laursen, J.F., Andersen, H.C., Hansen, H.P., "3D thin lead sheet compensating system", Medical Physics, 9, 741-745, (1982).

(22) Thomas, R.L., "Tissue compensation-difference compensators", British Journal of Radiology, 55, 859-861, (1982).

(23) Cohen, M., Burns, J.E., Sear, R., "Physical aspects of cobalt 60 teletherapy using wedge filters. 2 Dosimetric considerations", Acta Radiologica, 53, 486-504, (1960).

## REFERENCES (CONT'D)

(24) Leung, P.M.K., Van Dyk, J., Robins, J., "A method of large irregular field compensation", British Journal of Radiology, 47, 805-810, (1974).

(25) Ellis, F., Feldman, A., Oliver, R., "Compensation for tissue inhomogeneity in cobalt 60 therapy", British Journal of Radiology, 37, 795-798, (1964).

(26) Hall, E.J., Oliver, R., "The use of Standard Isodose Distributions with High Energy Radiation Beams-The Accuracy of a compensator Technique in Correcting for Body Contours", British Journal of Radiology, 34, 43-52, (1961).

(27) Wilks, R., Casebow, M.P., Loc. cit.

(28) Leung, P.M.K., Van Dyk, J., Robins, J., Loc. cit.

(29) Boyer, A.L., "Compensating filters for high energy x rays", Medical Physics, 9, 429-433, (1982).

(30) Huang, P., Chin, L.M., Bjarngard, B.E., "Scattered photons produced by beam-modifying filters", Medical Physics, 13, 57-63, (1986).

(31) Khan, F.M., Moore, V.C., Burns, D.J., "The Construction of Compensators for Cobalt Teletherapy", Radiology, 96, 187-192, (1970).

(32) Sewchand, W., Bautro, N., Scott, R.M., International Journal of Radiation Oncology, Biology and Physics, 6, 327-331, (1978).

(33) van de Geijn, J., "The construction of individual intensity modifying filters in cobalt 60 teletherapy", British Journal of Radiology, 38, 865-870, (1965).

(34) Ibid.

(35) Wilks, R.W., Casebow, M.P., Loc. cit.

(36) van de Geijn, J., Loc.cit.

## REFERENCES (CONT'D)

(37) Khan, F.M., Moore, V.C., Burns, D.J., "An Apparatus for the Construction of Irregular Surface Compensators for Use in Radiotherapy", Radiology, 90, 593-594, (1968).

(38) Watkins, D.M.B., "A proposed method for making reduced wax compensators for use with high-energy radiation beams", British Journal of Radiology, 48, 760-762,(1975).

(39) Sorensen, N.E., "A Simple Method for the Construction of Compensators for "Missing Tissue"", Physics in Medicine and Biology, 13, 113-115, (1968).

(40) Renner, W.D., O'Conner, T.P., Amtey, S.R., Reddi, P.R., Bahr, G.K., Kereiakes, J.G., "The Use of Photogrammetry in Tissue Compensator Design", Radiology, 125, 505-510, (1977).

(41) Lerch, I.A., Barish, R.J., "Development of optical process for accessing three-dimensional patient topology", Medical Physics, 5, 546-549, (1978).

(42) Boyer, A.L., Goitein, M., "Simulator mounted Moire topography camera for constructing Compensating filters", Medical Physics, 17, 19-25, (1980).

(43) Renner, W.D., "Photogrammetry applied to radiation therapy", Treatment Planning ,6, 10-17, (1981).

(44) Mok, E.C., Boyer, A.L., "Compensator filters made with compact Moire camera and computer", Medical Physics, 11, 513-515, (1984).

(45) Ellis, F., Lescrenier, C., "Combined Compensation for Contours and Hetrogeneity", Radiology, 106, 191-194, (1973).

(46) Dixon, R.L., Ekstrand, K.E., Ferree, C., "Compensating Filter Design Using Megavoltage Radiography", International Journal of Radiation Oncology, Biology and Physics, 5, 281-287, (1979).

## REFERENCES (CONT'D)

(47) Renner, W.D., O'Connor, T.P., Bermudez, N.M., "An electronic device for digitizing radiotherapy films for the construction of tissue compensators", Medical Physics, 9, 910-916, (1982).

(48) Renner W.D., O'Conner, T.P., Bermudez, N.M., "A note on designing tissue compensators for parallel opposed fields", Medical Physics, 10, 483-486, (1983).

(49) Lindskoug, B.A., Notter, G., "Design of flattening filters based on intercavitary absorbed dose measurements in external radiation therapy", British Journal of Radiology, 53, 976-980, (1980).

(50) Goitein, M., "Compensation for Inhomogeneities in Charged Particle Radiotherapy Using Computed Tomography", International Journal of Radiation Oncology, Biology and Physics, 4, 499-508, (1978).

(51) Flynn, M.J., "Dosimetric evaluation of automatic tissue compensator design", Medical Physics, 8, 558, (1981).

(52) Jackson, W., "Wax retraction as a technique for compensating the effect of surface irregularities in high-energy radiotherapy", British Journal of Radiology, 43, 859-867, (1970).

(53) Thomas, R.L., Loc. cit.

(54) Huang, P., Chin, L.M., Bjarngard, B.E., "Scattered photons produced by beam-modifying filters", Medical Physics, 13, 57-63, (1986).

(55) White, D.R., "The Photon Attenuation and Absorbtion Properties of Clear and White Polystyrene", British Journal of Radiology, 51, 379-380, (1978).